IntechOpen

Ceramic Materials

Edited by Wilfried Wunderlich

Ceramic Materials

edited by
Wilfried Wunderlich

Ceramic Materials
http://dx.doi.org/10.5772/243
Edited by Wilfried Wunderlich

© The Editor(s) and the Author(s) 2010
The moral rights of the and the author(s) have been asserted.
All rights to the book as a whole are reserved by INTECH. The book as a whole (compilation) cannot be reproduced, distributed or used for commercial or non-commercial purposes without INTECH's written permission.
Enquiries concerning the use of the book should be directed to INTECH rights and permissions department (permissions@intechopen.com).
Violations are liable to prosecution under the governing Copyright Law.

Individual chapters of this publication are distributed under the terms of the Creative Commons Attribution 3.0 Unported License which permits commercial use, distribution and reproduction of the individual chapters, provided the original author(s) and source publication are appropriately acknowledged. If so indicated, certain images may not be included under the Creative Commons license. In such cases users will need to obtain permission from the license holder to reproduce the material. More details and guidelines concerning content reuse and adaptation can be foundat http://www.intechopen.com/copyright-policy.html.

Notice

Statements and opinions expressed in the chapters are these of the individual contributors and not necessarily those of the editors or publisher. No responsibility is accepted for the accuracy of information contained in the published chapters. The publisher assumes no responsibility for any damage or injury to persons or property arising out of the use of any materials, instructions, methods or ideas contained in the book.

First published in Croatia, 2010 by INTECH d.o.o.
eBook (PDF) Published by IN TECH d.o.o.
Place and year of publication of eBook (PDF): Rijeka, 2019.
IntechOpen is the global imprint of IN TECH d.o.o.
Printed in Croatia

Legal deposit, Croatia: National and University Library in Zagreb

Additional hard and PDF copies can be obtained from orders@intechopen.com

Ceramic Materials
Edited by Wilfried Wunderlich

p. cm.

ISBN 978-953-307-145-9

eBook (PDF) ISBN 978-953-51-5923-0

We are IntechOpen, the world's leading publisher of Open Access books

Built by scientists, for scientists

4,200+
Open access books available

116,000+
International authors and editors

125M+
Downloads

Our authors are among the

151
Countries delivered to

Top 1%
most cited scientists

12.2%
Contributors from top 500 universities

WEB OF SCIENCE™

Selection of our books indexed in the Book Citation Index in Web of Science™ Core Collection (BKCI)

Interested in publishing with us?
Contact book.department@intechopen.com

Numbers displayed above are based on latest data collected.
For more information visit www.intechopen.com

Contents

Preface

"Ceramic materials" is the title of this book, which describes the state-of-the-art of some aspects in this large field in engineering materials. By invitation of the publisher, several authors from ten countries, most of them do not know each other, have collected a bunch of chapters which cover a wide area of engineering science. The first three chapters describe the fundamental aspects of functional ceramics for thermoelectric, semiconductor and fuel cell applications. Chapters 4, 5 and 6 describe the processing of nano-ceramics and their characterisation. The following chapters describe structural ceramics; chapter 7 describes a new hardness characterisation method for thin films, and chapters 8 and 9 describe ceramic materials for dental applications. Finally, chapters 10 and 11 describe the re-use of ceramics for new structural applications.

This is the first book of a series of forthcoming publications on this field by Sciyo publisher. The reader can enjoy both a classical printed version on demand for a small charge, as well as the online version free for download. Your citation decides about the acceptance, distribution, and impact of this piece of knowledge. Please enjoy reading and may this book help promote the progress in ceramic development for better life on earth.

Editor

Prof.Dr. Wilfried Wunderlich
Tokai University, Dept. Mat.Sci.,
Japan

1

Development of Thermoelectric materials based on $NaTaO_3$ - composite ceramics

Wilfried Wunderlich[1] and Bernd Baufeld[2]
[1] *Tokai University, Dept. Material Science., Kitakaname 1117, Hiratsuka-shi, Japan*
[2] *Kath. Universiteit Leuven, Dpt MTM Metallurgy and Ma. Eng., Leuven, Belgium*

1. Introduction

This chapter describes the development of novel thermoelectric materials for high-temperature applications like gas burners, combustion engines, nuclear fuel, or furnaces. The goal of this development is to recycle waste heat for energy harvesting in order to contribute in saving the environment. The research results are described in the following sub-chapters in four different sections.

After a general review about perovskites and $NaTaO_3$ in section 2, *ab-initio*-simulations of the Seebeck coefficient are described in section 3. The Seebeck coefficient strongly depends on the effective mass and carrier concentration. The electronic band-structure calculations showed a large electron effective mass for $NaTaO_3$. Heavily doping changes $NaTaO_3$'s band-structure in a similar way as the well-known thermoelectric material Nb-doped $SrTiO_3$. Hence, $NaTaO_3$, which is stable up 2083 K and which is known as a material with excellent photo-catalytic properties, was chosen as a candidate for thermoelectric materials.

Section 4 describes the finding of suitable doping elements by sintering $NaTaO_3$ with different raw materials. While both, pure $NaTaO_3$ and $NaTaO_3$ sintered with Fe_2O_3, are almost insulators, it was discovered that sintering with metallic iron increases both, electric conductivity and Seebeck coefficient. Microstructural characterization by SEM and XRD measurements showed that a $NaTaO_3$-Fe_2O_3 composite material is formed. The amount of Fe solved in the $NaTaO_3$ lattice is much higher when the starting materials consist of Fe instead of Fe_2O_3. Addition of several metals like Mn, Cr, Ti, Ni, Cu, Mo, W, Fe, and Ag were tested, but only the later two elements lead to remarkable electric conductivity observed above 773 K.

Section 5 describes the measurement of thermoelectric properties such as Seebeck-voltage at a large temperature gradient, a method which is close to applications, but not yet commonly used, because the thermoelectric theory is based on small temperature gradients. Thermal conductivity is not measured, but only estimated. The doping is achieved by sintering metallic iron or silver together with $NaTaO_3$. The results are high negative Seebeck voltages up to -320 mV at a temperature difference of 700 K, as well as high closed-circuit currents up to -250 μA for Fe-doping and positive values for Ag-doping. Besides reporting previous results, several new findings are described here for the first time. Composites with Cu yield

to a small Seebeck voltage of about -10 mV with a strong response, when heat flow direction is reversed.
In section 6 the thermokinetic measurement by differential scanning calorimetry (DSC) and thermoanalysis (TA) clarifies the reaction sintering between Fe and $NaTaO_3$. The experimental data obtained at different heating rates were analyzed by Friedman analysis and showed a characteristic shape in the plot of energy versus partial area. Further directions of improvement, like improving the densification by sintering, are mentioned in the last section under discussions.

2. Perovskite structure

2.1 Functional Engineering Materials based on Perovskite Crystal structure

The goal of this book chapter is to describe the development of new thermoelectric materials (TE), whose most important features are described first. Then the perovskite structure is reviewed, before focusing on the main topic, $NaTaO_3$.
Successful thermoelectrics have to be semiconductors [Sommerlate et al. 2007, Nolas et al. 2001, Ryan&Fleur 2002, Bulusu et al.2008], so there are two possible approaches in TE development, one from the ceramic side, which have large Seebeck coefficients, and one from the metal side, which have large electric conductivity, but a rather poor Seebeck coefficient. The main goal of development for ceramics, which are the focus in this book, is the improvement of the electric conductivity. The engineering targets of such TE-ceramics are applications in any combustion engines, gas turbines, power plants including nuclear power plants, furnaces, heaters, burners or in combination with solar cells or solar heaters as illustrated in fig. 1.

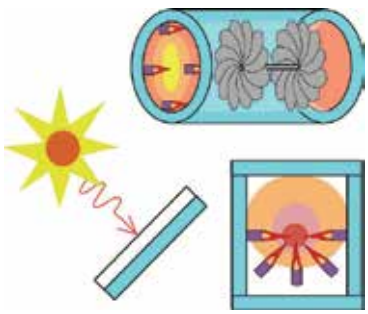

Fig. 1. Possible applications for high-temperature thermoelectric ceramics (in blue color) in solar cells, solar heaters, combustion engines or gas turbines.

The service temperatures of such devices are usually too high as to be applicable for other TE materials. The temperature difference [Ryan& Fleur 2002] between the hot chamber inside and the (cold) ambient environment is considered as the energy source for these energy conversion devices, which have a long life time and low maintenance costs, because there are no rotating parts. The main advantage is that any waste heat can be converted into electricity. Hence, advanced thermoelectrics are both, environment-friendly eco-materials and energy materials, which main purpose is producing energy. For a wide range of applications, materials with higher energy conversion efficiency than present TEs need to be found, in order to be considered as clean energy sources helping to solve the severe CO_2-

problem. One important indicator for efficient thermoelectric material is the figure-of-merit *ZT*

$$ZT=S^2\sigma T/\kappa, \quad (1)$$

which should have a value significantly larger than 1 to be economically reasonable. Improvement of *ZT* requires a high Seebeck coefficient *S* and electric conductivity σ, and a low thermal conductivity *κ*. For increasing *ZT* several concepts for materials design of thermoelectrics have been introduced [Nolas et al. 2001, Ryan&Fleur 2002, Bulusu et al.2008, Wunderlich et al. 2009-c]. These are phonon-glass electron-crystal (PGEC) [Terasaki et al.1997], heavy rattling atoms as phonon absorbers, proper carrier concentration [Vining 1991, Wunderlich et al.2006], differential temperature dependence of density of states, high density of states at the Fermi energy, high effective electron mass [Wunderlich et al. 2009-a], superlattice structures with their confined two-dimensional electron gas [Bulusu et al. 2008, Ohta et al. 2007, Vashaee & Shakouri 2004], and electron-phonon coupling [Sjakste et al. 2007]. As all these factors can influence also the material focused in this chapter $NaTaO_3$, at first basic principles of the Pervoskite crystal structure are briefly reviewed, as this interdisciplinary approach is supposed to gain important understanding for future improvement.

The interest on Perovskite structure related materials has dramatically increased in the past three decades after the discovery of many superior solid-state properties, which makes Perovskite materials or their layered derivatives record holders in many fields of solid state physics as shown in fig. 2. The most popular finding was the discovery of superconductivity in $Y_1Ba_2C_3O_{7-x}$ (YBCO) for which the Nobel Prize 1987 was provided. The present record holder is Bi2212 with a critical temperature of T_C=120K. A large scale application of YBCO since 1998 is the linear motor train using the magnetic levitation (Maglev) in Yamanashi-ken Japan, whose entire rail consists of Helium-cooled superconductors. Present portable phone technology is all based on layered (Ba,Sr)TiO_3 dielectric material [Ohsato 2001, Wunderlich et al. 2000] due to their high dielectric constant (e>10000) and quality factor. During the materials development detailed spectroscopic data of the electromagnetic resonance [Bobnar et al. 2002, Lichtenberg et al. 2001] have been measured, which further analysis can provide more understanding of electron-phonon interactions as one of the key issue for thermoelectrics based on perovskites. Piezoelectric materials on $Pb(Ti_{1-x}Zr_x)O_3$ (PZT) or the environmental benign lead free $K_{0.5}Na_{0.5}NbO_3$ (KNN) materials [Stegk et al. 2009] have an increasing application demand in actuators and sensors.

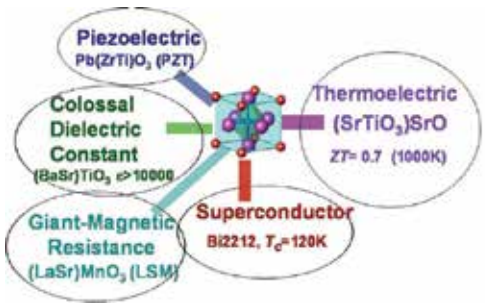

Fig. 2. As Perovskite-structure based mate-rials are record holders in many solid-state properties, they might become so in thermoelectrics too.

The main reason for the good piezoelectric properties with its large d_{33} shear component is that soft modes in the phonon spectrum appear near the morphotrophic phase boundary [Stegk et al. 2009]. This derives from the softening of the atomic bonds by adding other elements, or from increasing of the lattice constants as described in the next sub-section. The Nobel Prize 2007 has been provided for the discovery of the giant magnetic resonance (GMR) observed on Heusler-phases, but it also occurs on Perovskite interfaces as in (La,Sr)MnO_3 [Coey et al. 1999]. Similarly, for thermoelectric materials, like the layered Perovskite-relatives called Ruddlesden-Popper phases $(SrTiO_3)_n(SrO)_m$, large ZT values have been reported.

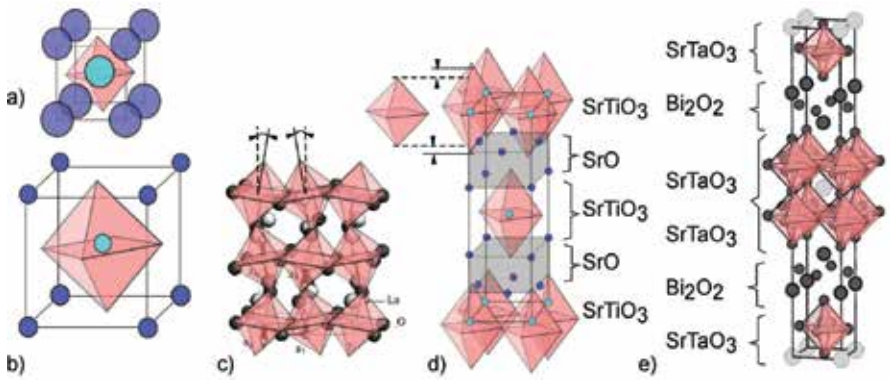

Fig. 3. Schematic drawing of the crystal structure of the perovskite structure and of relatives, (a) perovskite structure with small lattice constant compared to atomic radius, (b) same with large lattice constants, (c) tilted octahedron in $LaTiO_3$, (d) layered Ruddlesden-Popper phase with uniaxial distorted TiO_6-octahedron, (e) Aurivilius phase.

The Perovskite structure is schematically summarized in fig 3. In pure perovskites there are two extreme structural variants, expressed by the tolerance factor f [Imada et al. 1998]

$$f = \frac{r_A + r_O}{\sqrt{r_B + r_O}} \tag{2}$$

where r_A, r_B, r_O are the atom radii or the A-(alkali or rare earth-), B-(transition metal group-elements), and O-atom in ABO_3-perovskites. The first extreme with small f (fig. 3a) has small lattice constants compared to the atomic radii. Thus, the atoms fit almost without free volume into the cubic unit cell. The second variant with large f (fig. 3b) has large lattice constants compared to the atomic radii. Hence, phonon modes especially soft modes can easily be excited and this is considered as a beneficial factor for many of the superior solid-state properties mentioned above [Imada et al. 1998, Stegk et al. 2009]. If the space for the octahedron is too large, they start too tilt as shown in fig. 3 c for $LaTiO_3$. This is considered as bad for the thermoelectric properties. This holds also true for the case of the uniaxial octahedron extension as shown in fig. 3 d for the layered Ruddlesden-Popper phase [Ruddlesden & Popper 1958], which is a natural grown nano-composite consisting of SrO and $SrTiO_3$. They are explained in the section 2.3, as well as the Auirvillius phases (fig, 3 e), but before that the findings on perovskite-based thermo-electrics are briefly summarized.

2.2 Perovskite based thermoelectrics

Focusing from now on thermoelectric materials, it has been shown [Yamamoto et al. 2007, Sterzel & Kuehling 2002] that in the (Sr,Ba,Ca)TiO_3 ternary system only specimens at the Sr-rich corner show a large Seebeck-coefficient. Because pure $SrTiO_3$ is an insulator with a band gap of 3.2 eV, it needs to be doped in order to become a semiconductor. N-doping has successfully been demonstrated by partially substitution of Sr with La, or Ti with Nb, and a rather large thermoelectric figure of merit of 0.34 at 1000K is achieved [Ohta et al. 2005-a,b, Wunderlich et al. 2006] As shown in fig. 4, the principle is the same as doping in Si, electron donator elements from the right side of the host atoms in the period system are substituted. However, in these oxide ceramics, not only an electron is released, but also due to the valence change of Ti-atom, oxygen atoms are released (fig, 4 b). Hence, firing in reduced atmosphere improves the properties of Nb-doped $SrTiO_3$, as well as $NaTaO_3$ as explained later.

The oxygen deficit introduces an additional electronic state 300 mV below the valence band edge, as discussed elsewhere [Wunderlich et al. 2009-a]. In this paper also one of the reasons for the good thermoelectric performance of $SrTi_{1-x}Nb_xO_{3-v}$, has been discovered.

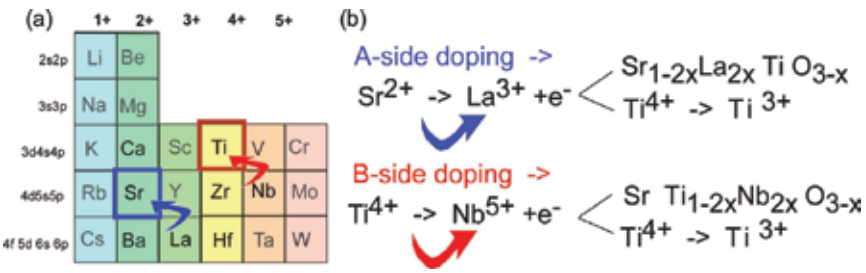

Fig. 4. N-type doping of $SrTiO_3$ for A- and B-side in shown (a) in the period table, (b) as reaction equation with either creation oxygen vacancies or changing the oxidation state of the Ti-atom.

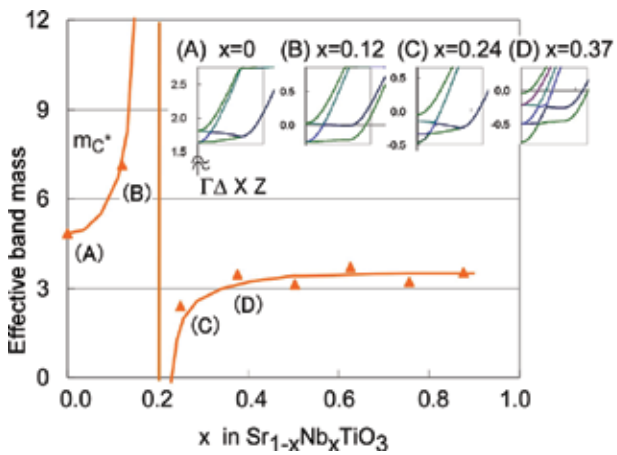

Fig. 5 Effective band mass in Nb-doped $SrTiO_3$ as a function of the Nb-content. The inset shows the conduction band features near the bandgap for different concentrations in Γ-Z direction, from which the effective mass was estimated [Wunderlich et al. 2009-a].

When x, the doping concentration ob Nb increases, the effective electronic mass increases as shown in fig. 5. When analyzing the band structure, this fact can be explained by the decrease in energy of a flat band as seen in the inset of fig. 5. At the concentration of x_{Nb} =0.24 the low-mass band stretching becomes too large and it forms an independent band section at the Γ-point (inset of fig. 5, case (C)). As a result the band mass suddenly becomes small, and in the experiments the bad TE-properties have been confirmed.
The finding expressed in fig. 5 [Wunderlich et al. 2009-a] can be considered as a kind of guideline for any functional material development. In contrary to structural materials, where a wide concentration range gives usual good performance, in functional materials only a narrow concentration range gives good properties. "A little bit increases the performance remarkable, but a little bit too much, deteriorates them", is a principle occurring often in nature, especially in organic or bio-chemistry.
Another reason for the success of Nb-doped $SrTiO_3$-Perovskite has been suggested by the decrease of the bandgap due to phonons [Wunderlich W., 2008-a]. This mechanism explains the importance of phonons for electron excitation as the origin of the heat conversion, and on the other hand it explains the large Seebeck coefficient due to reduction of recombination. Namely, when the excited electron wants to jump back to ground state, the phonon has traveled away and the bandgap is large as it is without phonon making a de-excitation unlikely.
The following formula [Wunderlich et al. 2009-a] relates the calculated band masses to the effective band mass m^* as determined in experiments

$$m^* = m_e^* = m_{B,i} \tag{3}$$

by taking $m_{B,i}$ with i=1, the next band to the band gap from band structure calculations, as an average of high and low band masses $m_{B,i,h}$ $m_{B,i,l}$ at two different reciprocal lattice points by

$$m_{B,i} = \left(m_{B,i,h}^{\ 3/2} + m_{B,i,l}^{\ 3/2} \right)^{2/3} \tag{4}.$$

Through these band mass calculations it was described for the first time [Wunderlich & Koumoto 2006], that $NaTO_3$, $KTaO_3$ and others are possible TE-candidates, because they possess a large effective mass of m^*/m_e=8, about two times larger than Nb-$SrTiO_3$. Before describing $NaTO_3$ in section 2.4., we briefly summarize findings on layered Perovskites.

2.3 Layered Perovskites as thermoelectrics

The electron confinement at Perovskite interfaces has been demonstrated first in [Ohmoto & Hwang 2004]. Due to such 2-dimensional electron gas (2DEG) at interfaces, also thermoelectric properties are enhanced as predicted theoretically (see references in [Bulusu & Walker 2008]). The confined electron gas has been successfully demonstrated for Nb-doped $SrTiO_3$, and this discovery leads to Seebeck coefficients ten times higher than bulk materials [Mune et al. 2007, Ohta et al. 2007, Hosono et al. 2006, Lee et al. 2008]. Theoretical calculations [Wunderlich et al. 2008] showed that the control of the concentration on

atomistic level, diffusion and structural stability is essential, as a $SrTiO_3$-$SrNbO_3$-$SrTiO_3$ composite is much more effective that an embedded Nb-doped $SrTiO_3$.
The idea that an insulating nano-layer of SrO inside Nb-doped $SrTiO_3$ reduces the thermal expansion of the composite, has been demonstrated for the Ruddlesden-Popper phase [Lee et al. 2007-a, Lee et al. 2007-b, Wunderlich et al. 2005], which are naturally grown superlattices [Haeni et al.2001]. As mentioned in section 2.2, in such case structural uniaxial distortions of the Ti-octahedron can occur, which deteriorate the thermoelectric properties due to their larger Ti-O-distance. By additional doping elements the extension can be restored and thermoelectric properties are improved [Wang et al. 2007].
Other Perovskite relatives are the various Aurivilius phases**,** which consists of Bi_2O_2 layers between Perovskite [Lichtenberg et al. 2001, Perez-Mato et al. 2004]. Their thermoelectric conversion power has yet been tested to a certain degree. Other Perovskite relatives are the Tungsten-bronze crystals [Ohsato 2001], which have not yet been tested.

2.4 Pure $NaTaO_3$ is a distorted Perovskite

The interest in $NaTaO_3$ recently increased after the discovery of its photo catalytic properties as water splitting [Kato et al. 1998], or degradation of organic molecules, especially when doped with rare earth elements like La [Yan et al., 2009]. In spite of its high melting point of 1810°C [Lee et al. 1995, Suzuki et al. 2004] it has a lattice energy of -940 kJ/mol, but not as low as Ta_2O_5 (-1493 kJ/mol). It can be produced at relatively low temperatures from $Na_2C_2O_4$ and Ta_2O_5 [Xu et al. 2005] and it reactives with Si_3N_4 [Lee et al. 1995]. $NaTaO_3$ forms an eutectic ceramic alloy with $CaCO_3$, which lowers the melting point to 813 K [Kjarsgaard & Mtchell 2008]. Ta in $NaTaO_3$ can be exchanged isomorphly by Nb, relating in similar properties as $NaNbO_3$ [Shirane et al. 1954, Shanker et al., 2009].
Detailed investigations showed that $NaTaO_3$ possesses the Pervoskite structure (*Pm-3m*) only above (893 K) before it lowers its symmetry becoming tetragonal (*P4/mbm*), and orthorhombic (*Cmcm, Pbnm*) below 843 K and 773 K, respectively [Kennedy et al. 1999]. $NaTaO_3$ is more stable compared to $NaNbO_3$, which becomes tetragonal at 653 K and orthorhombic at 543 K, or $KNbO_3$, where these transformations occur at 608 K and 498 K, respectively [Shirane et al. 1954]. $NaTaO_3$ has a bandgap of 4eV [Xu et al. 2005]. The phase transition is caused by the octahedron tilting (fig. 2 c), which can reach up to 8° in the case of $NaTaO_3$ [Kennedy. et al. 1999].
$NaTaO_3$ has been suggested as thermoelectric material [Wunderlich & Koumoto 2006, Wunderlich et al. 2009-a, Wunderlich & Soga 2010], as it shows a large Seebeck coefficient. The findings are briefly summarized, together with explanation of new research results in the following sections.

3. *Ab-initio* calculations of doped $NaTaO_3$

First-principle calculations based on the density-functional theory (DFT) are presented in this chapter. They should clarify the following topics, namely which doping element sits on *A*- or *B*-site of the perovskite lattice ABO_3, how the lattice constants change, how Fermi energy and bandgap change, and finally how the bandstructure and density-of-states (DOS) looks like.
The first principles calculations were performed using VASP software [Kresse & Hafner 1994] in the LDA-GGA approximation with a cut-off energy E=-280eV, U=0V and sufficient

number of k-points. The DOS is convoluted with a Gaussian distribution with a FWHM of 0.2eV, to approximate the broadening at room temperature. The relevant symmetry points in reciprocal space were chosen according to the standard notifications of the Perovskite space group *Pm-3m*, which was assumed as a first approximation to have untitled octahedra. The path in reciprocal space was focused on the three directions near the Γ-point, see discussion in [Wunderlich et al. 2009-a]. The supercell used in these calculations is a 2x2x2 extension of the unit cell, allowing calculations of minimal doping concentration steps of 0.125 = 1/8 for *A*- or *B*-side or 1/24 for O.

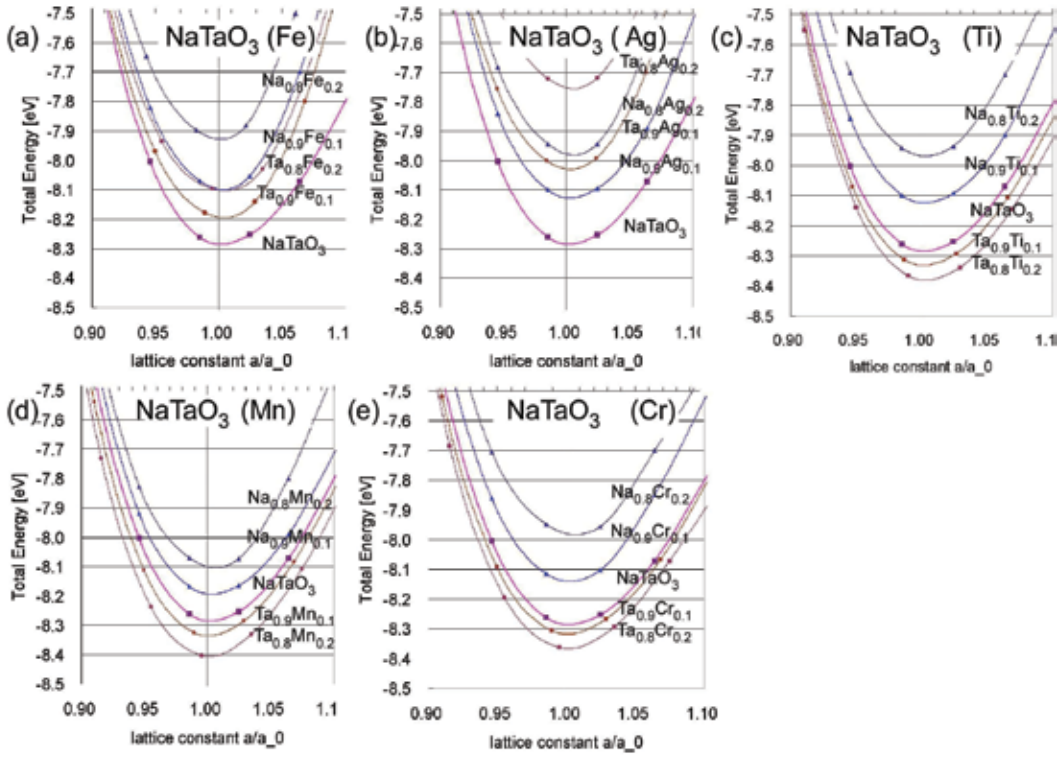

Fig. 6. The energy-volume dependence for pure $NaTaO_3$ (pink line) is shown and compared with different doping elements dissolved in $NaTaO_3$, either on Na- or Ta-side, each for two concentration. The variants with lowest energy are (a) Fe on Ta-side, (b) Ag on Na-side, and (c) Ti, (d) Mn, (e) Cr all three on Ta-side.

Doping element $NaTa_{0.9}Me_{0.1}O_3$	un-doped	Fe	Ag	Ti	Mn	Cr
Lattice constant [nm]	0.3909	0.3948	0.3968	0.3909	0.3952	0.3929
Band-gap [eV]	2.20	0.74	0.60	2.10	0.95	1.30
Fermi energy [eV]	2.37	1.91	1.80	2.17	1.95	2.54

Table 1. Lattice constants, band-gap and Fermi energy for Ta-site doped $NaTaO_3$ as estimated from *ab-initio* calculations

The results of the energy-versus-volume (E(V)) calculations are shown in fig. 6 for doping elements Fe, Ag, Ti, Mn, and Cr for either doping on *A*- or *B*- side. The obtained lattice constants are shown in table 1 and exhibit only a small change compared to pure $NaTaO_3$. As explained in the following section and in a previous paper [Wunderlich 2009-b], Ag and Fe are the two doping elements, which cause the highest Seebeck voltage due to their high solubility in the $NaTaO_3$ lattice. The data in fig. 6 show that both, Fe, and Ag, doped on *B*-site have a slightly higher energy, while according to the experimental data intuitively one would expect a lower energy than pure $NaTaO_3$, as it is in the case for all other doping elements. The discrepancy can be explained by the fact that pure $NaTaO_3$ has tilted octahedron. Furthermore, Ag shows a slightly lower energy for doping on *A*-side, but this makes no sense, because valence and hence band structure remains unchanged. As in the case of Nb-doped $SrTiO_3$ [Wunderlich et al. 2009-a] DFT-calculations of the combined defects $NaTa_{0.88}Me_{0.12}O_{3-x}$ might clarify this issue. As explained in fig. 4 b in the previous section, an increase in the electron concentration on *B*-side is always related to a deficit in oxygen.

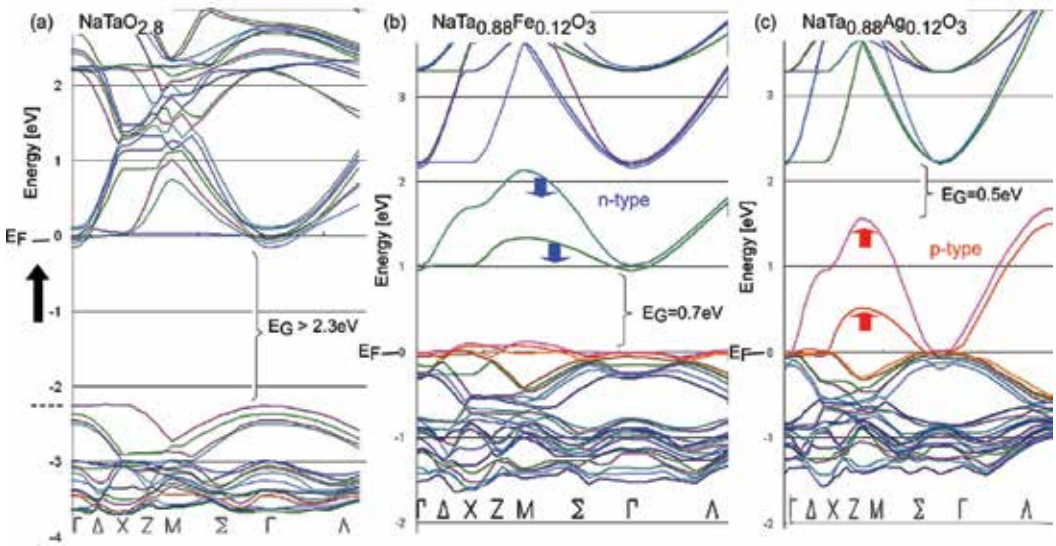

Fig. 7. Band structure of (a) $NaTaO_{2.8}$. (b) $NaTa_{0.88}Fe_{0.12}O_3$ (n-type) (c) $NaTa_{0.88}Ag_{0.12}O_3$ (p-type). The arrows show the change compared to un-doped $NaTaO_3$. (The band colors are just for distinguishing and have no other meaning).

The calculated band structure of Fe-doped $NaTaO_3$ is shown in fig. 7 b, that of Ag-doped $NaTaO_3$ in fig 7 c and the oxygen-deficit $NaTaO_{2.8}$ lattice in fig. 7 a. In all plots the Fermi energy level, which is shown in table 1, has been adjusted to 0 eV. In the case of n-doping the Ta-2*eg* bands have lowered their energy and the band gap is reduced remarkably from 2.2 eV in pure $NaTaO_3$ to 0.74 eV, so that excitations due to phonons become possible. The p-doping by Ag shifts the Ta-2*eg* bands towards the valence band, so that an indirect band gap with 0.6 eV occurs. As shown in table 1, the band structures of other doping elements show larger band gaps. The band gap widths correspond well to the electric resistivity of

such specimens as explained in the next section. Hence, the band-gap-reduction will be a future engineering challenge for obtaining a large electric conductivity.

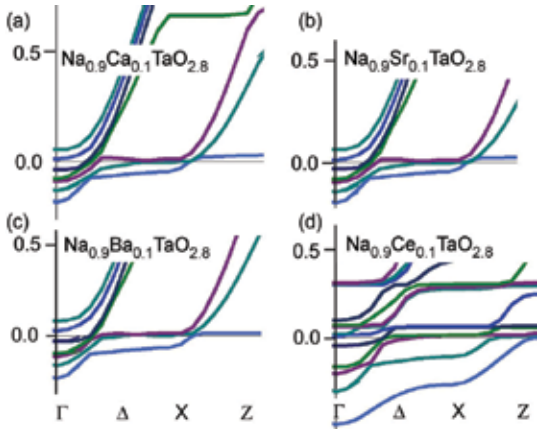

Fig. 8. Band structure near the conduction band edge at the Γ-point for Na-site doping, (a) $Na_{0.88}Ca_{0.12}TaO_{2.8}$, , (b) $Na_{0.88}Sr_{0.12}TaO_{2.8}$, (c) $Na_{0.88}Ba_{0.12}TaO_{2.8}$, , (d) $Na_{0.88}Ce_{0.12}TaO_{2.8}$.

The mechanism for electron conductivity is similar to that in Nb-doped $SrTiO_3$; for details see the discussions in [Wunderlich et al. 2009-a]. The oxygen vacancies introduce electronic states about 200 ~ 300 meV below the valence band edge, form which electrons from the conduction band can be excited into the valence band. Compared to pure and Nb-doped $SrTiO_3$ (m^*/m_0= 4.8 and 8), in pure $NaTaO_3$ (m^*/m_0= 8) the effective electron mass increases further (m^*/m_0= 12), as can be seen from the flat bands over the entire region Γ–Δ-X in all three cases of fig. 7. In un-doped $NaTaO_3$ the hole mass is also large (m^*/m_0= 8). The mass of Ag-doped $NaTaO_3$ (Fig. 7 c) is smaller due to the indirect bands at Z and Λ-points, but the large effective mass of the valence band minimum in un-doped regions (m^*/m_0> 20) seems to have also an large influence on the effective mass measured in experiments. Calculations for A-site doping analog to La-doped $SrTiO_3$ [Wunderlich et al. 2009-a] are shown for $NaTaO_{2.8}$ in fig. 8. In all cases the DOS near the band edge is increased, but for Ce-doping it became especially large as can be also seen on the increased number of bands (fig. 8 d). In spite of experimental difficulties with sintering of Ce_2O_3 containing samples [Wunderlich et al. 2009-d], a large TE-performance by co-doping might be expected. In following experimental results about Ta-site doping are reported.

4. Specimen preparation and microstructure characterization of $NaTaO_3$

$NaTaO_3$ composite ceramics were produced by conventional sintering. Well-defined weight ratios of fine powders of $NaTaO_3$ (Fine Chemicals Ltd.) and each of the pure metals Fe, Ag and other metals, or Fe_2O_3, were mixed in different concentration ratios in a mortar for more than 10 min. The specimens were pressed with 100 MPa as pellets, 10 mm in diameter and 3 mm height, and sintered in a muffle furnace in air at 1000 °C for 5h with slow heating and cooling rates (50K/h) as sketched in fig. 9. The electric properties of the specimens were analyzed as explained in the following section. Thereafter, the sintering was repeated several times at the same temperature. During sintering the white color of $NaTaO_3$

specimens turn into dark colors indicating that the band-gap has been reduced, when a large amount of metals was dissolved. However, specimens containing metals with low solubility such as Al, Cu, Sn, Sb, Mo, W remained white or turned into light orange or reddish color (Ti). The specimens were characterized by SEM (Hitachi 3200-N) at 30kV equipped with EDS (Noran), which allows chemical mapping. The X-ray diffraction (XRD) analysis was performed using a Rigaku Miniflex device with Co-source with 1.7889 nm wavelength. Simulation of the XRD-patterns was performed with the Carine V3 software (Cristmet).

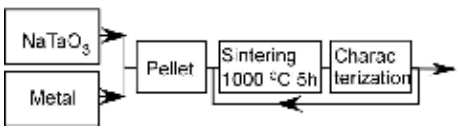

Fig. 9. Flowchart of the specimen preparation

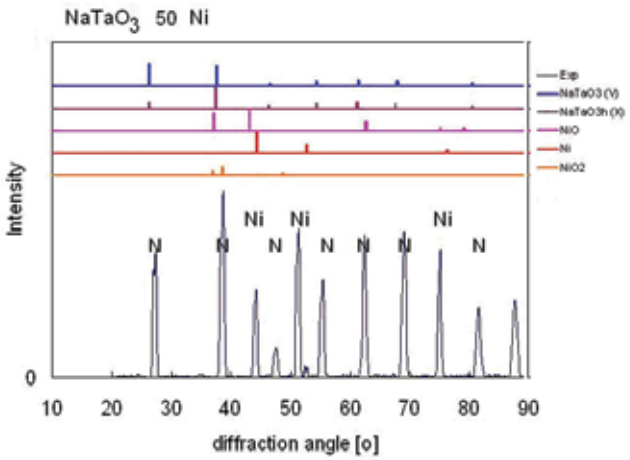

Fig. 10 XRD diffraction pattern of $NaTaO_3$ with 50 wt-% Ni. The letters N indicate $NaTaO_3$ reflexes.

The analysis of XRD-diffraction pattern of Fe- and Ti-doped $NaTaO_3$ showed [Wunderlich, Soga, 2010] that the initially mixed Fe or Ti-metallic powder gets oxidized as besides the $NaTaO_3$- XRD-peaks also such of FeO_3- or Ti_2O_3 are observed. Hence, during sintering a FeO_3- and Ti_2O_3–$NaTaO_3$ composite material is formed by reaction bonded sintering (RBS), a mechanism, which supports additional energy for sintering and has been successfully applied for many structural ceramics [Claussen et al. 1996]. Weight measurements of specimens before and after sintering confirmed the oxidation by weight gain even in quantitative manner.

In the case of Ag, evidences for oxidation have not yet been clearly approved, instead, cooling down a sintered specimen, metallic silver balls separated on the specimen surface are observed. In the case of Ni-added $NaTaO_3$, in spite of the greenish specimen surface color due to NiO, the XRD pattern in fig. 10 shows that the interior of the specimen consists of a composite $NaTaO_3$ with metallic Ni. In all specimens with Fe-, Ni-, Mn-, and Ag-doping the XRD peaks were indentified as Perovskite with space group *Pm-3m* as mentioned in

section 2.4. Hence, it can be concluded, that the octahedron tilting mentioned in section 2 was suppressed by the doping.

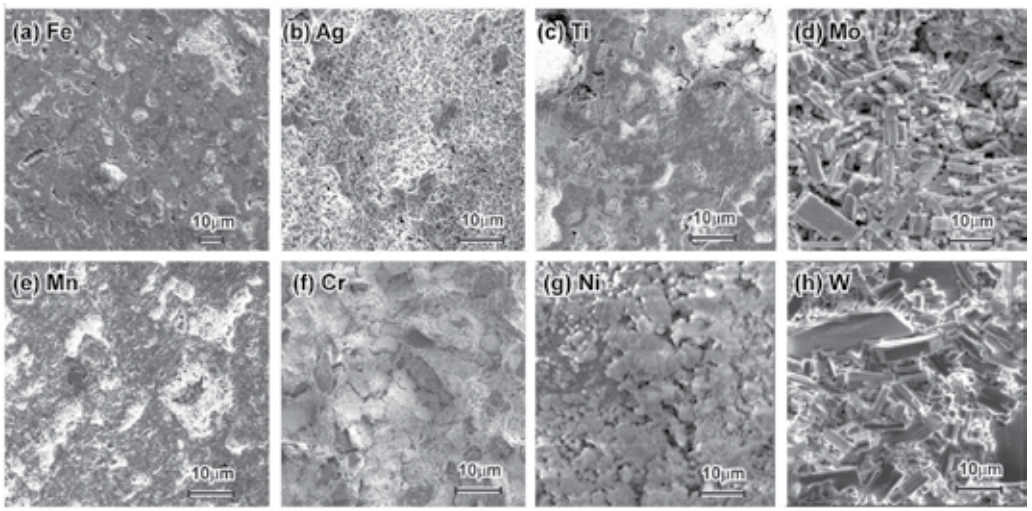

Fig. 12. SEM micrographs of the as-prepared surfaces of different $NaTaO_3$-composites processed by adding 40 wt% of (a) Fe, (b) Ag, (c) Ti, (d) Mo, (e) Mn, (e) Cr, (g) Ni, (h) W.

The microstructure of the $NaTaO_3$ composite processed with 50 wt% Fe consists of a $NaTaO_3$- 50 mol% Fe_2O_3 composite as shown in fig. 12 a. It consists of dark Fe_2O_3 particles, on average 10 μm in size, and appearing in streaks-like shape, which are embedded in a grey $NaTaO_3$ matrix. Detailed explanation is provided in a previous paper [Wunderlich & Soga 2010]. When $NaTaO_3$ is initially processed with Fe_2O_3 instead of Fe, the microstructure looks like a sintered ceramic composite with white Fe_2O_3 besides white $NaTaO_3$ particles. The change from black to white color can be explained by oxygen saturation as explained in section 6. Such a micrograph is shown in a previous paper [Wunderlich 2009-b]. The white areas in fig. 12 a are pores remaining from insufficient compaction during sintering or from released oxygen as explained in section 5.
In $NaTaO_3$-composites containing Ag, Ti, Mn, and Ni the dark, metallic particles are slightly bigger (5~10 μm). The particles have a volume fraction of about 30% which correspond well to the intensity ratios of the XRD-pattern. In specimens, which were produced from Fe_2O_3-instead of Fe-powder, the Fe_2O_3-particles form round particles as shown in fig. 3 a in [Wunderlich 2009-b]. In the case of Cr the dark, metallic Cr-particles are significantly larger (20 μm), which can be explained by their low diffusivity. The same would be expected for Mo and W with their high melting points, but instead they lead to faceted interfaces. By chemical mapping homogeneous distribution of Na, Ta, Mo or W was confirmed. The two elements, Mo, and W, having their location in the period system and their atomic radii close to Ta, and, hence, can inter-diffuse easily with Ta. They lower the surface energy of certain crystallographic planes, which is an important fact to be kept in mind when nano-layered composite materials based on $NaTaO_3$ are desired.
The main goal of doping is to increase the carrier concentration of $NaTaO_3$ in order to increase the conductivity. In a composite this can only be achieved by increasing the concentration of the dissolved element. Composition measurements by EDX in SEM with

lateral resolution of 1 μm were performed on the $NaTaO_3$-phase in the $NaTaO_3$-composites processed with different metals. For Cr, Mo and W concentrations below 2 at% were detected, for Ag, Ti, Mn, and Ni, 5 ~ 10 at% were detected and for Fe 14 at%. This result can Is a necessity for a thermoelectric material and explains the success of Fe and Ag for the TE-performance as explained in the following section.

5. Thermoelectric characterization

5.1 Measuring device

The thermoelectric measurements were performed with a self-manufactured device as shown in the inset of fig. 13. The specimen was attached to the device, so that its left side lies on a copper block as a heat sink and its right side on a micro-ceramic heater (Sakaguchi Ltd. MS1000) with a power of 1kW, and was heated up to 1000°C within 3 minutes. Hence, the bottom part of the specimen experienced the large temperature difference, while the upper part was heated through the heat conductivity of the specimen. The temperature distribution as measured by thermocouples is shown in fig. 1c of [Wunderlich & Soga 2010]. Seebeck voltages were measured on both, the bottom and top part of the specimen by Ni-wires, which were connected to voltmeters (Sanwa PC510), marked as V1 and V2 in the inset of fig. 13 b. The temperature was measured with thermocouples also attached to voltmeters. The data were recorded online by a personal computer.

Most TE-literature reports TE-data measured under small temperature gradient [Bulusu & Walkner 2008], where the theory is valid for. Our device however, measures the data under large temperature gradient, which is close to applications. When comparing such measured data with literature data on similar specimens (CoTiSb, Fe), in general about 1.5 times larger values for the Seebeck voltages are obtained.

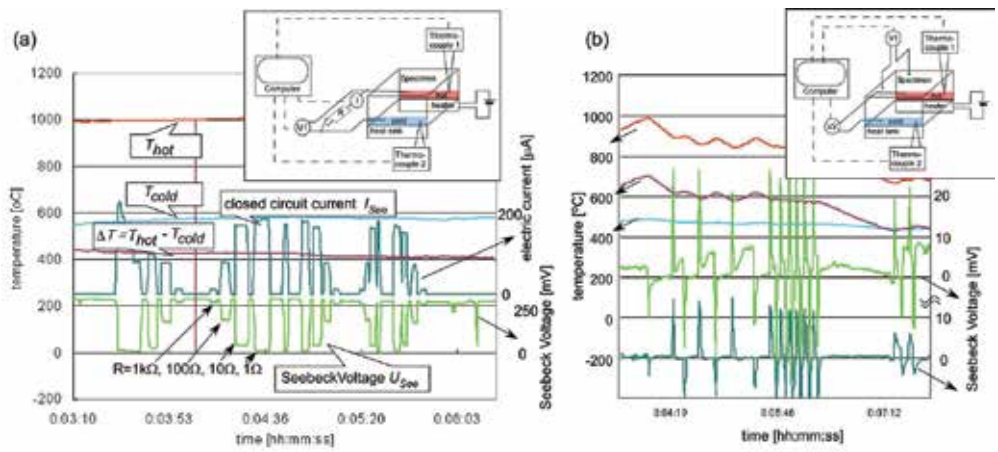

Fig. 13. Temperature (on the left y-axis), Seebeck Voltage and short-circuit current (both on the right y-axis) as a function of time. The inset shows the scheme of the experimental setup for measuring the Seebeck voltage and the closed circuit current. (a) Typical measurement for $NaTaO_3$ + 50 wt% Fe, (b) Seebeck voltage response for $NaTaO_3$ + 50 wt% Cu, when the heater is switched off or on (red line).

By putting the specimen completely above the ceramics heater, the temperature dependence of the electric resistivity was measured with the same device as shown previously [Wunderlich 2009-b, Wunderlich & Soga 2010]. The reason, why the Seebeck voltage only appears when heated above 500°C, can be explained by the poor electric conductivity at low temperatures. The room temperature resistivity of such samples decreases from about 10 MΩ to 0.1 MΩ when sintered in at least five sintering steps (1000°C, 5h) [Wunderlich & Soga 2010]. The temperature dependence of the resistivity ρ was measured. The activation energy E_A for thermal activation of the charge carriers n_e in this n-doped semiconductors was estimated according to $n_e = N \exp(-E_A/2kT)$ by a suitable data fit. This analysis yield to an activation energy for charge carriers of about 1 eV during heating and 0.6 eV during cooling [Wunderlich 2009-b].
Another option of this device is the measurement of the closed circuit current. For this option, the wires below the specimen are connected with resistances of 1Ω, 10Ω, 100Ω, 1kΩ, or 1MΩ in a closed circuit condition as seen in the inset of fig. 13 a. As the measured electric current is a material dependent property, it is recorded too. As shown in fig. 13 a or fig. 3 in [Wunderlich 2009-b], as soon as the circuit is closed, the voltage of the $NaTaO_3$- 30mol% Fe_2O_3 specimen drops down, and the current increases according to the amount of load with a short delay time of a few ms. The detection limits are about U=1mV and I=0.8μA.

5.2 Time-dependence of Seebeck voltage

For the most specimens, the Seebeck voltage is not time-dependent and only depends on the temperature gradient. Time-dependent effects of the Seebeck-voltage occurrence have been reported for Co-based rare-earth Perovskite-composites (for example Gd_2O_3+CoO_x) [Wunderlich & Fujizawa. 2009-d] and were explained as a combined occurrence of pyro-electricity and thermoelectricity. In some Co-based perovskite specimes remarkable non-linearities in the plot Seebeck voltage versus temperature difference appear, but not in $NaTaO_3$.
A time-dependent Seebeck voltage behavior appears at specimens $NaTaO_3$ + x Cu, with x from 30 to 50 wt%, as shown in fig. 13 b for x= 50wt%. On such specimens in general only a small Seebeck voltage of only -5 mV is measured, even at temperatures above 500 °C, when a sufficiently high charge carrier concentration is reached. However, when then the heater is switched off suddenly, a sharp pulse, a few milliseconds in length, of the Seebeck voltage with a value of 20 mV is measured with a negative sign. When switching on the heater again, the sign reverses to a positive pulse of Seebeck voltage with the same absolute value of 20mV. The Seebeck voltage on the backside of the specimen, which experiences the temperature gradient only indirectly through heat conduction, is not so high in its absolute value (12 mV for a 5 mm thick specimen), but it appears with the same sign and at the same time. In fig. 13 b this is shown in dark-green, while the pulse of the specimen side with the large temperature gradient is shown in light-green. The value of the Seebeck pulse is independent on the time-interval between the heat flow reversals, just the Seebeck voltage between the pulses fluctuates between 2 and 10 times of its absolute value. Only when the temperature gradient decreases (right side of fig. 13b), the absolute value of the pulse becomes smaller.
This heat flow dependent Seebeck pulse in time appears also in $NaTaO_3$ + x Ag specimens, which were sintered only for a short time (1000°C, 5h). The reason is not yet completely investigated, but the interface between $NaTaO_3$ and metallic particles, which are not reactive with $NaTaO_3$, is responsible for this effect. It is different from pyroelectricity, which showed a similar behavior like an electric capacitor. The heat-flow dependent Seebeck voltage pulse

can be utilized for building a heat-flow meter, which would be able to detect the forward or backward direction of the heat flow, due to the sign of the voltage pulse. By micro fabrication several such specimens could be arranged under different angles to heat flow, so that the vector of the heat flow can be determined, and when such devices are arranged in an array, even the heat flow tensor can be measured.

5.3 Seebeck voltage measured under large temperature gradients

The measurements of the Seebeck voltage U_{See} are shown in fig. 14, where a temperature gradient of up to ΔT = 800 K was applied to the specimens and the Seebeck voltage measured as explained in section 5.1. The specimens with $NaTaO_3$+x Fe were measured for x = 30, 40, 50, 60, 70, 80, 90 wt%. The specimen with x= 50, 60, 70 wt% showed the high Seebeck voltages of about -300 mV as shown in fig. 14 a, details are explained in previous publications [Wunderlich 2009-b, Wunderlich & Soga 2010]. From the plot temperature difference dT versus Seebeck voltage U_S a Seebeck coefficient S of 0.5 mV/K was estimated by the slope $S = dU_S/dT$.

As the XRD results showed the formation of Fe_2O_3, also $NaTaO_3$ + r Fe_2O_3 specimens were sintered, were r was 30, 50, 70, 90 wt%. These specimens showed all a Seebeck voltage of +60 mV at ΔT = 800K with a slightly nonlinear ΔT-dependence. Hence, different processing causes a different oxidation state of the second component in this composite, and changes the n-type $NaTaO_3$+x Fe into a p-type $NaTaO_3$ + r Fe_2O_3 composite. As mentioned above, the microstructure looks slightly different for both composites and the thermo-kinetic measurements in section 6 too.

When metallic Ni is added to $NaTaO_3$, the sintered composites with x= 30 wt% Ni showed the highest value of -320 mV with a Seebeck coefficient of 0.57 mV/K, as shown in fig. 14 b. In this case non-linear behavior at ΔT = 650 K during heating, and ΔT = 600K during cooling appears at all Ni-specimens, but not at other elements, and is probably related to some phase transitions. In the case of W additions to $NaTaO_3$ the specimens showed only a small Seebeck voltage of -30 mV for all concentrations in the range 30 to 90 wt% (fig. 14 c). A similar behavior is seen for Mo, where the 50 wt% sample showed a Seebeck voltage of -10 mV during heating and +10 mV during cooling. The plots of Seebeck voltage versus temperature difference are linear.

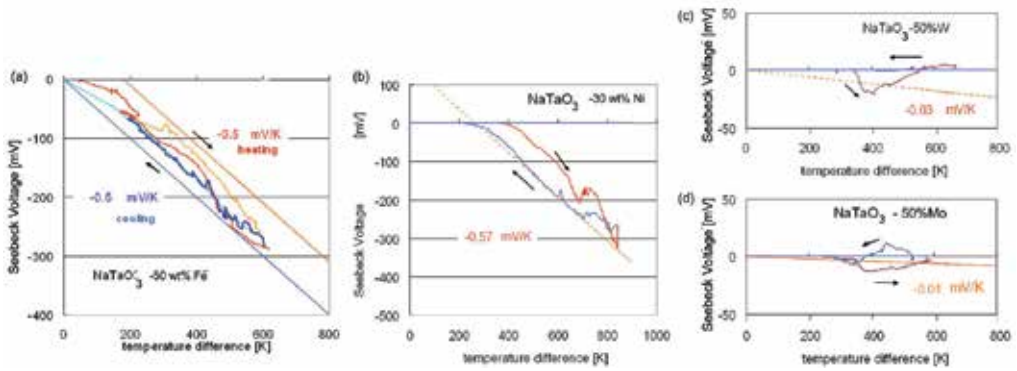

Fig. 14. Seebeck Voltage as a function of the temperature difference for (a) $NaTaO_3$+50 wt% Fe, (b) $NaTaO_3$+30 wt% Ni, (c) $NaTaO_3$+50 wt% W, (d) $NaTaO_3$+50 wt% Mo. The slope of the plots yield to the Seebeck-coefficients as mentioned.

Na --	Mg /	/										Al 0	Si /	P /
K * -30	Ca /	Sc /	Ti -20	V /	Cr -200	Mn -30	**Fe** **-320**	Co -20	Ni -360	Cu -20	Zn /	Ga /	Ge /	As /
Rb /	Sr /	Y /	Zr /	Nb /	Mo -10/+10	Tc /	Ru /	Rh /	Pd /	**Ag** **+250**	Cd /	In /	Sn 0	Sb 0
Cs /	Ba /		Hf /	Ta --	W -20	Re /	Os /	Ir /	Pt /	Au /	Hg /	Tl /	Pb /	Bi 0

* $KTaO_3$+Fe

Fig. 15. Part of the periodic table showing the elements which were tested as doping additives for $NaTaO_3$. The vale refers to the Seebeck voltage in mV at ΔT = 750K. In the case of K it means $KTaO_3$ with Fe-additions. Only the two elements in bold letters (Fe, Ag) showed a remarkable closed-circuit current.

Such measurements were performed by adding several metallic elements *Me* from the periodic system $NaTaO_3$+x *Me* specimens with x = 30, 50, 70, 90 wt%. Fig. 15 shows the largest Seebeck voltage at ΔT=800 K among these specimens, where the best results usually were achieved for x around 50 wt%. Al and those semiconducting elements which were measured did not dissolve in $NaTaO_3$ and such specimens remain white, a sign that they are still insulators.

Specimens sintered from $NaTaO_3$- x Ag powders with x= 30, 50, 60 wt% lead to p-type thermoelectrics. The Seebeck coefficient as deduced from fig. 14 a, Fe as n-type, and the corresponding plot for Ag as p-type [Wunderlich 2009-b] yield for both composites to almost the same value, namely +/- 0.5mV/K. In the case of $NaTaO_3$ + x Fe specimens, the Seebeck voltage increases during the first three sintering cycles (1000 ^{o}C 5h), and reached this saturation value, which was confirmed to be stable even after eight sintering cycles. In the case of Ag-doped $NaTaO_3$, the value also increases, however, after the fourth sintering cycle the Seebeck voltage drops to less than 30mV and the color turns into white again, indicating a structural instability of the $NaTaO_3$-Ag compound probably due to silver evaporation. The temperature dependence of the electric resistivity was shown previously [Wunderlich 2009-b, Wunderlich & Soga 2010] for both, n- and p-type specimens, with x= 50 wt%, which was found as the optimum concentration for low resistivity. According to the thermal activation of the carriers an activation energy in the order of the band gap (1 eV) can be estimated by fitting the data as shown in [Wunderlich 2009-b, Wunderlich & Soga 2010] by the formula $\sigma = N_0 \exp(-E_0/2kT)\ |e|\ \mu_e$. with E_0 activation energy.

There are further promising doping candidates, not yet checked, as Nb, or rare earth. As a conclusion, it can be stated that only the light transition metals like Fe, Cr, Mn, Ni showed remarkable Seebeck voltages. Among them, the closed-circuit measurements described in the following section, lead to further restrictions.

5.4 Electric current under closed circuit conditions

For power generation the performance under closed circuit conditions is important. Fig. 16 shows the measured current when different electric resistances as load are connected. While both composites, the one processed from $NaTaO_3$+x Fe and the $NaTaO_3$- x Ag one, showed

large Seebeck voltage in the range of x = 50 to 70 wt%, the closed circuit current measurements showed the highest value only for the specimen processed from $NaTaO_3$+x Fe with x= 50 wt%, which corresponds to $NaTaO_3$+r Fe_2O_3 with r = 32 mol% after sintering.
In the silver added composite, the specimen with 40 mol% Ag (about 50 wt%) yields to the optimum between large Seebeck coefficient and low resistivity. For the $NaTaO_3$-x Fe_2O_3-composite, the specimen with x = 32 mol % shows the highest current of 320 µA, but for the

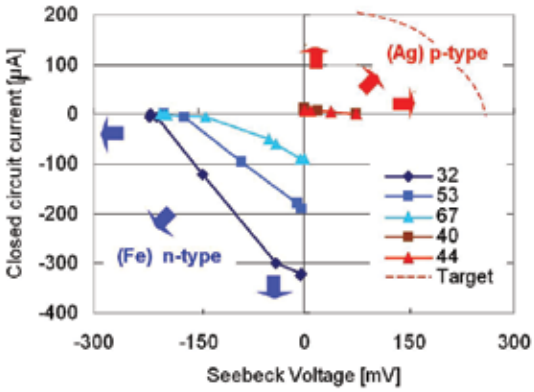

Fig. 16. Seebeck Voltage and closed circuit current for n- and p-type $NaTaO_3$ with Fe- or Ag-additions with the Mol-% as shown. The horizontal and vertical arrows indicate the target for current and voltage increase, the inclined ones indicate the target for power improvement. P- and n-type materials should have the same Seebeck voltage as expressed by the target-line.

$NaTaO_3$-x Ag-composite, it is only 1.2 µA. For the silver added composite, a part of Ag gets dissolved, another part gets oxidized as $NaTa_{1-x}Ag_xO_{3-y}$ + *t* AgO_u, when sintered in three cycles (1000 °C 5h). While $NaTaO_3$- Fe_2O_3 is a stable composite, the metallic Ag in the p-type composite with its low melting point decomposes into an insulating oxide after four sintering cycles (1000 °C, 5h), and metallic silver balls at the surface.
The microstructure of the p-type material needs to be stabilized and optimized for improving both, Seebeck voltage as well as resistivity. When this is realized, and the p-type material would have had the same short-circuit current as suggested by the target line in fig. 16, it is expected that modules with both n- and p-type materials work optimal. As p- and n-type material has been found, $NaTaO_3$ is suggested as a new thermoelectric for power generation suitable for applications in an upper range of application temperatures (500 to 1100 °C), when a sufficient performance is achieved as described in the next section.

5.5 Estimation of the figure-of-merit

The absolute value of the negative Seebeck Voltage increases linearly with the temperature and reaches -320 mV at a temperature difference of 800 K as shown in fig. 14 a for the specimen $NaTaO_3$-50mol% Fe_2O_3. From the slope of the Seebeck voltage versus temperature a Seebeck coefficient of -0.5 mV/K was estimated. Specimens in the range of 20 mol to 70 mol% Fe_2O_3 showed all a Seebeck coefficient larger than -0.45 mV/K. From these data the figure of merit can be deduced, a little bit more promising as previously [Wunderlich 2009-b]. For the thermal conductivity in the worst case a high value of 5 W/(m K) was assumed

according to the range of usual ceramics. This leads to an estimation of the figure-of merit ZT at 1000°C as:

$$Z = \frac{S^2 \cdot \sigma}{\kappa} = \frac{(0.5\,mV/K)^2 \cdot 1\ \mathrm{S/m}}{5\ W \cdot m^{-1} \cdot K^{-1}} = 10 \times 10^{-9}\ K^{-1}, \quad ZT_{1000'C} = 1.27 \times 10^{-5} \tag{5}$$

This estimated value of ZT is at the moment much lower than state-of-the-art materials, for example SiGe, or the above mentioned Nb-doped $SrTiO_3$, but materials development, like improved sintering, higher solubility of Fe, higher conductivity etc., will definitely increase the performance of $NaTaO_3$, for which the following thermokinetic investigations are helpful.

6. Thermo-kinetic characterization

In order to clarify the sintering behavior of the $NaTaO_3$-Fe_2O_3 composite differential scanning calorimetry (DSC) and thermo-gravimetric (TG) measurements were performed. The development in the field of thermo-kinetics in the last decade allows the estimation of activation energies for chemical reactions, when DSC and TG are measured simultaneously with at least three different heating rates [Opfermann et al. 1992, Opfermann 2000]. The analysis of the different sintering steps of alumina [Baca et al. 2001], and the oxidation of Magnetite to Fe_2O_3 [Sanders & Gallagher 2003] are examples, where this technique has successfully been applied for ceramics.

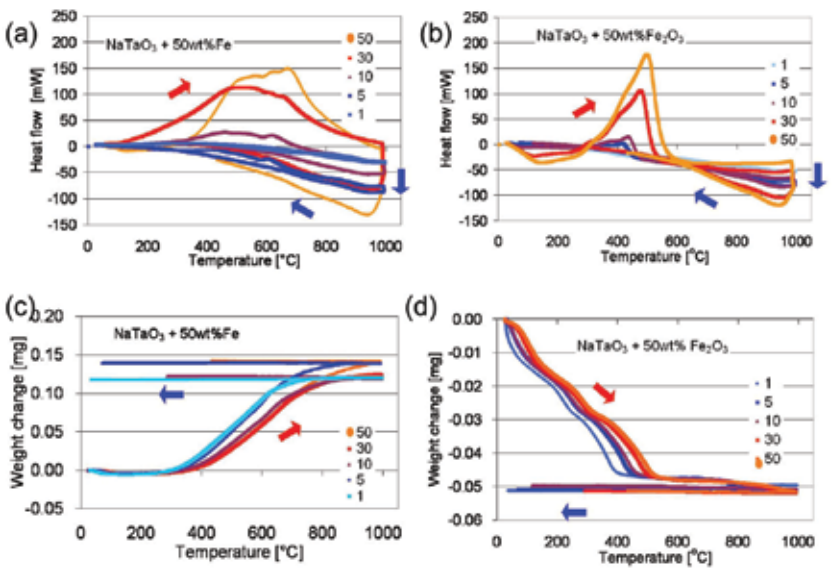

Fig. 17 Results of (a,b) DSC and (c,d) TGA measurements of (a,c) $NaTaO_3$ + 50 wt% Fe-, and (b,d) $NaTaO_3$ + 50 wt% Fe_2O_3-powder specimens. The numbers in the inset refer to heating rates in [K/min]. The red and blue arrows indicate heating and cooling, respectively.

Simultaneous DSC-TG measurements were performed on a SDT Q600 (T.A.instruments) by heating two different sets of mixed powder samples (26 mg $NaTaO_3$ + 50 wt% Fe, and 60 mg $NaTaO_3$ + 50 wt% Fe_2O_3) under air with five different heating rates up to 1000 °C. The

results are shown in fig. 17. The thermo-gravimetric measurements showed that the $NaTaO_3$-50wt% Fe powder gains 0.13 mg in weight (fig. 17c, increase of 0.5%) and the $NaTaO_3$-50wt%Fe_2O_3 powder looses 0.05 mg in weight (weight reduction of 0.2%). The fact that the weight gain in fig. 17c is not the same for all heating rates can be explained by concentration inhomogeneities in each specimen.

The interpretation of these results is that Fe gets oxidized forming Fe_2O_3 which was observed in the XRD pattern, see section 4 and [Wunderlich & Soga 2010]. The experimental results showed that a part of Fe gets dissolved in $NaTaO_3$, about 14 %. Assuming that the same amount of Fe is dissolved in $NaTaO_3$ in both composites ($NaTaO_3$ + 50 wt% Fe and $NaTaO_3$ + 50 wt% Fe_2O_3), this fact can explain why the weight decreases for the $NaTaO_3$ + Fe_2O_3 mixture. Namely, the dissolved Fe needs to be reduced from the initial Fe_2O_3 and the excess oxygen is released.

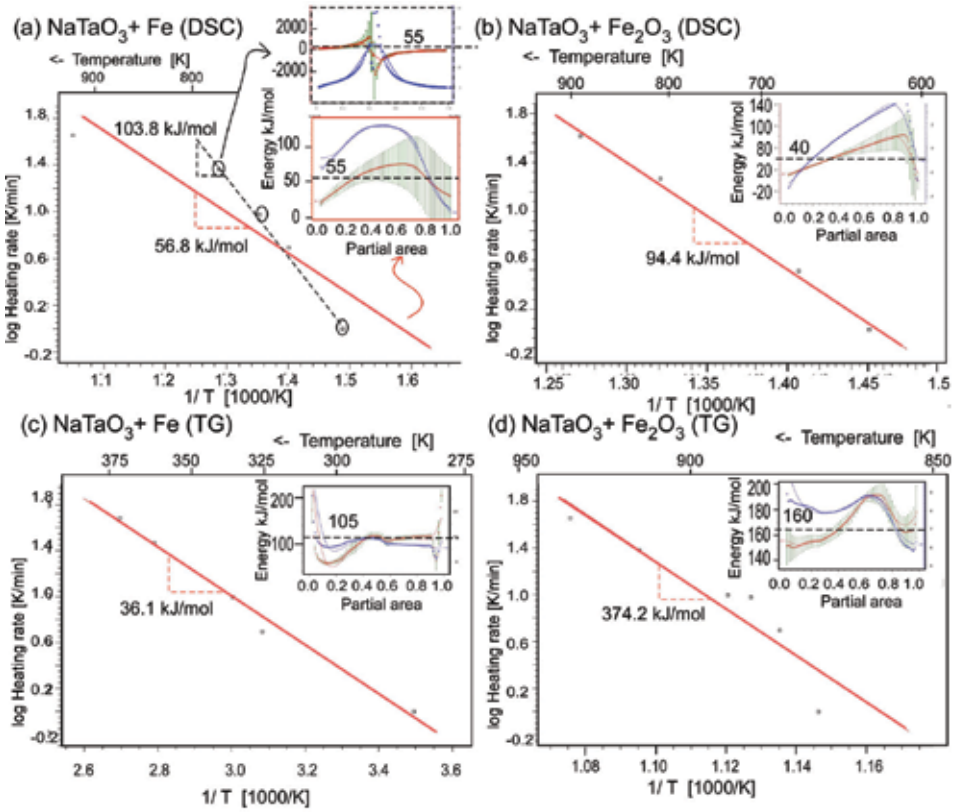

Fig. 18. Analysis of the (a,b) DSC-, (c,d) TG-data from fig. 17 for (a,c) $NaTaO_3$ + 50 wt% Fe and (b,d) $NaTaO_3$ + 50 wt% Fe_2O_3 using ASTM and Friedman method yielding to the activation energy from the slope in the logarithmic plot heating rate versus inverse temperature. The inset shows the distribution of the activation energy as a function of the partial fraction.

The DSC measurements showed an exothermic peak for $NaTaO_3$ + 50 wt% Fe (fig. 17 a), namely a positive heat flow, with a broad maximum at 500°C and small wiggles at 690 °C

and 700 °C, present in data obtained at all heating rates at the same temperature. On the other hand, at the $NaTaO_3$-Fe_2O_3 mixture the main exothermic peak shifts from 410 °C at slow heating rates (1 K/min, 3 K/min) to 510 °C at the fastest heating rate (50 K/min). At these temperatures the corresponding TG-data showed a large decrease in weight, indicating a chemical reaction.
The Netzsch Thermokinetics software package version 3 [Opfermann 2000] was used for data analysis. All four sets of data were analyzed separately and only the data during heating were used. For each set, the parameter-free analysis of the activation energy according to ASTM E698 was performed as shown in fig. 18. Then Friedman analysis [Opfermann et al. 1992, Opfermann 2000] of the activation energy as a function of the partial area was performed as shown in the insets of fig. 18.
The results show an activation energy of 56.8 kJ/mol for the $NaTaO_3$ + 50 wt% Fe- specimen (fig. 18a). The activation energy increases to 103.8 kJ/mol, when only the three data points with best correlation are used, as shown with the circles. In this case the Friedman analysis yields a curve, which looks in its shape like a resonance curve (inset of fig. 18a, upper part, fig. 5). As a function of partial area the energy increases to a partial area of 50%, then suddenly drops down and increases asymptotically. The pre-factor a of the logarithm shown in blue in the inset of fig. 18a has a maximum at the transition point at the partial area 0.5.
The activation energy of DSC of the Fe specimen (fig. 18a) is estimated as 118.4 kJ/mol, when also the fourth data point with good matching is included. This energy is exactly the formation enthalpy for Fe_3O_4 magnetite, but concerning the oxidation states (0, +2, +3, +4), the sequence is [Majzlan et al.2004]:

$$Fe - FeO\ (-266.3\ kJ/mol) - Fe_2O_3\ (-824.2\ kJ/mol) - Fe_3O_4\ (-118.4\ kJ/mol) \quad (6)$$

Such a change in oxidation state is impossible, and the formation of Fe_3O_4 magnetite is unlikely; instead, the formation of FeO could explain the change of the color from white to black for the $NaTaO_3$ + Fe composite and from brown to black for the $NaTaO_3$ +Fe_2O_3 composite. The XRD spectrum, which was measured on bulk specimens, however, showed only evidence for the presence of Fe_2O_3. Also, the other activation energies (fig. 18 c, d) do not fit to the mentioned sequence. The small activation energy of 36 kJ/mol estimated from TG on Fe is explained by the solution of Fe into the $NaTaO_3$ lattice. The Friedman analysis of this data shows the smoothest fit, almost constant energy for the entire region of the partial area (inset of fig. 18b).
As summarized in the following section, the sintering behavior of the $NaTaO_3$-Fe_2O_3 composite produced from Fe or Fe_2O_3 is a combined reaction between Fe-solution in the Perovskite lattice, the oxidation of Fe and the reaction bonding, so the quantitative analysis of the DSC and TG data remains a challenge, but some preliminary suggestions are made during the following discussion.

7. Discussion: Micro-structural and electronic model of $NaTaO_3$

In this section the above mentioned data are discussed and ideas for further development are provided. A detailed understanding for the reaction behavior and thermoelectric properties of $NaTaO_3$ + Fe composite would provide the opportunity to increase its performance. Two facts are obvious and should be tried first. The first task is to improve the

sintered density as the present material still contains pores (fig. 12). The next step is the increase in electric conductivity, which is considered as the main factor for the poor figure-of-merit. Thereafter, the Ag-doping need to be stabilized.
The quantitative explanation of the doping requires detailed understanding of the defect chemistry of iron oxides and Perovskites and is still a challenge. In the following, we present a suggestion for the coupled reaction equation, where the quantitative values are more or less rough estimations. $NaTaO_3$ sintered with Fe reacts in the following way to the n-type composite:

$$NaTaO_3 + x\ Fe \rightarrow NaTa_{1-x}Fe_xO_{3-y} + y\ O + 2x\ e^- \quad \text{with } x = 0.14,\ y = \sim 2/3\ x \tag{7}$$

$$z\ Fe + (y + w)\ O \rightarrow (z-x)/2\ Fe_2O_{3-u} \qquad \text{with } u = f(v, w, y, x, z) \tag{8}$$

where z is the molar ratio of the amount of $NaTaO_3$ relative to Fe in the mixed powder specimens before sintering. y is the estimated amount of oxygen released by the reduction of $NaTaO_3$ when Fe is dissolved, which gives two electrons and releases instead one of the three oxygen atoms. The value of x=0.14, maximum solubility of Fe in $NaTaO_3$, is an experimental result of the SEM-EDX analysis (section 4). w the weight gain in oxygen taken from air in order to oxidize metallic Fe, and is estimated from the TG –data measurements as w = 0.1. u is a complicate function of the other quantities and estimated from the differences between TG-data of the $NaTaO_3 + z$ Fe and $NaTaO_3 + x\ Fe_2O_{3\,u}$ composites as u = 0.2…0.6, while u=1 would yield to FeO, which was not observed in the XRD data. The sum formula yields to

$$NaTaO_3 + z\ Fe + w\ O \rightarrow NaTa_{1-x}Fe_xO_{3-y} + t\ Fe_2O_{3-u} + 2x\ e^- \quad \text{with } t = (z-x)/2 \tag{9}$$

Similarly, sintering from a certain amount m of Fe_2O_3 instead of Fe yields to the p-type composite:

$$NaTaO_3 + m\ Fe_2O_3 \rightarrow NaTa_{1-r}Fe_rO_{3-s} + v\ Fe_2O_{3-q} + s\ h^+ + (q+s)\ O \tag{10}$$
$$\text{with } r < x,\ s < y,\ q = \sim 0.5 < u$$

The *ab-initio* calculations explained in section 3, as well as the experiments, confirmed that Fe is a n-type dopant, and Ag a p-type dopant. In conventional semiconductors like Si as in $SrTiO_3$ the doping situation is straight-forward as illustrated in fig. 4 (section 2.2). Added elements from the right side in the periodic table provide one additional electron, so the material becomes n-type, those from the left side provide a hole and the material becomes p-type. In pure $NaTaO_3$ the valence of each elements are $Na^{1+}Ta^{5+}O^{2-}{}_3$. Doping with Fe, which has usual the valence Fe^{3+}, would create two holes. In contrary, as this material is a n-type material in TE-experiments, electrons are released, which cause the oxygen reduction, the same mechanism as it happens for Nb-doped $SrTiO_3$ illustrated in fig. 4 b. On the other hand, oxygen reduction of the specimens occurs, when $NaTaO_3$ is sintered with Fe_2O_3, then yielding to p-type behavior. Thus, it is concluded that the reaction path and the related oxygen partial pressure decide, whether this material is an n- or p-type material.
The thermoelectric data measured on the composite $NaTa_{1-x}Fe_xO_{3-y}$ + z Mol% Fe_2O_3 with z=32 % and produced from Fe, showed the highest n-type Seebeck voltage (-320mV at

ΔT=800K). As the exact oxygen content has not yet been measured, the reason for the Seebeck voltage remains unknown. One explanation can be found by considering percolation theory for composite materials consisting of the main phase A and inserted minor phase B. The volume fraction of 32% is the border line, where the entire connection between A-particles is changed, and connection between B-particles become dominant. In other words, around this concentration range the interfaces between A-B phase are dominant for the materials properties, while at lower concentrations A-phase and at higher concentrations the B-phase properties are dominant. This fact emphasizes that interface properties of this composite material are important.
At composite materials, the Fermi level of phase A and B are adjusted at the interface leading to a p-n-junction, when a remarkable difference between the Fermi level exists. In semiconductor engineering this is known as space charge region (SCR) which forms a large electric field on nano-scale at the p-n junction. In material science this has been emphasized also for improving properties [Gleiter et al. 2001]. In Co-based perovskite thermoelectric composite material this leads to time-dependent pyroelectric behavior [Wunderlich et al. 2009-d]. The strong electric field at the space charge region sucks the electrons towards the boundaries, in which they can travel due to the confinement of the two-dimensional electron gas (2DEG) faster than in usual ceramics. A difference in the electric field at grain boundaries between hot and cold end is necessary to explain the Seebeck voltage leading to a small net electric field macroscopically. The improvement of TE-properties due to 2DEG has been mentioned in section 2.3 especially the discovery of an ultra-high Seebeck-coefficent at the Nb-$SrTiO_3$ monolayer embedded in $SrTiO_3$ [Mune et al. 2007]. Another evidence that interfaces play an important role, is the finding that certain interfaces can filter crossing electrons according to their energy [Vashaee & Shakouri 2004]. This filtering behavior can explain enhanced thermoelectric performance, because electron-phonon interaction is changed and recombination of excited electrons is suppressed. Such consideration together with future improvement of the $NaTaO_3$ composites, such as nano-structuring or proper doping are expected to yield to materials with large Seebeck coefficient.

8. Conclusions

Historically, the intensive research and development of perovskite ceramics as microwave resonators in portable phones has accumulated much knowledge, from which Nb-$SrTiO_3$ was developed as semiconductor with high performance suitable for thermoelectric applications. The search for materials with large effective mass yielded then from Nb-$SrTiO_3$ to $NaTaO_3$. The following findings have been described in this book chapter:
(1) At present, the best *n*-type TE material is $NaTa_{1-x}Fe_xO_{3-y}$ + *t* Fe_2O_{3-u} with x = 0.14, t = 32 Mol-% and a Seebeck coefficient of 0.5 mV/K and a high closed circuit current of 0.25 mA.
(2) This material can be processed by reaction sintering of $NaTaO_3$ + *z* Fe with z =50 wt%, while sintering of $NaTaO_3$ + *r* Fe_2O_3 with r = 50 wt% leads to a *p*-type thermoelectric material.
(3) The remarkable conductivity above 500 °C can be improved by denser sintering (several cycles 1000oC 5h), as well as the *ZT*, in order to make $NaTaO_3$ + *z* Fe compatible with other materials.

(4) The Seebeck coefficient of the p-type-TE material $NaTa_{1-x}Ag_xO_{3-y}$ + *t* AgO_u is also 0.5 mV/K with a yet small closed circuit current of 0.001 mA.
(5) The $NaTaO_3$ + *z* Cu composite shows +/-20 mV high Seebeck voltage pulses when the heat flow is reversed, which might be utilized in a phonon flow-meter.
Further improvement of this promising material is expected. The goals for further materials development of $NaTaO_3$ – Fe_2O_3 composite are:
(1) Improvement of the sintering density,
(2) Improvement of the electric conductivity,
(3) Increase of the solubility of Fe or other elements into the cubic structure of $NaTaO_3$,
(4) Search for co-doping methods to increase of the charier concentration,
(5) Stabilization of the solubility of Ag in $NaTaO_3$ for example by co-doping of other elements
(6) Clarification of the reaction path during sintering.
(7) Finally the ultimate goal is most important: Search for n- and p-type TE-materials with higher efficiency.
This material has a great potential as thermoelectric material, especially when nano-layered composites are considered.

9. Acknowledgements

The publisher suggested this contribution as an invited paper, which is gratefully acknowledged. Experimental data were provided by Susumu Soga, Yoshiyuki Kondo, Naotoshi Okabe and Wataru Sasaki , which is appreciated gratefully.

10. References

[Baca et al. 2001] Baca L., Plewa P., Pach L., and J. Opfermann, Kinetic Analysis Crystallixation of a-Al2O3 by dynamic DTA technique, *Journal of Thermal Analysis and Calorimetry* 66 (2001) 803-813

[Bobnar et al. 2002] Bobnar V., Lunkenheimer P., Hemberger J., Loidl A., Lichtenberg F., and Mannhart J., Dielectric properties and charge transport in the (Sr,La)NbO3.5-x system, *Phys. Rev.* B 65, 155115 (2002)

[Bulusu & Walker 2008] Bulusu A., Walker D.G., Review of electronic transport models for thermoelectric materials, *Superlattices and Microstructures* 44 [1] (2008) 1-36, doi:10.1016/j.spmi.2008.02.008

[Claussen et al. 1996] Claussen N., Garcia D.E., Janssen R., Reaction Sintering of Alumina-Aluminide Alloys (3A), *J. Mater. Res.*11 [11] (1996) 2884-2888, doi: 10.1557/JMR.1996.0364

[Coey et al. 1999] Coey J.M.D., Viret M., Molnar S.von, Mixed valence magnetites, *Adv. Phys.* 48 (1999) 167

[Culp et al. 2006] Culp S.R., Poon S.J., Hickman M., Tritt T.M., Blumm H., Effect of substitutions on the thermoelectric figure of merit of half-Heusler phases at 800 °C, *Appl. Phys. Lett.* **88**, (2006) 042106 1-3, doi: 10.1063/1.2168019

[Gleiter et al. 2001] Gleiter H., Weißmüller J., Wollersheim O., Würschum R., Nanocrystalline materials: A way to solids with tunable electronic structures and properties?, *Acta materialia* 49 (2001) 737 – 745, doi:10.1016/S1359-6454(00)00221-4

[Grünberg 2001] Grünberg P, Layered magnetic structures: facts, figures, future, *J. Phys.: Condens. Matter* 13 (2001) 7691–7706, http://iopscience.iop.org/0953-8984/13/34/314

[Haeni et al.2001] Haeni, J.H., Theis C.D., Shlom, D.G., Tian W., Pan, X.Q., Chang H., Takeuchi, I., Xiang, X.D., Epitaxial growth of the first five members of the Sr_n+1 Ti_n O_3n+1 Ruddlesden–Popper homologous series, *Appl. Phys. Lett.* 78 [1] (2001) 3292-3294, doi: 10.1063/1.1371788

[Hosono et al. 2006] Hosono H., Hirano M,, Ohta H., Koumoto K. et al. "Thermoelectric conversion material based on an electron localization layer between a first and a second dielectric material" Int. Patent PCT/JP2005/020939, WO2006/054550 (2006)

[Imada M., et al. 1998] Imada, M., Fujimori, A., Tokura Y., Metal-insulator transitions, *Rev.Mod.Phys*.70[4](1998) 1039-1263, doi 10.1103/RevModPhys.70.1039

[Kato & Kudo 1998] Kato H. and Kudo A., New tantalate photocatalysts for water decomposition into H and O2, *Chem. Phys. Lett*. 295 [5–6] (1998) 487–492.

[Kennedy et al. 1999] Brendan J Kennedy B.J., Prodjosantoso A K and Howard C.J., Powder neutron diffraction study of the high temperature phase transitions in NaTaO3, *J. Phys.: Condens. Matter* 11 (1999) 6319–6327., 0953-8984/99/336319+09$30.00

[Kjarsgaard & Mitchell 2008] Kjarsgaard B.A., Mtchell R.H., Solubility of Ta in the system CaCO3 – Ca(OH)2 – NaTaO3 – NaNbO3 ± F at 0.1 GPa: implicationf for the crystallization of Pyrochlore-Group Minaerals in Carbonatites, *The Canadian Mineralogist* 46 (2008) 981-990, doi : 10.3749/canmin.46.4.981

[Kresse & Hafner 1994] Kresse, G.., Hafner, J., Ab initio molecular dynamics simulation of the liquid-metal- amorphous- semiconductor transition in germanium, *Phys. Rev. B* 4914251 (1994), doi: 10.1103/PhysRevB.49.14251

[Lee et al. 1995] Lee W.Y., Bae Y.W., Stinton D.P., Na2SO4 induced Corrosion of Si3N4 Coated by CVD with Ta2O5 *J.Am.Cer.Soc.* 78 [7] (1995) 1927-30

[Lee et al. 2006] Lee K.H., Kim S.W., Ohta H., and Koumoto K, Ruddlesden-Popper phases as thermoelectric oxides: Nb-doped SrO(SrTiO3)n (n=1,2), *J. Appl Phys* 101 (2006) 063717, doi: 10.1063/1.2349559

[Lee et al. 2007-a] Lee K.H., Muna Y., Ohta H., and Koumoto K., Thermoelectric Properties of Ruddlesden–Popper Phase n-Type Semiconducting Oxides: La-, Nd-, and Nb-Doped Sr3Ti2O7, *Int. J. Appl. Ceram. Technol.*, 4 [4] 326–331 (2007)

[Lee et al. 2007-b] Lee K.H., Kim S.W., Ohta H., and Koumoto K. *J. Appl Phys* 101 (2007) 083707, Doi: 10.1063/1.2349559

[Lee et al. 2008] Lee K.H., Muna Y., Ohta H., and Koumoto K., Thermal Stability of Giant Thermoelectric Seebeck Coefficient for SrTiO3/SrTi0:8Nb0:2O3 Superlattices at 900K, *Appl. Phys. Exp*. **1** 015007 (2008)

[Lichtenberg et al. 2001] Lichtenberg, F., Herrnberger, A., Wiedenmann, K., Mannhart, J., Synthesis of perovskite-related layered $A_nB_nO_{3n+2}$ -ABO_X type niobates and titanates and study of their structural, electric and magnetic properties, *Progress in Solid State Chemistry* 29 (2001) 1–70

[Majzlan et al.2004] Majzlan J, Navrotsky A., and Schwertmann U., Thermodynamics of iron oxides: Part III. *Geochimica et cosmochimica acta* ISSN 0016-7037 68 [5] (2004) 1049-1059, doi:10.1016/S0016-7037(03)00371-5

[Mune et al. 2007] Mune Y., Ohta H., Koumoto K., Mizoguchi T., and Ikuhara Y., Enhanced Seebeck coefficient of quantum-confined electrons in SrTiO3 /SrTi0.8Nb0.2O3 superlattices, *Appl. Phys. Lett.* **91**, 192105 (2007), doi: 10.1063/1.2809364

[Nolas et al. 2006] G.S.Nolas, Poon J., Kanatzidis M., Recent Developments in Bulk Thermoelectric Materials *MRS Bulletin* 31 (2006) 199-205; US Patent 6207888 (2001)

[Ohmoto & Hwang 2004] Ohtomo A., Hwang H. Y., A high-mobility electron gas at the LaAlO3/SrTiO3 heterointerface, *Nature* 427 [1] (2004) 423-426

[Ohsato 2001] Ohsato H., Science of tungstenbronze-type like Ba6-3xR8+2xTi18O54 (R=rare earth) microwave dielectric solid solutions, *Journal of the European Ceramic Society* 21 (2001) 2703–2711, doi:10.1016/S0955-2219(01)00349-1

[Ohta et al. 2005-a] Ohta S., Nomura T., Ohta H., and Koumoto K., High-temperature carrier transport and thermoelectric properties of heavily La- or Nb-doped SrTiO3 single crystals, *J. Appl. Phys*. 97 034106 (2005)

[Ohta et al. 2005-b] Ohta S., Nomura T., Ohta H., and Koumoto K., Large thermoelectric performance of heavily Nb-doped $SrTiO_3$ epitaxial film at high temperature, *Appl. Phys. Lett.* 87 (2005) 092108

[Ohta et al. 2007] Ohta, H., Kim, S., Mune, Y., Mizoguchi, T., Nomura, K., Ohta, S., Nomura, T., Nakanishi Y., Ikuhara Y., Hirano M, Hosono H., Koumoto, K,. Giant thermoelectric Seebeck coefficient of a two-dimensional electron gas in SrTiO3, *Nature Materials* 6 [2] (2007) 129-134, doi:10.1038/nmat1821

[Opfermann et al. 1992] Opfermann J., Kaisersberger E., An Advantageous variant of the Ozawa-Flynn-Wall analysis, *Thermochimica Acta* 203 (1992) 167-175

[Opfermann 2000] Opfermann J., Kinetic Analysis Using Multivariate Non-linear Regression. I. Basic concepts, *Journal of Thermal Analysis and Calorimetry*, 60 (2000) 641-658, doi:10.1023/A:1010167626551

[Perez-Mato et al. 2004] Perez-Mato J. M., Aroyo M., García A., Blaha P., Schwarz K., Schweifer J., Parlinski K., Competing structural instabilities in the ferroelectric Aurivillius compound SrBi2Ta2O9, *Phys. Rev. B* 70 (2004) 214111, doi: 10.1103/PhysRevB.70.214111

[Ruddlesden & Popper 1958] Ruddlesden, S.N.; Popper, P., The compound Sr3Ti2O7 and its structure, *Acta Crys.* 11 (1958) 54-55

[Ryan& Fleur 2002] Ryan M.A., Fleur J.P., Where There Is Heat, There Is a Way, *The Electrochem. Soc. Interface* (2002) 30-33 http://www.electrochem.org /publications/interface/summer2002/IF6-02-Pages30-33.pdf

[Sanders & Gallagher 2003] Sanders J. P., and Gallagher P. K., Kinetics of the oxidation of Magnetite using simultaneous TG/DSC, *Journal of Thermal Analysis and Calorimetry*, 72 (2003) 777–789, 1388 6150/2003/

[Shanker et al., 2009] Shanker V., Samal S.L., Pradhan G.K., Narayana C., Ganguli A.K., Nanocrystalline NaNbO3 and NaTaO3: Rietveld studies, Raman spectroscopy and dielectric properties, *Solid State Sciences* 11 (2009) 562–569, doi:10.1016/ j.solidstatesciences.2008.08.001

[Shirane et al. 1954] Shirane G., Newnham R., Pepinski R., Dielectric Properties and Pahse Transitions ab NaNbO3, *Phys. Rev.* 96 [1] (1954) 581- 588

[Shimizu et al. 2004] Shimizu T., Yamaguchi T., Band offset design with quantum-well gate insulating structures, *Appl. Phys. Lett.* 85 (2004)1167, doi:10.1063/1.1783012

[Sjakste et al. 2007] Sjakste J., Vast N., and Tyuterev V., Ab initio Method for Calculating Electron-Phonon Scattering Times in Semiconductors: Application to GaAs and GaP, *Phys. Rev. Lett.* 99 (2007) 236405, doi: 10.1103/PhysRevLett. 99.236405

[Sommerlate et al. 2007] Sommerlate J., Nielsch K., Boettner H., Thermoelektrische Multitalente (in German), *Physik Journal* 6 [5] (2007) 35-41 ISSN-Nr 1617-9439

[Stegk et al. 2009] Tobias A. Stegk, Henry Mgbemere, Ralf-Peter Herber, Rolf Janssen, Gerold A. Schneider, Investigation of phase boundaries in the system (KxNa1−x)1−yLiy(Nb1−zTaz)O3 using high-throughput experimentation (HTE), *Journal of the European Ceramic Society* 29 (2009) 1721–1727, doi:10.1016/ j.jeurceramsoc.2008.10.016

[Sterzel & Kuehling 2002] Sterzel, H,J, Kuehling, K, BASF, *Thermoelectric materials,* European Patent EP 1289026 A2 (2002)

[Suzuki et al. 2004] Suzuki A., Wu F., Murakami H., Imai H., High temperature characteristics of Ir–Ta coated superalloys, *Science and Technology of Advanced Materials* 5 (2004) 555–564, doi:10.1016/j.stam.2004.03.004

[Terasaki 1997] Terasaki, I. Sasago, Y., Uchinokura, K., "Large thermoelectric power in NaCo2O4 single crystals", *Phys. Rev. B*, 56 [20] (1997) R12685-R12687, doi: 10.1103/PhysRevB.56.R12685

[Vashaee & Shakouri 2004] Vashaee D. and Shakouri A., Improved Thermoelectric Power Factor in Metal-Based Superlattices, *Phys. Rev. Lett.* 92, 106103-4 (2004), doi: 10.1103/PhysRevLett.92.106103

[Vining 1991] Vining C.B., A model for the high-temperature transport properties of heavily doped n-type silicon-germanium alloys, *J. Appl. Phys.* 69 [1] (1991) 331- 341

[Wang et al. 2007-a] Y. Wang, K-H. Lee, H. Hyuga, H. Kita, K. Inaba, H. Ohta and K. Koumoto, Enhancement of Seebeck coefficient for SrO(SrTiO3)2 by Sm-substitution: Crystal symmetry restoration of disordered TiO6 octahedra, *Appl. Phys. Lett.,* 91 242102 (2007)

[Wunderlich et al. 2000] Wunderlich W., Fujimoto M., Ohsato H., Sekiguchi S., Suzuki T., Molecular Dynamics simulation about misfit dislocations at the $BaTiO_3$ / $SrTiO_3$ interface, *Thin Solid Films,* 375 [1-2] (2000) 9-14, doi:10.1016/S0040- 6090(00)01170-6

[Wunderlich et al. 2005] Wunderlich W., Ohta S., Ohta H., Koumoto K., Effective mass and thermoelectric properties of SrTiO3-based superlattices calculated by ab-initio, *Proc. Int. Conf. Thermoelectrics ICT2005*, IEEE (2005) 237-240

[Wunderlich et al. 2006-a] Wunderlich, W., Ohsato, H., Dielectric Constant-Dependence on atomic substitution of Y_2BaCuO_5 clarified by Ab-initio calculations *J. Europ. Ceram. Soc.* 16 (2006) 1869-1875 doi:10.1016/j.jeurceramsoc.2005.09.056

[Wunderlich & Koumoto 2006-b] Wunderlich W., Koumoto K., Development of high-temperature thermoelectric materials based on SrTiO3-layered perovskites, *International Journal of Materials Research* 97 [5] (2006) 657-662 http://www.ijmr.de/ directlink.asp?MK101286

[Wunderlich, 2008-a] Wunderlich W., Reduced bandgap due to phonons in SrTiO3 analyzed by ab-initio calculations, *Solid-State Electronics* 52 (2008) 1082–1087, doi:10.1016/j.sse.2008.03.017

[Wunderlich, et al. 2008-b] Wunderlich W., Ohta H., Koumoto K., Effective mass calculations of SrTiO3-based superlattices for thermoelectric applications lead to new layer design, *arXiv.org*/abs/0808.1772

[Wunderlich et al., 2009-a] Wunderlich W., Ohta H., Koumoto K., Enhanced effective mass in doped $SrTiO_3$ and related perovskites, *Physica B* 404 (2009) 2202-2212, doi:10.1016/j.physb.2009.04.012 (see also *arXiv/cond-mat* 0510013)

[Wunderlich 2009-b] Wunderlich W., $NaTaO_3$ composite ceramics - a new thermoelectric material for energy generation, *J Nucl. Mat.* 389 [1] (2009) 57-61, doi:10.1016/j.jnucmat.2009.01.007

[Wunderlich et al. 2009-c] Wunderlich W., Motoyama Y., Screening and Fabrication of Half-Heusler phases for thermoelectric applications, *Mater. Res. Soc. Symp. Proc.* Vol. 1128-U01-10 (2009)1-6., doi:10.1557/PROC-1128-U01-10, arXiv.org/abs/ 0901.1491

[Wunderlich et al. 2009-d] Wunderlich W., Fujiwara H., Difference between thermo- and pyroelectric Co- based RE-(= Nd, Y, Gd, Ce)-oxide composites measured by high-temperature gradient, http://*arxiv.org*/abs/0909.1618 (Proc. ICT 2009)

[Wunderlich & Soga 2010] Wunderlich W., Soga S., Microstructure and Seebeck voltage of Mn,Cr,Fe,Ti- added $NaTaO_3$ composite ceramics, *Journal of Ceramic Processing Research* 11 [2] 233~236 (2010)

[Xu et al. 2005] Xu J., Xue D., Yan S., Chemical synthesis of NaTaO3 powder at low-temperature, *Materials Letters* 59 (2005) 2920 – 2922, doi:10.1016/j.matlet.2005.04.043

[Yan et al., 2009] Yan S.C., Wang Z.Q., Li Z.S., Zou Z.G., Photocatalytic activities for water splitting of La-doped-NaTaO3 fabricated by microwave synthesis, *Solid State Ionics* 180 (2009) 1539–1542, doi:10.1016/j.ssi.2009.10.002

[Yamamoto et al. 2007] Yamamoto M., Ohta H., Koumoto K., Thermoelectric phase diagram in a CaTiO3–SrTiO3–BaTiO3 system, *Appl.Phys.Lett.* 90 (2007) 072101, doi: 10.1063/1.2475878

2

Glass-Ceramics Containing Nano-Crystallites of Oxide Semiconductor

Hirokazu Masai*, Yoshihiro Takahashi and Takumi Fujiwara
Tohoku University
**present affiliation: Kyoto University*
Japan

1. Introduction

1.1 Glass and Crystal

Inorganic glass materials generally possess high transparency, good formability, and tuneable chemical composition range. Since glass has no grain boundary, which is a characteristic of liquid, attained high transparency of glass makes it to be a fundamental material for our daily life, for examples, window, display panel glass and optical glass fibres. The good formability is originated from the random network structure with interstitial free volume, and therefore, large and long glassy material can be prepared much easier than inorganic crystal. Note that the term "random" in glass means a lack of the long-range ordering. Actually in glass there is a short-range ordering of atoms that constitute various coordination polyhedra. Thus, the short-range ordering in amorphous is basically identical to that in crystal. On the other hand, the random network of glass closely correlates with the chemical composition diversity, which in turn allows us to tailor physical property and various functionalities. The diversity is also a unique characteristic of amorphous glass materials.

The most conventional definition of glass is "an amorphous material possessing the glass transition behaviour". Figure 1 shows a typical volume change of glass and crystal as a function of temperature. In the case of crystal, transition from liquid to solidified crystal occurs at the melting temperature, T_m. On the other hand, a glass material takes the supercooled state below the T_m, and shows the transition to glass in the temperature range where the viscosity of glass increases to 10^{13} dPa·s. Temperature at which transition from supercooled liquid to glass occurs is mentioned as the glass transition temperature, T_g. In the temperature region, some physical parameters of glass material show "some steep" change. Since the T_g is a fictive temperature that depends on the fabrication process, a glass can take several values of T_g depending on the cooling rate. As shown in Fig. 1, there is a volume difference between crystal and the glass, which originates from the free volume of glass material possessing the random network. Because of the random network structure, the Gibbs free energy of a glass material is inherently larger than that of the corresponding crystal, and glass materials exist as a metastable state. It means that phase transition of glass to crystalline phase can progress above the T_g, at which migration of the compositional units

starts. The thermal transition process from glass to the corresponding crystal is called crystallization of glass. On the other hand, the resulted glassy material containing some precipitated crystallites is designated as a "glass-ceramic". Since the short-range ordering of glass is basically identical to that of crystal, the glass-ceramic can be said as a glassy material possessing partially long-range and/or medium-range ordering. Such glassy material containing both ordered and disordered parts is the main target of this chapter.

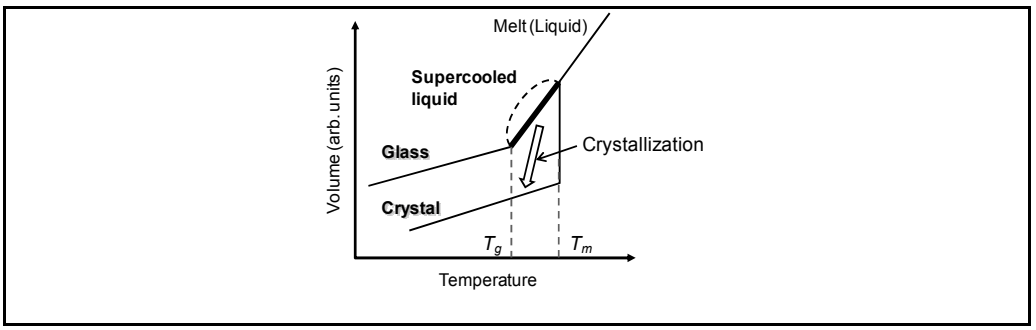

Fig. 1. A typical volume change of glass and crystal as a function of temperature.

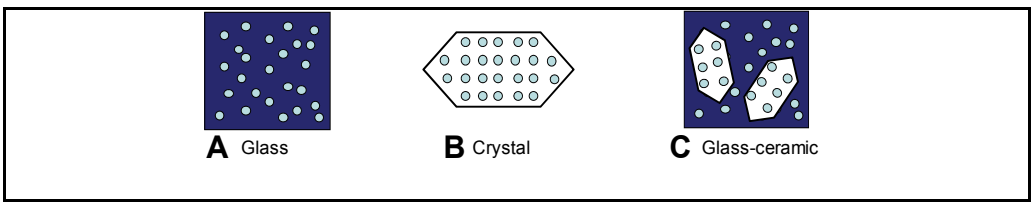

Fig. 2. Schematic images of (A) glass, (B) crystal, and (C) glass-ceramic.

1.2 Crystallization of Glass & Glass-Ceramic

It is natural that thermodynamically metastable amorphous glass changes into stable ordered crystal above the T_g. In earlier years, crystallization of glass was called devitrification of glass, because there is a difference in refractive index between the precipitated crystallites and the residual amorphous regions. The formation of boundary within a matrix by crystallization often brings about a loss of transparency of the material due to the Mie scattering. To overcome this problem, two approaches can be used: (I) tuning the refractive index by addition of various kinds of oxides, and (II) controlling the size of precipitated crystallites. The former approach is realized by using a database of optical property of glass matrix. Since the additivity between property and compositions usually holds in glass material, tailoring of refractive index can be attained empirically. On the other hand, the later approach is of importance even in a glass possessing the same chemical composition as the crystal, in that case the mismatch of refractive index between crystallites and residual amorphous is relatively small. Crystallization from a supercooled liquid state above the T_g progresses via two processes; i.e. nucleation and crystal growth. The rates of nucleation and crystal growth depend on the heat-treatment temperature as well as crystalline composition. Figure 3 shows a schematic depiction of rates of nucleation and crystal growth in glass. Although the details of these two processes are not mentioned here (please see some treatises, for examples, McMillan, 1979 or Strnad, 1986), an important point

is that nucleation and crystal growth can be independently controlled by careful heat-treatment procedure. As shown in Fig. 3, the maximum rates of nucleation and crystal growth occur at different temperatures. In addition, nucleation preferentially occurs in the low-temperature region above the T_g. Precipitation of either large crystallites (> several μm) or small crystallites (< several nm) is effective for maintaining the transparency of the glass after crystallization. The latter crystallization, in which nano-sized crystallites are precipitated, is often referred to as "nano-crystallization". In the case of precipitation of crystallites from the glass matrix that possesses chemical composition different from the stoichiometric composition of crystal, the nano-crystallization process is quite of importance. Glass-ceramic, which is usually obtained by heat-treatment, *i.e.* crystallization, of a precursor glass, is a kind of glassy material consisting of disordered glass regions and ordered precipitated crystalline regions. Since glass-ceramic permanently shows both glassy and crystalline characteristics without any temporal change below the T_g, it may be mentioned that glass-ceramic is an inorganic composite material possessing not only merits of glass materials but also its unique physical properties of the corresponding crystals. Conventional glass-ceramic is superior to the precursor glass in terms of strength, heat-resistance, and thermal shock resistance, because the nano-crystallites precipitated in the glass matrix. In addition, a combination of the physical properties of glass and crystal gives rise to novel functions. For example, commercially available low expansion glasses consist of both crystallites with negative thermal expansion and the residual amorphous parts that possess positive one. For obtaining desired glass-ceramic, control of the crystallization behaviour is needed as mentioned above. Indeed, several crystalline phases are sometimes simultaneously created from the same mother glass, and thus, the thermodynamic and kinetic control is necessary for obtaining the glass-ceramic with practical functions. However, in another respect, such diversity is the origin of various functionalities even in a glass-ceramic possessing the simple nominal chemical composition. A variety of properties of glass-ceramic, therefore, have motivated many researchers to fabricate novel functional devices (Beall & Pinckney, 1999, Takahashi et al., 2001, 2004, Masai et al., 2006).

In the chapter, the authors have described our recent works on fabrication of oxide semiconductor-containing transparent glass-ceramics. Such glass-ceramics will be a functional composite using the unique property of precipitated crystal. In addition, it is expected that physical property of precipitated crystallites in glass-ceramic is different from that of single crystal, because there is interface, which affects both the structure and physical property, between these materials. In the following sections, examination of correlation between chemical composition of glass and the precipitated crystal has been reported.

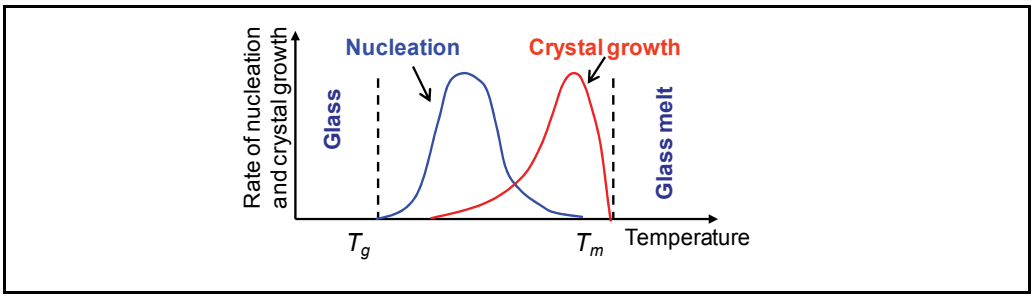

Fig. 3. Schematic depiction of rates of nucleation and crystal growth in glass.

2. Glass-Ceramics Containing TiO_2 Nano-Crystallites

2.1 Background

Titanium dioxide, TiO_2, has attractive characteristics, such as chemical stability, high refractive index, and it is used in electronic devices or as a photocatalyst. In particular, the photocatalysis of TiO_2 is industrially applied in many fields owing to its strong oxidation capability and high hydrophilicity (Fujishima & Honda, 1972). TiO_2-containing transparent materials are usually prepared by vapour deposition (Yeung & Lam, 1983), sputtering deposition, or by coating using a TiO_2-containing sol. However, the properties of TiO_2 produced by these deposition or coating techniques change over time by surface damage and thus a re-coating process of the material is necessary. In other words, there is the limitation of permanent performance in the TiO_2 deposition or coating materials. On the contrary, if the TiO_2 crystallites exist in the glass matrix, the TiO_2 crystallites dispersed in the glass matrix will exhibit a stable characteristic property even with surface polishing.

However, literature on crystallization of glass containing TiO_2 crystallites by a heat-treatment is scarce. Although studies of phase-separated TiO_2 glass have been reported, the obtained bulk glass is usually heterogeneous with a mixture of TiO_2 crystallites and other crystallites (Hosono et al., 1990). Indeed, it is extremely difficult to obtain selective crystallization of TiO_2, because a TiO_2 crystal acts as a nucleus of other crystalline phases and also because it forms another crystal structure with other glass forming oxides, such as Al_2O_3 or SiO_2 (as mentioned in 1.2). For example, there is a patent about the glass-ceramic containing TiO_2, in which rutile is crystallized by a heat-treatment (Brydges & Smith, 1976). Although it reported that the obtained glass-ceramics, which contained fibrous crystals of rutile, presented improvements of mechanical strength compared with the original mother glass, it also reported that additional crystallites $Al_4B_2O_9$ was coincidentally crystallized. In addition, it is difficult to attain a high degree of transparency in a TiO_2-crystallite-containing transparent glass, because of light scattering by TiO_2 crystallites with a large refractive index.

We can propose TiO_2 glass-ceramic as a promising material for several applications. First application is as a photocatalytic transparent material in which precipitated TiO_2 crystallites will play permanent photocatalytic property because of the fully dispersion. Second application is use in an optical element as a lasing optical device (Lawandy et al., 1994). The TiO_2 nano-crystallites in the glass matrix can confine light, which is suitable and interesting for random lasing, because the refractive index of TiO_2 is 2.52 (anatase) ~ 2.728 (rutile). Ling et al. demonstrated laser oscillation in a polymer film containing TiO_2 particles and an organic dye (Ling et al., 2001). If the host matrix of random media is an inorganic material, which has advantage in terms of durability better than organic material, it will break though the wall for the practical application of random lasing devices. On the other hand, if periodic nano-structure of TiO_2 can be fabricated, such material will be a photonic crystal that can control the lightwave. Since TiO_2-precipitated glass-ceramic can be a hybrid material such as solar sell (O'Regan, B. & Gratzel, 1991), there is wide diversity of the matrix using the unique physical property.

As a matter of fact, we have accidentally discovered the TiO_2-precipitated glass-ceramic. Different from a target Aurivillius $CaBi_4Ti_4O_{15}$ (Kato et al., 2004), unexpected TiO_2 crystalline phase was observed in the glass-ceramics in 2006. In other words, the present study was delivered by serendipity. The fact that such unexpected crystalline phase shows

the unique physical property in glass-ceramics is also an interesting point of study on glass-ceramics.

2.2 CaO-B_2O_3-Bi_2O_3-Al_2O_3-TiO_2 (CaBBAT) Glass

At an early stage, we investigated a glass forming region of the precursor glass using CaO-B_2O_3-Bi_2O_3-Al_2O_3-TiO_2 (CaBBAT) system. The molar ratio of CaO : Bi_2O_3 : TiO_2 was fixed at 1 : 2 : 4, which was a nominal stoichiometric composition ratio of $CaBi_4Ti_4O_{15}$, whereas that of B_2O_3, which belongs to network forming oxide group, was changed to obtain homogeneous transparent precursor glass. Glass samples were prepared by conventional melt-quenching method using alumina crucibles, and the eluted amount of Al_2O_3 from the crucible was estimated to be about 20 mol% using a fluorescence X-ray analysis. Table 1 shows the chemical compositions of the CaBBAT precursor glasses and their apparent transparencies. No homogenous precursor glass was obtained with the amount of B_2O_3 lower than 50 mol% (**1**, **2**, and **3**). On the other hand, we also found that about 10 mol% of Bi_2O_3 and 5 mol% of CaO were needed to prepare transparent precursor glasses (**7** and **8**). Note that only rutile crystallites were precipitated in all opaque precursor glasses after melt-quenching (Fig. 4). Therefore, it suggests that crystallization of rutile easily occurs in the glass system, and that quasi phase separation occurs during the crystallization process. Although the prepared $5CaO$-$65B_2O_3$-$10Bi_2O_3$-$20TiO_2$ glass melted in a platinum crucible was opaque because of crystallization of rutile TiO_2, the crystallization was prevented by addition of Al_2O_3 as a starting material. It indicates that Al_2O_3 was also essential for the transparency and homogeneity of the glass.

	Chemical composition (mol%)				Apparent	T_g (°C)	Precipitated
No.	CaO	Bi_2O_3	B_2O_3	TiO_2	transparency		crystalline phase
1	12.5	25	12.5	50	Opaque	–	Rutile
2	10	20	30	40	Translucent	–	Rutile
3	7	14	51	28	Translucent	–	Rutile
4	5	10	65	20	Transparent	569	–
5	5	10	75	10	Transparent	572	–
6	5	10	85	0	Transparent	510	–
7	5	5	70	20	Opaque	–	Rutile
8	0	10	70	20	Opaque	–	Rutile

Table 1. Several CaO-Bi_2O_3-B_2O_3-Al_2O_3-TiO_2 (CaBBAT) precursor glasses prepared using alumina crucible: Each value of T_g was measured using differential thermal analysis.

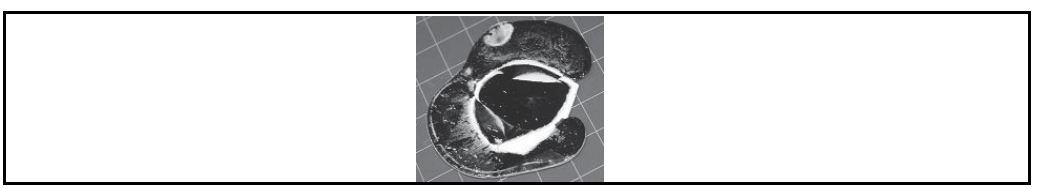

Fig. 4. Photograph of the CaBBAT glass (**3**). Rutile was selectively precipitated even in the precursor glass prepared by melt-quenching method.

The T_gs of TiO_2-containing transparent glasses were almost 570°C whereas TiO_2-free glass was 510°C. The result shows that T_g of the TiO_2-containing glass is dominated by local structure that correlates with titanium species. The obtained transparent precursor glasses were vinous in colour, and there was an absorption band around 490 nm (see Figs. 6A or 8B). These absorption bands are attributed to Bi-radical-like species or Bi_2 clusters (Khonthon et al., 2007, Murata & Mouri, 2007, Masai et al., 2009). Since shift of the absorption band in the visible region was observed by changing chemical composition, it is suggested that a structure consisting of several atoms affects formation of such Bi species.
Using the nominal composition of B_2O_3, we have called the CaBBAT glasses (**4**), (**5**), and (**6**) as CaBBAT65, CaBBAT75, and CaBBA85, respectively. Figure 5 depicts XRD patterns of the CaBBAT65, CaBBAT75, and CaBBA85 glass-ceramics heat-treated at 630°C for 3 h. Here, we have distinguished several samples by using an abbreviation, $\mathbf{C}_x$: a glass-ceramic with the heat-treatment temperature at x°C for 3 h. Compared the obtained patterns to the JCPDS pattern of rutile (JCPDS No. 01-084-1283), it is found that rutile was selectively precipitated in these glass-ceramics. Until 2007, there was no report on the selective crystallization of TiO_2 from glass matrix after heat-treatment. The obtained XRD patterns show the characteristic of the glass-ceramics.

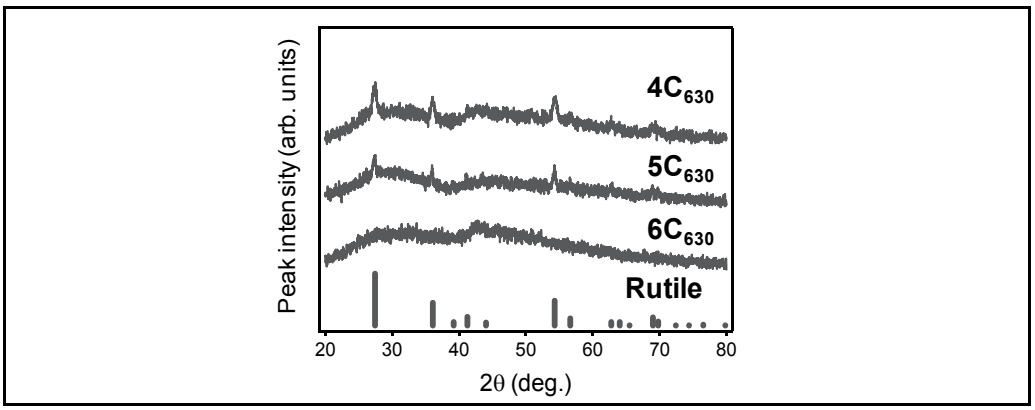

Fig. 5. XRD patterns of the CaBBAT65, CaBBAT75, and CaBBA85 glass-ceramics after heat-treatment at 630°C for 3 h: **4**$\mathbf{C}_{630}$, **5**$\mathbf{C}_{630}$, and **6**$\mathbf{C}_{630}$, respectively.

Figure 6A shows the absorption spectra of the CaBBAT65 glass (**4**), and the glass-ceramics (**4**$\mathbf{C}_{620}$, **4**$\mathbf{C}_{630}$, and **4**$\mathbf{C}_{640}$). The absorption coefficient increases with increasing heat-treatment temperature in the whole wavelength range covered. The apparent colour of the sample drastically changes after the heat-treatment above 625°C from transparent vinous to translucent blue. Figure 6B shows the photograph of the precursor glass (**4**) and the glass-ceramics (**4**$\mathbf{C}_{620}$ and **4**$\mathbf{C}_{640}$) whose thickness was about 500 μm. The colour of glass-ceramics depends on the heat-treatment temperature. On the other hand, Fig. 6C shows the photograph of the same samples with a white lighting from the backside. We can observe Chinese characters through these obtained glasses with backside lighting. Since the transmitted light is observable through these crystallized samples, it is suggested that this blue colour is scattered light originating from the microstructure consisting of nanoparticles. Moreover, the reflected light shows specific blue colour that originates with the specific microstructure in nano-scale. Since refractive index of the CaBBAT65 glass was 1.754 at 633

nm, there was a difference of refractive index, Δn, 0.8 or larger between the crystallized rutile and the surrounding glass matrix. Therefore, it is suggested that the nano-scale crystallization is the dominant factor for the transparency of the TiO_2 containing glass-ceramic even in such a large Δn situation. Note that such nanostructure was created using a conventional heat-treatment in an electric furnace. The nano-crystallization of TiO_2 is a kind of self-organization, and it is effective for making nano-scale particles in the matrix.

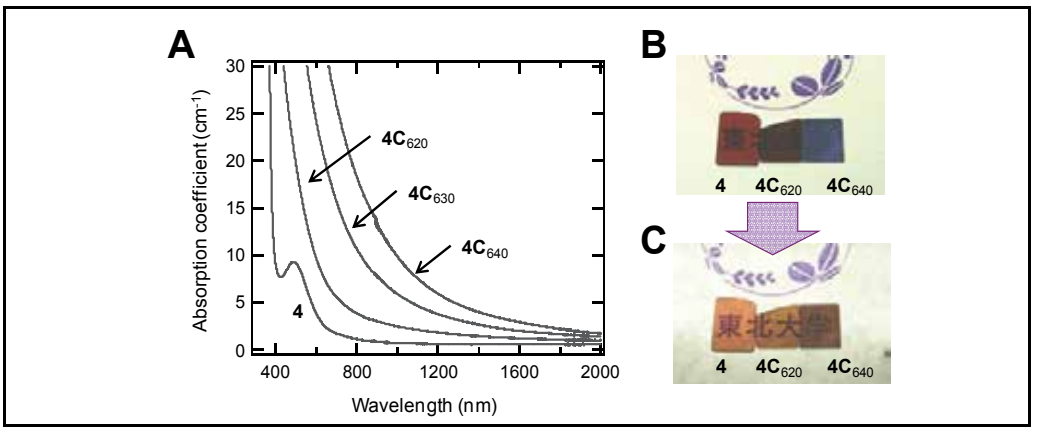

Fig. 6. (A) Absorption spectra of the CaBBAT65 glass **4** and the glass-ceramics (**4C**$_{620}$, **4C**$_{630}$, and **4C**$_{640}$). (B), (C) Photographs of several samples exposed by white light from front side (6(B)) and from the back side (6(C)).

Figure 7A shows XRD patterns of the CaBBAT65 glass-ceramics (**4C**$_{620}$, **4C**$_{630}$, and **4C**$_{640}$) together with that of the precursor glass (**4**). The glass-ceramics showed a mixture of the diffraction pattern of anatase (JCPDS No. 00-021-1272) and rutile. Since no diffraction peak assignable to other phases was observed, the obtained patterns show that TiO_2 crystallites were selectively formed as a single phase.

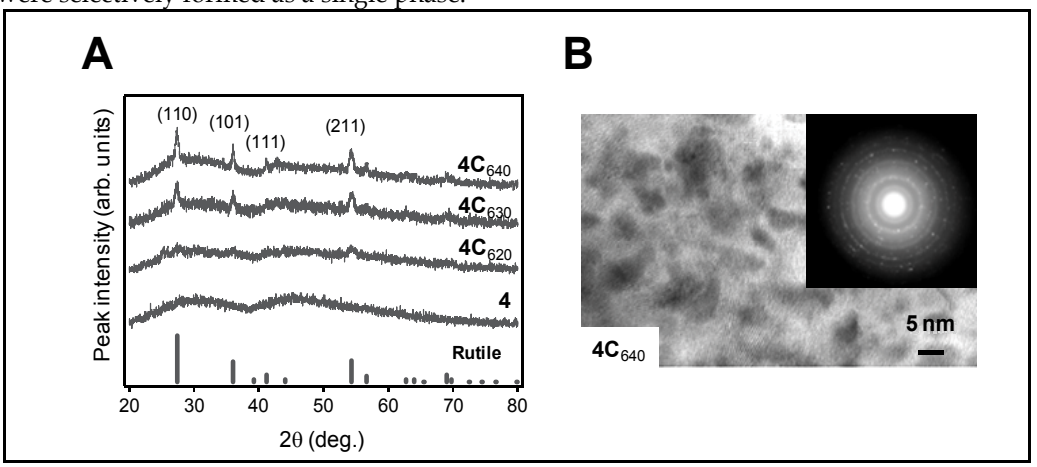

Fig. 7. (A) XRD patterns of the CaBBAT65 precursor glass **4**, and the glass-ceramics (**4C**$_{620}$, **4C**$_{630}$, and **4C**$_{640}$). (B) TEM image of the CaBBAT65 glass-ceramic (**4C**$_{640}$). Inset shows the electron diffraction pattern in which many satellites attributed to rutile are observed.

The average particle diameter measured by the Scherrer equation was 10~20 nm. Since no apparent change of the XRD pattern was observed after surface polishing of 500 μm, we can conclude that the bulk crystallization took place by the heat-treatment. Figure 7B shows the TEM image of the glass-ceramic (**4C**$_{640}$). Crystalline domains that have less than 10 nm diameter, which is comparable to the particle size of TiO_2 crystallites estimated by the XRD patterns, are observed. Inset shows the electron diffraction pattern of the glass-ceramic. The diffraction satellites attributable to rutile (110), (101), and (211) confirm the result of the XRD measurement. It is, therefore, suggested that the TiO_2 domains with small size distribution are the origin of the blue scattering from the glass matrix.

2.3 Sn-Doped CaBBAT Glass

As mentioned above, our group has prepared oxide semiconductor TiO_2-precipitated glass-ceramic for the first time in 2007. However, the CaBBAT precursor glass possesses a strong absorption band, which is correlated with the bismuth species, in the visible region. Since drastically compositional change was thought to be demerit for both a transparent glass and the glass-ceramic, addition of a small amount of other elements was considered to improve the transparency in the CaBBAT65 glass, and to maintain the selective crystallization behaviour of TiO_2 from the glass matrix.

Figure 8A shows the photograph of the CaBBAT65 glasses (**4**) and the SnO-containing CaBBAT glasses (**9**), (**10**), and (**11**), where the amounts of SnO were (**4**) 0, (**9**) 0.1, (**10**) 0.5, and (**11**) 1 mol%, respectively. The colours of the samples changed with increasing amount of SnO, and transparent glasses were obtained with SnO contents ranging from 0.1 to 1 mol%. On the other hand, precipitation of SnO_2 crystallites was observed in the sample containing 2 mol% of SnO, suggesting a limitation of SnO content. Figure 8B shows the absorption spectra of these glasses. The absorption coefficient in the visible region decreases drastically with addition of SnO and saturates with SnO of 0.5 mol%. The transmittance at 500 nm of the sample (**4**) was 10% whereas that of the glass (**10**) was about 70%, showing a clear improvement of the transparency by addition of SnO. If the change of valence of the Sn ion, from divalent to tetravalent in a glass melt or glass matrix, is responsible for the suppression of optical absorption, addition of oxides of multi-valent transition metals is expected to be also effective in improving the transparency. However, no improvement of transparency was observed in the CaBBAT glass containing such metal oxides as CeO_2, Cu_2O and Sb_2O_3 in which the valences of the metals are changeable. This indicates that the effect of SnO addition is not a simple redox-reaction. Since the absorption band depends on the chemical composition of a bismuth-containing glass, a structural change consisting of several ions should be considered for clarification of the mechanism.

In the Sn-doped CaBBAT glass, selective crystallization of TiO_2 was also attained by conventional heat-treatment. The Sn-doped CaBBAT glass-ceramic showed not only better transparency but also better photocatalytic property than the non-doped glass. Although the underlying mechanisms for the above effects remain to be clarified, the obtained results show that the SnO addition enhances both the transparency and the photocatalytic activity without any derogatory effect on the selective nature of TiO_2 precipitation.

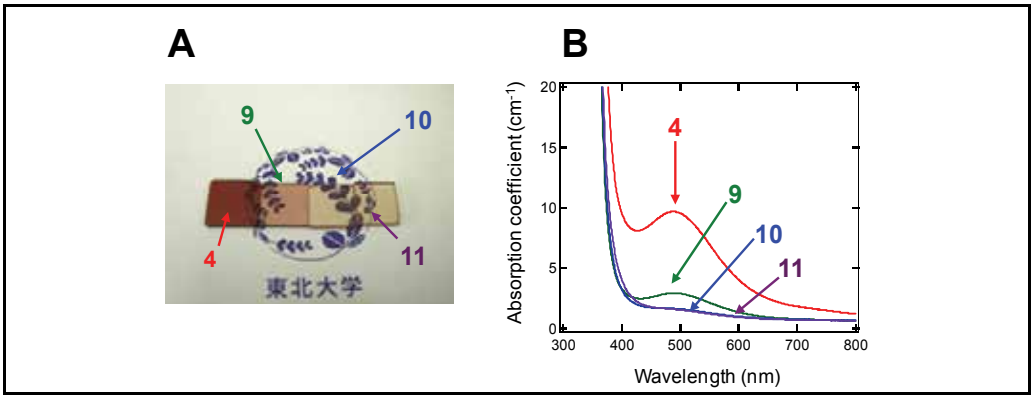

Fig. 8. (A) Photograph of the CaBBAT65 glasses with SnO-addition of (**4**) 0 mol%, (**9**) 0.1 mol%, (**10**) 0.5mol%, and (**11**) 1 mol%. (B) Absorption spectra of these CaBBAT65 glasses.

2.4 Bi-free TiO_2-Precipitated Glass-Ceramic

The CaBBAT glass, whether it contained SnO or not, contains a large amount of Bi_2O_3 as an essential component for TiO_2-glass-ceramic as well as transparent mother glass. Bi_2O_3 is, however, a hazardous material and there should be excluded from both environmental and industrial view point.

For fabrication of Bi-free TiO_2 glass-ceramics, we have focused on the bond dissociation energy of metal oxide in glass matrix (Sun, 1947). The concept is substitution several components, which have similar bond dissociation energy, for Bi_2O_3 in the CaBBAT glass. Since bond dissociation energy of Bi_2O_3 was not reported, we have calculated the single bond strength using the Born-Haber cyclic process (Lide & Kehiaian, 1994). The calculated value is shown as Eq. (1).

$$BiO1.5(s) \rightarrow Bi(g) + 1.5O(g) \quad + 868.2\ kJ/mol \tag{1}$$

Since the Bi unit in the oxide glass is reported as BiO_3 or BiO_6, we have estimated the single bond strength as 288.8 kJ/mol (BiO_3) and 142.3 kJ/mol (BiO_6), respectively. It follows that the former belongs to the intermediate group whereas the latter network modifier group. For substitution of Bi_2O_3, we have focused on ZnO that can belong to both intermediate (ZnO_2: bond dissociation energy 301.4 kJ/mol) or network modifier (ZnO_4: bond dissociation energy 150.7 kJ/mol) among several metal oxides. Since the bond dissociation energy of BiO_6 is similar to that of several alkaline earth oxides, RO, we have selected RO and ZnO for preparation of transparent Bi-free glass (R= Ca, Ba and Zn).

Table 2 shows the chemical composition of the obtained precursor glasses. Sample **4** depicts the previous CaBBAT65 glass whereas samples (**12**, **13**, **14**, and **15**) were transparent Bi-free glasses without devitrification during melt-quenching process. On the other hand, no homogeneous glass sample possessing composition of (**16**) or (**17**) was obtained. Therefore, it was found that neither direct substitution ZnO for Bi_2O_3 nor substitution without ZnO is effective for formation of transparent glass. The obtained results show that ZnO, which can play as an intermediate group or a network modifier group, has key for transparent homogeneous glass matrix.

No.	Chemical composition (mol%)						T_g (°C)
	TiO_2	ZnO	B_2O_3	CaO	BaO	Bi_2O_3	
4	20	0	65	5	0	10	570
12	20	10	65	5	10	0	580
13	20	10	65	0	15	0	589
14	20	20	65	5	0	0	587
15	20	25	65	0	0	0	608
16	20	10	65	5	0	0	–
17	20	0	65	25	0	0	–

Table 2. Chemical composition and T_gs of precursor glasses prepared with an alumina crucible. Homogeneous glasses possessing chemical composition of (**16**) and (**17**) were not obtained. (For easy comparison to the glass (**4**), the total amount of oxides exceeds 100 mol% in glasses (**12**) – (**17**).)

Figure 9A shows absorption spectra of the mother glasses: the CaBBAT65 glass (**4**), the SnO-doped CaBBAT65 glass (**10**), and the Bi-free glass (**12**). Figure 9B shows photograph of these glasses. The previous glasses were coloured (**4**, **10**) whereas the Bi-free glass (**12**) shows better transparency in the wavelength region. The result also confirms that Bi species are the origin of the absorption band around 500 nm as reported in several papers. Therefore, we can conclude that the substitution of Bi is effective for the improvement of transparency of the mother glass.

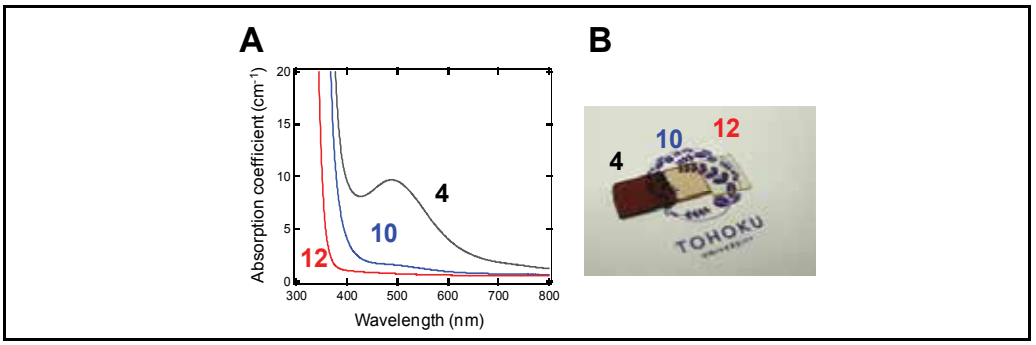

Fig. 9. (A) Absorption spectra of (**4**) the CaBBAT65 glass, (**10**) the SnO-doped CaBBAT65 glass, and (**12**) the Bi-free glass. (B) Photograph of these mother glasses.

Figure 10A shows the XRD patterns of the previous CaBBAT (**4**C_{630} and **10**C_{630}) and the Bi-free (**12**C_{630}) glass-ceramics together with photograph of these glasses. The JCPDS patterns of anatase and rutile are also shown in the figure for reference. The diffraction patterns of Bi-containing glass-ceramics (**4**C_{630} and **10**C_{630}) show precipitation of rutile whereas the pattern of the Bi-free glass-ceramic (**12**C_{630}) shows a mixture of anatase and rutile. We can estimate the average diameter of TiO_2 crystallites in the glass-ceramic (**12**C_{630}) as about 10 nm using the Scherrer equation. Note that the previous glass-ceramics (**4**C_{630} and **10**C_{630}) shows the blue colour, which is originated from the microstructure consisting of nano-particles, whereas the Bi-free glass-ceramic (**12**C_{630}) shows good transparency. The XRD

pattern and appearance of the glass-ceramic indicate that a TiO_2 nano-crystallization has been also attained without Bi_2O_3. Figure 10B shows the TEM image of the glass-ceramic (**12C**$_{630}$). The dashed circles show that the diameter of domains is several nanometres, which is comparable to the particle size of anatase crystallites estimated by the XRD patterns. Inset shows the electron diffraction pattern of the TiO_2 glass-ceramic at the circled region. The diffraction satellites attributable to anatase (101) confirm the result of the XRD measurement. These domains, therefore, are attributed to the anatase nano-crystallites in the glass matrix. It is also of interest that (101) diffraction of anatase is clearly observed in the Bi-free glass-ceramic (**12C**$_{630}$). Since anatase is metastable phase, we could observe no clear diffraction pattern of anatase in the Bi-containing CaBBAT glass-ceramics with various heat-treatment conditions. Therefore, we can conclude that the addition of ZnO improves the transparency of the TiO_2 glass-ceramics, and affects the crystallization of metastable phase.

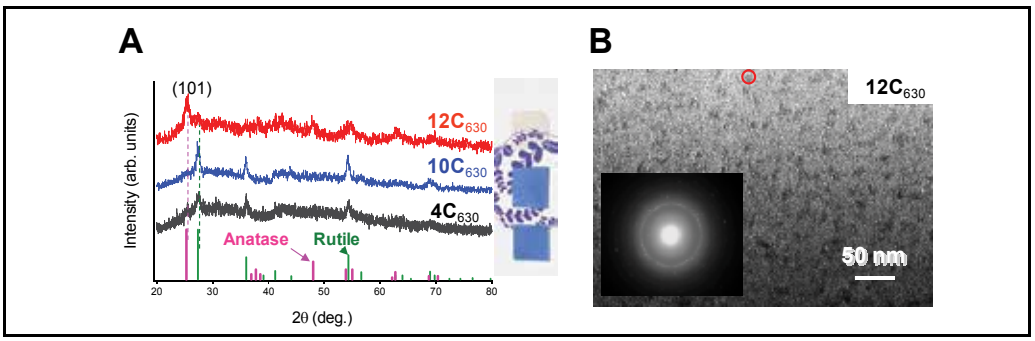

Fig. 10. (A) XRD patterns and photograph of TiO_2 glass-ceramics: the CaBBAT (**4C**$_{630}$), the SnO-doped CaBBAT (**10C**$_{630}$), and the Bi-free (**12C**$_{630}$) glass-ceramics. JCPDS patterns of anatase and rutile are also shown. (B) TEM image of the Bi-free glass-ceramic (**12C**$_{630}$). Inset shows electron diffraction pattern of the circled region.

Since the present approach for substitution of Bi_2O_3 is based on the bond dissociation energy, it can be said that the attempt is a kind of thermodynamically approach in homogeneous glass materials. We have hypothesized that Bi_2O_3 exists conjugated state of network modifier and intermediate. Although there is no clear evidence for coordination state of Bi_2O_3, our hypothesis is plausible, because (1) intermediate TiO_2 that possesses dissociation energy of 305.6 kJ/mol could not be substituted for ZnO, and (2) network modifier CaO makes no homogeneous glass without ZnO (see sample **17**). Therefore, ZnO, which can also play both roles, is effective for fabrication of Bi-free glass and the glass-ceramics. In the substitution, we have decided that amount of Bi cation should be equal to that of sum of other cations.

We examined the photocatalytic property of the TiO_2 glass-ceramics using a conventional decomposition reaction of methylene blue. Details of the measurement are shown in the paper (Masai et al. 2008). The decomposition reaction coefficient, *k*, of the previous glass-ceramic (**4C**$_{630}$) was 0.59 h^{-1} m^{-2}. On the other hand, *k* of the **12C**$_{630}$ glass-ceramics, in which anatase was crystallized, was 0.78 h^{-1} m^{-2}. If we consider the effective decomposition reaction rate per TiO_2, the rate of the previous glass-ceramic is 0.0295 h^{-1} m^{-2} mol^{-1} whereas that of the present glass-ceramic is 0.056 h^{-1} m^{-2} mol^{-1}. The obtained result shows that

precipitation of anatase is effective for high photocatalytic property of the glass-ceramics. The obtained result shows that precipitation of anatase is effective for high photocatalytic property of the glass-ceramics.
In summary, we have fabricated anatase precipitated glass-ceramics that possesses high transparency. The anatase nano-crystallites in the glass, confirmed by XRD and TEM measurements, show higher photocatalytic activity than the rutile nano-crystallites. It is also clarified that difference of precipitated TiO_2 phase is caused by the surrounding amorphous region. Our study has emphasized the potential of the transparent Bi-free glass-ceramic containing anatase nano-crystallites for transparent photocatalytic applications without any coating process. The result is a strong backup for fabrication of TiO_2 transparent glass-ceramics for photocatalytic application.

3. Glass-Ceramics Containing ZnO Nano-Crystallites

3.1 Background

ZnO is a kind of oxide semiconductors. As mentioned in many reports (Look, 2001, Özgür at al. 2005), semiconductor ZnO has attracted attention as a promising material for optoelectronic, optical, electronic, and photocatalytic devices. For examples, excitonic lasing that originates from the large exciton binding energy from ZnO thin film (Bagnall at al. 1998, Tang at al. 1999, Huang at al. 2001), luminescence from p-i-n ZnO junction (Tsukazaki et al., 2005), or green luminescence by oxygen vacancies in ZnO (Vanheusden et al., 1996) have been reported. On the other hand, using high refractive index of ZnO, random lasing from ZnO crystallites has been also reported (Cao et al., 2000). Although there have been many reports on the ZnO in thin film, powdered, or ceramic shape (Gupta, 1990), there is little report on the ZnO glass-ceramics that possesses both unique property of ZnO and good formability of glass material. Since Zn cation tends to form binary zinc crystallites with B_2O_3, SiO_2 during the crystallization process of glass matrix, it is difficult to obtain glass-ceramics with ZnO nano-crystallites. Recently, Pinckney has reported transparent glass-ceramics, in which ZnO nano-crystallites of 5-20 nm were selectively precipitated, by heat-treatment of SiO_2-Al_2O_3-ZnO-K_2O glass (Pinckney, 2006). The material was one of the few transparent glass-ceramics containing a semiconductor crystal phase. However, since amount of SiO_2 was 40-55 mol%, the melt temperature of the glass was relatively high (1575-1650°C), which is disadvantage for shaping process as well as crystallization process.
In this study, we have fabricated ZnO glass-ceramic based on borate glass. The CaO-B_2O_3-ZnO-Al_2O_3-K_2O-SiO_2 glass was prepared by conventional melt-quenching method with melt temperature at 1350°C, which was 200°C lower than the previous melt temperature. By investigation of chemical composition, we have found that Al_2O_3, alkali metal oxide and alkaline earth metal oxide are needed for obtaining transparent mother glass. On the other hand, precipitation of $Zn_3B_2O_6$ (Chen et al., 2006) or $KZn_4B_3O_9$ (Chen et al., 2005) was observed in glass-ceramics without SiO_2. According to the classification of oxide reported by Sun, SiO_2, Al_2O_3, and B_2O_3 belong to glass network former group that possess strong metal-oxygen bond whereas K_2O and CaO glass network modifier group that possess weak metaloxane bond. Since ZnO play intermediate group or network modifier group, it is suggested that ZnO can exist in the glass network in a diversified state. Considering the precipitation of ZnO phase after heat-treatment, we assume that ZnO disperses with weak bonding to main glass network.

3.2 CaO- B_2O_3-ZnO-Al_2O_3-K_2O (CaBZAK) Glass

For determination of chemical composition, we consulted the previous reports on TiO_2 glass-ceramics as mentioned above (Masai et al., 2007, 2008, 2009). Although we have investigated the crystallization behaviour of several glass systems, such as CaO-B_2O_3-Bi_2O_3-Al_2O_2-ZnO, CaO-B_2O_3-Al_2O_3-ZnO, CaO-B_2O_3-Al_2O_3-ZnO-SiO_2, crystallization of ZnO was hardly observed. Therefore, we firstly investigated the CaO-B_2O_3-ZnO-Al_2O_3-K_2O (CaBZAK) system for attainment of ZnO-precipitated glass-ceramics.

Glass samples were prepared by conventional melt-quenching method using alumina crucibles or platinum crucible. Table 3 shows the chemical compositions of the CaBZAK precursor glasses (**18**–**22**) together with their T_g values. Asterisks indicate that the corresponding glasses were prepared by alumina crucibles. Figure 11 shows XRD patterns of the 10CaO-40B_2O_3-40ZnO-Al_2O_3-10K_2O glass-ceramics. JCPDS pattern of ZnO (JCPDS No. 00-021-1272) was also shown. Heat-treatment of these glass-ceramics was performed at T_g +70~100 K for 3 h. It clearly shows that precipitated crystalline phase depended on the amount of Al_2O_3. Glass-ceramics with small amount of Al_2O_3 shows $KZn_4B_3O_9$ (**18C**$_{570}$) and α-$Zn_3B_2O_6$ (**19C**$_{550}$). On the other hand, ZnO was precipitated together with α-$Zn_3B_2O_6$ in the glass-ceramic containing over 10 mol% of Al_2O_3 (**20C**$_{595}$, **21C**$_{597}$, and **22C**$_{590}$,). Compared XRD pattern of glass-ceramic prepared with platinum crucible with that of glass-ceramic prepared with alumina crucible, the amount of Al_2O_3 eluted from crucible was estimated about 10~12 mol%. Compared ZnO-precipitated glass-ceramics with TiO_2-precipitated glass-ceramics, we have noticed that precipitation of oxide crystallites depends on the coordination state in glass matrix. In other words, even if oxide semiconductor was selectively precipitated from borate-based glasses, TiO_6 octahedra in glass cannot be directly substituted by ZnO_4 tetrahedra. The obtained XRD patterns show that Al_2O_3 strongly affects the crystallization behaviour of glass-ceramics. Since ZnO works as intermediate (ZnO_2: bond dissociation energy 301 kJ/mol) or network modifier (ZnO_4: bond dissociation energy 151 kJ/mol), it is suggested that additional Al_2O_3, which can work as a network former, affects coordination state of ZnO into a network modifier. Note that Zinc takes 4-coordination state in precipitated crystallites, such as $KZn_4B_3O_9$, α-$Zn_3B_2O_6$, or ZnO.

No.	Chemical composition (mol%)						T_g
	CaO	K_2O	SiO_2	B_2O_3	ZnO	Al_2O_3	(°C)
18	10	10	0	40	40	0	483
19	10	10	0	40	40	5	485
20	10	10	0	40	40	10	492
21	10	10	0	40	40	12	503
22	10	10	0	40	40	*	495
23	10	10	10	25	45	*	525
24	10	10	20	20	40	*	544
25	5	5	15	25	50	*	542
26	10	10	5	30	45	*	507
27	10	10	20	25	35	*	526

Table 3. Chemical composition and T_gs of precursor glasses for precipitation of ZnO. Asterisks indicate that the corresponding glasses were prepared by alumina crucibles.

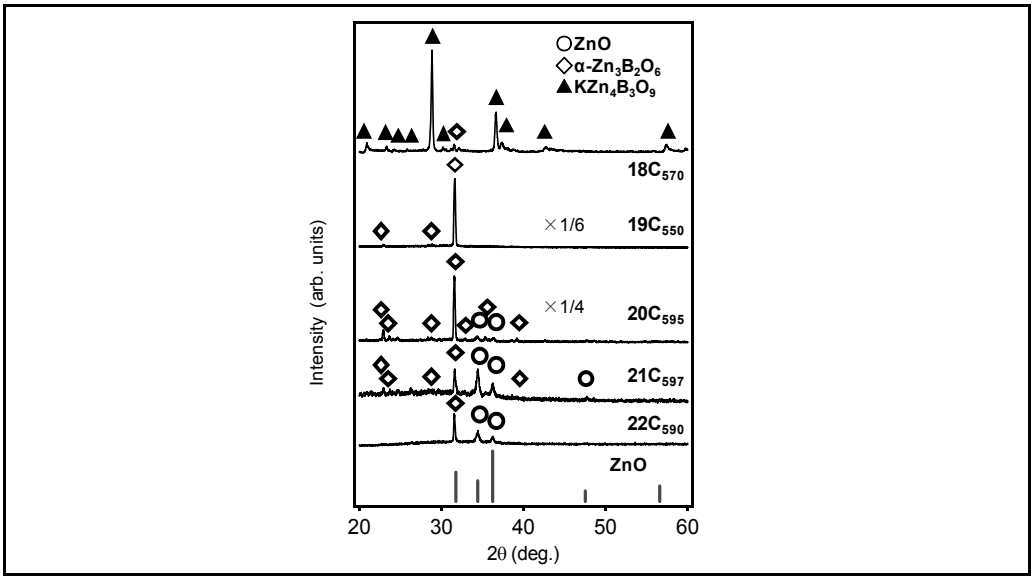

Fig. 11. Bulk XRD patterns of the CaBZAK glass-ceramics whose chemical compositions are listed in Table 3. Diffraction pattern of ZnO (JCPDS No. 00-021-1272) is also shown.

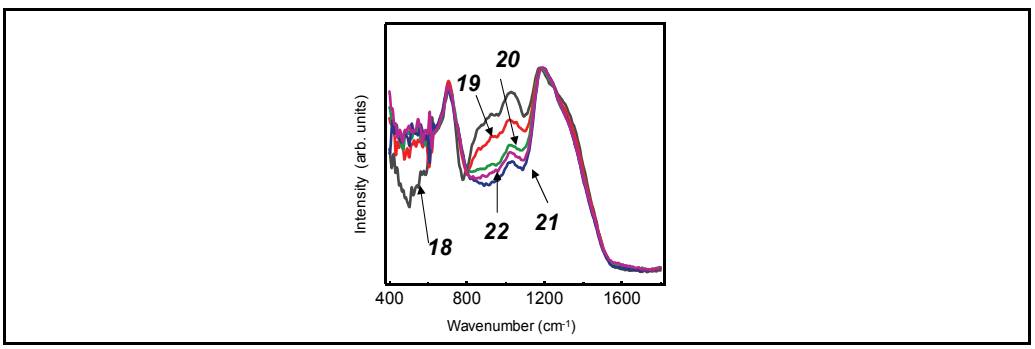

Fig. 12. IR spectra of the CaBZAK glasses (**18**–**22**)

Figure 12 shows IR spectra of the 10CaO-40B_2O_3-40ZnO-Al_2O_3-10K_2O glasses (**18**–**22**). Spectra are normalized using band around 1160 cm^{-1}, which belongs to the B–O–B vibration mode of the trigonal BO_3 unit. Band at 400~600 is attributed to ZnO_4 tetrahedra whereas the band around 700 cm^{-1} is assigned to the bending vibration of the B–O–B linkage. Band attributed to ZnO_4 increased by addition of Al_2O_3. On the other hand, signals from 800 to 1200 cm^{-1} that are assigned to tetrahedral BO_4 unit decrease with increasing amount of Al_2O_3. Observed band attributable to B-O-B was shifted to longer wavelength with increasing amount of Al_2O_3. The IR spectra of the glasses show that glass network has changed after addition of Al_2O_3. Since Al_2O_3 can make glass network, trigonal BO_3 unit that possess weaker network than tetrahedral BO_4 unit increases by addition of Al_2O_3 as a counterpart. Concurrently, band attributed to ZnO_4, which is similar structure of ZnO crystal, increased. Thus, it is speculated that isolated ZnO_4 was formed in glass matrix after addition of Al_2O_3. On the other hand, observed band around 1170 cm^{-1} attributable to B-O-B was shifted to

longer wavelength with increasing amount of Al_2O_3. Since the stretching force constant of Zn–O bond is lower than that of B–O, the frequency of Zn–O–B might appear at lower region. Thus, it is suggested that observed shift by addition of Al_2O_3 reflects the change from Zn-O-B bond to B-O-B bond in the glass. The decrease of number of Zn-O-B bond will affect the crystallization behaviour with precipitation of ZnO. That is a plausible mechanism for precipitation of ZnO instead of α-$Zn_3B_2O_6$.

3.3 CaO-B_2O_3-ZnO-Al_2O_3-K_2O-SiO_2 (CaBZAKS) Glass

Although we found that Al_2O_3 affected the crystallization behaviour of glass-ceramics, there was a limit of Al_2O_3 content for vitrification of glass. To attain selective crystallization of ZnO after heat-treatment, precipitation of α-$Zn_3B_2O_6$ should be prevented. Since homogeneous transparent glass was not obtained by addition over 12 mol% of Al_2O_3, we used partially substitution of network former from B_2O_3 to SiO_2. Here, we called the CaO-B_2O_3-ZnO-Al_2O_3-K_2O-SiO_2 glass system as CaBZAKS. Figure 13A shows photograph of the CaBZAKS mother glass (**23**) and the glass-ceramics (**23C**$_{610}$). The obtained glass-ceramics showed transparency despite of large difference of refractive index between ZnO and surrounding glass matrix. Figure 13B shows TEM image of the CaBZAKS glass-ceramics (**23C**$_{610}$). Rod-like ZnO crystallites were precipitated from the surface of the sample, and the crystal size was less than 1 μm. It is noted that the obtained glass-ceramic shows transparency despite a difference of refractive index, Δn, 0.4 between the precipitated ZnO (~2.0) and surrounding glass matrix (1.59~1.63). Figure 13C depicts XRD patterns of several CaBZAKS glass-ceramics (**23C**$_{610}$, **24C**$_{660}$, **25C**$_{660}$, **26C**$_{610}$, and **27C**$_{620}$) together with diffraction pattern of ZnO. Although diffraction intensities of each sample are different from the JCPDS pattern, we have confirmed that ZnO was selectively crystallized in all cases.

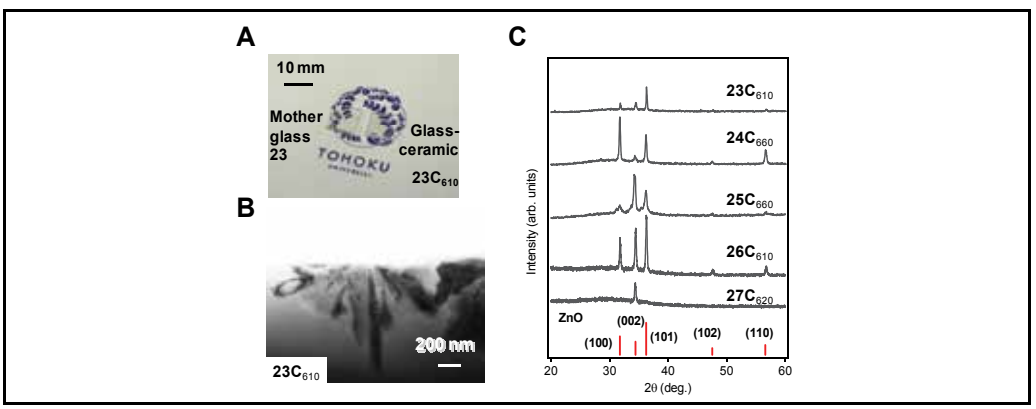

Fig. 13. (A) Photograph of the CaBZAKS glass-ceramic (**23C**$_{610}$) and the mother glass (**23**). (B) TEM image of the CaBZAKS glass-ceramic (**23C**$_{610}$). (C) XRD patterns of several CaBZAKS glass-ceramics together with JCDPS pattern of ZnO.

We have found the emission property of the ZnO precipitated glass-ceramics similar to that of ZnO single crystal. Figure 14 shows photoluminescence spectra of the ZnO glass-ceramics (**23C**$_{600}$, **23C**$_{610}$, and **23C**$_{640}$) and the mother glass (**23**). The spectra were measured at room temperature using a He-Cd laser as a light source. The glass-ceramic **23C**$_{640}$ was opaque because of scattering by surface crystallized ZnO. The glass-ceramic shows emission

at 3.28 eV, which is assigned to free exciton emission of ZnO. The emission spectrum of ZnO glass-ceramic is similar to that of ZnO single crystal. It indicates that crystal growth of ZnO occurred enough to show the exciton emission. We can find several characteristics in the obtained emission spectra of the ZnO glass-ceramics and the mother glass. The mother glass roughly consists of two broad bands at 1.4~2.6 eV. The emission at 1.4-2.6 eV is attributable to oxygen vacancies of ZnO (Vanheusden et al., 1996, Djurisic et al., 2007). On the other hand, the intensity of emission at 3.28 eV, which is assigned to free exciton emission of ZnO, clearly observed in the glass-ceramic. Since the thickness of crystallized region in the ZnO-precipitated glass-ceramics was about 1 μm from the surface, the volume percentage of ZnO crystals shown in Fig. 14 was less than 1 volume %. The results indicate that emission from the glass-ceramics depends on the state of precipitated ZnO crystallites, and that unique property of ZnO can be equipped in the glass-ceramics by optimized crystallization process (Masai et al., 2009).

In summary, we have obtained transparent ZnO-precipitated glass-ceramic. The ZnO nano-crystallites that were precipitated at the surface of the glass showed both broad emission and free exciton emission. The observed emission depends on the precipitated state of ZnO in the glass matrix, and has great potential for optical devices. The large Δn between ZnO crystallites and the surrounding glass matrix warrants the localization of photon, which is also attractive as optical ceramic devices. Note that crystallization behaviour, such as orientation of precipitated phase, or size of crystallites, in the glass matrix can be controlled. The present ZnO glass-ceramics could be an attractive functional material using the advantage of the amorphous glass material, which is quite different from conventional ZnO material.

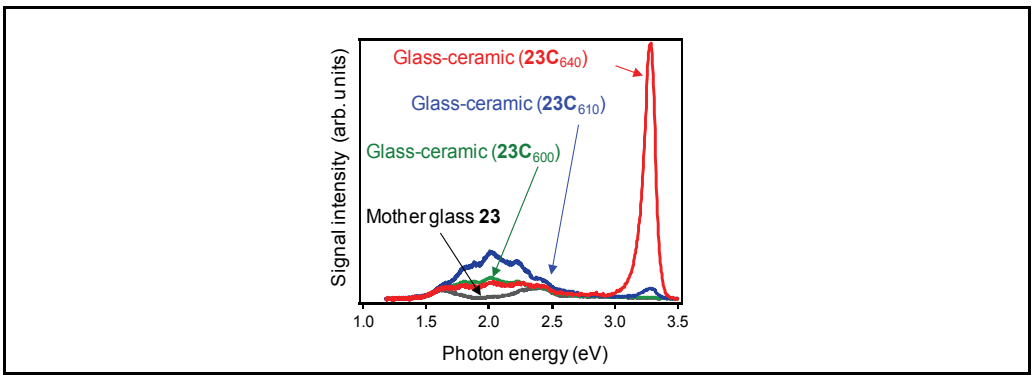

Fig. 14. Photoluminescence spectra of ZnO glass-ceramics (**23C**$_{600}$, **23C**$_{610}$, and **23C**$_{640}$) and the mother glass (**23**) using a He-Cd laser as a light source.

4. Current and Future Trends in Glass-Ceramics

Our results above-mentioned were achieved by examination of both the chemical composition and the crystallization process by traditional heat-treatment using electric furnace. Since the crystallization of glass by conventional heat-treatment is based on the self-organization of crystal above the T_g, the crystallization technique is favourable for industrial process in which simplified process and mass production are required. However, the method is not suitable for microstructuring of glass-ceramics consisting of locally

crystallized region at less than micrometres. Recently, there have been many reports on another process for space selective crystallization: laser-induced crystallization. The crystallization has been attained by several kinds of lasers, such as ultra-fast (e.g. femto-second) pulsed laser (Kondo et al., 1998, Yonesaki et al., 2005), nano-second pulsed laser (Fujiwara et al., 2002, Mizuno et al., 2006, Masai et al., 2008), or continuous wave (CW) laser (Sato et al., 2001, Honma et al., 2003 & 2006). Laser irradiation can induce a geometrically selective structural change, which is quite different from uniform bulk structural change caused by a conventional heating process using a furnace. If laser irradiation can induce a change of refractive index or crystallization in a glass matrix, such laser-induced structures provide unique properties without temporal decay. However, there is a difference between a femto-second laser and a nano-pulsed laser and a CW laser from the view point of the mechanism of laser-induced change in the irradiated material. The former can induce local changes with little thermal effect whereas the latter two actively exploits the thermal effect for laser-induced change. If we use the crystallization of oxides for functionalization of glass, control of the thermal process should be necessary. Irradiation of glass materials with a laser having a thermal effect, therefore, is thought to be effective in preparing functional devices using controllable crystallization behaviour. In using a thermal effect for a laser-induced structural change, the change depends on temperature and holding duration above the T_g. If we can control the temperature and a holding duration of the temperature, we can control the formation of crystallite nuclei and the growth of crystallites the respective, which is of great importance in creating tailored local structures. For example, nano-second pulsed laser irradiation can induce surface structural change of glass, in which nanostructure at tens or hundreds of nanometres are formed (see Fig. 15A & 15B). On the other hand, irradiation of not only a femto-second pulsed laser but also a CW laser (Fig. 15C) can induce crystallization inside the matrix. Such glass-ceramics are expected to be functional devices possessing lightwave controllability that is not inherent property of amorphous glasses.

By using the laser-irradiation technique, it is expected that above-mentioned oxide semiconductor-precipitated glass-ceramics will show the novel development. Designed nanostructure at the surface of glass-ceramic is effective not only for photocatalyst that requires large surface area but also light controllable device, such as photonic crystal, using the high refractive index. Control of orientation of precipitated crystallites at the surface is also of interest for applied science. On the other hand, internal structural change will work as an integrated circuit or an origin for emission centre.

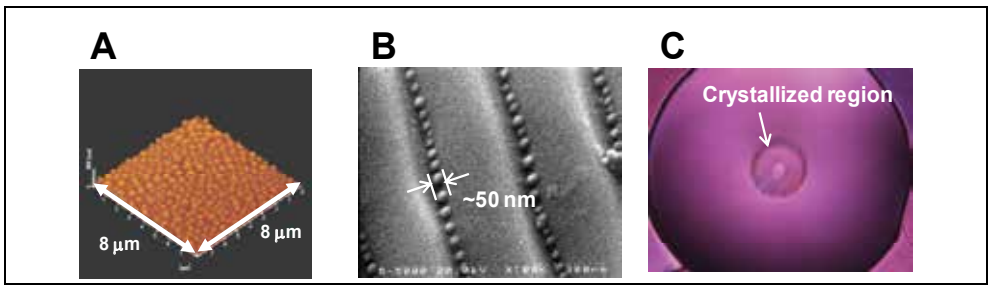

Fig. 15. Various laser-induced structural changes: AFM and SEM images of structural change of glass induced by a pulsed laser with (A) uniform and (B) interfering irradiations. (C) Photograph of the internal crystallization in a multi-structured fibre by irradiation of CW laser (reported by Ohara et al., 2009).

However, besides examination of crystallization of glass by laser-irradiation technique or conventional heat-treatment, deeper understanding of glass material itself is of necessity. The glass-ceramics can open up an application field for functional glass-based device, and therefore, the design and control of nanostructure in these materials will be of great importance.

5. Conclusion

In the present study, we have demonstrated fabrication of glass-ceramics containing two oxide semiconductors, TiO_2 and ZnO. It is notable that selective crystallization of these crystallites was successfully attained by examination of both the chemical composition of glass and the heat-treatment procedure. Moreover, the obtained glass-ceramics possessed transparency despite of large difference of refractive index. Our results mentioned were demonstrated by conventional heat-treatment using an electric furnace that is favourable for industrial process. As mentioned in the introduction and the last sections, crystallization of glass can take wide diversity of structure and the related physical property. The investigation of the novel property using glass-ceramics will be continued now and for the future.

6. References

Bagnall, D. M.; Chen, Y. F.; Zhu, Z.; Yao, T.; Shen, M. Y. & Goto, T. (1998). High temperature excitonic stimulated emission from ZnO epitaxial layers. *Appl. Phys. Lett.* 73, 8, 1038-1040, 0003-6951.

Beall, G. H. & Pinckney, L. R. (1999). Nanophase glass-ceramics. *J. Am. Ceram. Soc.* 82, 1, 5-16, 0002-7820.

Brydges, W. T. III & Smith, D. W. *US Patent* 3948669 (1976).

Cao, H.; Xu, J. Y.; Seelig, E. W. & Chang, R. P. H. (2000). Microlaser made of disordered media. *Appl. Phys. Lett.* 76, 21, 2997-2999, 0003-6951.

Ling, Y.; CaO, H.; Burin A. L.;Ratner, M. A.; Liu, X. & Chang, R. P. H. (2001). Investigation of random lasers with resonant feedback. *Phys. Rev. A* 64, 6, 063808, 1050-2947.

Chen, X.; Xue, H.; Chang, X.; Zhang, L.; Zhao, Y.; Zuo, J.; Zang, H. & Xiao, W. (2006). Syntheses and crystal structures of the alpha- and beta-forms of zinc orthoborate, $Zn_3B_2O_6$. *J. Alloy. Compd*, 425, 1-2, 96-100, 0925-8388.

Chen, D.-G.; Cheng, W.-D.; Wu, D.-S.; Zhang, H.; Zhang, Y.-C.; Gong, Y.-J. & Kan, Z.-G. (2005). Syntheses, band structures and optical properties of $Zn_3B_2O_6$ and $KZn_4B_3O_9$. *Solid State Sci*, 7, 2, 179-188, 1293-2558.

Djurisic, A. B.; Leung, Y. H.; Tam, K. H.; Hsu, Y. F.; Ding, L.; Ge, W. K.; Zhong, Y. C.; Wong, K. S.; Tam, H. L.; Cheah, K. W.; Kwok, W. M. & Phillips, D. L. (2007). Defect emissions in ZnO nanostructures. *Nanotechnology*, 18, 9, 095702, 0957-4484.

Fujishima, A. & Honda, K. (1972). Electrochemical photolysis of water at a semiconductor electrode. *Nature*, 238, 5358, 37-38, 0028-0836.

Fujiwara, T.; Ogawa, R.; Takahashi, Y.; Benino, Y. & Komatsu, T. (2002). Laser-induced photonic periodic structure in tellurite based glass ceramics. *Phys. Chem. Glasses*, 43C, 213-216, 0031-9090.

Gupta, T. K. (1990). Application of Zinc-oxide varistors. *J. Am. Ceram. Soc.* 73, 7, 1817-1840, 0002-7820.

Honma, T.; Benino, Y.; Fujiwara, T. & Komatsu, T. (2006). Transition metal atom heat processing for writing of crystal lines in glass. *Appl. Phys. Lett.* 88, 23, 231105, 0003-6951.

Honma, T.; Benino, Y.; Fujiwara, T.; Komatsu, T. & Sato, R. (2003). Technique for writing of nonlinear optical single-crystal lines in glass. *Appl. Phys. Lett.* 83, 14, 2796-2798, 003-6951.

Hosono, H.; Sakai, Y.; Fasano, M. & Abe, Y. (1990). Preparation of monolithic porous titania silica ceramics. *J. Am. Ceram. Soc.* 73, 8, 2536-2538, 0002-7820.

Huang, M. H.; Mao, S.; Feick, H.; Yan, H.; Wu, Y.; Kind, H.; Weber, E.; Russo, R. & Yang, P. (2001). Room-temperature ultraviolet nanowire nanolasers. *Science* 292, 5523, 1897-1899, 0036-8075.

Kato, K.; Fu, D.; Suzuki, K.; Tanaka, K.; Nishizawa, K. & Miki, T. (2004). High piezoelectric response in polar-axis-oriented $CaBi_4Ti_4O_{15}$ ferroelectric thin films. *Appl. Phys. Lett.* 84, 19, 3771-3773, 0003-6951.

Khonthon, S.; Morimoto, S.; Arai, Y. & Ohishi, Y. (2007). Luminescence characteristics of Te- and Bi-doped glasses and glass-ceramics. *J. Ceram. Soc. Jpn*, 115, 1340, 259-263, 0914-5400.

Kondo, Y.; Suzuki, T.; Inouye, H.; Miura, K.; Mitsuyu, T. & Hirao, K. (1998). Three-dimensional microscopic crystallization in photosensitive glass by femtosecond laser pulses at nonresonant wavelength. *Jpn. J. Appl. Phys.* 37, 1AB, L94-L96, 0021-4922.

Lawandy, N. M.; Balachandran, R. M.; Gomes, A. S. L. & Sauvain, E. (1994). Laser action in strongly scattering media. *Nature* 368, 6470, 436-438, 0028-0836.

Lide, D. R. & Kehiaian, H. V. (1994). *CRC handbook of thermophysical & thermochemical data*, CRC Press, 0849301971, Tokyo.

Look, D. C. (2001). Recent advances in ZnO materials and devices. *Mater. Sci. Engineer. B* 80, 1-3, 383-387, 0921-5107.

Masai, H.; Fujiwara, T.; Benino, Y. & Komatsu, T. (2006). Large second-order optical nonlinearity in $30BaO\text{-}15TiO_2\text{-}55GeO_2$ surface crystallized glass with strong orientation. *J. Appl. Phys.* 100, 2, 023526, 0021-8979.

Masai, H.; Fujiwara, T. & Mori, H. (2007). Fabrication of TiO_2 nano-crystallized glass, *Appl. Phys. Lett.* 90, 8, 081907, 0003-6951.

Masai, H.; Fujiwara, T. & Mori, H. (2008). Effect of SnO addition on optical absorption of bismuth borate glass and photocatalytic property of the crystallized glass. *Appl. Phys. Lett.* 92, 14, 141902, 0003-6951.

Masai, H.; Mizuno, S.; Fujiwara, T.; Mori, H. & Komatsu, T. (2008). Fabrication of metal nanocluster and nanoparticles in the $CaO\text{-}Bi_2O_3\text{-}B_2O_3\text{-}Al_2O_3\text{-}TiO_2$ glass by irradiation of XeCl pulsed laser. *Opt. Express*, 16, 4, 2614-2620, 1094-4087.

Masai, H.; Takahashi, Y.; Fujiwara, T.; Suzuki, T. & Ohishi Y. (2009). Correlation between NIR emission and bismuth radical species of Bi_2O_3-containing aluminoborate glass. *J. Appl. Phys.* 106, 10, 103523, 0021-8979.

Masai, H.; Toda, T.; Takahashi, Y. & Fujiwara, T. (2009). Fabrication of anatase precipitated glass-ceramics possessing high transparency. *Appl. Phys. Lett.* 94, 15, 151910, 0003-6951.

Masai, H.; Toda, T.; Ueno, T.; Takahashi, Y. & Fujiwara, T. (2009). ZnO glass-ceramics: An alternative way to produce semiconductor materials. *Appl. Phys. Lett.* 94, 15, 151908, 0003-6951.

McMillan, P. W. (1979). *Glass ceramics*, Academic Prss, 0124856608, London.

Mizuno, S.; Fujiwara, T.; Benino, Y. & Komatsu, T. (2006). Novel technique for fabrication of nanoparticle structures in $KNbO_3$-TeO_2 glass for photonic integrated circuits. *Jpn. J. Appl. Phys.* 45, 8A, 6121-6125, 0021-4922.

Murata, T. & Mouri, T. (2007). Matrix effect on absorption and infrared fluorescence properties of Bi ions in oxide glasses. *J. Non-Cryst. Solids* 353, 24-25, 2403-2407, 0022-3093.

Ohara, S.; Masai, H.; Takahashi, Y.; Fujiwara, T.; Kondo, Y. & Sugimoto, N. (2009). Space-selectively crystallized fiber with second-order optical nonlinearity for variable optical attenuation Opt. Lett. 34, 7, 1027-1029, 0146-9592.

O'Regan, B. & Gratzel, M. (1991). A Low-cost, high-efficiency solar-cell based on dye-sensitized colloidal TiO_2 films. *Nature* 353, 6346, 737-740, 0028-0836.

Özgür, Ü.; Alivov, Y. I. ; Liu, C.; Take, A.; Reshchikov, M. A.; Doğan, S.; Avrutin, V.; Cho, S.-J. & Morkoç, H. (2005). A comprehensive review of ZnO materials and devices. *J. Appl. Phys.* 98, 4, 041301, 0021-8979.

Pinckney, L. R. (2006). Transparent glass-ceramics based on ZnO crystals. *Phys. Chem. Glass: Eur. J. Glass Sci. Technol. B* 47, 2, 127-130. 0031-9090.

Sato, R.; Benino, Y.; Fujiwara, T. & Komatsu, T. (2001). YAG laser-induced crystalline dot patterning in samarium tellurite glasses. *J. Non-Cryst. Solids* 289, 1-3, 228-232, 0022-3093.

Strnad, Z. (1986). *Glass-ceramic materials*, Elesevier, 0444995242, Amsterdam.

Sun, K. H. (1947). Fundamental condition of glass formation. *J. Am. Ceram. Soc.* 30, 9, 277-281, 0002-7820.

Takahashi, Y.; Benino, Y.; Fujiwara, T. & Komatsu, T. (2001). Second harmonic generation in transparent surface crystallized glasses with stillwellite-type $LaBGeO_5$. *J. Appl. Phys.* 89, 10, 5282-5287, 0021-8979.

Takahashi, Y.; Benino, Y.; Fujiwara, T. & Komatsu, T. (2004). Large second-order optical nonlinearities of fresnoite-type crystals in transparent surface-crystallized glasses. *J. Appl. Phys.* 95, 7, 3503-3508, 0021-8979.

Tang, Z. K.; Wong, G. K.; Yu, P.; Kawasaki, M.; Ohtomo, A.; Koinuma, H. & Segawa Y. (1998). Room-temperature ultraviolet laser emission from self-assembled ZnO microcrystallite thin films. *Appl. Phys. Lett.* 72, 25, 3270-3272, 0003-6951.

Tsukazaki, A.; Ohtomo, A.; Onuma, T.; Ohtani, M.; Makino, T.; Sumiya, M.; Ohtani, K.; Chichibu, S. F.; Fuke, S.; Segawa, Y.; Ohno, H.; Koinuma, H. & Kawasaki, M. (2005). Repeated temperature modulation epitaxy for p-type doping and light-emitting diode based on ZnO. *Nature Materials* 4, 1, 42-46, 1476-1122.

Vanheusden, K.; Seager, C.H.; Warren W.L.; Tallant, D. R. & Voigt, J. A. (1996). Correlation between photoluminescence and oxygen vacancies in ZnO phosphors. *Appl. Phys. Lett.* 68, 3, 403-405, 0003-6951.

Yeung, K. S. & Lam, Y. W. (1983). A simple chemical vapor-deposition method for depositing thin TiO_2 films. *Thin Solid Films*, 109, 2, 169-178, 0040-6090.

Yonesaki, Y.; Miura, K.; Araki, R.; Fujita, K. & Hirao, K. (2005). Space-selective precipitation of non-linear optical crystals inside silicate glasses using near-infrared femtosecond laser. J. Non-Cryst. Solids 351, 10-11, 885-892, 0022-3093.

3

Tape Casting Ceramics for high temperature Fuel Cell applications

Alain S.Thorel
Materials Centre, Mines-ParisTech,
UMR CNRS 7633
BP87, 91003 Evry Cedex
France

1. Introduction

1.1. General

The objective of this book chapter is to detail how to apply an a priori easy to implement shaping technique to fabricate high temperature fuel cell elements. High temperature fuel cells (SOFC for Solid Oxide Fuel Cell, PCFC for Proton Ceramic Fuel Cell) are sophisticated objects, made of thin active elements differing in composition and microstructure (≈ 50-300 μm porous cathode, 10 to 50 μm dense electrolyte, 50-300 μm porous anode, typically) that are operated at high temperature (from 500 °C to 1000 °C, typically) and that are supposed to last some 40000 hrs under oxidizing atmosphere on the cathode side and reducing atmosphere on the anode side. The fabrication costs of high temperature fuel cells remains the major brake against their rapid development. Tape-casting is a supposedly low cost and simple shaping process, but it appears to become quickly complicated to implement if it aims at producing a thin tri-layer ready for co-sintering as it can the case in high temperature fuel cells. The operability of tape-casting requires that one understands clearly each step of the process, from the slurry formulation to the final sintering treatment via the drying step. The present text offers a discussion about tape-casting and co-sintering of the bi- or tri-layers components of SOFCs and PCFCs, and gives some indications on how to circumvent the difficulties in certain cases. It raises several important issues and problems regarding aqueous and organic tape-casting. It shows that each step of the process is important, but that the formulation of the slurry is crucial for the final product. It gives also evidence that this process requires to be backed by modelling and computer simulation to take into account all the mechanisms that lead to instabilities and residual deformation. This book chapter is illustrated by concrete examples and micrographs from the fabrication of YSZ based SOFC and BCY10 based PCFC, but also from the first attempts to realize a new type of high temperature fuel cell (IDEAL-Cell) based on an innovative new concept under intensive research in a European consortium today; they show that in some cases tape-casting and co-sintering are impracticable, and that a sequence of processes is highly preferable than a single process.

1.2. High Temperature Fuel Cells context

Solid Oxide Fuel Cells are promising power generating systems which are currently based on anionic solid conductors (SOFC), mostly Yttria-Stabilized Zirconia (YSZ), or more recently on protonic conductors (PCFC) in which the electrolyte may be an yttrium doped barium cerate (BCY) or zirconate (BZY) (see Fig. 1 and 2). The operating temperature of YSZ-based SOFC is usually high (> 900 °C) in order to reach the highest anionic conduction performance. This presents significant advantages (chemical stability with CO and CO_2, direct CH_4 feeding, etc…), but also severe pitfalls (thermomechanical failure of components, sophisticated glass seals, chemical instabilities during ageing and cycling…). These difficulties can be significantly diminished if the operating temperature is reduced to 600 °C - 700 °C; but then the loss of conductivity associated with the temperature drop must be compensated either by changing the electrolyte material (*i.e.* shifting to Ceria) or by drastically diminishing the electrolyte thickness.

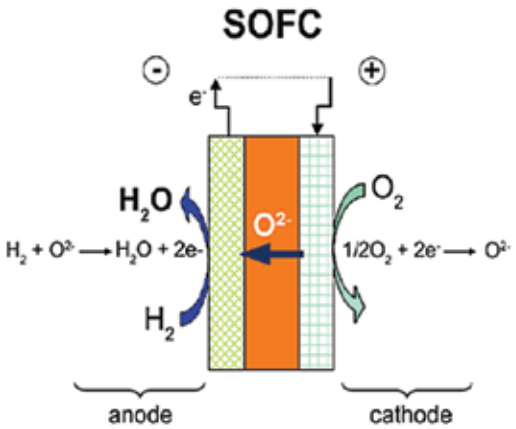

Fig. 1. SOFC, water at the anode side

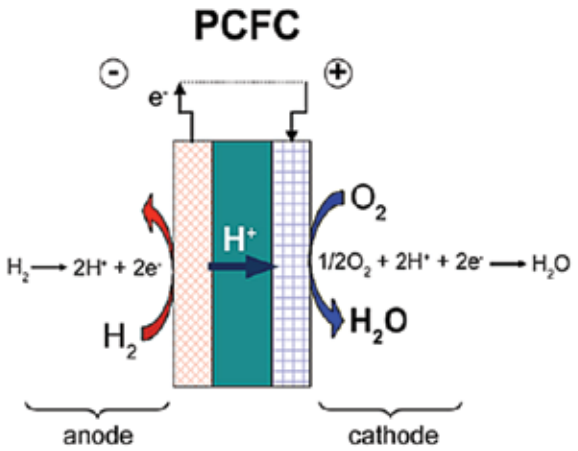

Fig. 2. PCFC, water at the cathode side

PCFCs are quite credible alternatives, though at a much less mature state of development than SOFC. Among all the perovskite based proton conductors, 10% Yttria-substituted

Barium cerate (BCY10) is widely studied for its high level of protonic conduction below 700 °C under hydrogen-and/or water-containing atmospheres (10^{-2} S cm^{-1} at 600 °C under wet hydrogen). But this class of materials displays some particularities (high basicity, high sensitivity to water and CO_2, high refractarity, chemical decomposition at high temperature, residual oxygen conduction under certain conditions…), which make them requiring still a certain amount of basic research prior to development. An innovative design is under scrutiny for a couple of years now (IDEAL-Cell); it consists of a mixed conducting cell that will potentially eliminate all the problems associated with the presence of water at electrodes in both SOFCs and PCFCs since the water is formed and evacuated from a porous central membrane made of a composite of the two types of electrolytes (Fig.3)(see www.ideal-cell-eu; Thorel et al, 2009a; Thorel et al, 2009b).

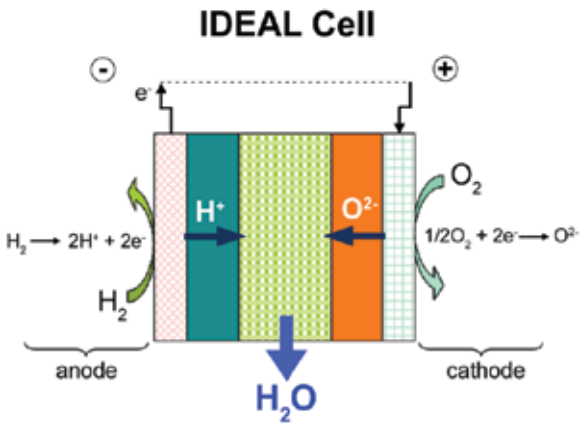

Fig. 3. IDEAL-Cell concept, water production in the central compartment

1.3. Designs and Fabrication Processes

The general geometries for these high temperature cells -at least SOFCs and PCFCs, IDEAL-Cell being just at the proof of the concept step- are either planar or tubular, industrials giving their own twist between these two basic designs. Though less tested on the long term, planar designs provide a higher current density than tubular designs, between 0.50 and 1.5 W cm^{-2}. The major brake to the development of high temperature fuel cells is the cost of fabrication compared to the market requirements. Whatever the geometry, a single cell is a complex quasi-2D multilayered structure made of different sophisticated materials having different microstructures and functions. If one focuses on the planar geometry, many processing routes can be envisioned, but the community considers only a limited number of low cost shaping processes. They can be divided into 2 classes, i/ those that require the use of a slurry (tape-casting, screen-printing, slip-coating, dip-coating…), and ii/ those in which the powder is projected on a target (essentially plasma spraying related deposition processes). Other excellent processes (PVD-CVD, SPS, hot-pressing…) are a priori too expensive and difficult to scale-up, and therefore not competitive enough to meet with the market constraints (*i.e.* US SECA program cost target = $400/kW by 2010). Plasma-spraying, tape-casting and screen-printing have given first-rate results for fabrication of SOFCs [Hui et al, 2007; Syed et al, 2006; Grosjean, 2004; Bitterlich et al, 2001;Xia et al, 2001). Surprisingly, very few studies have been carried out so far on shaping PCFC via these processes (Costa et

al, 2009; Hafsaoui, 2009; Costa, 2009), which are all presently considered for shaping IDEAL-Cell (Presto et al, 2009).
Ideally, a low-cost process that allows co-sintering the multilayer would be very profitable in terms of fast development of SOFCs or PCFCs; but this is an extremely difficult problem that aims at obtaining flat well bonded layers with appropriate densities and fine-tuned microstructures, with no appearance of cracks, secondary phases, chemical reactivity, unwanted allotropic transformations. Apart from processes derived from the plasma deposition and if we focus on the more traditional ceramic processes, the previous characteristics are all being governed ultimately only by three common parameters: sintering temperature, duration of the treatment and atmosphere. Obviously, this very limited number of levers that we can act on for-co-sintering can only trigger a differentiate evolution of the layers only if the green layers have the potential to allow for it, that is to say exhibit an appropriate geometry, composition, grain size distribution, initial density… The green layers characteristics are in turn completely determined by the slurry composition and powders morphology, the way the layers are superimposed and bonded, and how the multilayer is being dried prior to sintering. In the present paper, that gathers results from different projects (Grosjean, 2004; Costa et al, 2009; Hafsaoui, 2009; Costa, 2009), we will focus on the problems encountered when one fabricates SOFC and PCFC by tape-casting and co-sintering, and will detail some of the ideas suggested above.

2. Shaping by tape-casting

2.1. General considerations on tape-casting

Tape-casting is a low cost process particularly well-suited for the fabrication of thin (10 μm up to 500 μm) flat components for high temperature fuel cell. It allows producing a wide variety of controlled morphologies, from highly porous to fully dense microstructures, such as electrodes and electrolytes. Green layers can be easily superimposed if one wants to co-sinter the multilayer in a one-step operation. As seen in Fig. 4, the whole process gathers consecutive steps: the first one and probably the most important is the fabrication of the slurry with the powder under consideration, which is previously formulated, calcined and eventually sieved to reach appropriate phase content, grain size distribution and morphology.
Organic and/or inorganic additives, which role will be described below, are added to the powder to form the slurry. The slurry is then mixed and grinded mostly by ball-milling to ensure homogenization and destruction of agglomerates. Then the solution is de-aired under primary vacuum depending on which level of porosity/density is desired at the end of the process. The slurry is then ready for the casting of a green tape, which thickness is governed by the height of the Doctor blade above the substrate (Fig. 5 and Fig. 6). The ratio between the green and the sintered sample thicknesses depends on the properties of the slurry and on the degree of freedom of the system when the layers shrink during drying and during sintering, which in turn depends on numerous intrinsic parameters (*i.e.* those taken into account in a dilatometry curve, such as powder nature, size, composition and formulation of the slurry, temperature and duration of sintering…), but also on extrinsic parameters linked to the nature of the substrates for drying or sintering, that may lead to friction and wear inhibiting radial shrinkage and increasing then the level of vertical/longitudinal shrinkage.

This may even be more effective if a light weight is deposited on top of the samples to maintain its flatness. The different wet layers can then be cast on top of the others via dedicated technical systems (*i.e.* series of Mylar masks) if the solvent is organic; if the solvent is water, then the layers must go through a gel-forming step prior to superimposition since otherwise they do not exhibit any mechanical strength. Technical adjustments can be carried out between these two solutions, but it is important to note that a good final bonding between two layers requires that at least one layer is wet. Drying single layers or multilayers is also a prime importance step. Any geometric deformation or defect occurring during the drying process will only worsen during sintering. It is therefore essential that the flatness be maintained, depending on how isotropic the mechanism of humidity withdrawal is, above, below and along the radius of the sample. If one uses a dense substrate, then humidity cannot escape from the bottom and the dried sample is usually warped with strong deformation in the z+ direction, along with edge sinusoidal deformation. Sandwiching the sample between two dense substrates does not usually help and ends up with extensive cracking. We have had excellent results when sandwiching the layers or multilayers between two light honeycomb Mullite substrates left at 70 °C (Fig. 7).

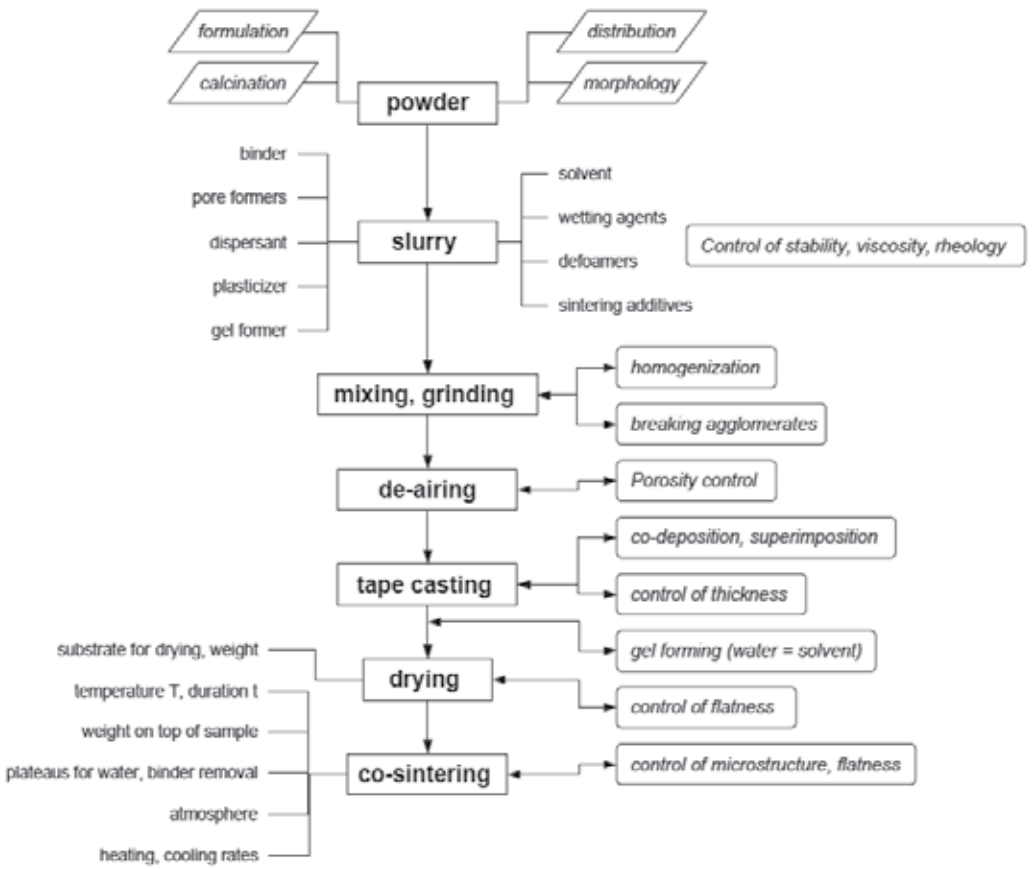

Fig. 4. Flowchart for organic or aqueous tape-casting and co-sintering of multilayers

We have shown thus that the drying mechanism was related to the evacuation of liquid water facilitated by capillary forces acting across the sample, thanks to the porous honeycomb supports, which in addition were efficient to maintain the flatness of the sample (Grosjean, 2004; Costa et al, 2009).
Obviously, the sintering step is the key-moment of the whole process. One should not use more time and temperature than what is needed; therefore the level of the sintering temperature and duration will be as little as possible.

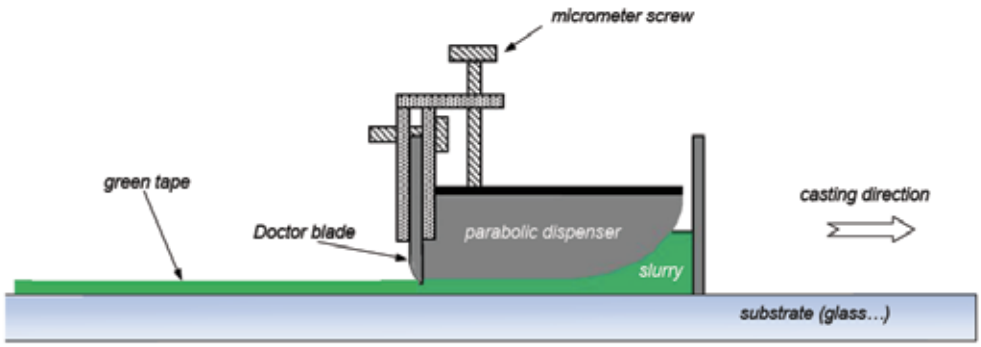

Fig. 5. Schematic of a laboratory tape-casting set-up

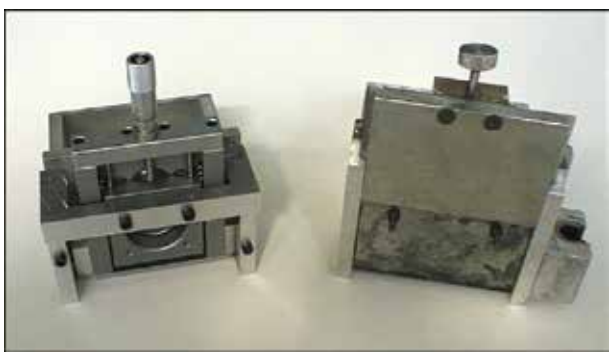

Fig. 6. Tape-casting experimental set-up

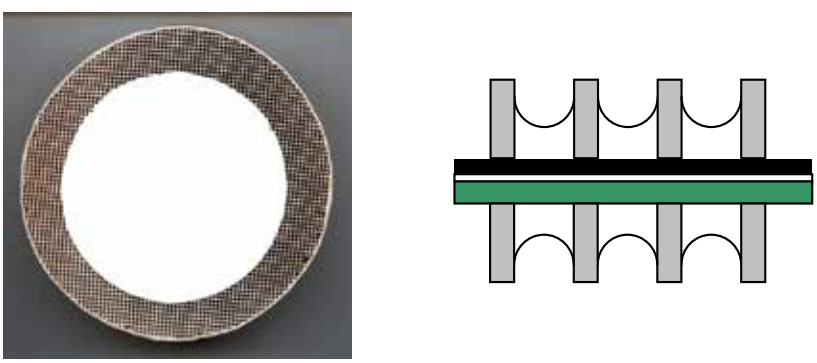

Fig. 7. Drying of a YSZ layer sandwiched between two Mullite honeycomb substrates (left); detail of the capillary mechanism acting across a SOFC trilayer during drying between 2 honeycomb substrates

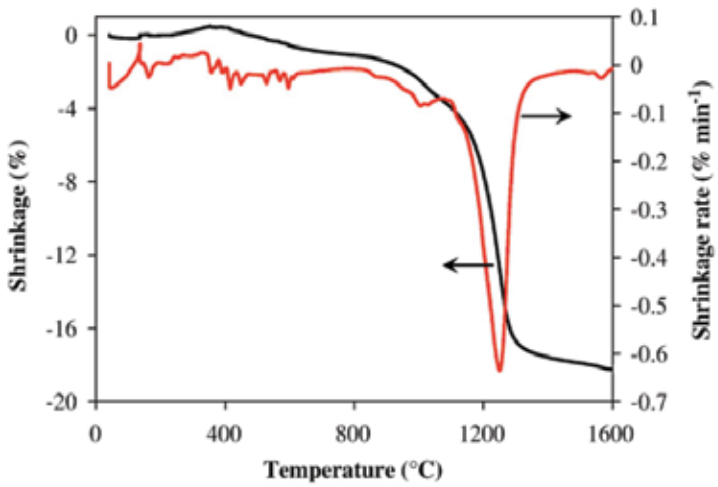

Fig. 8. Shrinkage curve for BCY10; left: shrinkage (%), right: shrinkage rate (% mm^{-1}) (from Bassano et al, 2009)

The sintering temperature is usually chosen as to correspond to the temperature where the sintering rate is maximum (*i.e.* 1250 °C for BCY10 in Fig. 8 from Bassano et al, 2009); in that case a density higher than 95% of the theoretical density is attained rapidly with very limited grain coarsening if the slurry has the characteristics for a fully dense final material. This may be adapted if one wants to obtain a porous final material or in the case of co-sintering of multilayers. The choice of the support is of uttermost importance since it must obviously not react with the sample and must not present any roughness that could generate unwanted friction and interference with the radial shrinkage. Ideally the support should be made with the same material as the layer in contact with it. Sometimes a powder bed is used as a buffer for reactivity, but in that case the powder bed has to be thin and very flat.

2.2. Details on the slurry formulation

For a given powder or mixture of powders the sintering behaviour of green tapes, and hence their final microstructure, depends on the arrangement, dispersion and homogeneity of the starting ceramic particles in the slurry (Moreno, 1992a); therefore, the slurry formulation is a crucial step for tape-casting, as it is also for related processes such as screen-printing, spin or dip-coating. Roughly, a good slurry is the one in which the ceramic grains are electrostatically interacting so that the particles are the farthest away from each other, that no agglomerates are formed, that gravity is negligible, hence no sedimentation occurs, and so that the viscosity is low enough to allow for an easy casting, and high enough for the green tape to have a sufficient creep resistance to maintain its geometry. As a rule of thumb, and respecting the indications given above, the highest possible the ratio solid/liquid, the highest the density of the green tape, hence the highest the density of the sintered tape.

Generally, the slurry is composed of a mixture of numerous organic compounds (binder, dispersant, plasticizer (Moreno, 1992b), solvent if organic tape-casting, and possibly wetting agents, defoamers, pore formers if needed) and inorganic compounds (ceramic powder to be

shaped, sintering additives, water if aqueous tape-casting). All the organic components remain in the green tape after drying. Since they are removed when heated at elevated temperature in air (between 300 °C and 700 °C, from polymers to graphite), they give rise to pores, which cannot -or must not- always be eliminated during the sintering treatment. Consequently, the ratio of the amount of powder to the organic compounds, and hence the final formulation of the slurry, must be fine-tuned in order to tailor the final microstructure and density. Concerning water based tape-casting, the slurry is gelled after casting and the water is removed during drying; the gel is decomposed at 350 °C at the onset of the thermal treatment giving place to porosity. Here again the ratio between the solid phase and the liquid in the slurry will tailor the level of porosity, in addition to pore formers. In both cases, organic or aqueous tape-casting, the ratio of the solid phase to the liquid/or organic phases will lead to the control of a 1-2 μm size interconnected porosity, which can be extremely useful for increasing the quantity of triple phase boundaries.
Amongst the slurry characteristics, the stability is of utmost importance. Polarization interactions must take place at the solid-liquid interface, interactions whose intensity governs the slurry stability (Moreno, 1992). Consequently, the value of the dielectric constant of the liquid determines the slurry stability, and hence the choice of solvent, which in turn determines the choice of all the other additives. The other forces acting on the particles in the slurry are gravity, which depends on the particles mass (and indirectly size), and the attractive Van der Waals interactions, which promote flocculation and act against the stability of the slurry. On the other hand, thermal agitation, electrostatic and steric repulsive forces promote the dispersion of the particles and therefore increase the stability of the slurry. The role of the dispersant agent is precisely to enhance the intensity of these dispersive forces. The second important slurry characteristic is the viscosity, which determines the operability of the process to cast green tapes. The slurry viscosity varies as a function of the amount of solvent per unit volume; the solvent quantity needs to be precisely adjusted to allow for a good dispersion of the powder as well as for an efficient dissolution of the binder.

2.3. Co-sintering

- co-sintering parameters

To fabricate such sophisticated multilayered objects -SOCFs, PCFCs or IDEAL-Cells- one must have in view that the first order outcome parameter is the function of the object, and the second order outcome parameter is its long-term thermomechanical behaviour necessary to accomplish this function. Therefore efforts have to be put first on reaching the highest possible level of electrochemical properties, and once it is reached one must work on the optimization of the mechanical properties. This is a general frame that might be amended when interests converge, *i.e.* quality of the bonding at interfaces, cracking…
Obviously, during co-sintering all the layers will have to face the same treatment characterized by a given sintering temperature, duration and specific atmosphere. To a certain extent there is interchangeability between time and temperature of co-sintering through the Fick's laws and temperature dependant diffusion coefficients, provided that no unexpected thermo-activated mechanism occurs (phase change, precipitation…). This means that the common temperature is necessarily a compromise between the highest and the lowest sintering temperature of the different layers taken separately, which compromise can be smoothed to a certain extent by playing on the sintering time (*i.e.* sintering the multilayer at a temperature intermediate between the lowest and the highest sintering temperature, but for a longer time than necessary for the sintering of the less refractory layer). For a standard composition of YSZ based SOFCs and BCY

based PCFCs the usually lowest refractory layers (anode and cathode, *i.e.* respectively NiO/YSZ and NiO/BCY, lanthanum-strontium manganites and lanthanum-strontium-iron cobaltites) are also those which must be highly porous; since they will be co-sintered at a temperature higher than their normal sintering temperature, and for a longer time than necessary (so that the electrolyte can reach full density), then the slurry formulation for electrodes must be thought for correspondingly (higher Liquid/Solid ratio, addition of pore formers…) to inhibit any tendency for over densification.

The thermal treatment may also present second order parameters, such as heating and cooling rates, plateaus…; heating ramps and cooling ramps are not equivalent since at the onset of the sintering the materials are just shaped and cast powders, with no capability to transfer any elastic stress within the ceramic, whereas at the end of the sintering the material is a rigid body highly sensitive to elastic stress originating from the differential mismatch of thermal expansion coefficients between layers. The role of heating ramps and plateaus at the onset of the sintering has more to do respectively with the plastic deformation of the green layers, due to a differential behaviour with temperature, and with the complete combustion of the organic slurry compounds. It is highly important that the combustion occurs gently and completely at the lowest possible temperature so that the evacuation of gas is rendered easy via the still widely open porosity that the combustion has just created. Any increase of gas pressure inside the layers is obviously highly detrimental for the sample integrity (deformation, stresses, cracking…). The length of all the plateaus is determined by thermal analysis so that the corresponding organic compounds can totally disappear.

In most cases co-sintering necessitates reaching a certain level of compromise that can be adjusted by playing on the slurry composition and geometry of green layers (Bitterlich et al, 2001; Costa et al, 2009; Hafsaoui, 2009; Costa, 2009; Yoon et al, 2007) on the basis of the modelling of polarization mechanisms as a function of microstructural parameters (Yoon et al, 2007; Ou et al, 2009). In some cases, co-sintering appears highly impracticable, such as in SOFCs between YSZ and LSM when co-sintering above 1150 °C leads to resistive pyrochlore phases (Grosjean et al, 2006), and in PCFCs between BCY10 and NiO since we showed that there is a significant diffusion of Ni in the electrolyte material (Costa, 2009). When such difficulties arise, one must consider changing the materials or implementing a sequence of processes and consecutive sintering treatments starting from the fabrication of the layer having the highest sintering temperature and finishing with the one having the lowest (Fontaine et al, 2009). As an example, screen-printing or plasma-spraying can easily be performed on top of tape cast layers. This may be at the expenses of cost, but in that case there are less compromises to carry out and probably higher functional properties can be achieved.

- differential sintering kinetic

Deformation during sintering is composed of four terms: elastic deformation, thermal deformation, visco-plastic deformation and shrinkage due to the densification. The latter is by far the largest contribution to the overall deformation; its driving force is the reduction of surface energy and curvatures, hence the disappearance of the porosity. Different materials and/or different slurry formulations lead to strong differences in the shrinkage kinetic. Co-sintering bi-layers is extremely difficult since there is almost no way to compensate for this shrinkage kinetic differential; this is a general rule for an even number of layers. An odd number of layers is much more favourable since the deformation on one side (*i.e.* due to the bi-layer anode/electrolyte) can be compensated by the deformation on the other side (*i.e.* by the cathode) by playing on the thickness, and to a certain extent on the slurry composition (*i.e.* pore formers amount).

Obviously, one must seek a situation where deformations at both electrodes put the electrolyte layer under compression, as seen in Fig. 9.

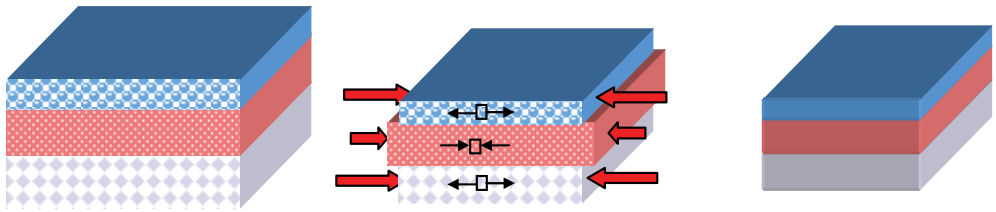

Fig. 9. Schematic of the compensation of the deformation during sintering across a tri-layer

The compensation of the deformation by the third layer may be very difficult to evaluate since it results from several mechanisms acting at different steps of the sintering. Useful information can be drawn from the observation of the final deformation of bilayers having different thicknesses, but much more efficient is the modelling of the deformation kinetic by a finite elements approach; when followed carefully, this route can reveal phenomena that occur in the furnace during the sintering, which are by essence extremely difficult to detect.

Thus, we have quantitatively detected a strong deformation peak very early at the sintering temperature originating in the differential shrinkage kinetic between a YBC10 PCFC electrolyte layer and a YBC10 + NiO PCFC anode layer; in that case, the sintering rate of the electrolyte was higher than that of the anode, whose deformation caught up little by little during the remaining time. We have also given evidence for a scale effect, the large the diameter of the bi-layer the larger the final deformation (Costa et al, 2009). The deformation transforms into stresses if the multilayer is topped by a substrate, which aims at maintaining it flat. The weight of this substrate must be carefully tuned for allowing only planar deformation to occur, that is to say large enough to block the vertical deformation, but light enough to allow for a radial deformation. If this support is too light or too heavy, the final object will be either warped or cracked.

But nothing is free of charge regarding sintering ceramics; if one wants to identify and model quantitatively the pertinent mechanisms taking place during sintering, one must feed the model with microstructural information related to these mechanisms; this means that either we are able to gather microstructural observations during sintering -which is extremely difficult considering the high sintering temperature -, or rather that we make these observations after interrupted sintering tests. In that case, one must pay attention that these interruptions do not bring additional interference to the observations (cooling rate high enough to efficiently stop quickly all the mechanisms related to the diffusion of species, but low enough to avoid any cracking). The most pertinent parameter to follow through these interrupted tests is the surface fraction of porosity, which equals the volume fraction of porosity, provided that the material is stationary in a statistical sense. Therefore, we will associate the speed of deformation, hence the densification rate, with the evolution of the porosity versus time drawn from interrupted tests (Costa et al, 2009; Costa, 2009). 2D porosity information can easily be evaluated by SEM observations of polished surface after appropriate segmentation and binarization; better, 3D information can directly be obtained by microtomography (Costa et al, 2009). Experimental preparation of the samples for the analysis of interrupted tests is quite straightforward when exploring the end of

the sintering, but is quite delicate at the onset of the consolidation, *i.e.* just after the plateaus for the calcination of the binders. If non-consolidated samples are embedded in resin prior to observation (Fig. 10), one must pay a careful attention on the choice of the polymer that must not retract significantly, otherwise the surface (or volume) fraction of pores will be highly underestimated.

Observation of the microstructure after interrupted tests has allowed us to detect an unexpected second order deformation mechanism, that acts also in single layers (in that case, no differential shrinkage kinetic between different materials can possibly be invoked): this mechanism originates from a shrinkage kinetic difference within the anode itself associated with a porosity gradient (from the top to the bottom of the sample) that is caused by the sedimentation of the larger BCY10 grains from the moment the tape is cast until it is totally dried (Fig. 11). The effectiveness of the slurry stability is essentially a function of the grains surface since electrostatic forces intensity derived from the adsorbed species. Large grains present an unfavourable surface/volume ratio in that respect, and then are more sensitive to gravity. This effect is effective when the grains size distribution is not narrow enough, and it aggravates the differential shrinkage kinetics when multilayers are concerned.

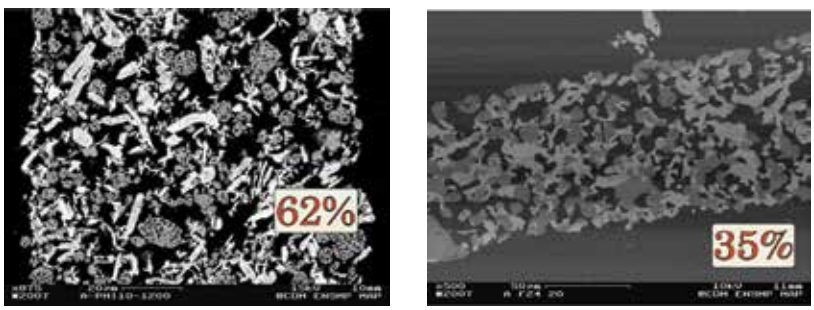

Fig. 10. SEM observation of the polished surface of a PCFC anode (50 vol.% BCY10 = white phase + 50 vol.% NiO = grey phase; dark areas are porosity) taken from the same dried green tape about 100 µm thick; left: test was interrupted at 1000 °C during heating (surface fraction or pores = 62%); right: test was interrupted after 10 hours at 1450 °C (surface fraction of pores = 35%); scales are on the micrographs; note the large shrinkage of the thickness (Costa et al, 2009; Costa, 2009)

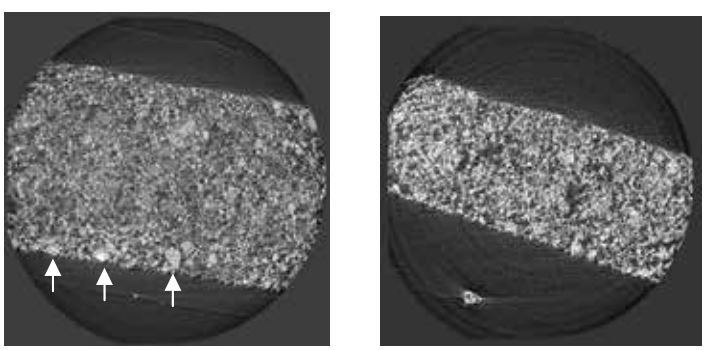

350 °C / 1 hour 1450 °C / 1 hour

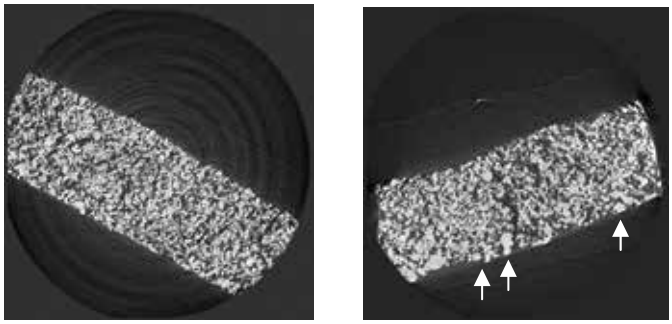

1450 °C / 8 hours 1450 °C / 24 hours

Fig. 11. Morphology of a PCFC anode (50 vol.% BCY10 + 50 vol.% NiO = white phase; dark areas are porosity); 2D surfaces taken from 3D microtomography (ESRF, Grenoble, France) corresponding to interrupted sintering tests; initial anode thickness = 250 μm, upper surface during test is up on the micrographs; sedimentation of large BCY10 grains is easily detected at the bottom of the anode, especially on the top left and bottom right images; note the high level of shrinkage of the thickness (Costa et al, 2009; Costa, 2009)

Owing to the transport of matter during sintering (diffusion, visco-plastic flow, densification…), one may assume that the multilayer is free of stresses at the end of the sintering plateau. When the flatness of the multilayer is maintained by a weight, thermo-elastic stresses due to thermal expansion mismatch and different elastic constants will develop upon cooling, which will cause either remnant deformation or cracking when removing the weight. When the flatness is maintained by counterbalancing the deformation (in multilayers with an odd number of components) during all the length of the plateau, residual deformation will also develop. In either cases this residual deformation can be eliminated to a certain extent by playing again on the layers thickness if possible, and/or on the apparent Young's modulus, *i.e.* by the addition of more pore formers (Grosjean, 2004).

3. Experimental examples

3.1. Aqueous tape-casting of SOFCs

We have used standard commercial powders for this study [6] as described below:

- Electrolyte: YSZ (TZ8-Y, Tosoh),
- Anode: porous Ni-YSZ cermet (Ni precursor = NiO, Novamet A Type),
- Cathode: composite YSZ-$La_{0.80}Sr_{0.20}MnO_{3-\delta}$ (LSM, Rhodia).

Following what has been extensively discussed above, the slurry composition for each layer was formulated to obtain the same final shrinkage for the three components of the cell; the thickness of the cast tape was adjusted so that the thermoelastic mechanical stresses were minimized during the cooling following Timoshenko's bilayer model (Timoshenko and Gere, 1991). The slurries composition was based on the following chemicals:

- Water (solvent)/sodium alginate (binder) in the ratio (100:1),
- Dispersant: Dolapix ET85 (droplets),
- Macro pore-former when needed: acrylic polymer.

Slurries for the electrodes and for the electrolyte were cast separately, with appropriate thickness, on a glass support. Green tapes were then obtained by the chemical gelation of the sodium

alginate through the complexation of Ca^{2+} ions in the presence of a $CaCl_2$ solution. The three different green tapes were then cut and stacked to obtain a full green single cell. The three-layer stacks obtained in this way were then dried between two hydrophilic honeycomb supports at 70 °C so that the water could be desorbed symmetrically from the two surfaces to avoid any warping of the stack. After the drying was completed, the stacks were placed between two Mullite alveolar supports, whose weight was appropriate to maintain the flatness of the cell without interfering with the planar shrinkage. Two-inch flat SOFC single cells with high quality interfaces between electrolyte and electrodes were routinely obtained after sintering at 1350 °C for 8 hours (Fig. 12 and Fig. 13).

Nevertheless, co-sintering the whole cell at 1350 °C led to poor electrochemical properties owing to reactivity between YSZ and LSM [6,18]. In that specific case, we have developed a sequential organic tape-casting approach to cast the cathode layer on top of an already sintered Anode/Electrolyte half-cell prepared by the water based process described above. It is to be noted here that, owing to surface tension considerations, water-based tape-casting does not lend itself to the successful deposit of a layer on top of an already sintered material. With this method the cathode could be heat-treated at a lower temperature (1200 °C for 1 hour), conditions where reactivity with YSZ does not appear significant.

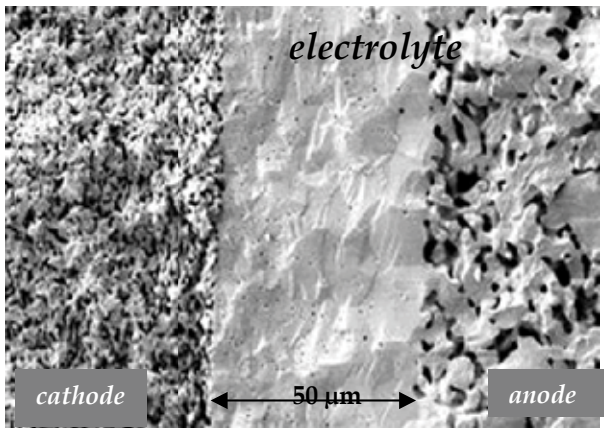

Fig. 12. SEM observation of a cross section of a SOFC (YSZ + LSM/YSZ/YSZ + NiO) obtained by tape-casting (from Grosjean, 2004)

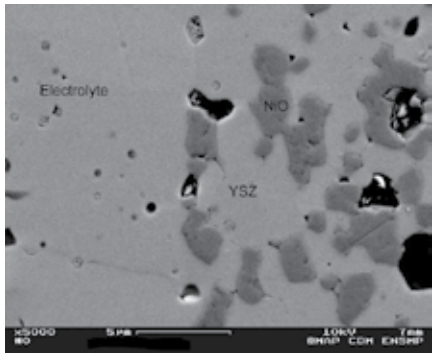

Fig. 13. SEM observation of a polished cross section of the interface between the anode and the electrolyte in a SOFC (YSZ + LSM/YSZ/YSZ + NiO) obtained by tape-casting (from Grosjean, 2004)

3.2. Organic tape-casting of PCFC

In this study only the fabrication of bi-layers or symmetrical cells Anode/Electrolyte/Anode was attempted since no cathode material for PCFC was available at this time (Costa et al, 2009; Costa, 2009). The following materials were either home made or commercially supplied:

- Electrolyte: BCY10 was produced via a chemical route based on oxalate co-precipitation following exactly the procedure described by Almeida de Olivera et al (Almeida de Oliveira et al, 2007),
- Anode: porous Ni-BCY10 cermet (Ni precursor = NiO, Novamet A Type) in the volume ratio 1:1 (corresponding weight ratio = 1:1.08).

Water-based tape-casting was not applicable for BCY10 shaping because BCY10 exhibits a strong basic behaviour; since water is an amphoteric electrolyte, the pH of such a suspension is quite high and hydrolysis of the material occurs rapidly. Therefore, tape-casting of PCFC based on BCY powder must be carried out with an organic solvent totally deprived of water. Among all of the organic solvent/binder possible couples, we have chosen the couple Ethanol/PVB: it limits the toxicity of the slurries and makes BCY10 suspensions stable rather easily. The following products were used:

- Absolute Ethanol (Fisher Scientific),
- Poly(Vinyl Butyral) (PVB) (Acros Organics) as the binder (and as a pore former for the anode),
- PolyEthylene Glycol-400 grade (PEG) (Fisher Scientific) as the plasticizer.

Table 1 below gives the quantity of products for the electrolyte and anode slurries for a typical tape-casting experiment; the compositions are optimized for the anode and electrolyte in respect with the desired final microstructures (dense BYC10, porous anode with interconnected Ni particles, BCY10 and network of pores). Slurries were ball-milled for 4 hours prior to casting in order to obtain homogeneous suspensions.

Slurries were cast on a glass support coated with glycerol to prevent the adhesion of the green tapes. First a 500 µm thick anode layer was cast, and left twenty minutes at room temperature for the drying process to start taking place. Then a 150 µm thick electrolyte layer was cast on top of the anode tape. For the fabrication of symmetric half-cells, a second 500 µm thick anode layer was cast on top of the electrolyte layer, again twenty minutes later. The stack of green tapes was then dried at room temperature for two hours before being cut into discs. Since $BaCeO_3$ based perovskite reacts at high temperature (> 1200 °C) with most of the materials used as sintering supports (Al_2O_3, ZrO_2), the sintering of BCY10 was made on a BCY10 powder layer. After a plateau of 1 hour at 350°C for burning the organic products, the sintering was carried out at 1450°C for 24 hours for a full densification of the electrolyte (Fig. 14 and Fig. 15).

Chemicals	Anode / g	Electrolyte / g
BCY10	2.5	6.0
NiO	2.7	-
Ethanol	4.5	4.8
PVB	2.0	0.60
PEG	0.70	0.30
Glycerol	0.45	-

Table 1. Composition (in g) of optimized slurries in regards to the final microstructure

Flat symmetrical half-cells 20 mm in diameter were routinely obtained via this procedure. Bi-layers anode/electrolyte could not be obtained without a very strong warping for the reasons discussed in section 2.3. Solutions range from narrowing the BCY10 grain size distribution, adding an effective dispersant to the slurry, or compensating the deformation by that of the cathode when such material is available.

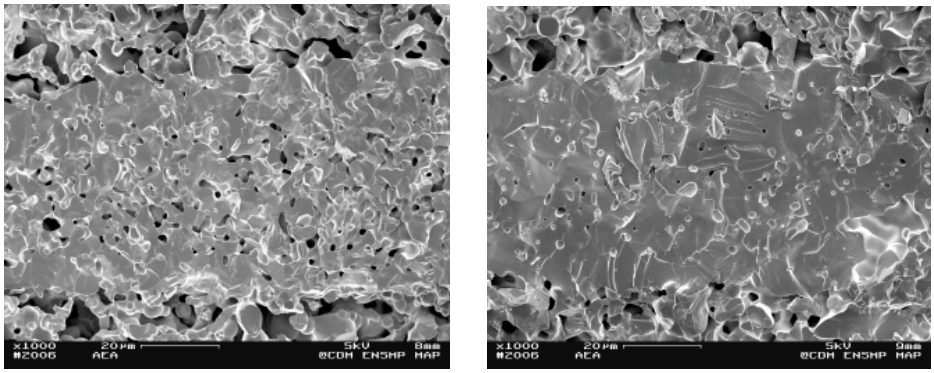

1450 °C / 10 hours 1450 °C / 24 hours

Fig. 14. SEM observation of a cross section of a PCFC half-cell anode/electrolyte/anode sintered at 1450 °C for different durations (from Costa et al, 2009; Costa, 2009)

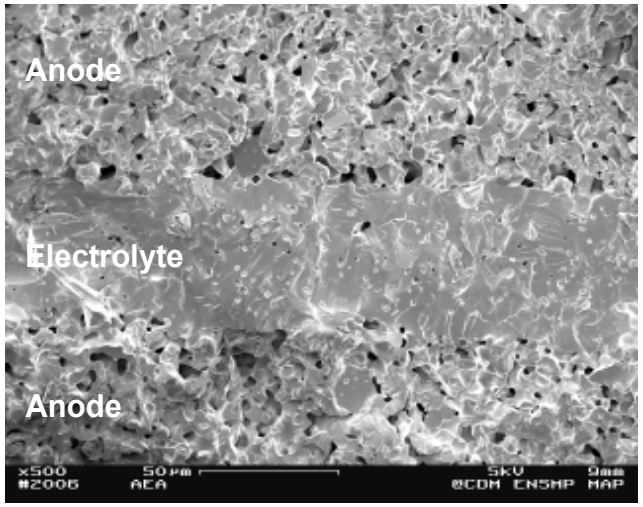

Fig. 15. SEM observation of a cross section of a PCFC half-cell Anode/Electrolyte/Anode sintered at 1450 °C (from Costa et al, 2009; Costa, 2009)

3.3. First realizations of IDEAL-Cell

This new innovative concept is described here, and its characteristics, specificities and advantages compared to SOFCs and PCFCs are given. This concept has just reached the Proof of Concept step at the end of the year 2009, in the frame of a 4-years FP7 European project. The major difference of this concept compared to the others is that it is based on a central porous membrane that displays a mixed conduction (proton and oxygen). This section will show how tape casting is applied to shape the different elements of this new cell.

The basic ideas behind the IDEAL-Cell concept consists in isolating the hydrogen and oxygen compartments from the exhaust water to avoid the main problems associated with the presence of water at electrodes in SOFC (Fig. 1) and in PCFC (Fig. 2). In the IDEAL-Cell design each compartment has a single role to play, for which it can be fully optimized. Such a three independent compartments system is being developed by an European consortium (ARMINES, France; Université de Bourgogne, France, CNR, Italy; DLR, Germany; IEES, Bulgaria; AGH, Poland; Marion Technologies, France; Naxagoras, France; Visimbel, germany) by joining the cathode part of a SOFC to the anode part of a PCFC, rejecting thus the production of water toward a common central compartment (Fig. 3). The protons created at the anode side and the oxygen ions produced at the cathode side diffuse through the corresponding electrolytes toward the central membrane, where they combine. The electrons that are torn off atomic hydrogen at the anode will go to the external circuit and feed atomic oxygen to create oxygen ions at the cathode side. The central membrane is a mixed proton and oxygen composite conductor with highly porous microstructure to allow the evacuation of water.

Unlike in SOFCs and PCFCs, this design will avoid gas dilution, condensation of water on the catalytic sites, inhibition of mass transfer, corrosion by oxygenized water at high temperature. In addition, it allows for an easy and independent application of gas pressure on both electrodes to enhance the overall efficiency. The concept, patented by ARMINES/Mines-ParisTech, has been proved in 2009 via four criteria: i/ a stable OCV, ii/ a stable polarization curve, iii/ complex impedance fingerprint typical of water formation, iv/ measurement of water formation as a function of the current across the cell. Up to now, as first attempts to prove the concept, different processes have been implemented (SPS, HP, tape casting) (Thorel et al, 2009a; Thorel et al, 2009b, Presto et al, 2009); the shaping technique developed at ARMINES/Mines-ParisTech (Abreu, 2011) is based on the cold-pressed and sintered BCY electrolyte support, on which all additional layers are deposited by tape-casting (Fig. 16). The cell is not yet at all optimized and is still very thick for experimental purposes (about 2 mm), but already shows highly attracting performances (5 mW/cm^2). Extrapolation towards typical cell thickness indicates that the level of performances attained by IDEAL-Cell after 2 years of operation of the project is even better than that of PCFCs. In addition, modelling shows that the concept exhibits very little electrodes overpotentials and extremely high potentialities for improvements.

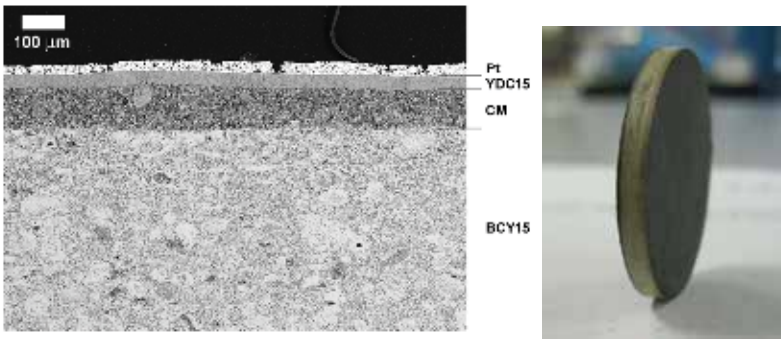

Fig. 16. Left: SEM observation of a cross section of the IDEAL-Cell Proof of Concept sample with Pt electrodes; right: full BCY supported IDEAL-Cell with : cathode = LSCF; oxygen

electrolyte = YDC15; central membrane = YDC15 + BCY15; proton electrolyte = BCY15; anode = BCY15 + Ni (Abreu, 2011)

4. Conclusion

High temperature fuel cells are very sophisticated objects, and as such are very complicated to shape. The fabrication costs constitute the major brake to their development in a highly competitive segment where competitor alternative power sources progress at a high rate. Decades of efforts and accumulated knowledge on one of the most known ceramic (Zirconia) did not allow putting yet a low cost operating SOFC on the market.

Taking into account the numerous parameters that define the operability of a process such as tape-casting for shaping ceramic fuel cells becomes very difficult. Empiricism should be backed by modelling and computer simulation, which is far from being routinely available for processes in general, and tape-casting in particular.

One must also pay attention to the fact that cutting the fabrication costs at any prices is not necessarily a good option since it may raise unexpected issues (*i.e.* co-sintering); rather, a sequence of compatible processes can be an efficient solution (*i.e.* coupling tape-casting with screen-printing and/or plasma spraying…). The community should also be imaginative and open to innovative solutions that may be less energy efficient but infinitely simpler (monochamber concept), or a bit more complicated to fabricate but having enormous advantages (IDEAL-Cell).

Acknowledgements

Part of the research leading to the results presented here has received funding from the European Community's Seventh Framework Programme (FP7/2007-2013) under grant agreement N° 213389. This work was also partly supported by a grant from the French ''Agence Nationale de la Recherche'' ANR (Project TECTONIC), and by the ''Groupement des Ecoles des Mines'' (GEM). The tomography images presented here were obtained at the ESRF (Grenoble) on the ID19 beamline.

The author wishes to thank the Ph.D students (Olivier Sanséau, Arnaud Grosjean, Julien Hafsaoui, Rémi Costa, Joao Abreu), master students (Ali Addada, Matthieu Caruel) and post-doc (Anthony Chesnaud) of his group for all their work from which most of the results in the present papers are drawn.

5. References

Abreu, J. (2010). Contribution à l'étude et à la réalisation d'IDEAL-Cell, un concept innovant de pile à combustible à haute température. Ph.D thesis, Mines-ParisTech, in press

Almeida de Oliveira, A-P., Hafsaoui, J., Hochepied, J-F., Berger, M-H., Thorel, A. (2007). Synthesis of $BaCeO_3$ and $BaCe_{0.9}Y_{0.1}O_{3-\delta}$ from mixed oxalate precursors. Journal of the European Ceramic Society, Vol. 27, 3597-3600

Bassano, A., Buscaglia, V., Viviani, M., Bassoli, M., Buscaglia, M.T., Sennour, M., Thorel, A., Nanni, P. (2009). Synthesis of Y-doped $BaCeO_3$ nanopowders by a modified solid-state process and conductivity of dense fine-grained ceramics. Solid State Ionics, Vol. 180, 168-174

Bitterlich, B., Lutz, C., Roosen, A. (2001). Preparation of Planar SOFC-Components via Tape-Casting of Aqueous Systems, Lamination and Cofiring, in: Chapter 9: Ceramic Materials and Components for Engines, J. G. Heinrich, F. Aldinger (Ed.), WILEY-VCH Verlag GmbH, Print ISBN: 9783527304165

Costa, R., Hafsaoui, J., Almeida de Oliveira, A-P., Grosjean, A., Caruel, M., Chesnaud, A., Thorel, A. (2009). Tape-Casting of Protonic Conducting Ceramic Materials. Journal of Applied Electrochemistry, Vol. 39, No. 4, 48

Costa, R. (2009). Contribution à l'étude et à la mise en forme d'une cellule de pile à combustible à conduction protonique PCFC. Ph.D thesis, Mines-ParisTech

Fontaine, M.L., Larring, Y., Smith, J.B., Raeder, H., Andersen, Ø.S., Einarsrud, M.A., Wiik, K., Bredesen, R. (2009). Shaping of advanced asymmetric structures of proton conducting ceramic materials for SOFC and membrane-based process applications. Journal of the European Ceramic Society, Vol. 29, 931-935

Grosjean, A. (2004). Etude et réalisation par coulage en bande et co-frittage de cellules de pile à combustible à oxydes solides. Ph.D thesis, Mines-ParisTech

Grosjean, A., Sanséau, O., Radmilovic, V., Thorel, A. (2006). Reactivity and diffusion between $La_{0.8}Sr_{0.2}MnO_3$ and ZrO_2 at interfaces in SOFC cores by TEM analyses on FIB samples", Solid State Ionics, Vol. 177, 1977-1980

Hafsaoui, J. (2009). Membrane duale de reformage et de filtration pour la production d'hydrogène par réaction de craquage de méthane. Ph.D thesis, Mines-ParisTech

Huia, R., Wanga, Z., Keslera, O., Rosea, L., Jankovica, J., Yicka, S., Marica, R., Ghosha, D. (2007). Thermal plasma spraying for SOFCs: Applications, potential advantages, and challenges. Journal of Power Sources, Vol. 170, No. 2, 308-323

Moreno, R. (1992a). The Role of Slip Additives in Tape-Casting Technology - Part I : Solvents and Dispersants. American Ceramic Society Bulletin. Vol. 71, No. 10, 1521-1531

Moreno, R. (1992b). The Role of Slip Additives in Tape-Casting Technology - Part II : Binders and Plasticizers. American Ceramic Society Bulletin. Vol. 71, No. 10, 1647-1657

Ou, T., Delloro, F., Nicolella, C., Bessler, W. G., Thorel, A.S. (2009). Mathematical model of mass and charge transport and reaction in the central membrane of the IDEAL-Cell. ECS transactions, Vol. 25, No. 2, (2009) 1295-1304, ISBN 978-1-56677-739-1

Presto, S., Barbucci, A., Viviani, M., Ilhan, Z., Ansar, S.A., Soysal, D., Thorel, A., Abreu, J., Chesnaud, A., Politova, T., Przybylski, K., Prazuch, J., Brylewski, T., Zhao, Z., Vladikova, D., Stoynov, Z. (2009). IDEAL-Cell, an Innovative Dual mEmbrAne fueL-Cell: fabrication and electrochemical testing of first prototypes. ECS transactions, Vol. 25, No. 2, (2009) 773-782, ISBN 978-1-56677-739-1

Syed, A. et al. (2006). Improving plasma sprayed YSZ coatings for SOFC electrolytes. Journal of Thermal Spray Technology, Vol. 15, No. 4, 617

Thorel, A.S., Chesnaud, A., Viviani, M., Barbucci, A., Presto, S., Piccardo, P., Ilhan, Z., Vladikova, D., Stoynov, Z. (2009a). IDEAL-Cell, first experimental proves of an innovative concept", Proceedings of the "Advances and Innovations in SOFC" International Workshop, pp. 1-8, ISBN 978-954-92483-1-9, Katarino, Bulgaria, September 2009

Thorel, A.S., Chesnaud, A., Viviani, M., Barbucci, A., Presto, S., Piccardo, P., Ilhan, Z., Vladikova, D., Stoynov, Z. (2009b). IDEAL-Cell, a high temperature Innovative Dual mEmbrAne fuel-Cell. ECS transactions, Vol. 25, No. 2, (2009) 753-762, ISBN 978-1-56677-739-1

Timoshenko, S.P., Gere, J.M. (1991). Mechanics of Materials", Chapman and Hall (Ed.)

Xia, C., Chen, F., Liu, M. (2001). Reduced-Temperature Solid Oxide Fuel Cells Fabricated by Screen-Printing. Electrochem. Solid-State Lett., Vol. 4, No. 5, A52-A54

Yoon, J., Huang, W., Ye, G., Gopalan, S., Pal, U.B., Seccombe Jr., D.A. (2007). Electrochemical Performance of Solid Oxide Fuel Cells (SOFCs) Manufactured by Single Step Co-firing Process. Journal of the Electrochemical Society, Vol. 154, No. 4, B389

4

Alkoxide Molecular Precursors for Nanomaterials: A One Step Strategy for Oxide Ceramics

Łukasz John and Piotr Sobota
University of Wrocław, Faculty of Chemistry, 14 F. Joliot-Curie St., 50-383 Wrocław Poland

1. Introduction

For the last two decades, there has been a growing interest in the development of the chemistry of mixed-metal bi- and polynuclear alkoxo and alkoxo-organometallic complexes. Such interest derives from their fascinating structural chemistry, interesting catalytic properties, and high potential for industrial applications.[1] The fact that most of the heterometallic alkoxo species can generate bimetallic or multimetallic oxides has resulted in high research activity in the field. The most attractive applicable routes for preparation of oxide materials are those involving alkoxides and their derivatives. First of all, their attractiveness lies in the fact that they are easily accessible and consist inexpensive compounds. Furthermore, alkoxide ligands are easily removable via thermal treatments. Finally, these compounds already have metal-oxygen bonds established. Molecular precursors derive from alkoxide complexes can generate ceramic materials in a single step (so-called single-source precursors – SSPs).[2] In the case of bi- or polyoxides, such materials deliver appropriate metal elements of a final product eliminating the need to match the reaction rates required from a multicomponent precursor mixture. It is worth noting that their thermal deposition or decomposition processes can be performed at relatively low temperatures compare to conventional methods involving inorganic salts. These features made the metal oxides, that derived from metal alkoxides, highly pure products with specific properties like high hardness, chemical and mechanical resistance, and high temperature stability. From presented above point of view, metal alkoxides play the key role for preparing materials of excellent functions and shapes. The aim of this chapter will be to serve as a guide in understanding the principles in the one step strategy for oxide ceramics using alkoxide precursors. The major accent will be made on design of molecular precursors. The chapter will include synthesis of alkoxides and their derivatives. Among these methods one of the less explored reaction of organometallic complexes with alkoxides that bear free alcohols at the metal site will be discussed. Moreover, it will also contain sub-chapters describing the concept of SSPs strategy and preparation of oxide materials and their properties.

2. Structures of Alkoxides

Alkoxides $M(OR)_x$ (M = metal cation of valency x; R = alkyl or aryl group) are formed by the replacement of the hydroxylic hydrogen of an alcohol (ROH) by a metal cation. According to Bradley's concept,[3] alkoxides with the lower primary or secondary alkyl groups have a strong tendency to polymerization creating coordination polymers $[M(OR)_x]_y$ (where y is the degree of polymerization). Degree of polymerization increases with the metal atomic ratio. Coordination polymers that they form are relatively smaller than usual organic or silicon polymers. Moreover, alkoxides take the smallest structural unit for the highest possible coordination number of the metal. Metal alkoxides $[M(OR)_x]_y$ that are well soluble in common organic solvents, create small oligomers with y = 2, 3, or 4.[3]
Alkoxo RO^- anion possesses donor oxygen atom with three unpaired electrons, which form covalent bond with metal. These anions might be coordinated to metal sites in terminal or bridging way. Alkoxides have a tendency to form oligomeric compounds $[M(OR)_x]_y$, where RO^- groups are connected to two or even more metal sites. This phenomenon is affected on reactivity and properties of these compounds. Heterobi- or heteropolymetallic alkoxo complexes constitute an enormous family of compounds with a very broad structural diversity. These species form structural motifs which range from simple bimetallic compounds to very complex aggregates that result from the versatile coordinating abilities of an alkoxo ligands (Scheme 1).[4]

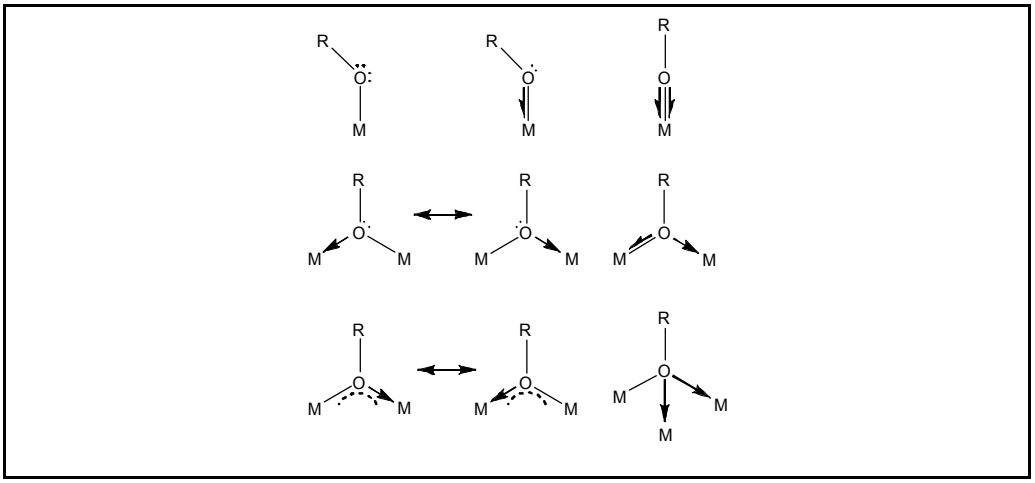

Scheme 1. Coordination modes of an alkoxo ligand according to Bradley, Mehrotra, Rothwell, and Singh.[1a]

Electron and steric demand of alkoxo groups have an influence on metal alkoxides they form. For instance, the presence of halide or aryl ligands affected on decreasing of electron density onto oxygen atom. Because of these, possibility to form bridging structures is inhibited. Furthermore, electrofilic nature of metal cations allows to attach neutral ligands (e.g. tetrahydrofurane, pyridine, etc.) to the metal spheres. Due to the saturating of metal sites, it is possible to obtain monomeric alkoxides $[M(OR)_xL_y]$ (where L = neutral ligand).[1a] Although in the literature there are a lot of examples of metal alkoxides, it would be very

difficult to formulate a precise rule that could fully explained the process of a specific geometry formation and predict the final geometry of forming alkoxide complex.

Complex	Structural motif	Ref. 4
$[Mg_4(\mu_3\text{-}OMe)_4(OMe)_4(MeOH)_8]$	$Mg_4(\mu_3\text{-}O)_4O_{12}$ core	b
$[Ca_9(OCH_2CH_2OCH_3)_{18}(HOCH_2CH_2OCH_3)_2]$	layers of open dicubanes with $Mg_4(\mu_3\text{-}O)_2(\mu\text{-}O)_4O_2$ core	c
$[(C_5H_4CH_3)_4Y(\mu\text{-}OCH{=}CH_2)]_2$	$Y_2(\mu\text{-}O)_2$ core	d
$[Y_3(\mu_3\text{-}O^tBu)(\mu_3\text{-}Cl)(\mu\text{-}O^tBu)_3(O^tBu)_4(thf)_2]$	$Y_3(\mu_3\text{-}O)(\mu\text{-}O)_3O_4$ core	e
$[Ti_2(\mu\text{-}OR)_2(OR)_4(acac)_2]^a$ (R = Me, Et, ^{i}Pr)	$Ti_2(\mu\text{-}O)_2O_4$ core	f
$[Me_4Zn_4(\mu_3\text{-}O^tBu)_4]$	$Zn_4(\mu_3\text{-}O)_4$ core	g
$[W_2(OCMe_2CMe_2O)_3]$	$O_3W{\equiv}WO_3$ core	h
$[Ga_2(\mu\text{-}O^tBu)_2{}^tBu_4]$	$Ga_2(\mu\text{-}O)_2$ core	i
$[Mg_2V_2(thffo)_6Cl_4]^b$	$Mg_2V_2(\mu_3\text{-}O)_2(\mu\text{-}O)_4$ core	j
$[(thf)(O^tBu)Y\{(\mu\text{-}O^tBu)(\mu\text{-}CH_3)AlMe_2\}_3]$	$YAl_3(\mu\text{-}O)_3O$ core	k
$[Zr_2Co_2(\mu_3\text{-}O^nPr)_2(\mu\text{-}O^nPr)_4(O^nPr)_4(acac)_2]^a$	$Zr_2Co_2(\mu_3\text{-}O)_2(\mu\text{-}O)_4O_4$ core	l
$[Al\{(OEt)_2GaMe_2\}_3]$	$AlGa_3(\mu\text{-}O)_6$ core	m
$[Nb_2(\mu\text{-}OMe)_2(OMe)_2(HOMe)_2Cl_4]$	Nb-Nb$(\mu\text{-}O)_2O_4$ core	n
$[Mo_2(O^iPr)_4(HO^iPr)_4]$	$O_4Mo{=}MoO_4$ core	o
$[Pb(\mu\text{-}OC_2H_4OMe)_2]_n$	chain structure with $Pb(\mu\text{-}O)_2$ core	p
$[Y_{10}(OCH_2CH_2OMe)_{30}]$	cyclic decameric structure with $Y(\mu\text{-}O)_2O$ core	r
$[Pr_3(\mu_3\text{-}tftb)_2(\mu\text{-}tftb)_3(tftb)_2]^c$	$Pr_3(\mu_3\text{-}O)_2(\mu\text{-}O)_3O_4$ core	s
$[\{Co_8(\mu\text{-}OMe)_{16}(O_2CMe)_8\}(NH_4{}^+)]$	cyclic structure with $NH_4{}^+$ guest and $Co_8(\mu\text{-}O)_{16}O_{16}$ core	t
$[YNa_8(\mu_9\text{-}Cl)(\mu_4\text{-}O^tBu)(\mu_3\text{-}O^tBu)_8(O^tBu)]$	$YNa_8(\mu_4\text{-}O)(\mu_3\text{-}O)_8O$ core	u
$[Na_4Zr_6(\mu_5\text{-}O)_2(\mu_3\text{-}OEt)_4(\mu\text{-}OEt)_{14}(OEt)_6]$	$Na_4Zr_6(\mu_5\text{-}O)_2(\mu_3\text{-}O)_4(\mu\text{-}O)_{14}O_6$ core	v
$[Ti_7(\mu_4\text{-}O)(\mu_3\text{-}O)_2(\mu\text{-}OEt)_8(OEt)_{12}]$	$Ti_7(\mu_4\text{-}O)(\mu_3\text{-}O)_2(\mu\text{-}O)_8O_{12}$ core	w

[a]acac = acetylacetonato; [b]thffo = tetrahydrofuryloxo; [c]tftb = $OCMe_2(CF_3)$

Table 1. Different structural motifs of metal alkoxides.

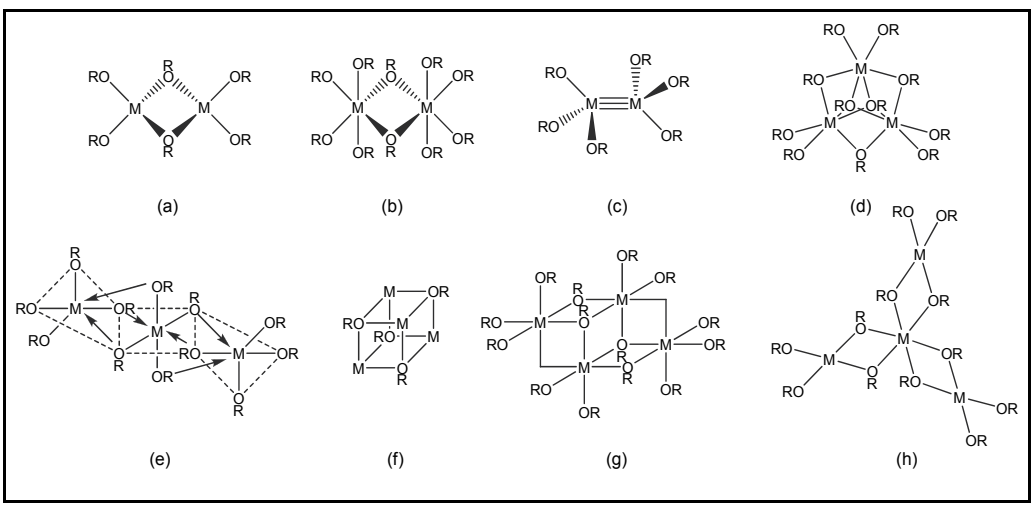

Scheme 2. Various structure motifs of metal alkoxides.[1a]

In fact even minor changes in a ligand structure or reaction conditions can cause the geometry of the whole compound to be fundamentally different. To the most common alkoxide structural motifs are included (Scheme 2): (a) $[M_2(\mu\text{-}OR)_2(OR)_4]$ with M_2O_6 core, (b) $[M_2(\mu\text{-}OR)_2(OR)_8]$ with M_2O_{10} core, (c) $[M_2(OR)_6]$ with M_2O_6 core and triple bond between metal sites, (d) $[M_3(\mu_3\text{-}OR)_2(\mu\text{-}OR)_3(OR)_4(HOR)_2]$ with M_3O_{11} core, (e) $[M_3(\mu\text{-}OR)_6(OR)_6]$ with M_3O_{12} core, (f) $[M_4(\mu_3\text{-}OR)_4]$ with M_4O_4 core, (g) $[M_4(\mu\text{-}OR)_2(\mu\text{-}OR)_4(OR)_{10}]$ with M_4O_{10} core, and (h) $[M_4(\mu\text{-}OR)_6(OR)_6]$ with M_4O_{12} core units. A few examples from the wide geometrical palette of alkoxo species are shown in Table 1.[4]

3. Alkoxides – General Methods of Synthesis

There are many methods of synthesis of metal alkoxides or aryloxides. Their choice depends on the ionization energy of the metal, which alkoxide is formed. The less electronegative alkali metals react spontaneously with alcohols, but for instance magnesium, aluminium etc. need some so-called activation agent, e.g. small amounts of crystalline I_2 or $HgCl_2$. For other metals more complex reactions need to be applied. Below, we will briefly discuss the most common methods of synthesis.

3.1. Direct reaction of metal with an alcohol

This method is the most popular in laboratory scale but limited to less electronegative alkali metals (Li, Na, K, Rb, Cs). It is based on hydroxyl hydrogen substitution by appropriate metal cation accompanied by intense heat and H_2 evolution (Eq. 1):

$$M + (1+x)ROH \rightarrow 1/y\{MOR\cdot xROH\}_y + 1/2H_2\uparrow \quad (1)$$

Second group metals possess higher ionization energy and are liable to passive process. Because of this, their reactions are much slower than with group 1 metals. Well soluble alkoxides can be obtained in direct reaction using sterically ramified alcohols (where R = ^{t}Bu, CF_3, aryl etc.).[5] The use of alcohols with "bulky" R groups prevent oligomerization, and resulting alkoxides are well soluble in common aliphatic hydrocarbons.

3.2. Electrochemical method

Synthesis of metal alkoxides by anodic dissolution of metals in alcohols was firstly used in 1906 by Szilard et al. for copper and lead methoxides.[6] In the seventies of the last century, this technique was spread by Lehmkhul et al. for the synthesis of $M(OR)_2$ complexes (where M is Fe^{2+}, Co^{2+}, Ni^{2+}; R = Me, Et, ^{n}Bu, ^{t}Bu).[7] Electrode processes can be summarized as follows: Due to the oxidation of metal at the anode, cation and electron are formed. The electron and alcohol create hydrogen radical $H\cdot$ and alkoxide anion. Molecular hydrogen is exude at the cathode. Because of electrode reactions appropriate cations and anions RO^- are obtained.[7] This method is employed of metals with high ionization energy. It is easy, effective technique, and final products are extremely pure. At present, electrochemical method is applied in synthesis of Y, Ti, Zr, Nb, Ta, Mo, W, Cu, Ge, Sn, etc. alkoxides.[8]

3.3. Reaction of alcohols with metal halides

The reaction between alcohol and metal halide leads to the substitution of halide anion into RO^- group forming appropriate metal alkoxide (Eq. 2).

$$MCl_z + (x + y)ROH \rightarrow MCl_{z-x}(OR)_x(ROH)_y + xHCl\uparrow \quad (2)$$

Depending on the solvent, molar ratio of reagents, and temperature, different compounds can be obtained. Classic example is a reaction of $TiCl_4$ with ^{i}PrOH in CH_2Cl_2, where $[Ti(\mu\text{-}Cl)_2Cl_2(O^iPr)_4]$, $[TiCl_3(O^iPr)(HO^iPr)_2]$, and $[Ti_2Cl_4(\mu\text{-}O^iPr)_2(O^iPr)_2(HO^iPr)_2]$ are formed.[9]

3.4. Reactions of alcohols with metal hydroxides and oxides

Metal hydroxides and oxides react with alcohols forming appropriate alkoxides and water (Eqs. 3-4).

$$M(OH)_x + xROH \rightleftarrows M(OR)_x + xH_2O \quad (3)$$

$$MO_x + 2xROH \rightleftarrows M(OR)_{2x} + xH_2O \quad (4)$$

Due to the reversible nature of these reactions, it is necessary to remove water from the reaction system. This method applies to receive alkoxides, both main and side groups of metals.[10]

3.5. Ligands exchange reactions

One of the characteristic properties of metal alkoxides is their activity in the substitution reactions of alkoxo groups (Eq. 5). In this way several homo- and heteroleptic alkoxide complexes were synthesized.[11]

$$M(OR)_x + yR'OH \rightarrow M(OR)_{x-y}(OR')_y + yROH \quad (5)$$

Ligands exchange reactions are affected: (a) the steric ramified of the RO and R'O groups, (b) the values of H-O bond energies, and (c) the relative M-O bond strengths.

3.6. Reactions of alcohols with metal amides

Dialkyl amides $M(NR_2)_x$ (R = Me, Et, $SiMe_3$) react with alcohols according to below equation (Eq. 6):

$$M(NR_2)_x + xR'OH \rightarrow M(OR')_x + xR_2NH\uparrow \quad (6)$$

This method is useful for metals that have a higher affinity for oxygen atoms, rather than to nitrogen. Its advantage is that forming dialkyl amines are easy to remove from the reaction environment and resulting alkoxide product is highly pure.[12]

3.7. Reactions of alcohols with organometallics

Reactions of organometallics with alcohols are quite popular in the literature.[13] These reactions are extremely useful for the preparation of mono- and mixed-metal alkoxides (Eqs. 7-9) but their disadvantage is that organometallics are air/moisture sensitive and working with them is cumbersome.

$$MR_2 + R'OH \rightarrow 1/x[MOR']_x + RH\uparrow \quad (7)$$

$$MR_3 + R'OH \rightarrow 1/x[R_2MOR']_x + RH\uparrow \quad (8)$$

$$R_2MX + M'OR' \rightarrow 1/x[R_2MOR']_x + M'X \quad (9)$$

Very interesting modification of this reaction is a direct reaction of organometallic complexes with alkoxides that bear free alcohols at the metal site (Eq. 10).[14]

$$M(OR)_x(ROH)_y + yM'R'_z \rightarrow M'R'_{z-1}M(OR)_{x+y} \quad (10)$$

In this reaction there is an organometallic driven abstraction of the OH hydrogens from M coordination sphere. This leads to the subsequent evolution of simple hydrocarbons like methane or ethane and results in a linkage of RO ligands. Because of the simple gases evolution, resulting products are highly pure.

4. A One Step Strategy for Oxide Ceramics

Mono- and mixed-metal alkoxides with fixed ratio of participating metals can be used for oxide ceramic preparation via thermolysis to give high purity materials. Metal alkoxides as so-called single-source precursors (SSPs) already have metal-oxygen bonds established. Because of this, their thermal decomposition can be performed at relatively low temperatures and maintains the M-O core. What is extremely important here, the metal oxides derived from alkoxide SSPs are highly pure and have specific properties like high hardness, chemical and mechanical resistance, and high temperature stability. They constitute a group of advanced ceramics.[4a]

Bimetallic SSPs can generate ceramic materials in a single step. Their advantage over the inorganic salt mixtures lies in the fact that both or more elements of a final product eliminating the need to match the reaction rates required from a multicomponent precursor mixture in conventional methods.[15] In general, careful and appropriate choice of metals and alkoxo ligands is necessary in this strategy if undesired side reactions occur.

Interesting and useful classification of SSPs was proposed by Veith.[16] This approach is based on their differences in thermal decomposition/deposition pathways. Approach discussed can be subdivided into three different types of precursors: SSP-I, SSP-II, and SSP-III.

4.1. SSP-I

In the first type of SSPs, metals stoichiometry on molecular level of precursor is also present in a correct ratio of the final oxide product (Eq. 11).

$$MM'_xLL' \rightarrow MM'_x + L + L' \quad (11)$$

M and M′ are denoted oxide units. L and L′ are ligands which can survive thermolysis conditions unchanged or they can be modified during this process.
Complexes $[BaM(OH)(O^iPr)_5(HO^iPr)_3]_2$ (where M = Ti, Zr) and $[BaTi_{0.5}Zr_{0.5}(O^iPr)_6]_2$ constitute the examples of SSP-I (Fig. 1).[17] From these precursors perovskites and related perovskites $BaTiO_3$, $BaZrO_3$ and $BaTi_{0.5}Zr_{0.5}O_3$, respectively, were obtained.

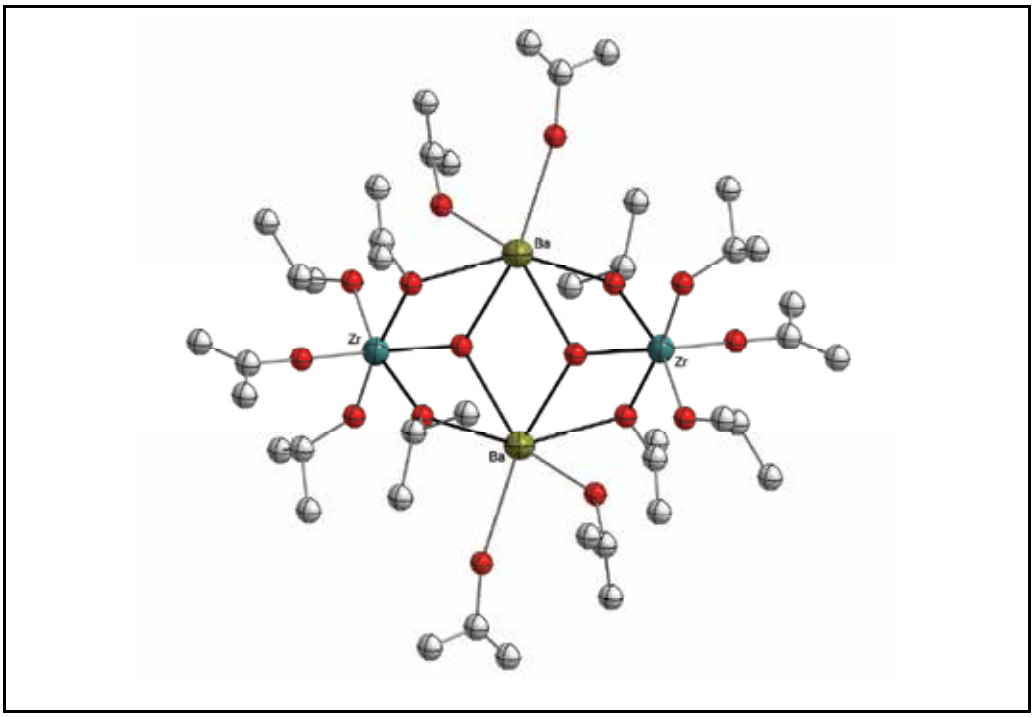

Fig. 1. Molecular structure of $[BaZr(OH)(O^iPr)_5(HO^iPr)_3]_2$ (the H atoms are omitted for clarity).[17b]

4.2. SSP-II

In this case, M and M′ components are in the same stoichiometry in the precursor and final oxide product (Eq. 12).

$$MM'_xLL' \rightarrow MM'_x + L\text{-}L' \quad (12)$$

Moreover, ligands L and L′ are chosen in such a way that react with each other. Because of this phenomenon, final products are well-defined volatiles and the presence of undesired side products is limited. Complex $[Ba\{(\mu\text{-}OR)_2AlEt_2\}_2]$ (where ROH = 2,3-dihydro-2,2-dimethylbenzofuran-7-ol) is an example of SSP-II. Its thermal decomposition leads to $BaAl_2O_4$ spinel-like heterobimetallic oxide ceramic (Fig. 2).[14]

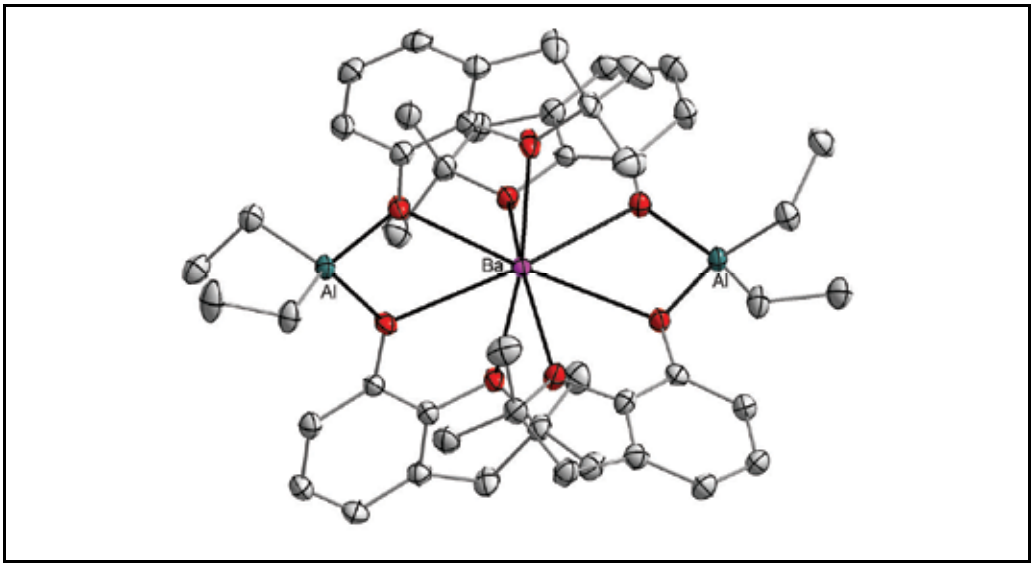

Fig. 2. Molecular structure of $[Ba\{(\mu\text{-}OR)_2AlEt_2\}_2]$ (the H atoms are omitted for clarity).[14]

4.3. SPP-III

Thermolysis of SSP-III leads to the multi phase systems. In this case, from molecular precursors at least two oxide phases are obtained. Although the chemical pathway for such process may be complex, general equation can be presented in this way (Eq. 13).

$$MM'_xLL' \rightarrow MM'_{x-y} + yM' + L\text{-}L' \quad (13)$$

For instance, $[Ca_2Ti(\mu,\eta^2\text{-}OR)_6Cl_2]$[18] (where ROH = $Me_2NCH_2CH_2OH$) (Fig. 3) after thermal decomposition leads to the mixture of double- and monooxides, perovskite $CaTiO_3$ and CaO, respectively.

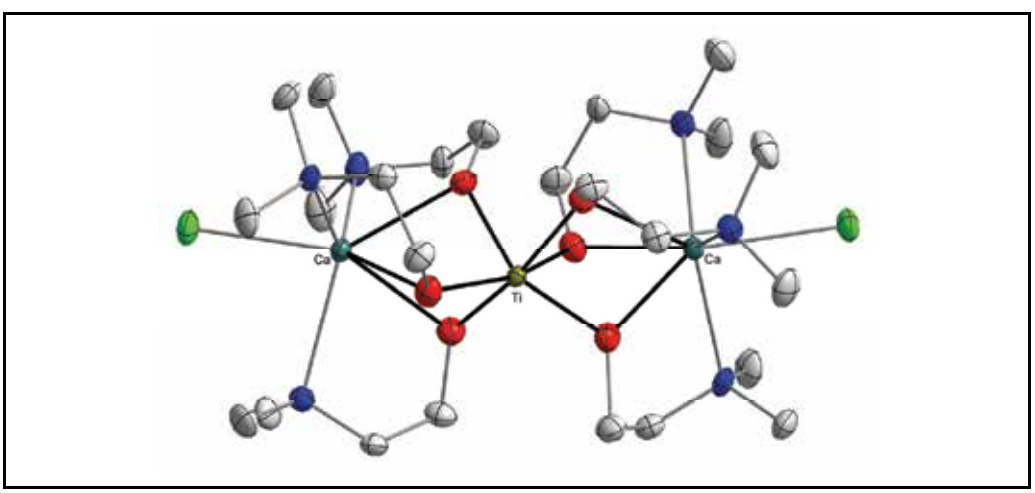

Fig. 3. Molecular structure of $[Ca_2Ti(\mu,\eta^2\text{-}OR)_6Cl_2]$ (the H atoms are omitted for clarity).[18]

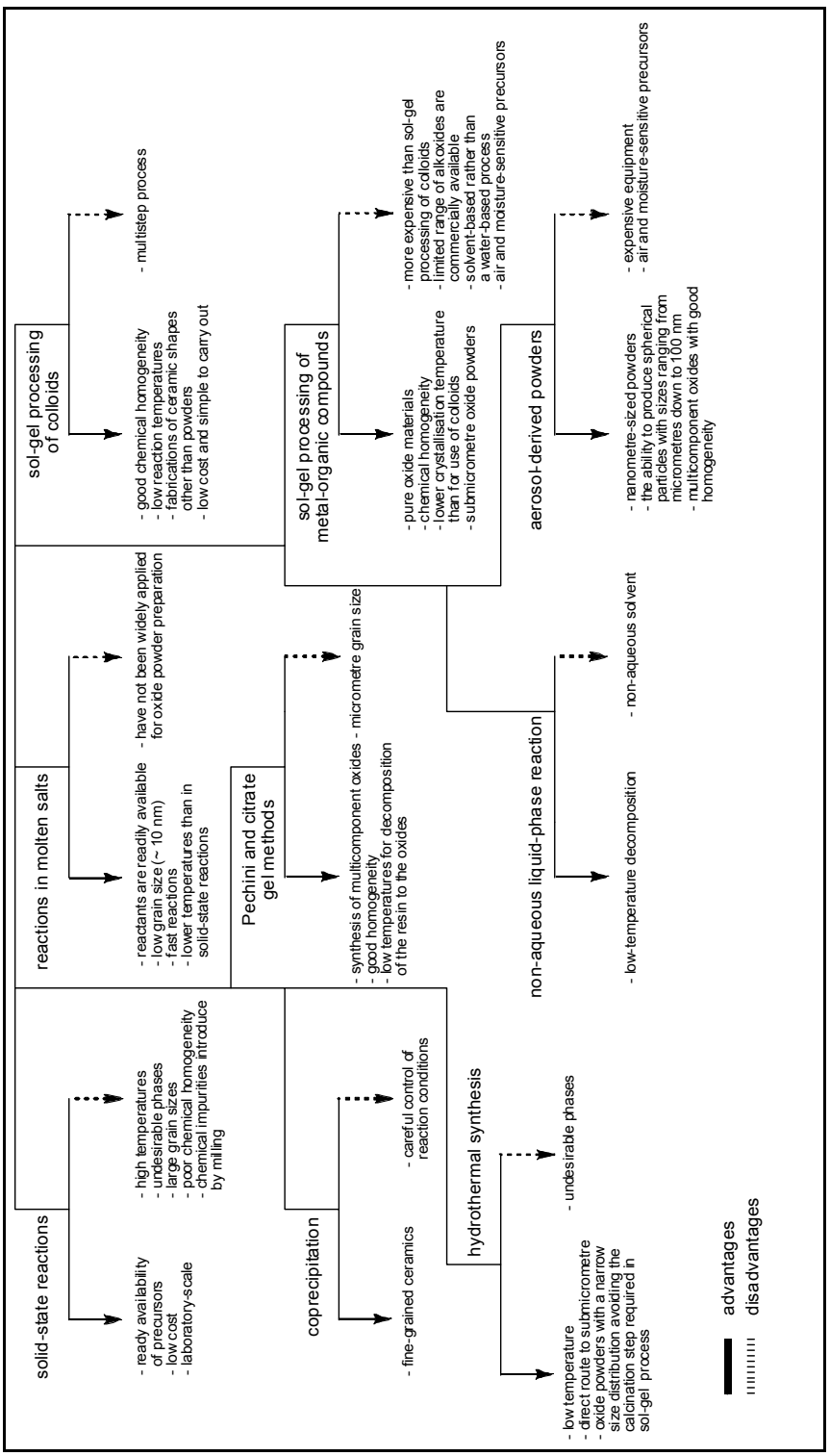

Scheme 3. Applicable routes for preparation of oxide materials.[4a]

5. Alkoxides as the SSPs for Oxides

In the following section we will illustrate the above types of SSPs by examples taken from our studies. These examples are restricted to oxide ceramics, in which only oxide phases are present. The major key point of this discussion will be emphasized on synthetic approach for this kind of materials.

Why do alkoxides and their derivatives are in the center of interest in materials science? Metal alkoxides are inexpensive compounds which are quite easy to obtain in laboratory scale. Because of the close contact of metal-oxygen bonds, they have already prepared, on molecular level, network for oxide materials. Complement of all of these advantages is that alkoxide ligands are easy to removed during thermal treatments leaving stable M-O core. From these point of view, they are perfect candidates for single-source precursors for oxide ceramic materials. Unfortunately, in general these kind of precursors are extremely air and moisture sensitive. For example titanium alkoxides $Ti(OR)_4$ are not easy to store and working with them can be cumbersome, especially with those possessing small OR groups (where R = Me, Et, ^{i}Pr). Oxophilic metal site of $M(OR)_x$ containing small monodentate ligands can be protected against air and moisture decomposition by larger bi- or polydentate ligands for some or all of the alkoxides OR groups. The most popular strategy utilizes functionalized alcohols with additional ether oxygen or amine nitrogen atoms. Such precursors are not only less moisture sensitive. The greater steric demand of the bulky ligands and the increased donor ability of the additional donor atoms are the advantages in forming monomeric or dimeric complexes, which is favourable for instance in the CVD applications.[19]

There are a number of well-known applicable routes for preparation of oxide materials using inorganic and organic precursors. The most common chemical approaches to these are presented in Scheme 3. Among these methods, the most attractive are those involving alkoxides and their derivatives.

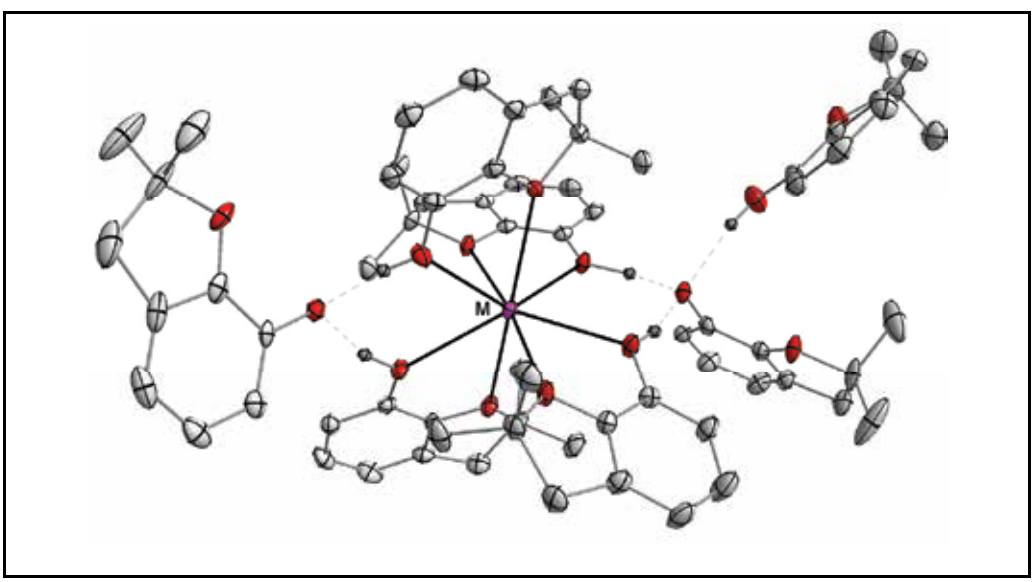

Fig. 4. Molecular structure of $[M(ddbfoH)_4](ddbfo)_2 \cdot ddbfoH$ (where M = Sr^{2+}, Ba^{2+}).[20]

In our research we were mainly interested in heterobi- and heteropolymetallic alkoxides of different transition metals with group 2 elements. As an initial point of this strategy we have obtained well-defined homoleptic alkoxides, which constituted starting materials for further transformations. Group 2 metals create divalent ions and prefer high coordination numbers, e.g. six, eight and higher. For example, the reaction for barium or strontium gave monomeric, ionic complexes in which the central atom is eight-coordinated and surrounded by four chelating ligands and additionally solvated by three RO(H) groups (Fig. 4).

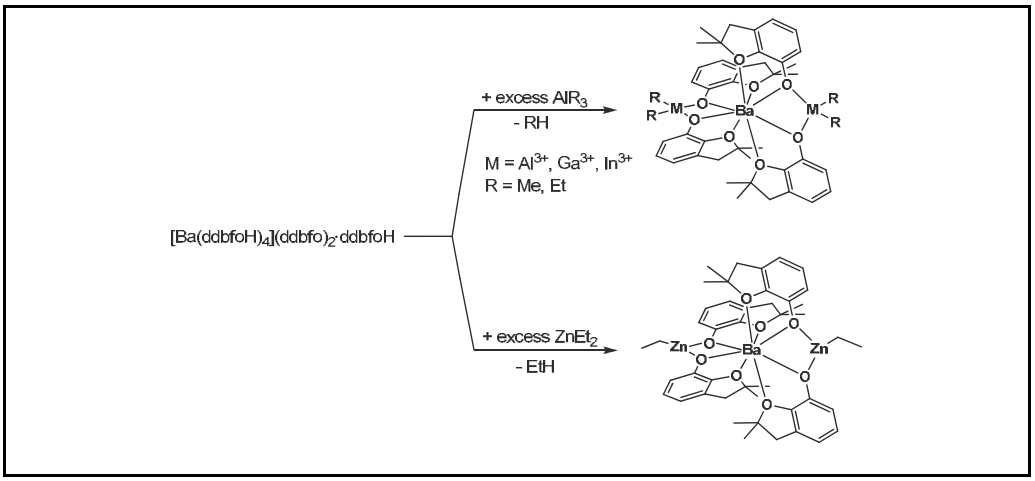

Scheme 4. Syntheses of heterobimetallic barium/group 12 and 13 complexes.[14]

It is worth noting that there are not so many examples of crystallographically characterized homoleptic complexes of these metals in the literature. In the case of the ligands, we have mainly concentrated on chelating functionalized alcohols possessing two or more donor atoms, for example ether-alcohols like 2,3-dihydro-2,2-dimethylbenzofuran-7-ol (ddbfoH), tetrahydrofurfuryl alcohol (thffoH), 2-methoxyethanol ($CH_3OCH_2CH_2OH$) and amine-alcohols, for instance N,N-dimethylethanolamine ($Me_2NCH_2CH_2OH$) etc.

Several studies have shown that starting compounds which possess a protonated hydroxyl group(s) at the metal site are perfect anchor for other organometallic fragments.[14, 21] The concept of the proposed synthetic route is presented in Scheme 4. In general, the driving force for this reactions is an organometallic-driven abstraction of the OH protons from the ROH groups attached to the metal sphere. This leads to the simple alkanes (e.g. methane, ethane etc.) evolution and results in a linkage of RO ligands with appropriate MR_x^+ moieties (where M = Zn^{2+}, Al^{3+}, Ga^{3+}, In^{3+}; R = Me, Et; x = 1, 2).

For monometallic homoleptic SSPs with no free alcohol ligands in metal coordination sphere, a different reaction pathway is observed. For example, oligomeric magnesium or calcium alkoxides which possesses open dicubane geometry (Scheme 2g) do not have any possibility for simple hydrocarbon eliminations. A direct reaction of $[Ca_4(OR)_8]$ (ROH = 2,3-dihydro-2,2-dimethylbenzofuran-7-ol) with $AlMe_3$ in toluene leads to deoligomerization of the starting alkoxide and cocomplexation of $AlMe_3$, forming the molecular dimeric tetranuclear adduct $[Ca(\mu\text{-}OR)\{(\mu\text{-}OR)(\mu\text{-}CH_3)Al(CH_3)_2\}]_2$ shown in Fig. 5.[22]

As mentioned-above, alkoxides have a strong tendency to oligomerization. The oligomeric structure can easily be broken by addition of organometallics or even weak donors to

reaction system. Our previous studies clearly show that the strategy of blocking the bridging alkoxo groups to deoligomerize calcium alkoxides and obtain low-nuclearity species works effectively. The general idea of this phenomenon is presented in Scheme 5. For instance, the addition of THF to oligomeric calcium-aluminium complexes leads to the formation of the molecular six-coordinate adduct (Fig. 6).

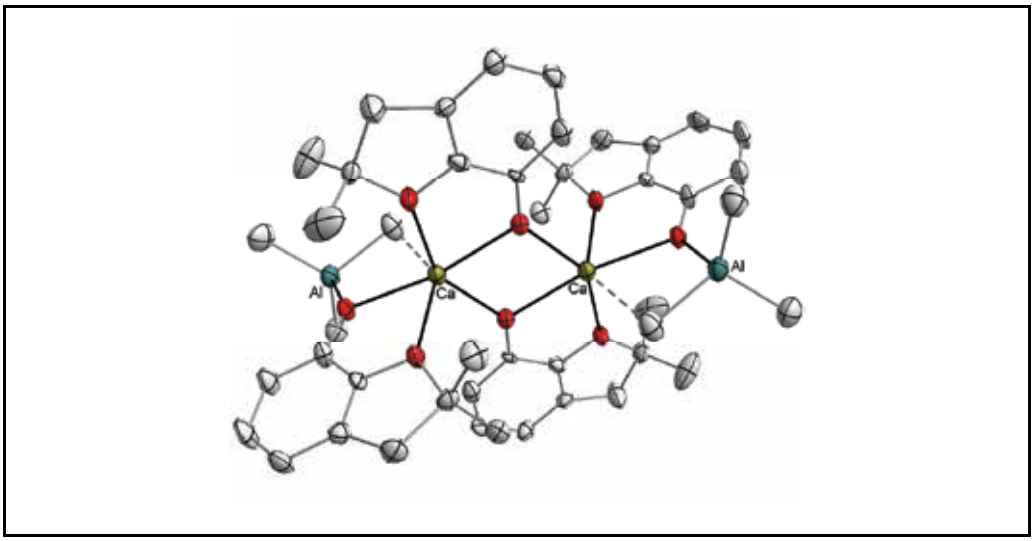

Fig. 5. Molecular structure of $[Ca(\mu\text{-}OR)\{(\mu\text{-}OR)(\mu\text{-}CH_3)Al(CH_3)_2\}]_2$ (the H atoms are omitted for clarity).[22]

These examples demonstrate that the alkoxo groups responsible for oligomerization of metal alkoxides can be easily blocked with organometallic agents and donor solvents to prevent agglomeration.[22]

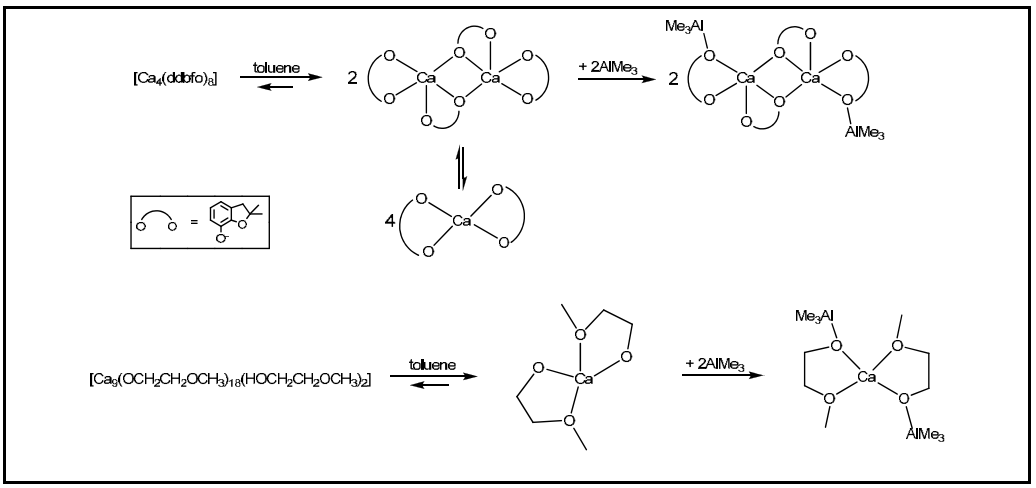

Scheme 5. General idea of blocking alkoxo oxygen atoms by $AlMe_3$.

Interesting group of single-source precursors constitute chloro-alkoxides. Generally chloride-substituted alkoxides are considered as inefficient precursors for metal oxides. One of the disadvantages is that Cl ligands are corrosive agents.

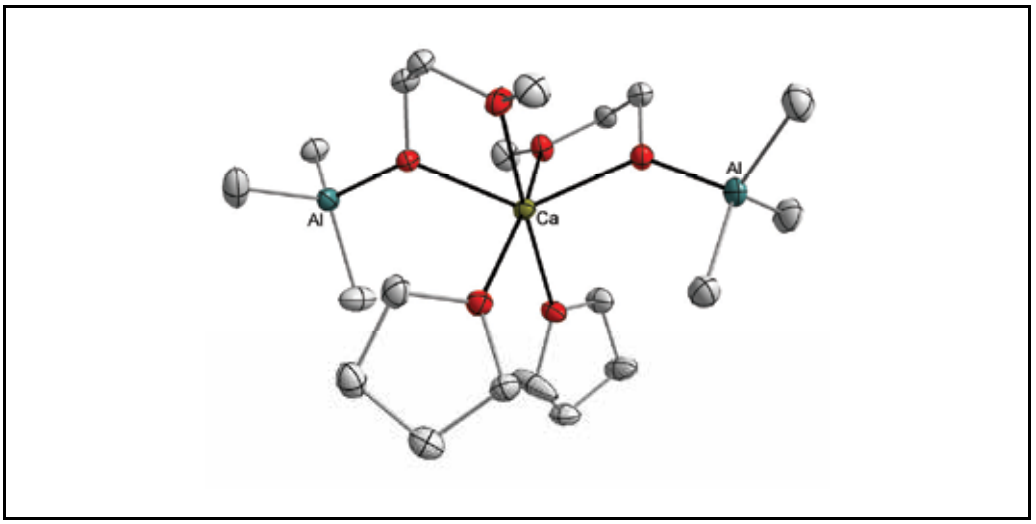

Fig. 6. Molecular structure of $[Ca\{(\mu\text{-}OR)Al(CH_3)_3\}_2(THF)_2]$ (where ROH = $CH_3OCH_2CH_2OH$) (the H atoms are omitted for clarity).

Moreover, in many cases oxide material is contaminated by Cl-products. However, in the literature there are a few examples of chloro-alkoxides utilized as the SSPs for highly pure oxide ceramics.[23] For instance, $[Zn_7(OAc)_{10}(\mu\text{-}OH)_6Cu_5(dmae)_4Cl_4]$ (where dmaeH = (N,N-dimethylamino)ethanol), which was used in the chemical vapor deposition and gave copper-zinc $Cu_5Zn_7O_{12}$ double-oxide and possesses metal to metal stoichiometry fixed on molecular level.[24]

Another efficient and simple strategy involves reaction of cheap organometallic Cp_2MCl_2 (where M = Ti^{4+}, Zr^{4+}, Hf^{4+}) with $M'(OR)_2$ (where M' = Ca^{2+}, Sr^{2+}, Ba^{2+}, Mn^{2+}; ROH = functionalized alcohol) in the presence of alcohol. General idea is presented bellow (Eq. 14).

$$2Cp_2MCl_2 + 4M'(OR)_2 + 8ROH \rightarrow [M'_4M_2(O)Cl_4(OR)_{10}(HOR)_4] + 4CpH + \text{by-product(s)} \qquad (14)$$

In this method formation of M'-Cl bond constitutes the driving force for this reaction. As a source of protons functionalized alcohols, e.g. $CH_3OCH_2CH_2OH$ or $Me_2NCH_2CH_2OH$ can be used. Using this synthetic approach a series of heterobimetallic complexes were obtained (Table 2).[18]

All of these compounds possess interesting molecular structures, especially those with octahedral geometry. Generally, their metallic cores can be described as follows: first, as an octahedron with six metal sites and a μ_6-O^{2-} encapsulated oxygen atom in the central position and each of the triangular faces being capped by a μ_3-oxygen atom from OR group (Fig. 7a). Second motif, as a cube formed by the eight oxygen atoms of the alkoxide groups, with metal cations located outside of the six faces of the cube and O^{2-} anion occupying the central position (Fig. 7b). In third core type, octahedral unit in which each edge of polyhedron is alternatively capped by μ_2-O(alkoxide) groups or μ_2-Cl anions (Fig. 7c).[18]

Although the mentioned-above complexes possess chloride ligands, they are attractive precursors for highly phase pure binary metal oxides. For instance, thermal decomposition of $[Ba_4Ti_2(\mu_6\text{-}O)Cl_4(OCH_2CH_2OCH_3)_{10}(HOCH_2CHOCH_3)_4]$ leads to the mixture of $BaTiO_3$ and $BaCl_2$. Barium dichloride is easily removed by washing the resulting powder with water. Because of the presence of group 2 cations of the precursor, obtaining chloride is stable (ionic bond) at the temperature of perovskite phase appearing.

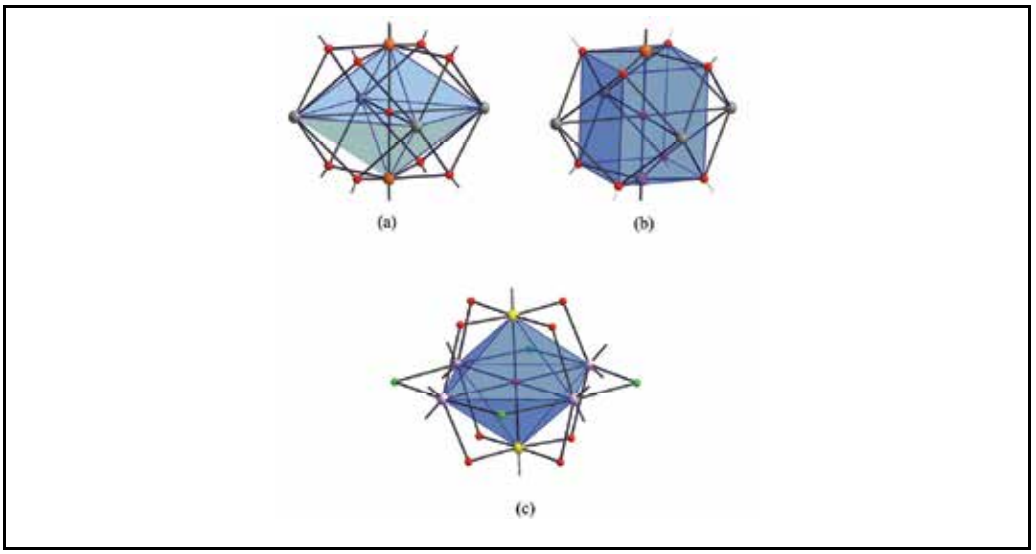

Fig. 7. View of the octahedral cores.

Compound	Ref.
$[Ca_4Ti_2(\mu_6\text{-}O)(\mu_3,\eta^2\text{-}OR)_8(\eta\text{-}OR)_2Cl_4]$	18a
$[Sr_4Hf_2(\mu_6\text{-}O)(\mu_3,\eta^2\text{-}OR)_8(\eta\text{-}OR)_2(\eta\text{-}HOR)_4Cl_4]$	18a
$[Ca_4Zr_2(\mu_6\text{-}O)(\mu\text{-}Cl)_4(\mu,\eta^2\text{-}OR)_8Cl_2]$	18a
$[Sr_4Ti_2(\mu_6\text{-}O)(\mu_3,\eta^2\text{-}OR)_8(\eta\text{-}OR)_2(\eta\text{-}HOR)_2Cl_4]$	18a
$[Ca_4Zr_2Cp_2(\mu_4\text{-}Cl)(\mu\text{-}Cl)_3(\mu_3,\eta^2\text{-}OR)_4(\mu,\eta^2\text{-}OR)_4Cl_2]$	18a
$[CaTiCl_2(\mu,\eta^2\text{-}OR')_3(\eta\text{-}HOR')_3][OR']$	18a
$[Ca_2Ti(\mu,\eta^2\text{-}OR')_6Cl_2]$	18a
$[Mn_4Ti_4(\mu\text{-}Cl)_2(\mu_3,\eta^2\text{-}OR)_2(\mu,\eta^2\text{-}OR)_{10}Cl_6]$	18a
$[Mn_{10}Zr_{10}(\mu_4\text{-}O)_{10}(\mu_3\text{-}O)_4(\mu_3,\eta^2\text{-}OR)_2(\mu,\eta^2\text{-}OR)_{16}(\mu,\eta\text{-}OR)_4(\eta\text{-}OR)_2Cl_8]$	18a
$[Ba_4Ti_2(\mu_6\text{-}O)Cl_4(OR)_{10}(HOR)_4]$	18b
$[Ba_4Zr_2(\mu_6\text{-}O)Cl_4(OR)_{10}(HOR)_4]$	18b
$[Ba_4Hf_2(\mu_6\text{-}O)Cl_4(OR)_{10}(HOR)_4]$	18b

ROH = $CH_3OCH_2CH_2OH$; R'OH = $Me_2NCH_2CH_2OH$

Table 2. Examples of series heterometallic chloro-alkoxides obtained from Cp_2MCl_2 precursors.

The above presented alkoxide complexes seem to be natural candidates for oxide ceramic materials. They have already designed oxygen-bound units that bring metal atoms close one to another. Furthermore, they also have a fixed ratio of metals appropriate for desired oxide

systems. It is worth noting here, that compounds possessing steric ramified ligands, e.g. aryloxo, decompose in much more complicated way, compare to alkoxides with small RO groups (e.g. Me, Et, ^{i}Pr etc.).

In general, metal complexes with chelating and bulky aryloxo ligands are non-volatile and much more stable in contrast to monodentate alkoxides. Hence, thermal decomposition of metal aryloxo derivatives is much more complex and usually a long lasting process. In each case the decomposition is multi-step with mass losses that do not clearly correspond to an extrusion of a specific number of leaving ligands.[4a, 14]

In Table 3, there are a few examples of synthesized SSPs and corresponding with them mono- and double-oxide ceramic materials.

SSP	Oxide(s)	Ref.
$[Me_2Al(\mu\text{-ddbfo})]_2$[a]	Al_2O_3	25
$[Me_2In(\mu\text{-ddbfo})]_2$[a]	In_2O_3	25
$[Ti_2(\mu\text{-ddbfo})_2(ddbfo)_6]$[a]	TiO_2	26, 27
$[Ti(O^iPr)_2(maltolato)_2]$[b]	TiO_2	26, 28
$[(VO)Cl_x(OCH_3)_y]$[c]	V_2O_5	23a
$[Ba\{(\mu\text{-ddbfo})_2AlMe_2\}_2]$[a]	$BaAl_2O_4$	14
$[Ba\{(\mu\text{-ddbfo})_2GaMe_2\}_2]$[a]	$BaGa_2O_4$	14
$[Ca\{(\mu\text{-}OCH_2CH_2OCH_3)(\mu\text{-Me})(AlMe_2)\}_2]$	$CaAl_2O_4$	22, 25
$[Ca\{(\mu\text{-}OCH_2CH_2OCH_3)(AlMe_3)\}_2(THF)_2]$	$CaAl_2O_4$	22, 25
$[CaTiCl_2(\mu,\eta^2\text{-}OCH_2CH_2NMe_2)_3(\eta\text{-}OCH_2CH_2NMe_2)_3][OCH_2CH_2NMe_2]$	$CaTiO_3$	18a
$[Ca_2Ti(\mu,\eta^2\text{-}OCH_2CH_2NMe_2)_6Cl_2]$	$CaTiO_3 + CaO$	18a
$[MnAl(acac)_3(O^iPr)_4(OAc)]$[d]	$MnAl_2O_4$	29
$[CoAl(acac)_3(O^iPr)_4(OAc)]$[d]	$CoAl_2O_4$	29
$[ZnAl(acac)_3(O^iPr)_4(OAc)]$[d]	$ZnAl_2O_4$	29
$[NiAl_2(acac)_4(O^iPr)_4]$[d]	$NiAl_2O_4$	30
$[MgAl_2(O^iPr)_8]$	$MgAl_2O_4$	31
$[MgAl_2(O^tBu)_8]$	$MgAl_2O_4$	31
$[Nd\{Al(O^iPr)_4\}_3(^iPrOH)]$	$NdAlO_3 + Al_2O_3$	32
$[Ba_4Ti_2(\mu_6\text{-O})Cl_4(OCH_2CH_2OCH_3)_{10}(HOCH_2CHOCH_3)_4]$	$BaTiO_3$	18b
$[Ba_4Zr_2(\mu_6\text{-O})Cl_4(OCH_2CH_2OCH_3)_{10}(HOCH_2CHOCH_3)_4]$	$BaZrO_3$	18b
$[Ba_4Hf_2(\mu_6\text{-O})Cl_4(OCH_2CH_2OCH_3)_{10}(HOCH_2CHOCH_3)_4]$	$BaHfO_3$	18b
$[Ba\{(\mu\text{-ddbfo})_2InMe_2\}_2]$[a]	$BaIn_2O_4$	25
$[Sr\{(\mu\text{-ddbfo})_2AlMe_2\}_2]$[a]	$SrAl_2O_4$	25

[a]ddbfoH = 2,3-dihydro-2,2-dimethylbenzofuran-7-ol; [b]maltol = 3-hydroxy-2-methyl-4H-pyran-4-one); [c](x + y) = 4; [d]acac = acetylacetonato.

Table 3. Examples of various oxide ceramic materials derived from SSPs.

6. Conclusion

In this chapter, we have shown that metal alkoxides are extremely attractive starting materials for oxide ceramics. They constitute so-called single source precursors (SSPs), which major advantage is that their thermal transitions give highly pure materials, destitute

undesired oxide phases and organic contaminations. Because of fixed metals ratio on molecular level, final materials have specific and the same stoichiometry as starting precursor. Due to the alkoxo groups are quite easy to remove during thermal treatments, it is possible to obtain appropriate oxides in lower temperatures in contrast to conventional methods. In view of use flexibility of alkoxides, they have successfully been used in various deposition and decomposition techniques giving ultra thin layers, nanopowders and other shapes depending on potential applications.

7. References

1. (a) Bradley, D. C.; Mehrotra, R. C.; Rothwell, I. P. & Singh, A. (2001). *Alkoxo and Aryloxo Derivatives of Metals*, Academic Press, ISBN-10: 0-12-124140-8, ISBN-13: 978-0-12-124140-7, London. (b) Turova, N. Y.; Turevskaya, E. P.; Kessler, V. G. & Yanovskaya, M. I. (2002). *The Chemistry of Metal Alkoxides*, Kluwer Academic Publisher, ISBN-10: 0792375211, ISBN-13: 978-0792375210, USA.
2. Veith, M. (2002). *Journal of Chemical Society, Dalton Transactions*, 12, 2405-2412.
3. Bradley, D. C. (1958). *Nature*, 182, 1211-1214.
4. (a) Szafert, S.; John, Ł.; Sobota, P. (2008). *Dalton Transactions*, 46, 6509-6520. (b) Starikova, Z. A.; Yanovsky, A. I.; Turevskaya, E. P. & Turova, N. Ya. (1997). *Polyhedron*, 16, 967-974. (c) Goel, S. C.; Matchett, M. A.; Chiang, M. Y. & Buhro, W. E. (1991). *Journal of the American Chemical Society*, 113, 1844-1845. (d) Evans, W. J.; Dominguez, R. & Hanusa, T. P. (1986). *Organometallics*, 5, 1291-1296. (e) Evans, W. J.; Sollberger, M. S. & Hanusa, T. P. (1988). *Journal of the American Chemical Society*, 110, 1841-1850. (f) Errington, R. J. (1998). Conference communication. (g) Hermann, W. A.; Bogdanovic, S.; Behm, J. & Denk, M. (1992). *Journal of Organometallic Chemistry*, 430, C33-C38. (h) Chisholm, M. H.; Folting, K.; Hampden-Smith, M. & Smith, C. A. (1987). *Polyhedron*, 6, 1747-1755. (i) Power, M. B.; Cleaver, W. M.; Apblett, A. W. A.; Barron, R. & Ziller, J. W. (1992). *Polyhedron*, 11, 477-486. (j) Janas, Z.; Sobota, P.; Klimowicz, M.; Szafert, S.; Szczegot, K. & Jerzykiewicz, L. B. (1997). *Journal of Chemical Society, Dalton Transactions*, 20, 3897-3902. (k) Evans, W. J.; Boyle, T. J. & Ziller, J. W. (1993). *Journal of the American Chemical Society*, 115, 5084-5092. (l) Schmid, R.; Mosset, A. & Galy, J. (1991). *Acta Crystallographica*, C47, 750-752. (m) Atwood, D. A.; Jegier, J. A.; Liu, S.; Rutherford, D.; Wie, P. & Tucher, R. C. (1999). *Organometallics*, 18, 976-981. (n) Cotton, F. A.; Diebold, M. P. & Roth, W. J. (1985). *Inorganic Chemistry*, 24, 3509-3510. (o) Chisholm, M. H.; Folting, K.; Huffman, J. C. & Tatz, R. J. (1984). *Journal of the American Chemical Society*, 106, 1153-1154. (p) Goel, S. C.; Chiang, M. Y. & Buhro, W. E. (1990). *Inorganic Chemistry*, 29, 4640-4646. (r) Poncelet, O.; Hubert-Pfalzgraf, L. G.; Daron, J.-C. & Astier, R. (1989). *Journal of Chemical Society, Chemical Communications*, 23, 1846-1848. (s) Bradley, D. C.; Chudzynska, H.; Hursthouse, M. B.; Motevalli, M. & Ruowen W. (1994). *Polyhedron*, 13, 1-6. (t) Beattie, J. K.; Hambley, T. W.; Klepetko, J. A.; Masters, A. F. & Turner, P. (1998). *Chemical Communications*, 1, 45-46. (u) Evans, W. J.; Sollberger, M. S. & Ziller, J. W. (1993). *Journal of the American Chemical Society*, 115, 4120-4127. (v) Mehrotra, R. C. & Chandler, G. (1962). *Journal of the Indian Chemical Society*, 39, 235-240. (w) van der Boom, M. E.; Lion, S.-Y.; Ben-David, Y.; Shimon, L. J. W. & Milstein, D. (1998). *Journal of the American Chemical Society*, 120, 6531-6541.

5. Drake, S. R.; Streib, W. E.; Folting, K.; Chisholm, M. H. & Caulton, K. G. (1992). *Inorganic Chemistry*, 31, 3205-3210.
6. Szilard, B. (1906). *Electrochemistry*, 12, 373-378.
7. Lehmkhul, H. & Eisenbach, W. (1975). *Annual Chemistry*, 4, 672-691.
8. Kovsman, E. P.; Andruseva, S. I.; Solovjeva. L. I.; Fedyaev, V. I.; Adamova, M. N. & Rogova, T. V. (1994). *Journal of Sol-Gel Science and Technology*, 2, 61-66.
9. Wu, Y.; Ho, Y. C.; Lin, C. C. & Gau, H. M. (1996). *Inorganic Chemistry* 35, 5948-5952.
10. Mehrotra, R. C. (1981). *Coordination Chemistry Reviews*, 21, 113-121.
11. (a) Mehrotra, R. C. (1954). *Journal of the Indian Chemical Society*, 31, 904-910. (b) Mehrotra, R. C. (1953). *Journal of the Indian Chemical Society*, 30, 585-591. (c) Bradley, D. C.; Chakravarti, B. N.; Chatterjee, A. K.; Wardlaw, W. & Whitley, A. (1958). *Journal of Chemical Society*, 99.
12. (a) Boyle, T. J.; Hernandez-Sanchez, B. A.; Baros, C. M.; Brewer, L. N. & Rodriguez, M. A. (2007). *Chemistry of Materials*, 19, 2016-2026. (b) Matchett, M. A.; Chiang, M. Y. & Buhro, W. E. (1990). *Inorganic Chemistry*, 29, 358-360. (c) Chisholm, M. H.; Huffman, J. C.; Kirkpatric, J.; Leonelli, J. & Folting, K. (1981). *Journal of the American Chemical Society*, 103, 6093-6099.
13. (a) Neumüller, B. (2003). *Chemical Society Reviews*, 32, 50-55. (b) Basharat, S.; Carmalt, C. J.; Barnett, S. A.; Tocher, D. A. & Davies, H. O. (2007). *Inorganic Chemistry*, 46, 9473-9480. (c) Basharat, S.; Betchley, W.; Carmalt, C. J.; Barnett, S.; Tocher, D. A. & Davies, H. O. (2007). Organometallics, 26, 403-407. (d) Jerzykiewicz, L. B.; Utko, J. & Sobota, P. (2006). *Organometallics*, 25, 4924-4926. (e) Sobota, P.; Utko, J.; Sztajnowska, K.; Ejfler, J. & Jerzykiewicz, L. B. (2000). *Inorganic Chemistry*, 39, 235-239.
14. John, Ł.; Utko, J.; Szafert, S.; Jerzykiewicz, L. B.; Kępiński, L. & Sobota, P. (2008). *Chemistry of Materials*, 20, 4231-4239.
15. (a) Segal, D. (1997). *Journal of Materials Chemistry*, 7, 1297-1305. (b) Moulson, A. J. & Herbert, J. M. *Electroceramics: Materials, Properties and Applications*, Chapman and Hall, London, 1990, p. 86.
16. Veith, M. (2002). *Journal of Chemical Society, Dalton Transactions*, 12, 2405-2412.
17. (a) Veith, M.; Mathur, S.; Lecerf, N.; Huch, V.; Decker, T.; Beck, H. P.; Eiser, W. & Haberkorn, R. (2000). *Journal of Sol-Gel Science and Technology*, 15, 145-158. (b) Veith, M.; Mathur, S.; Huch, V. & Decker, T. (1998). *European Journal of Inorganic Chemistry*, 9, 1327-1332.
18. (a) Sobota, P.; Drąg-Jarząbek, A.; John, Ł.; Utko, J.; Jerzykiewicz, L. B. & Duczmal, M. (2009). *Inorganic Chemistry*, 48, 6584-6593. (b) Drąg-Jarząbek, A.; Sobota, P., submitted.
19. McElwee-White, L. (2006). *Dalton Transactions*, 45, 5327-5333.
20. Utko, J.; Szafert, S.; Jerzykiewicz, L. B. & Sobota, P. (2005). *Inorganic Chemistry*, 44, 5194-5196.
21. (a) Singh, S. & Roesky, H. W. (2007). *Journal of Chemical Society, Dalton Transactions*, 14, 1360-1370. (b) Sharma, M.; Singh, A. & Mehrotra, R. C. (2002). *Synthesis and Reactivity in Inorganic and Metal-Organic Chemistry*, 32, 1223-1233.
22. Utko, J.; Ejfler, J.; Szafert, S.; John, Ł.; Jerzykiewicz, L. B. & Sobota, P. (2006). *Inorganic Chemistry*, 45, 5302-5306.

23. (a) Epifani, M.; Andreu, T.; Arbiol, J.; Diaz, R.; Siciliano, P. & Morante, J. R. (2009). *Chemistry of Materials*, 21, 5215-5221. (b) Epifani, M.; Andreu, T.; Magana, C. R.; Arbiol, J.; Siciliano, P.; D'Arienzo, M.; Scotti, R.; Morazzoni, F. & Morante, J. R. (2009). *Chemistry of Materials*, 21, 1618-1626. (c) Vioux, A. (1997). *Chemistry of Materials*, 9, 2292-2299. (d) Chang, S.-M.; Doong, R.-A. (2006). *The Journal of Physical Chemistry B*, 110, 20808-20814. (e) Tang, J.; Fabbri, J.; Robinson, R. D.; Zhu, Y.; Herman, I. P.; Steigerwald, M. L. & Brus, L. E. (2004). *Chemistry of Materials*, 16, 1336-1342. (f) de A. A. Soler-Illia, G. J.; Sanchez, C.; Lebeau, B. & Patarin, J. (2002). *Chemical Reviews*, 102, 4093-4138. (g) Crepaldi, E. L.; de A. A. Soler-Illia, G. J.; Grosso, D.; Cagnol, F.; Ribot, F. & Sanchez, C. (2003). *Journal of the American Chemical Society*, 125, 9770-9786.
24. Hamid, M.; Tahir, A. A.; Mazhar, M.; Zeller, M. & A. D. Hunter (2007). *Inorganic Chemistry*, 46, 4120-4127.
25. John, Ł. (2008). PhD Dissertation: *Alkoxo metal complexes as precursors for new materials.* Faculty of Chemistry, University of Wrocław, Poland.
26. John, Ł.; Krauzy-Dziedzic, K.; Drąg-Jarząbek, A. & Sobota, P. (2010), submitted.
27. Krauzy-Dziedzic, K.; Ejfler, J.; Szafert, S. & Sobota, P. (2008). *Dalton Transactions*, 19, 2620-2626.
28. Sobota, P.; Przybylak, K.; Utko, J.; Jerzykiewicz, L. B.; Pombeiro, A. J. L.; Guedes da Silva, M. F. C. & Szczegot, K. (2001). *Chemistry – A European Journal*, 7, 951-958.
29. Seisenbaeva, G. A.; Suslova, E. V.; Kritikos, M.; Kessler, V. G.; Rapenne, L.; Andrieux, M.; Chassagneux, F. & Parola, S. (2004). *Journal of Materials Chemistry*, 14, 3150-3157.
30. Kessler, V. G.; Seisenbaeva, G. A. & Parola, S. (2004). *Journal of Sol-Gel Science and Technology*, 31, 63-66.
31. Mathur, S.; Veith, M.; Ruegamer, T.; Hemmer, E. & Shen, H. (2004). *Chemistry of Materials*, 16, 1304-1312.
32. Veith, M.; Mathur, S.; Lecerf, N.; Bartz, K.; Heintz, M. & Huch, V. (2000). *Chemistry of Materials*, 12, 271-274.

5

New ceramic microfiltration membranes from Tunisian natural materials: Application for the cuttlefish effluents treatment

Sabeur Khemakhem[1], André Larbot[2], Raja Ben Amar[1]
[1-]*Université de Sfax, Laboratoire des Sciences de Matériaux et Environnement, Faculté des Sciences de Sfax, Route de Soukra Km 4, 3038, Sfax, Tunisie.*
[2-]*Université de Montpellier II, Institut Européen des Membranes, UMR 5635-CNRS, ENSCM, UMII, 1919 Route de Mende 34293 Montpellier Cedex5, France.*

1. Introduction

Interest in separation by the use of membranes has rapidly increased during the last 10 - 15 years. The membrane technologies are utilized in various fields: chemistry, food, biotechnology and recently waste water treatment (Cham & Brownstein, 1991). For economic consideration, a great deal of research has been devoted to the development of new type of inorganic membranes, which have displayed improved resistance to heat, chemicals and corrosion. Rapid development and innovation have already been realised in this area (Uhlhorn et al., 1987; Zespalis et al., 1989; Cot, 1998). Clay minerals have well-known structural adsorption, rheological and thermal properties (Jones & Galan, 1988; Pérez, 1994). Research on clay as a membrane material has concentrated mainly on pillared clays (Mishra & Parida, 1997; Cool et al., 1997). Studies of membranes prepared entirely from clay have just started (Messaoudi et al., 1995 ; Ishiguro et al., 1995; Le Van Mao et al., 1999; Rakib et al., 2000). The industry of conservation of sea products is very important in Tunisia. It produces a great amount of waste water which is generally rejected in the littoral and then is responsible for an enormous pollution, by supporting the eutrophication phenomenon (Dégrement, 1978). Before freezing, the cuttlefish must be washed to eliminate black colour caused by the ink contained in the animal bag, resulting in highly coloured wastewater (Abdelmouleh, 1997).

In this study, we investigate the development of ceramic membranes based on Tunisian natural materials which are in abundance and need lower firing temperature in comparison with metal oxide materials. The prepared microfiltration membranes were used for the treatment and the decoloration of cuttlefish effluent.

New microfiltration membranes from Tunisian natural materials are obtained using ceramic method. Paste from Tunisian silty marls refereed (M_{11}) is extruded to elaborate a porous tubular configuration used as supports. The support heated at 1190°C, shows an average pore diameters and porosity of about 9.2µm and 49 % respectively. The properties in term of mechanical and corrosion resistances are very interesting. The elaboration of the layer based on Tunisian clay refereed (JM_{18}) is performed by slip casting method. The heating treatment at 900°C leads to an

average pore size of 0.18µm. The water permeability determined of this membrane is 867 $l.h^{-1}.m^{-2}.bar^{-1}$. This membrane can be used for crossflow microfiltration. The application to the cuttlefish effluent clarification shows an important decrease of turbidity (inferior to 1 NTU) and chemical organic demand (COD) values (retention rate of about 65%). So, it seems that the prepared membrane is suitable for such waste water treatment.

2. Experimental results

Microfiltration ceramic membranes were developed and prepared in the laboratory. They consist of a clay skin layer prepared by slip-casting method (Guizard t al., 1997) deposited on a silty marls support.

2.1 Support shaping and characterisation:

For this study, the supports were prepared from Tunisian silty marls (M_{11}). The chemical composition of these materials is shown in Table 1.

Elements (%)	SiO_2	Al_2O_3	Fe_2O_3	CaO	MgO	Na_2O	K_2O	TiO_2
M_{11}	31.61	10.38	6.53	24.17	19.92	2.21	3.43	1.55

Table 1. Composition of silty marls (M_{11}).

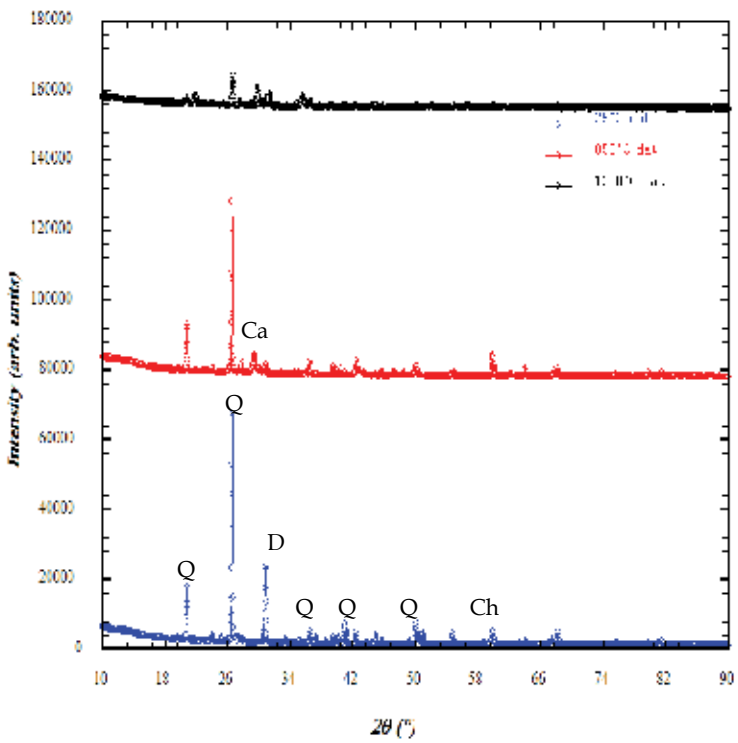

Fig. 1. X-ray diffractograms of the silty marls sample at different temperatures (Q=quartz, Ca=calcite, Ch=chlorite, D=dolomite).

The chemical analysis reveals that this kind of silty marls is essentially formed with a great amount of silica and calcium oxide. Figure 1 presents the XRD patterns of raw silty marls, it shows that Quartz (Q) is the main crystalline mineral present in this powder.
The particle size analysis of the powder after crushing for 2 h with the assistance of a planetary crusher at a rate of 250 revolutions /min and calibrated with 100µm was determined using a Particle Sizing Systems (Inc. Santa Barbara, Calif., USA Model 770 AccuSizer). The particle diameters range varied from 0.5 to 54µm. (Fig 2).

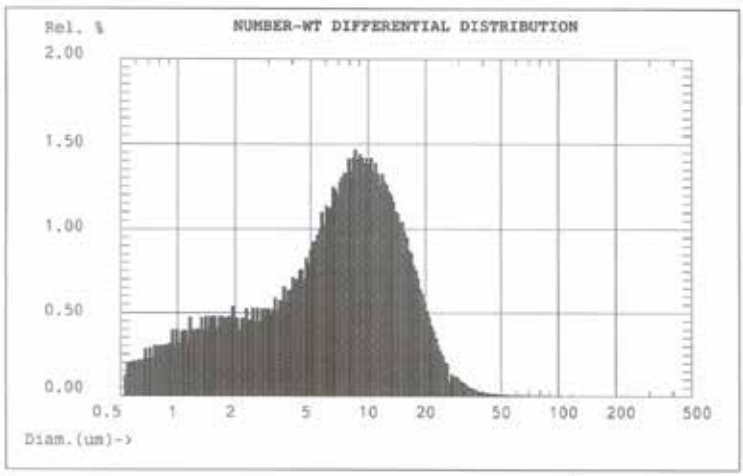

Fig. 2. Silty marls (M_{11}) particle-size distribution.

Plastic pastes are prepared from ceramic powder of silty marls mixed with organic additives:

- 4% w/w of Amijel: pregelated starch, as plasticizer (Cplus 12072, cerestar).
- 4% w/w of Methocel: cellulose derivative, as binder (The dow chemical company).
- 8% w/w of starch of corn as porosity agent (RG 03408, Cerestar).
- 25% w/w of water.

The rheological properties must be studied to obtain a paste allowing shaping by extrusion process (Khemakhem et al., 2006). Figure 3 shows the different configurations of tubes extruded in our laboratory (Two monochannel of different diameter and one multichannel tube).

Fig. 3. A photograph of variety of configurations of porous ceramic supports.

Thermogravimetric analysis (TGA) and differential scanning calorimetry (DSC) were performed with simultaneous DSC-TGA 2960 TA instrument. The sample was heated at room temperature to 1250°C at a rate of 5°C/min under static atmospheric conditions. Two endothermic peaks were detected (Fig. 4). First peak appears at 51.38°C, due to a weight loss of 1.81% of the initial weight. It corresponds to the departure of water (moisture or adsorption) due to attraction on the surface of the sample and zeolitic water inserted between the layers or in the cavities of the crystalline structure. Second peak which maximum appears toward 749,87°C corresponds to the dehydroxylation.

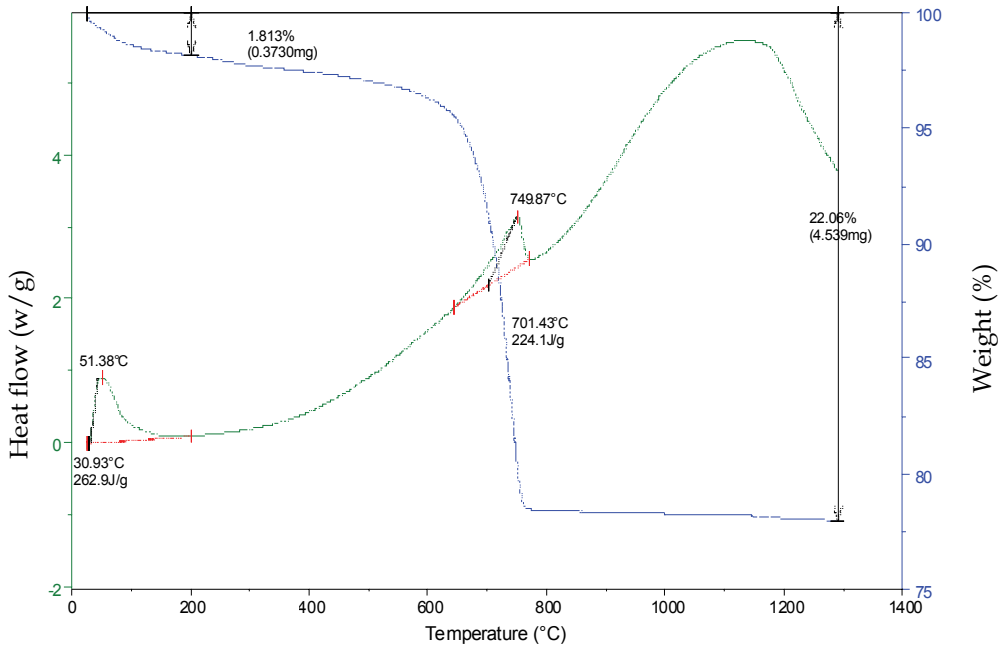

Fig. 4. Thermal analysis curve: DSC and TGA for silty marls powder.

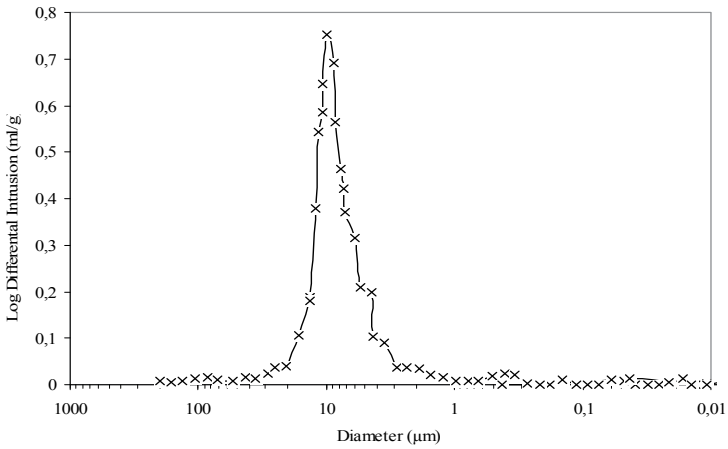

Fig. 5. Pore diameters of the silty marls supports.

Sintering experiments of the support were carried out in air. Two steps has been realised: the first for the elimination of organic additives at 250°C, and the second for the sintering at 1190°C. The temperature-time schedule not only affects the pore diameters and porous volume of the final product but also determines the final morphology and mechanical strength. By controlling the sintering temperature of the ceramic, it is possible to increase the pore size and to obtain a higher mechanical strength. We have also observed that the obtained silty marls support presents the highest mean pore diameter for the highest mechanical strength: The support fired at 1190°C and characterised by mercury porosimetry showed mean pore diameters and porosity of about 9.2µm and 49% respectively (Fig.5).

Powders	Temperature (°C)	Pore size (µm)	Porous Volume (%)
Crushed during one	1160	9.6	58
hour and calibrated	1170	10.9	56
with 125 µm	1180	12.8	53
	1190	14.3	52
	1200	16.5	51
Crushed during two	1160	5.9	52
hours and calibrated	1170	7.3	50
with 100 µm	1180	8.5	49
	1190	9.2	49
	1200	12.5	46

Table 2. Variation of pore size and porous volume according to the powder particle sizes for the silty marls (M11).

It can also be observed that the porosity and the pore size parameters are strongly dependent on the sintering temperature and particle size of the powders (Table 2).

2.2. Membrane shaping and characterisation:

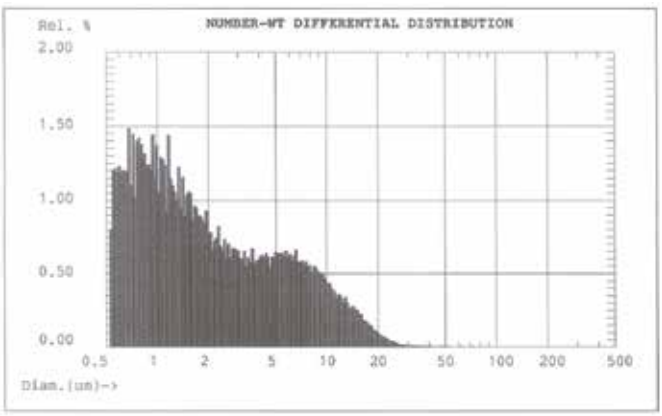

Fig. 6. Clay (JM_{18}) particle-size distribution.

The material used for the membrane preparation is a Tunisian clay powder (JM_{18}) taken from the area of Sidi Bouzid (Central Tunisia). This powder is crushed for 4 hours with a planetary crusher at 250 revolution/min and calibrated with 50µm. The obtained particle diameters range from about 0.5 to 23µm. (Fig 6).
The chemical composition of the clay (JM_{18}) is shown in Table 3. It reveals that this material is essentially formed with a large amount of silica 62.64%.

Elements (%)	SiO_2	Al_2O_3	FeO_3	MgO	Na_2O	K_2O	Mn_2O_3	SO_3	Loss on the ignition
JM_{18}	62.64	17.09	8.5	0.07	0.32	4.8	0.02	0.4	6.16

Table 3. Composition of clay (JM_{18}).

For preparing a microfiltration layer with JM_{18}, the suspended powder technique was used. A defloculated slip was obtained by mixing 5% w/w of JM_{18}, 30% w/w of Polyvinyl alcohol (PVA) (12% w/w aqueous solution) as binder and water (65% w/w). The thickness of microfiltration layer can be controlled by the percentage of the clay powder added to the suspension and the deposition time.

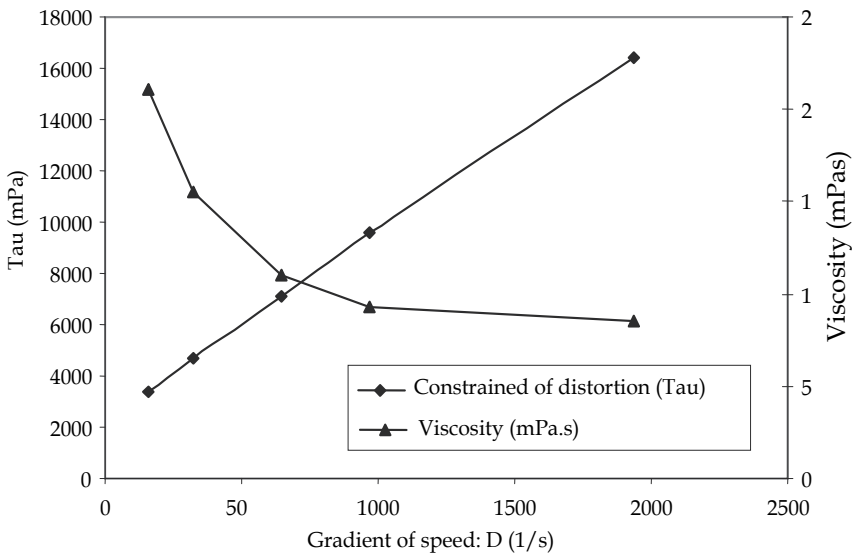

Fig. 7. Evolution of the stress (τ) and the viscosity (µ) vs. deformation of clay (JM 18) slip.

The viscosity of the slip elaborated according to the protocol described previously has been studied right before deposition. The used viscosimeter (LAMY, TVe-05) permits to use 5 speeds of rotation for the determination of the dynamic viscosity of the substance to characterize.
Figure 7 shows the rheogram of the slip used. It is done by the curve of schear stress (τ) versus speed of rotation (D). The slip has a plastic behaviour of Bingham, controlled by the

presence of PVA; the value of the limiting shear stress is 4 mPa. Such behaviour permits the maintenance of particles in a stable suspension.
The deposition of the slip on the M_{11} support was performed by slip casting using a deposition time between 10 and 15 min. After drying at room temperature for 24h. The clay membrane was sintered at 900°C for 2h, after debonding at 250°C for 1h.
Total porous volume and pore size distribution are measured by Mercury porosimetry. This technique relies on the penetration of mercury into a membrane's pores under pressure. The intrusion volume is recorded as a function of the applied pressure and then the pore size was determined. The pore diameters measured were centered near 0.18µm (Fig. 8).

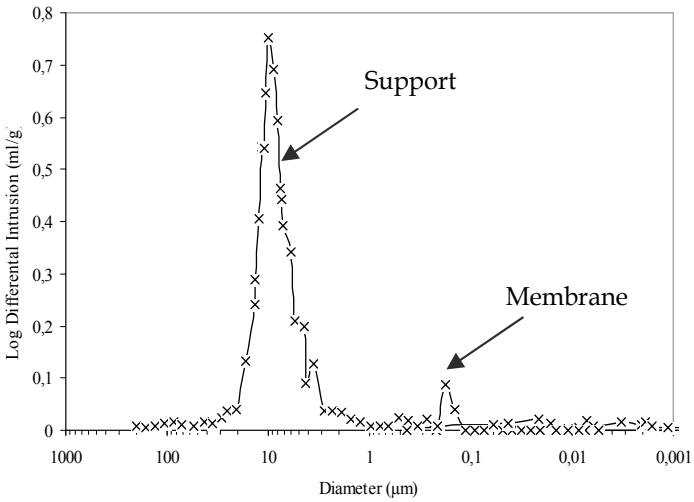

Fig. 8. Pore diameters of the clay (JM_{18}) membrane.

The pore size in the microfiltration layer can also be varied using powders with different particle size distributions.
Different microfiltration membranes with different layers thickness (between 5 and 50µm) were prepared. SEM (scanning electron microscopy) images of the resulting membranes are shown in Figure 9. This figure gives information on the texture of the elaborated membrane surface. A defect free membrane was only obtained for membrane thickness less than 10µm (in order to 7µm).

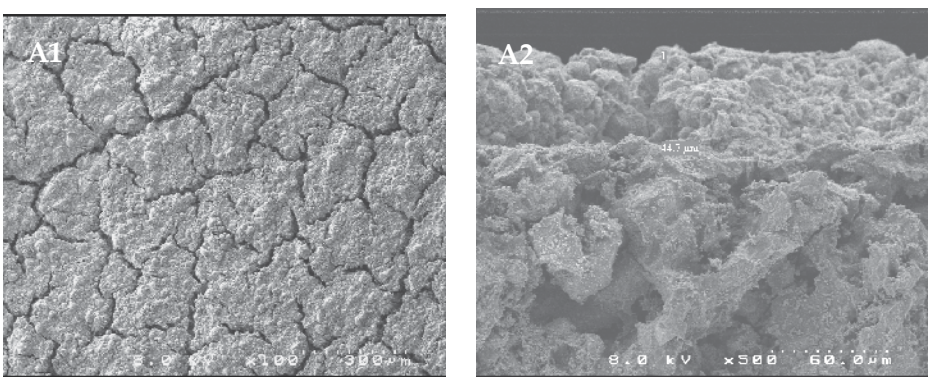

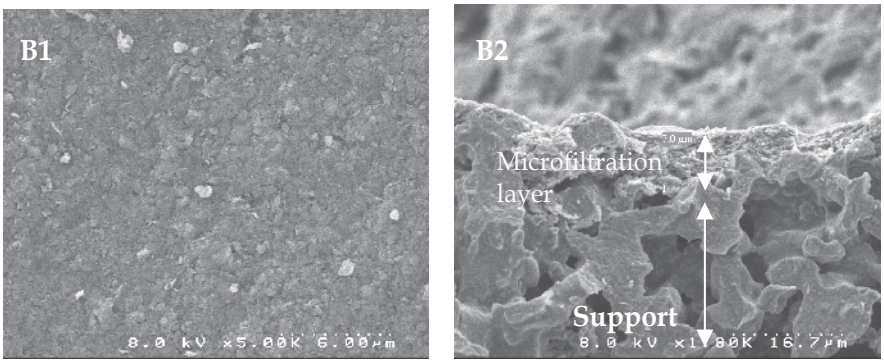

Fig. 9. Scanning electron micrographs of clay (JM_{18}) membrane: (A: Membrane thickness upper than10 µm, B: Membrane thickness less than 10 µm, 1: surface, 2: cross section)

Crossflow microfiltration tests were performed using a home-made pilot plant (Fig. 10) at a temperature of 25°C and transmembrane pressure (TMP) range between 1 and 4 bars.

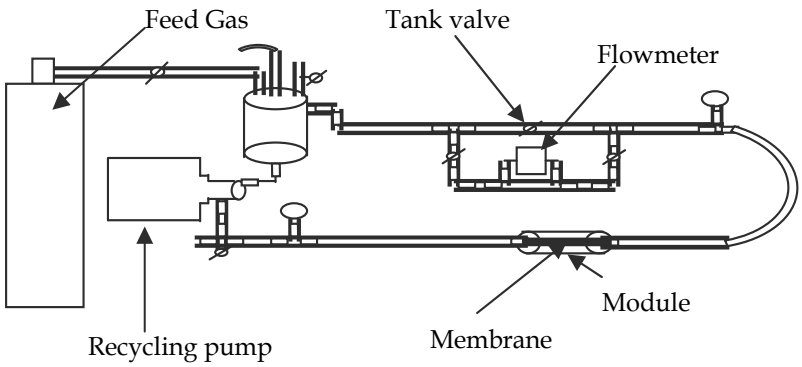

Fig. 10. Flow schema of experimental apparatus.

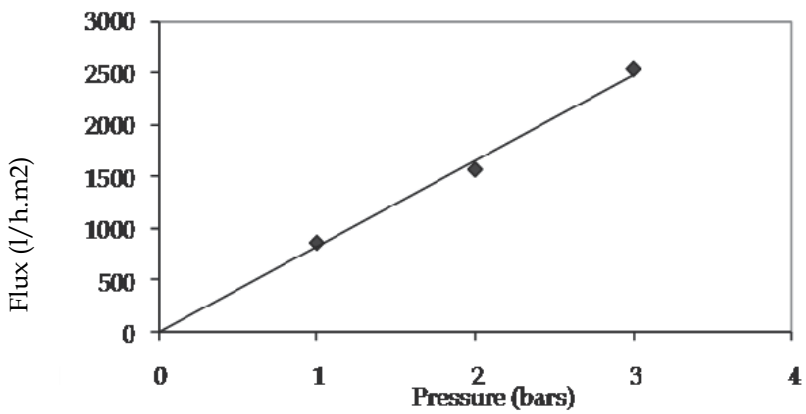

Fig. 11. Water fluxes vs. working pressure.

The flow rate was fixed at 2.5 $m.s^{-1}$. Before the tests, the membrane was conditioned by immersion in pure deionised water for a minimum of 24 h. The working pressure was obtained using a nitrogen gas source. The membrane was initially characterized by the determination of water permeability which was 870 $l.h^{-1}.m^{-2}.bar^{-1}$ (Fig. 11).

2.3 Application for cuttlefish effluents treatment

Membrane processes can be used for the treatment of wastewater produced by the sea products conditioning (Afonso et al., 2002). In our case, the prepared Microfiltration membranes have been applied to the cuttlefish effluent produced from cuttlefish conditioning and freezing process. The used samples were collected from a sea product-freezing factory located in Sfax (Tunisia). The dark colour in this type of effluent was due to the presence of particles in suspension (sepia ink) which has a size range between 56 nm and 161 nm (Flood et al., 1993).

Figure 12 gives the variation of permeate flux with transmembrane pressure which is done by: $(P_{inlet} + P_{oulet})/2 - Pf$ where: P_{inlet} and are respectively the inlet and the outlet pressures across the filtration module.

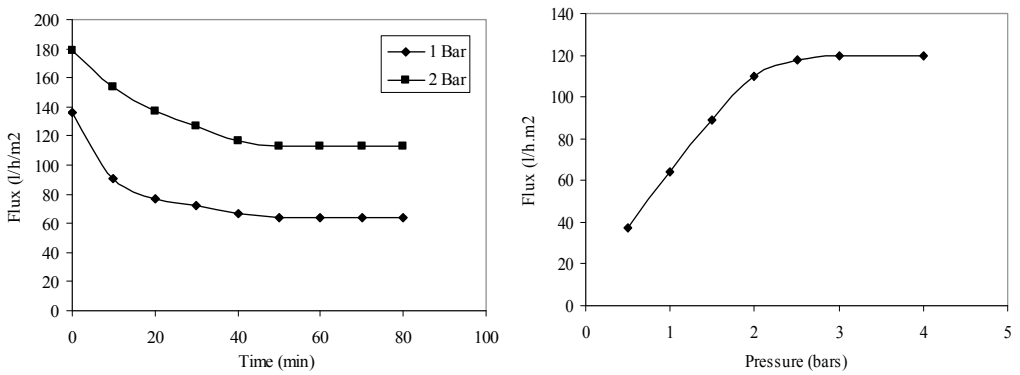

Fig. 12. Variation of flow according to the use pressure and time of filtration.

Permeate flux increased linearly with transmembrane pressure until a value of 2 bars and then stabilized at a value of 120 $l/h.m^2$. This behavior can be explained by the formation of a concentrated polarization layer. The variation of permeate flux with time shows that the fouling phenomenon is not very important: The permeate flux decreased by only 33%.

Table 4 gives the main characteristics of the raw and treated effluent. It can be observed that the permeate turbidity determined by using a Turbidimeter (HACH RATIO 2100A); is very low (inferior to 1 NTU) and that the COD retention rate (COD is chemical organic demand determined by colorimetric method) is superior to 65%.

These results confirm the efficiency of these microfiltration prepared membranes to cuttlefish effluent treatment.

In term of quality, figure 13 shows a noticeable elimination of suspended matter illustrated by the change of the effluent colour as well as the elimination of the turbidity.

Sample	Conductiviy (mS/cm)	Turbidity (NTU)	DCO (mg/l)
Raw effluent	80	> 2000	6000-6500
Filtrate (P = 1 bar)	72	0,89	2460
Filtrate (P = 2 bar)	70.5	0,62	1930

Table 4. Characteristics of the effluent befor and after filtration.

Fig. 13. A photograph of cuttlefish effluent before and after MF treatment.

3. Conclusion

In this work we have prepared new microfiltration membranes using natural powder derived from Tunisian natural material. The ceramic support was formed by the extrusion of a ceramic paste of silty marls (M_{11}). The microfiltration layer base on clay (JM_{18}), deposited onto the supports, was obtained by slip-casting method. An excellent link between the support and the microfiltration layer was obtained.

The support pore sizes could be carefully controlled by the choice of the particle diameters sizes of natural materials (silty marls). The desired pore sizes of the microfiltration layer (<1µm) were achieved by optimisation of the calcination temperatures. Microfiltration membranes from Tunisian clay with pore sizes as small as 0.18 µm could be then produced. This membrane have a water permeability of 870 $l.h^{1}.m^{-2}.bar^{-1}$.

One application of these membranes is the washing cuttle-fish effluent treatment. These membranes can also be used as a support for ultrafiltration layer.

4. References

Cham, K. K. & Brownstein, A. M. (1991). Ceramic membranes growth prospects and apportunities. *Am. Ceram. Soc. Bull*. Vol. 70, pp. 703-707.

R. Uhlhorn, J. R.; Huis M. H.; Veld, J in ' t B.; Keizer, K.; & Burggraaf, A. J. (1987). Science of ceramics, Vol. 14, pp. 551-556.

Zespalis,V. T.; Van Praag, W.; Keizer, K.; Van Ommen, J. G.; Ross, J. R. H. & Burggraaf, A. J. (1989). Modified alumina membranes as active materials in catalytic processes, First Intern, *ICIM*, pp. 367-372, Montpellier, 3-6 July.

Cot, L. (1998). Inorganic membranes: academic exercise or industrial reality, inorganic membranes, *Fifth Internal Conference on Inorganic Membranes*, Nagoya, 22-26 June.

Jones,B. F. & Galan, E. (1988). Sepiolite and palygorskite, in: S. W. Bailey (Ed.), Reviews in Mineralogy, Hydrous Phyllosilicates, *Mineralogical Society of America*, Washington Vol. 19, pp. 631-674.

Pérez, J.L. & Rodriguez, E. Ga. (1994). Determination of impurity in sepiolite by thermal analysis, *Thermal Anal*, vol. 42, pp. 131-141.

Mishra, T. & Parida, K. (1997). Transition-metal oxide pillared clays, part 2-A comparative study of textural and acidic properties of manganese(III) pillared montmorillonite and pillared acid-activited montmorillonite, *J. Mater. Chem,* Vol.7, No.(1), pp. 147-152.

Cool, R.; Clearfiled, A.; Mariagnanam, Ellistrem, V.; L.J.Mc.; Crooks, R.M. & Vansant, E.F. (1997). Self-assembly of aluminium-pillared clay on a gold support, *J. Mater. Chem,* Vol. 7, No. (3), pp. 443-448.

Messaoudi, L. ; Larbot, A. ; Rafiq, M. & Cot, L. (1995). Mise au point d'une membrane de microfiltration sur supports tubulaires à base d'une argile marocaine, *Ind. Ceram*, Vol. 12, No. (910), pp. 831-835.

Ishiguro, M.; Matsuura, T. & Detellier, C. (1995). Reverse osmosis separation for a montmorillonite membrane, *j. Membr. Sci*, Vol. 107, pp. 87-92.

Le Van Mao, R.; Rutinduka, E.; Detellier, C.; Gougay, P.; Hascoet, V.; Tavakoliyan, S.; Hoa, S.V. & Matsura, T. (1999). Mechanical and pore characteristics of zeolite composite membrane, *J. Mater. Chem*, vol. 9, pp. 783-788.

Rakib, S.; Sghyar, M.; Rafiq, M. ; Larbot, A. & Cot, L. (2000). Elaboration et caracterisation d'une ceramique marcroporeuse à base d'arène granitique, *Ann. Chim. Sci. Mat*, vol 25, pp. 567-576.

Dégrement, L. (1978). Mémento technique de l'eau, Paris, pp. 232-965.

Abdelmouleh, A. (1997). *Etude expérimentale de la valorisation de l'allache et de la seiche en Tunisie*, Thése de doctorat, p. 130-135.

Flood, R.; Deibel D. & Morris, C. (1993). Oikopleura Vanhoeffeni Using Sepia Ink. *Biol. Bull,* vol. 178, p. 118-125.

Guizard, C.; Julbe, A.; Larbot A.; Cot, L.; Lee. in B.I. & Pope (Eds.), E.J. (1994). Chemical Processing of Ceramics, *Marcel Dekker Inc*., New York, 501.

Khemakhem, S.; Ben Amar, R.; Larbot, A. Ben Salah, A. & Cot, L. (2006). Fabrication of mineral supports of membranes for microfiltration/ultrafiltration from Tunisian clay, *Ann. Chim. Sci. Mat*., vol. 31, No. 2, pp. 169-181.

Afonso M.D., & Borquez R., (2002). Review of the treatment of seafood processing waste-waters from the fish meal industry. *Desalination*, vol. 142, pp. 29-45.

6

Electron Microscopy and Microanalysis of the Fiber, Matrix and Fiber/Matrix Interface in SiC Based Ceramic Composite Material for Use in a Fusion Reactor Application

Tea Toplisek[1], Goran Drazic[1], Vilibald Bukosek[2],
Sasa Novak[1] and Spomenka Kobe[1]
[1]*Institute Jozef Stefan, Department for Nanostructured Materials*
[2]*Faculty of Natural Science and Engineering*
Slovenia

1. Introduction

Composite materials are engineered materials made from two or more constituent materials. They have significantly different physical or chemical properties which remain separate and distinct on a macroscopic level within the finished structure. The advantage of composite material is that they exhibit the best qualities of their components or constituents and often some qualities that neither constituent possesses. The properties that can be improved by forming a composite material are strength, stiffness, corrosion resistance, wear resistance, weight, thermal insulation, thermal conductivity, etc. Composite materials can be classified and characterized into four commonly accepted types; (1) fibrous composite materials that consist of fibers in a matrix, (2) laminated composite materials that consist of layers of various materials, (3) particulate composite materials that are composed of particles in a matrix and (4) the combination of some or all the first three types (Jones, 1999). According to the matrix phase the composites are divided into three groups; (1) metal matrix composites (MMCs), (2) polymer matrix composites (PMCs) and (3) ceramic matrix composites (CMCs). Ceramic materials in general have very attractive properties e.g.: high strength and high stiffness at very high temperatures, chemical inertness and low density. In the presence of flaws (surface or internal) they are prone to catastrophic failures. Ceramic materials can be toughened by incorporating fibers and thus exploit the attractive high-temperature strength and environmental resistance of ceramic materials without risking a catastrophic failure (Chawla, 1987). According to the basics written above, a monolithic silicone carbide (SiC) was used as a matrix phase, which has been recognized as one of the most promising structural materials for many thermo-mechanical applications because of its excellent high-temperature strength and modulus, good oxidation resistance, high hardness, low specific weight and low density (Xin-Bo & Hui, 2005; Xin-Bo et al., 2000; She et al., 1999). The problem with monolithic SiC is its low thermal shock resistance, which leads to cracking and catastrophic failure of the material. Thermal shock resistance and crack propagation can

be improved by introducing a reinforcement phase, continuous SiC fibers, into the monolithic SiC matrix to produce a SiC_f/SiC composite material (Kowbel et al., 1995). This kind of composite materials is being considered for a future fusion reactor because of its low induced radioactivity after neutron irradiation, non-catastrophic failure mode, specific thermal conductivity and low porosity (Zhang et al., 1998; Taguchi et al., 2005). It is known that the properties of the fiber/matrix interface play an important role in determining the mechanical and physical properties of ceramic matrix composites (CMCs). It can be defined as a bonding surface where a discontinuity of some kind occurs. In general it is a bidimensional region through which material parameters, such as concentration of an element, crystal structure, atomic registry, elastic modulus, density, and coefficient of thermal expansion, change from one side to another. It is important to be able to control the degree of bonding between the matrix and the reinforcement. The pure mechanical bonding usually is not enough but it is efficient in load transfer when the applied force is parallel to the interface. The chemical bonding is also important and can be divided into two types; dissolution and wettability bonding, where surface should be appropriately treated to remove any impurities; and reaction bonding where a transport of atoms occurs from one or both of the components to the reaction site, the interface (Chawla, 1987). In general, if the fiber/matrix interface is weak, the composite has low strength and stiffness, but a high resistance to fracture. In the case of a strong interface, which allows a crack to propagate straight through the fibers, the strength and stiffness of the composite are high, but the composite itself is brittle (Xin-Bo & Hui, 2005; Xin-Bo et al., 2000; Bertrand et al., 2001; Nuriel et al., 2005). However, the composite's brittleness remains a problem. This can be improved by adding a thin film of compliant material, called the "interphase", between the fiber and the brittle matrix, which has three main functions: protection of the fibers, load transfer between the fiber and the matrix and control of the crack deflection at the interface (Zhang et al., 1998; Jacques et al., 2000; Bertrand et al., 2000). The most commonly used interphase materials for SiC_f/SiC composites are pyrolitic carbon (PyC), boron nitride (BN) and, recently, a multilayer of (PyC/SiC). All these materials have their advantages and disadvantages. PyC has low oxidation resistance; BN is not suitable for fusion applications because the nitrogen transmutes into ^{14}C, which has a very long half-life as a β emitter after the neutron irradiation.

The processing of SiC_f/SiC is a complex, multi-stage process. Common processing techniques for the production of SiC_f/SiC composites include chemical vapor infiltration (CVI), polymer impregnation and pyrolysis (PIP), molten silicon infiltration (MI), reaction sintering (RS) and the nano-infiltrated transient eutectoid (NITE) process (Katoh et al., 2002). In this paper we present a microstructural and micro-indentation study of a material, fabricated by a novel method for preparing SiC_f/SiC composite materials for fusion-reactor applications. The method consists of the adapted dip coating and infiltration of the SiC-fibers with a water suspension of SiC-particles and sintering additives. In order to study the crack deflection, introduced by the Vickers indenter, we deposited various layers (diamond-like carbon (DLC), CrC, CrN and WC) on the fibers' surface using physical vapor deposition. A comparison between the uncoated and coated fibers was made.

The microstructures of the SiC_f/SiC composite materials with different interphases between the fibers and the brittle matrix were examined using conventional transmission electron microscopy (TEM) and high-resolution (HR) TEM.

Specimen preparation methods for ceramic fibers are often unsatisfactory. We tried to optimize and develop different preparation techniques which have an important role in study of these materials.
The fracture surfaces of the samples were observed using scanning electron microscopy (SEM). Z-contrast imaging (STEM/HAADF) and different techniques of electron diffraction were applied for the phase identification. The chemical composition of the individual phases was determined using XEDS.

2. Materials and Methods

The starting material was commercially available 0.5 μm SiC powder BF-12 (HC Starck, Goslar, Germany), Nicalon and Hi-Nicalon Type S fibers (COI Ceramics, San Diego, CA), Tyranno SA fibers (UBE Industries LTD., Düsseldorf, Germany), aluminium dihydrogen phosphate, Bindal A (TKI Hrastnik, Slovenia), anionic surface active agent, sodium dioctylsulfosuccinate, SDOSS and polymer Starfire (Starfire systems, Malta, NY).
Among several known methods for the preparation of the SiC_f/SiC composite material, which are described elsewhere (Drazic et al., 2005; Novak et al., 2006; Novak et al., 2010), we used infiltration with micro particles suspension. The process begins with immersion of the fibers into a water suspension made from micro-sized particles and a sintering additive based on the Al-Si-P-O system, dip-coating and drainage. All samples were sintered at 1300 °C in pure argon. Because of the hydrophobic nature of the fibers we impregnated them with anionic surface active agent. It consists of liophobic and liophilic groups, which arrange on the substrate surface in a way to increase its wettability with our water suspension.
Using reactive sputtering the fibers were coated with a thin layer of interphase material (CrC, WC and diamond like carbon – DLC) with relevant chemical composition in terms of neutron activation. The coatings were sputtered with a Sputron (Balzers AG, Liechtenstein). The thickness of the interphase layer was varied between a few and 500 nm, depending on the experimental conditions and geometry of the fibers (overlapping) during the deposition.
The nanohardness of the fibers and the matrix was measured using Vickers indenter on the Fischerscope instrument H100C (Helmut Fischer, Germany), which records indentation depth and load. The load we used was in both cases 10 mN. On the other hand, a Vickers microhardness tester (MVK-H2 Hardness tester, Mitutoyo, Japan) was used in order to observe the cracks in the matrix and its deviation from the primary direction. A maximum load of 1 N was applied in order to initiate the cracks.
The mechanical properties of the coated and uncoated fibers were also measured on dynamometer Instron 5567 (Instron, Great Britain). The fiber was put between two clamps and extended till breaking. With special program we can follow internal changes in material structure during testing. This program also allows later interpretation of all values that were measured.
For observing the samples' surface, morphology, topography and the particles size we used scanning electron microscope, JEOL JSM-5800. The working voltage was 20 keV. The energy-dispersive X-ray spectrometer (Link ISIS 300, Oxford Instruments) was used for determining the chemical composition.
The fibers' topography was also observed with atomic force microscopy (VEECO Dimension 3100) before and after the coating.

Ceramic fibers are key components in a number of technologically important applications, such as reinforcements in structural ceramic matrix composites. Application of transmission electron microscopy is often required for characterization of such fibers. Preparation of electron transparent sections of thin ceramic fibers is a challenging task often limits the use of TEM studies on such fibers (Mogilevsky, 2001). A special paragraph is dedicated to the TEM specimen preparation techniques. The structure and chemical composition of the materials on micrometer, nanometer or even atomic level were set and characterized with transmission electron microscope, JEOL 2010 F FEG-STEM and JEOL 2100 and a Link ISIS 300M XEDS analysis.

3. TEM Specimen Preparation Techniques

Different techniques were used for TEM specimen preparation because of the variety of the samples. The basic goal of the specimen preparation is to get a thin area (thickness from 10 to 50 nm) in the material to be transparent for the electrons with high energy (from 100 keV to 200 keV). It is desired that this area is as big as possible, that it has uniform thickness and should not cause artifacts in a way of changing the chemical structure or the structure itself (amorphization or crystallization). It is also important that during the preparation we do not put the impurities on the samples which can cause a contamination of the sample in the microscope (Gec & Ceh, 2006).

The conventional technique which is mechanical thinning, dimpling and ion-milling was used for the bulk material. This method is not suitable for observing the SiC fibers because the fibers are much stiffer then the epoxy in which the fibers are embedded during the preparation. Problems also occur during ion-milling; the fibers are either not transparent for the electrons or they are pulled out of the high-temperature epoxy. So we looked for the alternative methods. Some of the methods we used are described later on.

The first method (Figure 1) is very simple and fast. The fibers are prepared by gluing them parallel on a TEM grid or a ring, finally cured on a hot plate and ion-milled (Bal-Tec RES 010) till the perforation.

The second method (Figure 2) combines a technique for preparing fiber/epoxy assemblies with mechanical polishing to a thickness of less than 5 μm, thus minimizing the time of ion milling (Mogilevsky, 2001). Fibers are put between two 500 μm glasses coated with high-temperature epoxy, clamped with a pair of Teflon plates to squeeze out excessive epoxy and finally cured on a hot plate. This sandwich structure was first thinned on diamond lapping films (Allied) of different gradation, using a Tripod Polisher (Allied) till approximately one half of the fibers' diameter. Then a TEM grid was glued on the polished surface to strengthen the specimen. This grid was also used for thickness measurements during the polishing. It is important that no air bubbles are trapped between the grid and polished side of the specimen. The thinning process is continued on the other side of the specimen to the final thickness of less than 5 μm. The thinned sample was milled in ion miller at 4 keV with incident angle of 10° until a perforation was observed. This method requires a long preparation time, frequent observations under the optical microscope to ensure parallel thinning and accuracy. The method can be extended to other types of materials, such as fiber-reinforced ceramic composites.

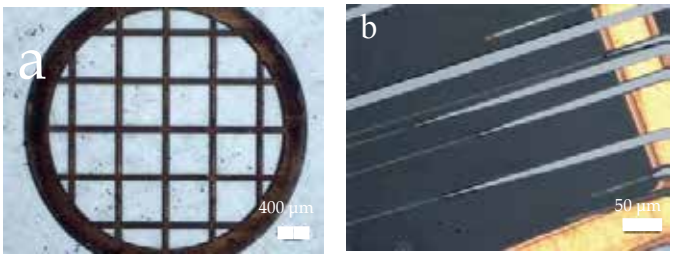

Fig. 1. Optical micrographs: (a) TEM grid on which the fibers were glued parallel and (b) interferences in Tyranno SA SiC fibers after ion-milling.

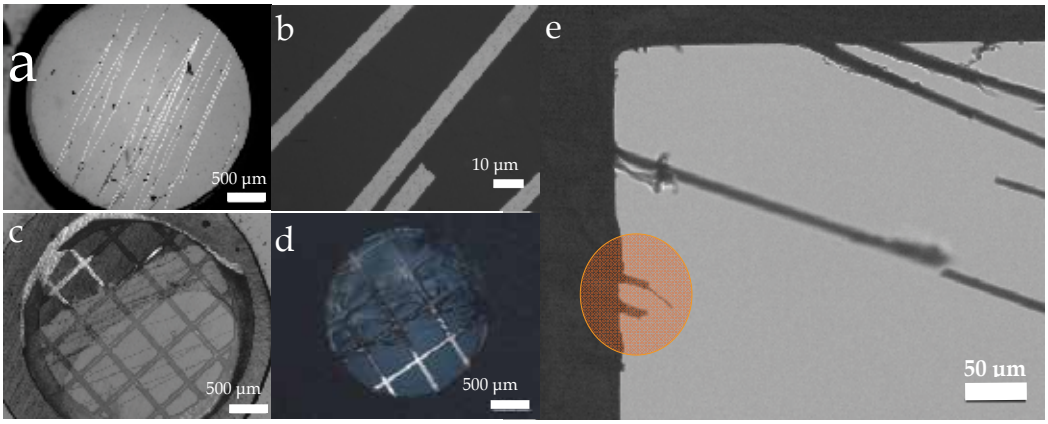

Fig. 2. Optical micrographs of the Tyranno SA SiC fibers using tripod polishing method: (a) specimen polished on one side through approximately one half of the fiber diameter; (b) same as in (a) but at higher magnification; (c) specimen mounted on a supporting grid, turned over and polished to the final thickness; (d) specimen after ion-milling; (e) same as in (d) but at higher magnification. The marked circle is transparent enough for observing with transmission electron microscope.

For observing the coatings on the fiber surface, the cross-section method was used. It is important to have a high ratio between the fibers and epoxy. The fibers were cut on short segments and put parallel into the groove made in silicon plate. To get a sandwich structure another silicon plate was put on it and clamped between two Teflon plates to squeeze out excessive epoxy, followed by curing on a hot plate. Then the sandwich structure was put into a brass ring with blind tracks to strengthen the sample. A conventional technique was used further on. Figure 3 show optical micrographs of Nicalon SiC fibers coated with a thin layer and prepared as a cross-section by conventional method including mechanical thinning, dimpling and ion-milling. Figure 3a shows optical micrograph of coated fibers in the groove between Si plates after dimpling. The thickness in the center of the specimen is 16 µm. After mechanical thinning, the quality of the specimen is improved with polishing to eliminate all the imperfections in the sample. This sample is ready for ion-milling. Figure 3b shows the same sample as in Figure 3a but after ion-milling. The sample was bombarded with Argon ions till the perforation. Because of the difference in hardness, we can see that epoxy resin starts to ion-mill much faster and quicker than the SiC fibers.

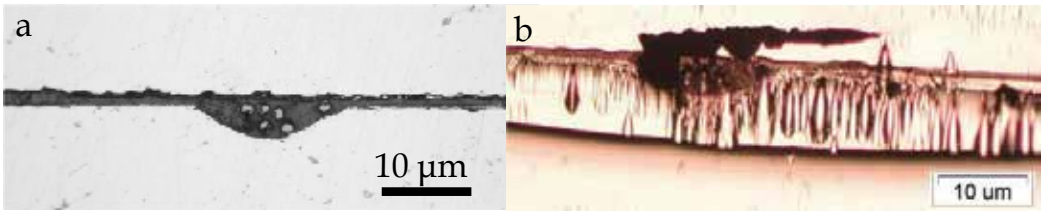

Fig. 3. Optical micrographs of the Nicalon SiC fibers coated with a thin layer and prepared as cross-section by conventional method: (a) after dimpling; (b) after ion-milling.

The SiC_f/SiC samples were prepared by conventional method (Figure 4a) and a wedge-polishing method (Figure 4b) which allows very accurately controlled thinning. In a conventional method, thin foils were cut on a wire saw from the composites, perpendicular to the fiber axis. After mechanical thinning to a thickness of approximately 80-100 µm the samples were polished to a final thickness of 20 µm, by dimpling. Ion-milling was used as a final step to get a perforation of the samples. TEM investigation revealed more or less complete erosion of the matrix during the preparation process. The mechanical thinning with a wedge-polishing method was performed on diamond lapping films at a very small wedge angle of 1°. This method is far superior then the conventional ion-milling. It is suitable for any multiphase specimens with large hardness differences.

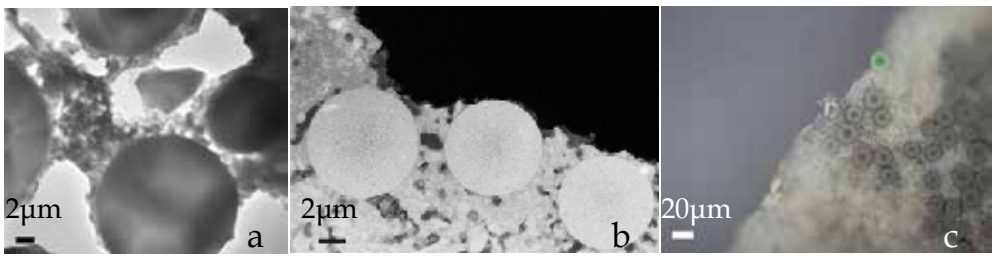

Fig. 4. TEM and optical micrographs of SiC_f/SiC composite material: (a) SiC_f/SiC after ion-milling where erosion of the matrix is visible; (b) HAADF-STEM micrograph of SiC_f/SiC prepared by tripod polishing; (c) Optical micrograph of tripod polished specimen prepared as a cross-section where interference fringes at the edge of the specimen are visible.

4. Results and Discussion

4.1 The Microstructure of the SiC fibers

As mentioned above we used different SiC fibers; Nicalon, Hi-Nicalon S and Tyranno SA. In this paragraph the microstructure, the topography and the chemical composition will be discussed for all three SiC fibers.

Figure 5a shows SEM micrograph of the Nicalon SiC fiber with a diameter of 15 µm. Its surface is smooth and without any visible defects. The fibers are consisted of Silicon, Carbon and Oxygen in a determined ratio. A detailed TEM analysis revealed that at room temperature these fibers consist of amorphous matrix phase (Figure 5b) with a small amount of β-SiC nanocrystallites, 1-3 nm in size. The SAED pattern (Figure 5c) shows diffused rings which can be indexed as cubic SiC. In the inset of SAED pattern (Figure 5c) simulated

pattern is displayed. For calculations EMS program code was used (Stadelmann, 1987) and particle size of 1 nm. The average roughness of the amorphous Nicalon SiC fibers was measured on AFM (Figure 5d) and was around 2 nm.

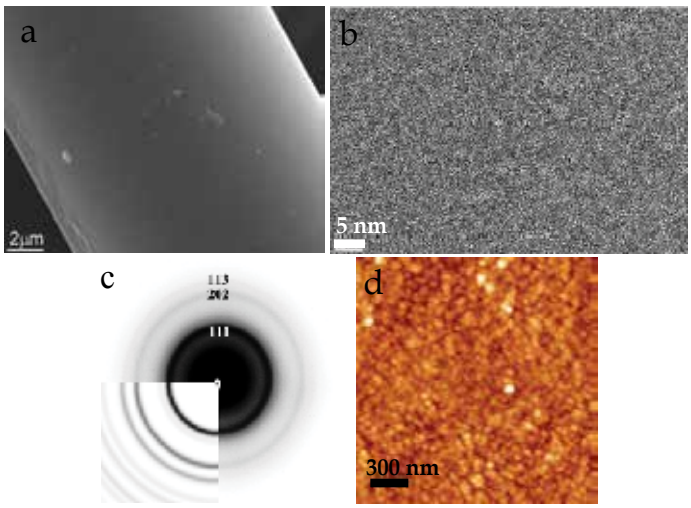

Fig. 5. Nicalon SiC fiber: (a) SEM micrograph; (b) HR-TEM micrograph; (c) Diffraction pattern; (d) AFM micrograph.

Contrary to the Nicalon SiC fibers, the Hi-Nicalon S SiC fibers consist of two clearly defined phases (Figure 6b); crystalline phase in the inner part of the fiber and amorphous phase in the outer part of the fibers. The crystalline phase consists of SiC crystallites, 5 to 20 nm in size; while the amorphous phase was determined as pyrolitic carbon in a lamellar microstructure. From the SEM micrograph (Figure 6a) we can see that the fiber has a diameter of 12 μm, the surface morphology is similar to the Nicalon SiC fibers.

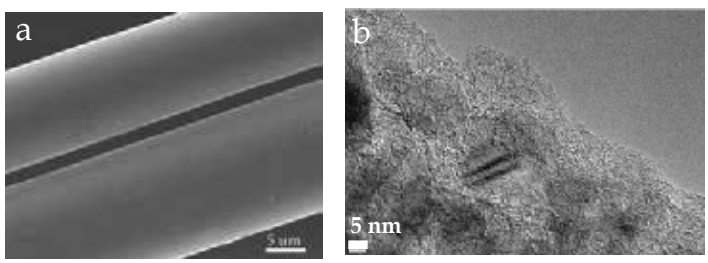

Fig. 6. Hi Nicalon S SiC fiber: (a) SEM micrograph; (b) TEM micrograph.

The newest SiC fibers are Tyranno SA SiC fibers with a diameter of 7 μm. The surface is much rougher than the surface of the Nicalon SiC fibers but also without any imperfections (Figure 7a). The roughness is around 9 nm (Figure 7e). These fibers are already crystalline at room temperature. They consist of small crystallites up to 50 nm in size what is seen from TEM micrograph (Figure 7b). The diffraction patterns (Figure 7c, d) show circles, where individual dots are visible and can be indexed as a mixture of cubic and hexagonal SiC (β- and α-SiC).

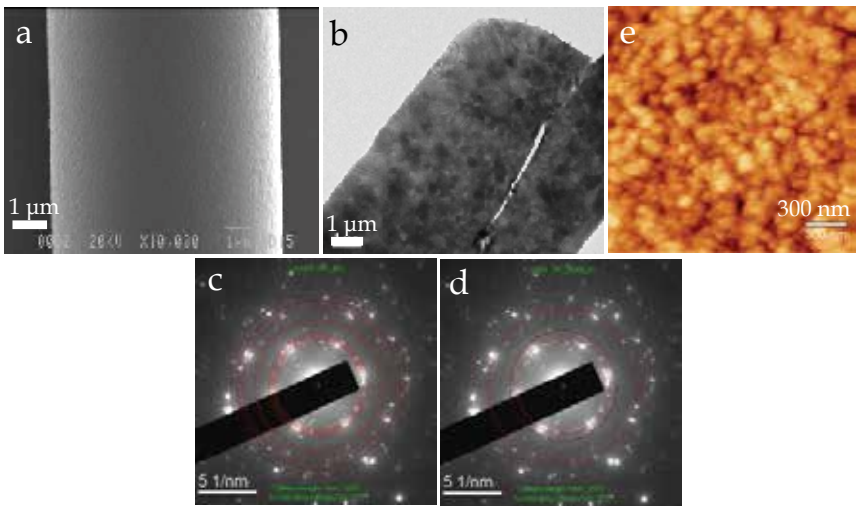

Fig. 7. Tyranno SA SiC fiber: (a) SEM micrograph; (b) TEM micrograph; (c, d) Diffraction patterns for β- and α-SiC grains; (e) AFM micrograph.

4.2 The Mechanical Properties of the SiC fibers

SiC fibers exhibit a wide distribution of diameters which was took into account to get a reliable tensile strength data. Before measurement was done each fiber was checked with optical microscope. All the samples were glued onto paper in the shape of letter "U" to make sure, that the presence of the creep inside the clamps was eliminated. Before measuring the side section of the paper was removed using a pair of ceramic scissors. The dynamometer Instron 5567 was used, with a clamping length of 1 cm and a crosshead speed of 1 mm/min. Figure 8 shows the stress - strain curves, measured at room temperature for untreated SiC fiber (Nicalon SiC fiber @ RT) and after thermal treatment at 1300 °C for 3 h in pure argon (Nicalon SiC fiber @ 1300 °C).

Nicalon SiC fiber sample at room temperature shows, except for small deformations, mainly proportional stress dependence of the strain until the fracture at ε_p = 2,40% , stress σ_p = 86,31 cNtex^{-1} = 2,20 GPa. Stress at yield point is σ_y = 7,91 cNtex^{-1} = 0,20 GPa at elastic deformation of ε_y = 0,303%. Elastic modulus E = 55,20 GPa is small. Work to fracture is $A_p = 4{,}20 \cdot 10^{-2}$ mJ and elastic work to yield point is $A_y = 3{,}35 \cdot 10^{-4}$ mJ, which represents 0,80% of the total energy to break. Specific work is $A_{sp} = 1{,}00 \cdot 10^{-2}$ Jkg^{-1} and a fracture work factor which represents the toughness of the material is f_A = 0,483.

Stress-strain curve of Nicalon SiC fiber sample after thermal treatment at 1300 °C shows different behavior. Heat treatment increases the crystallinity of SiC fiber which reflects in the strong increase of the initial elastic modulus. After the yield point, sample exhibit plastic deformation at slight increase of stress at strain of about 0,4 %. This plastic deformation is a consequence of some rearrangement of the structure which requires even higher energy at further deformation until the fracture at strain ε_p = 1,30 % and fracture strength of σ_p = 49,52 cNtex^{-1} = 1,26 GPa. Stress at yield point is σ_y = 13,25 cNtex^{-1} = 0,33 GPa at elastic strain of ε_y = 0,107 %. After heat treatment the elastic modulus substantially increase to E = 328,14 GPa. Fracture work of heat-treated sample is due to the smaller strain smaller (A_p =1,34 10^{-2} mJ) compared to untreated sample. Contrary, the elastic work is due

to higher stress at yield point higher (A_y = 2,98 ·10^{-4} mJ) and represents 2,22 % of total fracture energy. Specific work is A_{sp} = 3,20 ·10^{-3} Jkg^{-1} and a fracture work factor is f_A = 0,497.

Parameter	Nicalon SiC fiber @ RT	Nicalon SiC fiber @ 1300 °C
Fracture strength σ_p (GPa)	2,20	1,26
Fracture strain ε_p (%)	2,40	1,30
Yield strength σ_y (GPa)	0,20	0,33
Yield strain ε_y (%)	0,303	0,107
Fracture work A_p (mJ)	4,20 ·10^{-2}	1,34 ·10^{-2}
Work to yield point A_y (mJ)	3,35 · 10^{-4}	2,98 ·10^{-4}
Specific work A_{sp} (Jkg^{-1})	1,00 ·10^{-2}	3,20 ·10^{-3}
Elastic modulus E (GPa)	55,20	328,14
Fracture-work factor f_A	0,483	0,497

Table 1. Comparison of viscoelastic parameters for untreated and thermally treated Nicalon SiC fibers.

Comparison of viscoelastic properties of both samples allows the following conclusions: After heat treatment, the elastic modulus increased by a factor 6, the material becomes more crystalline and reduces the ability of strain, as well as reduces the fracture strength. Heat-treated material has a greater capability to strain (0,4 %). In heat-treated material, the elastic deformation zone is lowered, at the same time the yield strength is higher by a factor 1,7. Yield point represents the boundary between elastic and plastic deformation. This gives the material greater stability in an otherwise narrower elastic region. Toughness of heat-treated material is reduced as can be seen from comparison of fracture work factor and specific work (energy needed to deform one kg of material).

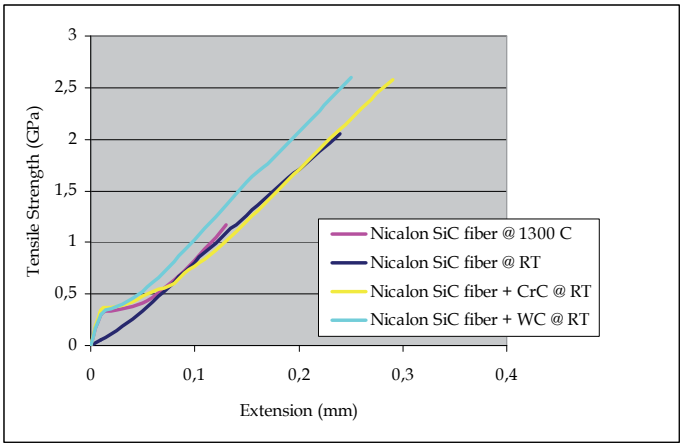

Fig. 8. Stress/strain curves for untreated and thermally treated (1300 °C for 3 h in pure argon) Nicalon SiC fibers and Nicalon SiC fibers coated with CrC and WC measured at room temperature.

In Figure 8, the stress–strain curves, measured at room temperature for Nicalon SiC fibers, coated with CrC and WC are displayed. From the curves of both samples it could be

concluded that they have approximately the same initial modulus with clearly expressed yield point at 0,12 %, the transition to plastic deformation and further hardening until fracture. High value of initial modulus is due to the presence of WC and CrC. Viscoelastic properties of both types of samples are very similar. Comparison of viscoelastic parameters for samples coated with CrC and WC is displayed in table 2.

Parameter	Nicalon SiC fiber + CrC	Nicalon SiC fiber + WC
Fracture strength σ_p (GPa)	2,77	2,78
Fracture strain ε_p (%)	2,90	2,50
Yield strength σ_y (GPa)	0,390	0,342
Yield strain ε_y (%)	0,117	0,117
Fracture work A_p (mJ)	$6,41 \cdot 10^{-2}$	$5,81 \cdot 10^{-2}$
Delo do polzišča A_y (mJ)	$3,83 \cdot 10^{-4}$	$3,39 \cdot 10^{-4}$
Specific work A_{sp} (Jkg^{-1})	$1,53 \cdot 10^{-2}$	$1,38 \cdot 10^{-2}$
Elastic modulus E (Gpa)	345,14	302,33
Fracture-work factor f_A	0,484	0,507

Table 2. Comparison of viscoelastic parameters for Nicalon SiC fibers coated with CrC and WC.

Parameters of viscoelastic properties of samples of Nicalon SiC fiber + CrC and Nicalon SiC fiber + WC, measured at room temperature indicate that materials have similar viscoelastic properties. Nicalon SiC fiber, coated with CrC has slightly higher initial elastic modulus and yield strength, the difference between the two types of sample is in strain between 0,5 % and fracture and consequently also higher fracture work for sample coated with CrC.
Heat treated SiC Nicalon SiC fiber sample and WC coated Nicalon SiC fiber sample have similar elastic properties up to yield point (comparable starting elastic modulus and yield strength and stress).
Tyranno SA SiC fibers are very brittle at room temperature and as such impossible to handle or measure.

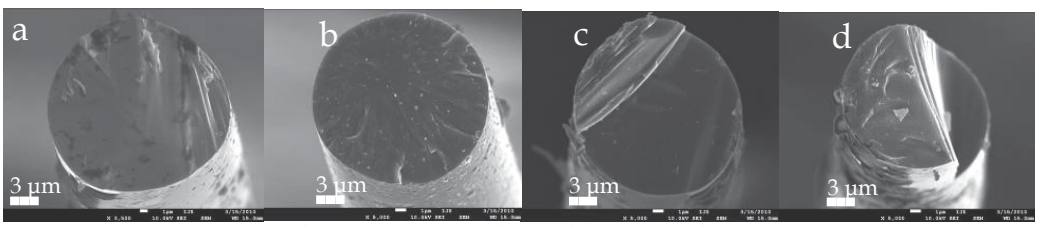

Fig. 9. SEM micrographs of the Nicalon SiC fibers fracture surfaces.

After tensile measurements all fracture surfaces of the fibers were investigated with scanning electron microscope (Figure 9a-d). In general, fracture in fibers initiates at some flaw(s), internal or on the surface. Very frequently, a near-surface flaw such as a microvoid or an inclusion is responsible for the initiation of fracture of fiber. Surface flaws are common in SiC based fibers because of the processing technique. Airborne particles as well as other elements tend to attach to the surface of the fiber during process and handling. One important feature of ceramic fiber is the surface texture. Their surface roughness scales with

gain size. The rough surface of such brittle fibers makes them break at very low strains and it makes very difficult to handle them in practice. The grain boundaries on the surface can act as notches and weaken the fiber (Elices & Llorca, 2002).

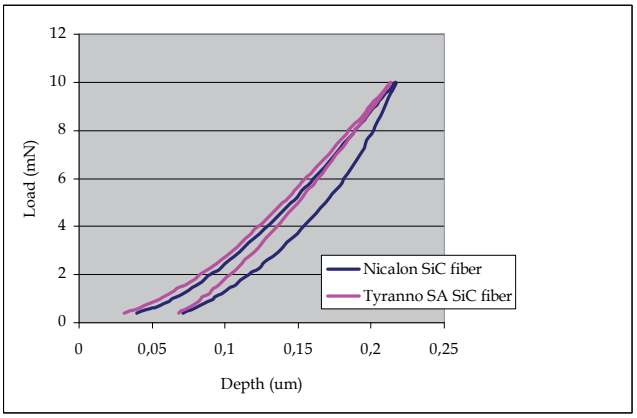

Fig. 10. Load/Depth curves for Nicalon SiC fiber and Tyranno SA SiC fiber measured at room temperature.

We also measured the nanohardness of Nicalon and Tyranno SA SiC fibers at room temperature using Vickers indenter on the Fischerscope instrument. The load we used was 10 mN. Figure 10 shows two load/depth curves, average of 10 measurements, for mentioned SiC fibers. The nanohardness for Nicalon SiC fiber is around 1800 HV and for Tyranno SA SiC fiber around 2800 HV. From the curve load/depth we can see that the elastoplastic deformation appears in both cases.

4.3 SiC Based Matrix and SiC_f/SiC composite material

In previous paragraphs the microstructure and mechanical properties of different SiC fibers were described. To produce the composite material we had to prepare a SiC matrix phase. It was made from water suspension of SiC particles and sintering additive based on low-melting-point eutectic composition of the Al-Si-P-O system, which enables sintering at low temperature and thus avoids the change in the microstructure of the SiC fibers. Figure 11a shows SEM micrograph of the matrix, from where we can see that the size of the particles is less than 1 μm. Figures 11b, c show cross-sectional SEM micrographs at different magnifications of the composite material with Nicalon SiC fibers produced with a method described above. Large pores observed in all the samples were made during the mechanical grinding and polishing as part of the sample preparation. The matrix was fully filled up the areas around the fiber bundle. The effectiveness of the adhesion between the fibers and the matrix was checked on thermally treated samples using TEM and microanalysis (Figures 11d, e). Nicalon SiC fibers have a 50 nm thick SiO_2 amorphous layer on the surface after thermal treatment (Figure 11e).

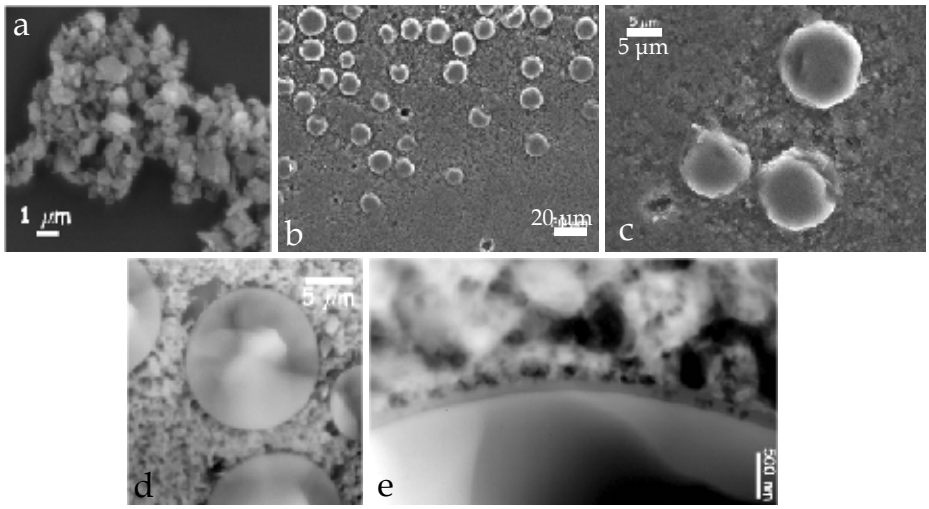

Fig. 11. SEM and TEM micrographs of SiC matrix and SiC_f/SiC composite material: (a) SiC matrix; (b) SiC_f/SiC composite material; (c) The same as (b) but at higher magnification; (d) SiC_f/SiC prepared by tripod polishing; (e) Reaction layer on the fiber surface.

4.4 Interphases in SiC_f/SiC composite material

According to the literature (Xin-Bo & Hui, 2005; Xin-Bo et al., 2000; Bertrand et al., 2001; Nuriel et al., 2005) the role of the interphase is very important. It determines the mechanical and physical properties of ceramic matrix composites (CMCs). Although the SiC_f/SiC composite material has many advantages, it also has one important disadvantage; the brittleness. Figure 12a shows SEM micrograph of the SiC_f/SiC composite material, where the crack path introduced by the Vickers indenter continued through the fibers. This would lead to a catastrophic failure of the composite material.

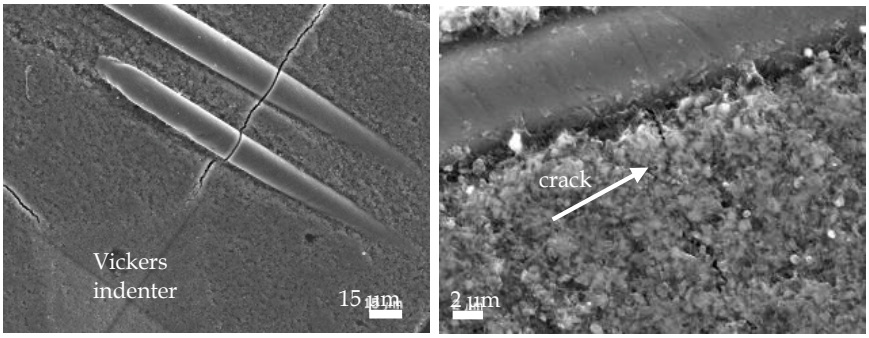

Fig. 12. SEM micrographs of (a) a failure of the composite material and (b) the crack deflection on the fiber/matrix interface (500 nm thick CrN was used as an interphase).

A crack deflection mechanism requires a weak fiber/matrix bond so that as a matrix crack reaches the interface, it gets deflected along the interface rather than passing straight through the fiber. A weak interfacial bond also leads to fiber pullout.

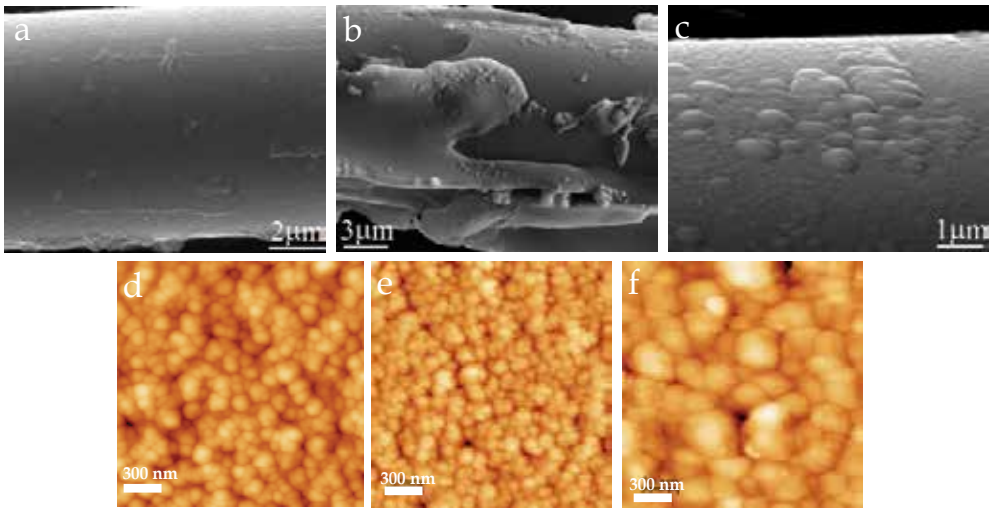

Fig. 13. SEM and AFM micrographs of Nicalon SiC and Tyranno SA SiC fibers: (a, d) Tyranno SA SiC fiber coated with DLC; (b, e) Nicalon SiC fiber coated with WC; (c, f) Nicalon SiC fiber coated with CrC.

In order to prevent a catastrophic failure of the composite material under load, various thin layers have been deposited on the surface of the fibers by physical vapor deposition, using reactive sputtering. The layers were selected on the basis of the relevant chemical composition appropriate for use in a future fusion reactor. Figure 13 shows SEM micrographs of three interface materials; DLC (diamond-like carbon), WC and CrC. All three layers were deposited along the fiber axis with the thickness varying between a few nm and 0.5 μm, depending on the geometry and conditions during the deposition. From AFM micrographs we can see the difference in roughness before and after the deposition. DLC layer was deposited on Tyranno SA SiC fiber. The roughness is almost the same, around 9 nm. WC and CrC were deposited on Nicalon SiC fibers from where we can see that the difference in roughness is quite big. In the case of WC, the roughness changes from 2 to 7 nm and in the case of CrC from 2 to 15 nm.
We also used CrN, but according to the literature (Taguchi et al., 2005) this kind of interface is not suitable for fusion applications because the nitrogen transmutes into ^{14}C, which has a very long half-life as a β emitter after the neutron irradiation. We also encountered another problem, a reaction between the thin layer (CrN) and the matrix. TEM analysis showed that after sintering the CrN partially diffused into the matrix around the fibers. Nevertheless, the CrN layer caused a deflection of the crack from its primary direction and thus prevents the fiber from cracking (Figure 12b).
In the case of WC coating, a multilayer (sandwich structure) approach was used in order to improve the mechanical properties. Figure 14a shows TEM micrograph of the WC coating on the surface of the Nicalon SiC fiber. The WC was deposited as a sandwich structure. The first layer, with a thickness of 40 nm, is crystalline chromium, which ensures better cling of WC to the fiber surface. The second layer, with a thickness of 18 nm, is pure tungsten which enables a more continuous transition of WC. These layers also ensured better adhesion of

the coating to the fiber surface. The third layer is amorphous tungsten carbide, with a thickness of 400–500 nm.
Similar approach was also used in the case of CrC. The first layer, with a thickness up to 80 nm was nanocrystalline chromium, which ensures better cling of CrC to the fiber surface. The second layer was chromium carbide, with a thickness of 400-500 nm (Figure 14b). The problem that was observed was a columnar growth of CrC. The crack that would initiate in the matrix phase would not stop at the CrC/matrix interface but because of the columnar growth it could continue between columns until it would reach the CrC/Cr interface.

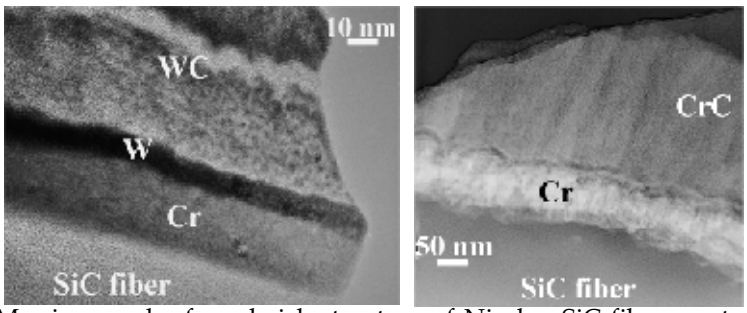

Fig. 14. TEM micrograph of sandwich structure of Nicalon SiC fibers coated with (a) WC and (b) CrC.

5. Conclusion

Different TEM specimen preparation techniques for uncoated and coated SiC fibers, ceramic material and ceramic composite material were described, all with their advantages and disadvantages. The conventional technique which is made up from mechanical thinning, dimpling and ion-milling is not suitable for observing the SiC fibers because the fibers are much stiffer then the epoxy in which the fibers are embedded during the preparation. Although the method that combines a technique for preparing fiber/epoxy assemblies with mechanical polishing to a thickness of less than 5 μm, thus minimizing the time of ion milling, requires a long preparation time, frequently observations under optical microscope to ensure parallel thinning and accuracy it is suitable for SiC fibers.
The microstructure of SiC fibers was observed using scanning and transmission electron microscope and atomic force microscope.
Using dynamometer Instron 5567 the tensile properties were measured. If we compare untreated and thermally treated Nicalon SiC fibers we can see, that the elastic modulus is increased by a factor 6, the material becomes more crystalline and reduces the ability of strain, as well as reduces the fracture strength. Nicalon SiC fibers, coated with CrC and WC, have similar viscoelastic properties which are similar to thermally treated Nicalon SiC fibers up to yield point (comparable starting elastic modulus and yield strength).
The nanohardness of the matrix is 300 HV, which is 6 times lower than for Nicalon SiC fibers and 9 times lower than for Tyranno SA SiC fibers.
A novel method for preparing SiC_f/SiC composite material for a future fusion reactor has been shown to be quite promising. The sintering additive used in the matrix was based on a low-melting-point eutectic composition in the Al–Si–P–O system, which enables sintering at low temperatures, in order to avoid the recrystallization of the Nicalon SiC-fibers and thus avoid embrittlement of the fibers and degradation of the mechanical properties.

Uncoated SiC-fibers have, after thermal treatment, a 50-nm-thick SiO_2 amorphous layer on the surface, which does not prevent the cracks from propagating at the fiber/matrix interface. This leads to a catastrophic failure of the composites. To control the matrix-to-fiber stress transfer (crack deflection at the fiber/matrix interface) Nicalon and Tyranno SiC-fibers were coated with various thin layers of different chemical compositions, such as CrC, WC and DLC, by physical vapor deposition, leading to composites with different degrees of toughness. Of the deposited layers that deflect cracks, CrN is not useful because nitrogen transmutes into ^{14}C and the CrN diffused into the matrix around the fibers.

6. Acknowledgements

Mrs. Medeja Gec is acknowledged for her help in TEM sample preparation and Mr. Matjaz Panjan and Dr. Peter Panjan from the Department of Thin films and Surfaces, Jozef Stefan Institute, Slovenia, are thanked for their help in depositing the thin films on the fiber surface and the Vickers indent experiments. This work was performed under the contract P2-0084 and was financially supported by the Ministry of Higher Education, Science and Technology of the Republic of Slovenia and the European Commission within the Contract of Association Euratom FU06-CT-2004-00083.

7. References

Bertrand, S.; Droillard, C.; Pailler, R.; Bourrat, X. & Naslain, R. (2000). TEM structure of $(PyC/SiC)_n$ multilayered interphases in SiC/SiC composites. *Journal of the European Ceramic Society,* Vol. 20, No. 1, (January 2000) 1-13

Bertrand, S.; Pailler, R. & Lamon, J. (2001). SiC/SiC minicomposites with nanoscale multilayered fibre coatings. *Composites Science and Technology,* Vol. 61, No. 3, (February 2001) 363-367

Chawla, K. K. (1987). *Composite Materials: Science and Engineering*, Springer-Verlag, ISBN 0-387-96478-9, New York

Drazic, G.; Novak, S.; Daneu, N. & Mejak, K. (2005). Preparation and Analytical Electron Microscopy of a SiC Continuous-Fiber Ceramic Composite. *Journal of Materials Engineering and Performance,* Vol. 14, No. 4, (August 2005) 424-429, ISSN 1059-9495

Elices, M. & Llorca, J. (2002). *Fiber Fracture,* Elsevier Science, ISBN-13 : 978-0-08-044104-7, Kidlington, Oxford

Gec, M. & Ceh, M. (2006). Tehnike priprave vzorcev za preiskave na TEM (1. del) – Mehanska predpriprava vzorca. *Vakuumist,* Vol. 26, No. 1-2, (June 2006) 23-29, ISSN 0351-9716

Jacques, S.; Lopez-Marure, A.; Vincent, C.; Vincent, H. & Bouix, J. (2000). SiC/SiC minicomposites with structure-graded BN interphases. *Journal of the European Ceramic Society,* Vol. 20, No. 12, (November 2000) 1929-1938

Katoh, Y.; Dong, S. M. & Kohyama, A. (2002). Thermo-mechanical properties and microstructure of silicon carbide composites fabricated by nano-infiltrated transient eutectoid process. *Fusion Engineering and Design,* Vol. 61-62, (November 2002) 723-731

Kowbel, W.; Withers, J. C.; Loutfy, R. O.; Bruce, C. & Kyriacou, C. (1995). Silicon carbide fibers and composites from graphite precursors for fusion energy applications. *Journal of Nuclear Materials,* Vol. 219, (1995) 15-25, ISSN 0022-3115

Mogilevsky, P. (2002). Preparation of thin ceramic monofilaments for characterization by TEM. *Ultramicroscopy,* Vol. 92, No. 3-4, (August 2002) 159-164

Novak, S.; Koenig, K. & Drazic, G. (2006). The preparation of LPS SiC-fibre-reinforced SiC ceramics using electrophoretic deposition. *Journal of Material Science,* Vol. 41, No. 24, (October 2006) 8093-8100

Novak, S.; Drazic, G.; Koenig, K. & Ivekovic, A. (2010). Preparation of SiCf/SiC composites by the slip infiltration and transient eutectoid (SITE) process. *Journal of Nuclear Materials,* Vol. 399, No. 2-3, (2010) 167- 174

Nuriel, S.; Liu, L.; Barber, A. H. & Wagner, H. D. (2005). Direct measurement of multiwall nanotube surface tension. *Chemical Physics Letter,* Vol. 404, No. 4-6, (March 2005) 263-266

She, J. H. & Ueno, K. (1999). Effect of additive content on liquid-phase sintering on silicon carbide ceramics. *Materials Research Bulletin,* Vol. 34, (1999) 1629-1636

Stadelman, P. A. (1987). EMS - a software package for electron diffraction analysis and HREM image simulation in materials science. *Ultramicroscopy,* Vol. 21, No. 2, (1987) 131

Taguchi, T.; Igawa, N.; Yamada, R. & Jitsukawa, S. (2005). Effect of thick SiC interphase layers on microstructure, mechanical and thermal properties of reaction-bonded SiC/SiC composites. *Journal of Physics and Chemistry of Solids,* Vol. 66, No. 2-4, (February-April 2005) 576-580

Xin-Bo, H. & Hui, Y. (2005). Preparation of SiC fiber-reinforced SiC composites. *Journal of Materials Processing Technology,* Vol. 159, No. 1, (January 2005) 135-138

Xin-Bo, H.; Xin-Ming, Z.; Chang-Rui, Z.; Xin-Gui, Z. & An-Chen, Z. (2000). Microstructures and mechanical properties of Cf/SiC composites by precursor pyrolysis-hot pressing. *Materials Science and Engineering A,* Vol. 284, No. 1-2, (May 2000) 211-218

Zhang, W.; Hinoki, T.; Katoh, Y.; Kohyama, A.; Noda, T.; Muroga, T. & Yu, J. (1998). Crack initiation and growth characteristics in SiC/SiC under indentation test. *Journal of Nuclear Materials,* Vol. 258-263, No. 2, (October 1998) 1577-1581

7

Mechanical Properties of Ceramics by Indentation: Principle and Applications

Didier Chicot[1] and Arnaud Tricoteaux[2]
1) Laboratory of Mechanics, University of Science and Technology of Lille,
2) Laboratory of Materials and Process, University of Valenciennes and Hainaut Cambrésis, France

1. Introduction

Mechanical properties such as hardness, bulk modulus, tensile properties and toughness of massive ceramics and adhesion or cohesion of ceramic coatings can be determined by indentation tests. From a general point of view, the indentation test simply consists of performing a print at the surface of a material by the penetration of a hard indenter at a given indentation load. For this purpose, the indenter can have different geometrical shapes such as spherical, conical or pyramidal, the objective being to produce a different elastoplastic deformation of the material below the indenter. The indentation load can be chosen in the nano-, micro- or macro-indentation ranges thus allowing the study of local or global mechanical properties. The mechanical properties are determined by analysing the geometrical dimensions of the residual indent (usual indentation) or from the analysis of a load-depth curve (instrumented indentation tests). Generally, pyramidal indenters are used to determine hardness, bulk modulus and cracking resistance of the material, whereas spherical indenters are mainly used to determine the tensile properties and bulk modulus. The objective of this chapter is to give theoretical and experimental tools for determining the mechanical properties by indentation of massive ceramics and ceramic coatings. The chapter is divided in five parts: 1) Hardness definition, indentation size effect, dynamic hardness and hardness of thin films, 2) Bulk modulus of massive materials using the Marshall's method and the Oliver and Pharr's method, spherical and Vickers indentations and bulk modulus modelling for thin films, 3) Vickers indentation fracture toughness, 4) Tensile mechanical properties and 5) Adhesive properties by scratch tests for thin films and interface indentation tests for thick coatings.

2. Hardness

2.1 Definition

The hardness of a material represents its resistance to plastic deformation usually by indentation. The general relation to calculate a hardness number is given by:

$$H = \frac{P}{A} \tag{1}$$

where H is the hardness number, P the applied load and A, a representative area of the residual indent.

For usual indentation, the hardness number can be calculated considering the true or the projected contact area. Indeed, the true contact area is used for Vickers (pyramidal square based) indentation, HV, whereas the projected contact area is used for both Meyer hardness, Hm, also using a Vickers indenter and for Knoop (pyramidal lozenge based) indentation, HK_P. Depending on the geometrical dimensions of the indenter, the hardness calculation is related to the Vickers indent diagonal, d, and to the large diagonal of the Knoop indent, L, according to the hardness definitions (Table 1).

	True contact area	Projected contact area
Vickers indenter	$HV = 1.8544\frac{P}{d^2}$	$Hm = 2\frac{P}{d^2}$
Knoop indenter	$HK_T = 12.873\frac{P}{L^2}$	$HK_P = 14.229\frac{P}{L^2}$

Table 1. Hardness calculation considering true or projected contact area for Vickers and Knoop indentions.

Note that in Table 1, the Knoop hardness, HK_T, is not a conventional hardness number. On the other hand, direct comparison between, as actually performed, Vickers hardness and Knoop hardness is not possible, whereas it is correct when considering the Meyer hardness. Nevertheless, for a valid comparison between Vickers and Knoop hardness numbers, Chicot et al. (2007a) suggested the consideration of the true contact area in the Knoop hardness calculation, i.e. HK_T. Figure 1a shows a typical comparison of hardness data deduced from indentation of different ceramics (Mukhopadhyay et al., 1990; Ullner et al., 2001 & 2002; Gong et al., 2002).

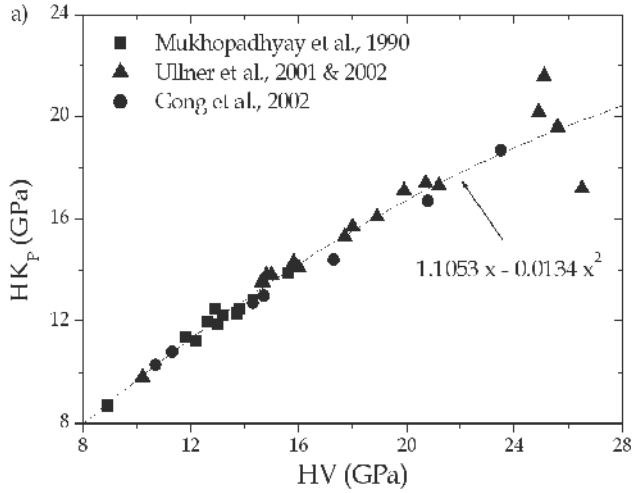

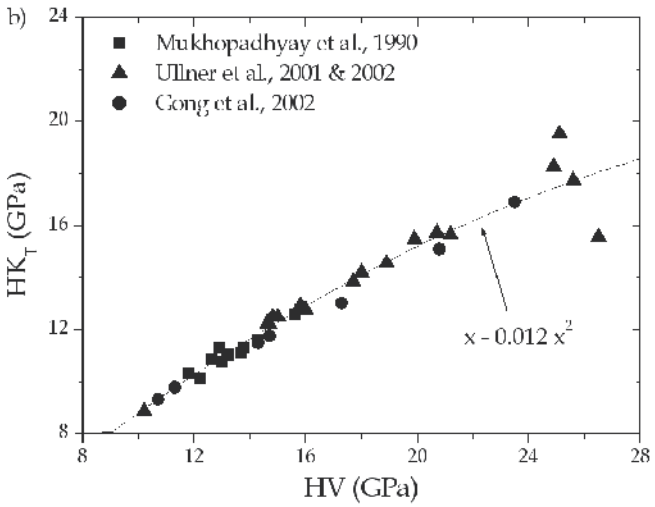

Fig. 1. Knoop hardness number as a function of Vickers hardness number for a variety of ceramics, where HK is calculated considering the projected contact area, HK_P, (a) or the true contact area, HK_T, (b).

Figure 1a shows that the conventional Knoop hardness number, HK_P, can be represented as a function of the Vickers hardness number, HV, by a second order polynomial, as follows:

$$HK_P = 1.1053 \cdot HV - 0.0134 \cdot HV^2 \tag{2}$$

The solution of this equation is obtained when the limit hardness, i.e. H_{lim}, is equal to 7.9 GPa, which respects the two following conditions:

$$\begin{aligned} &\text{If } HV < H_{lim} \text{ then } HK_P > HV \\ &\text{If } HV > H_{lim} \text{ then } HK_P < HV \end{aligned} \tag{3}$$

In any case, existence of such limit hardness has no physical justification. On the other hand, in fig. 1b the Knoop hardness number, HK_T, is expressed as a function of the Vickers hardness number, HV, by the polynomial:

$$HK_T = HV - 0.012 \cdot HV^2 \tag{4}$$

It is noticeable that the fitting coefficient in front of HV in eq. 4 is equal to 1. Nevertheless, this result was expected since the theoretical ratio to convert HK_P to HK_T is given by (14.229/12.873) = 1.1053 (see Table 1), which is the coefficient appearing in eq. 2. As a main conclusion, the two hardness numbers are the same only when the hardness value tends to zero. Consequently, no surprising change of the hardness will occur over the entire range of the hardness data.

For instrumented indentation tests (IIT), which allow the plot of a load-depth curve, the calculation of a hardness number can use the maximum distance (*maximum indentation depth,* h_m*, reached by the indenter during the indentation test*), the residual depth (*indentation depth,* h_r,

obtained after the complete withdrawal of the indenter) or the contact depth *(indentation depth,* h_c*, taking into account the deformation of the indent under load and calculated using the method of Oliver and Pharr (1992)*). Consequently, the hardness calculation can have different forms (Table 2) according to the indentation depth which is considered. As a result, comparison with hardness data obtained by several laboratories is somewhat difficult, even impossible if the hardness calculation is not well specified.

Indentation depth	Maximum	Residual	Contact
True contact area	$HM = \frac{P}{26.43 h_m^2}$	$H = \frac{P}{26.43 h_r^2}$	$H = \frac{P}{26.43 h_c^2}$
Projected contact area	$H = \frac{P}{24.5 h_m^2}$	$H = \frac{P}{24.5 h_r^2}$	$HIT = \frac{P}{24.5 h_c^2}$

Table 2. Hardness numbers considering true or projected contact areas and different indentation depth definitions.

To visualize the indentation depths, figure 2a represents schematically the cross-section of an indent and figure 2b shows the corresponding calculation of the indentation depths based on the analysis of a load-depth curve (Oliver and Pharr, 1992).

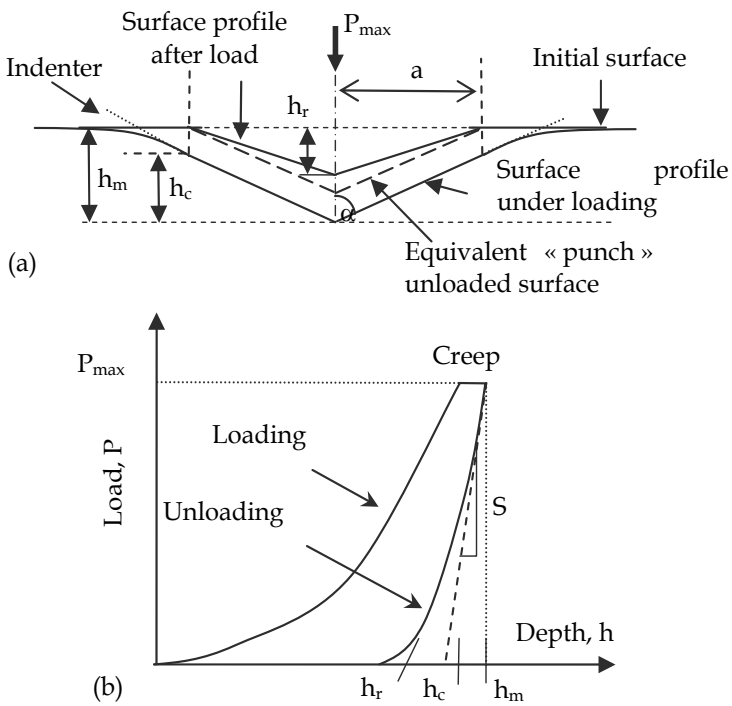

Fig. 2. (a) Schematic cross-section of a conical indent and (b) Load-depth curve and indentation depths used to calculate the hardness numbers.

Note that the Martens hardness, HM, and the contact hardness, HIT, are mainly used in micro and nano-indentation, respectively. The others hardness numbers are only given as a possibility of hardness calculation. In addition, HM is equivalent to HV if considering the diagonal to depth ratio of a Vickers indenter. As a conclusion, the different possibilities for calculating a hardness number must oblige the authors to specify correctly the hardness calculation (indenter type, contact area and the indentation depth), in order to have a sound discussion on the hardness behaviour of the material.

2.2 Indentation Size Effect

Whatever the shape of the indenter, the hardness number could be independent of load, it could increase or decrease with load, and it could show a complex variation with load changes depending on the material. This hardness-load dependence is known as the Indentation Size Effect (ISE). This phenomenon has been associated with various causes such as work hardening, roughness, piling-up, sinking-in, shape of the indenter, surface energy, varying composition and crystal anisotropy, which have been all discussed extensively by Cheng and Cheng (2004). Many relationships collected in a non-exhaustive list in table 3 (Chicot et al., 2007b), dating from 1885 to the present, have been suggested to describe the hardness-load dependence by expressing the applied load, P, as a function of the indent diagonal, d, or the hardness, H, as a function of the indentation depth, h.

Equations: Polynomial laws	Referring	Equations: Strain Gradient Plasticity Theory	Referring
$P = A_0 \cdot d^2$	Kick, 1885	$\frac{H}{H_0} = \sqrt{1 + \frac{h^*}{h}}$	Nix & Gao, 1998
$P = A_1 \cdot d^n$	Meyer, 1908	$\frac{H}{H_0} = 1 + \sqrt{\frac{h^*}{h}}$	Chong & Lam, 1999
$P - W = A_2 \cdot d^2$	Hays & Kendall, 1973	$\begin{cases} H = H_0\sqrt{1 + \frac{h^*}{h}} + H_1 \\ H = H_0\left(1 + \sqrt{\frac{h^*}{h}}\right) + H_1 \end{cases}$, $H_1 = g \cdot \frac{f}{h}$	Qiu et al., 2001
$P = c_0 + c_1 d + c_2 d^2 + \cdots + c_n d^n$	Bückle, 1973		
$P = A_3 \cdot (d + d_0)^2$	Bull et al., 1989		
$P = A_4 d + B_4 d^2$	Li & Bradt, 1993		
$Pd = w_1 d^2 + w_2 d^3$	Gong et al., 1999		
$P = c_0 + c_1 d + c_2 d^2$	Sangwal et al., 2002	$\left(\frac{H}{H_0}\right)^{\beta} = 1 + \left(\frac{h^*}{h}\right)^{\beta/2}$	Abu Al-Rub, 2004

Table 3. Parametric laws for modelling the Indentation Size Effect.

By analysing experimental hardness results, the majority of these relations are able to adequately represent the hardness-load dependence from a mathematical point of view. However, when studying ISE in nano and micro-indentation, it is observed that the fitting parameters and the theoretical ones change without any clear justification. Then, to explain this difference, Chicot (2009) suggested the use of a hardness-length scale factor based on the strain gradient plasticity theory formerly proposed by Nix and Gao (1998). These authors showed that the ISE behaviour of crystalline materials can be accurately modelled

by introducing the concept of geometrically necessary dislocations (GND) based on Taylor's dislocation theory. They based their reasoning on the experimental law needed to advance a mechanism-based theory of strain gradient plasticity. The relation between the hardness and the indentation depth is:

$$\left(\frac{H}{Ho}\right)^2 = 1 + \left(\frac{h^*}{h}\right) \tag{5}$$

where Ho is the macro-hardness and h* the characteristic scale-length representing the hardness-load dependence.
Nix and Gao (1998) assumed for simplicity that the indentation deformation process is accommodated by geometrically necessary dislocations which are required to account for the permanent shape change at the surface. In these conditions, the macro-hardness and the characteristic scale-length of eq. 5 are expressed as follows:

$$Ho = \frac{3\sqrt{3}}{2}\mu b\sqrt{\rho_s} \quad \text{and} \quad h^* = \frac{81}{8}\frac{1}{f^3} b \tan^2\theta \left(\frac{\mu}{Ho}\right)^2 \tag{6}$$

where μ is the shear modulus, b the Burger's vector, ρ_s the density of statistically stored dislocations and θ is equal to 19.3°. f is a corrective factor introduced by Durst et al. (2005) to take into account the GND effect on the size of the plastic zone. The factor f is equal to 1 in micro-indentation whereas it is equal to 1.9 for Durst et al. (2005) and to 1.44 for Nix and Gao (1998) in nano-indentation.
However, no direct comparison between the two couples $(Ho, h^*)_{micro}$ in micro-indentation and $(Ho, h^*)_{nano}$ in nano-indentation can be concluded due to the presence of the dislocation density which is not easily accessible prior to the indentation test and due to the relationship between h* and Ho, as shown in eq. 6. For these reasons, Chicot (2009) suggested the study of the indentation behaviour at the two scales of measurement by expressing the square of the hardness versus the reciprocal of the indentation depth. The slope, expressed as a function of the macro-hardness and the characteristic scale-length, is then proportional to an indentation toughness expressed in $MPa.m^{1/2}$. This parameter is called the hardness length-scale factor, H_{LSF}, which is equivalent to:

$$H_{LSF} = H_o\sqrt{h^*} \quad \text{when} \quad H^2 = H_o^2 + \frac{\left(H_o\sqrt{h^*}\right)^2}{h} \tag{7}$$

Then, by using eq. 6 and taking f equal to 1 in micro-indentation and 1.44 for nano-indentation according to Nix and Gao (1998), the hardness length-scale factor is simply written as a proportionality function of the shear modulus and the Burger's vector as follows:

$$H_{LSF\,micro} = 1.14 \cdot \mu\sqrt{b} \quad \text{and} \quad H_{LSF\,nano} = 0.66 \cdot \mu\sqrt{b} \tag{8}$$

It is important to add that eq. 8 is only applicable for crystals. For other types of materials, eq. 7 is always appropriate but the hardness length-scale factor can only be used for

representing the ability of the material to deform by indentation but not for determining the above mentioned intrinsic parameters. However, the experimental hardness length-scale factor can be plotted as a function of the theoretical product $\mu.b^{1/2}$ for some indentation data obtained on various crystals using nano and micro-indentation experiments (Chicot, 2009). Figure 3 shows two straight lines with proportionality factors of 1.17 and 0.65 for micro-indentation and nano-indentation, respectively. These results agree very well with the theory (eq. 8).

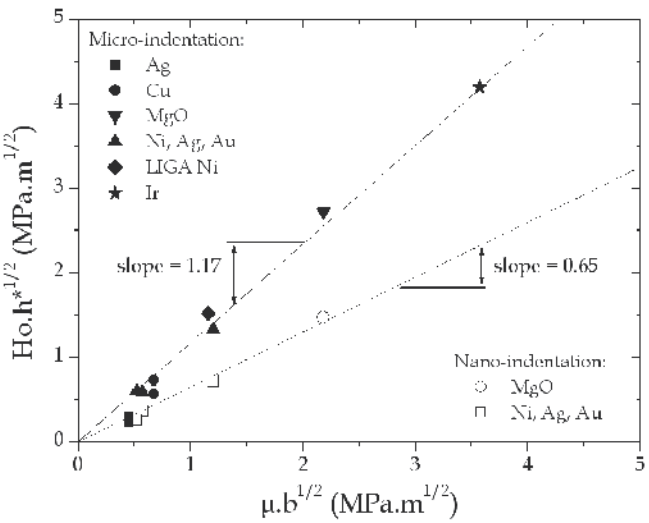

Fig. 3. Hardness length-scale factor, $Ho.h^{*1/2}$, as a function of the product, $\mu.b^{1/2}$, for various crystals.

As an example, we analysed the indentation size effect of a free porosity beta tricalcium phosphate bioceramic (called dense β-TCP ceramic in the following). The models of Meyer (1908), Li & Bradt (1993), Chong & Lam (1999) and Nix & Gao (1998) have been selected from the list (Table 3) and applied. Figure 4 shows that the models can adequately represent the ISE.

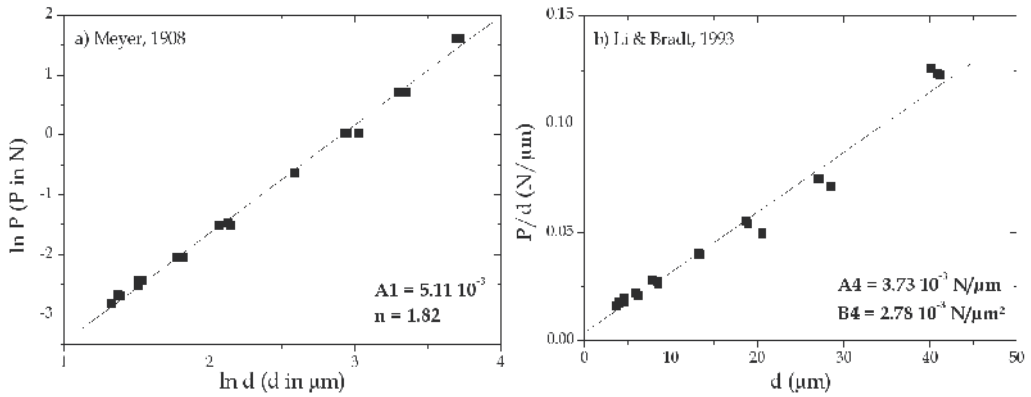

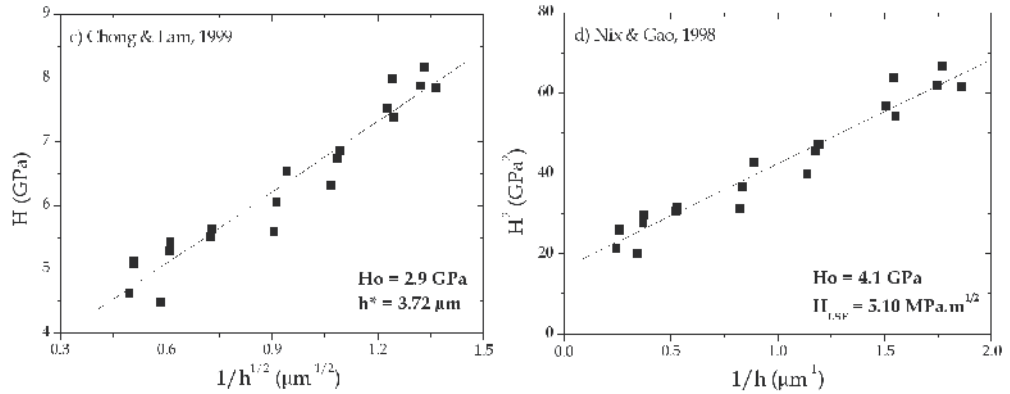

Fig. 4. Models of Meyer (1908) (a), Li & Bradt (1993) (b), Chong & Lam (1999) (c) and Nix & Gao (1998) (d) to represent the indentation size effect of the dense β-TCP ceramic.

Nevertheless, we prefer to use the model of Nix and Gao (1998) by introducing the hardness length-scale factor, which gives additional information about the ability of the material to deform plastically (Chicot, 2009).

2.3 Dynamic hardness

Usually the loading part of a load-depth curve (Fig. 2b) performed with a sharp indenter is described by a simple parabolic relationship between the applied load and the indentation depth of the form:

$$P = C_1 \cdot h^2 \tag{9}$$

where C_1 is a constant which depends on the geometry of the indenter tip and the material properties.

The validity of this relation has been demonstrated by means of numerical analysis of elastic-perfectly plastic and elastic-plastic materials (Giannkopoulos et al., 1994; Larsson et al., 1996; Giannakopoulos & Larsson, 1997; Briscoe et al., 1994; Bilodeau, 1992). Depending on the mechanical behaviour of the material, constant C_1 takes different forms expressed as a function of the elastic properties, yielding stress and stress measured at 29 % of strain of the material. However, numerous results (Giannkopoulos et al., 1994; Larsson et al., 1996; Giannakopoulos & Larsson, 1997) have shown that the experimental load-indentation depth relationship deviates from eq. 9 and that a better fit of the loading curve can be obtained by a more general power law taking a similar form of the Meyer's law (Meyer, 1908):

$$P = C_2 \cdot h^n \tag{10}$$

where C_2 is a material constant and n an exponent generally found to be less than 2.

Thus, the discrepancy between the experimental data and the theoretical description compromises the validity of the material properties derived from the loading curves analysis. Zeng and Chiu (2001) explained that the difference arises from the influence of the tip indenter defects. As a consequence, due to the rounding up of a sharp tip indenter, the initial part of the loading curve corresponding to the lowest indentation depth could be

modelled assuming that the indenter behaves as a spherical one. According to different authors, this approach is valid for the first 20-50 data points of the loading curve. For this region, the following relation could be applied:

$$P = C_3 \cdot h^{3/2} \tag{11}$$

where constant C_3 can be determined from fitting of the experimental data.
Beyond this point and until the maximum applied load, the authors consider a sharp indentation, but they introduce a constant P_0 to obtain a better fit of the second part of the loading curve, such that:

$$P = P_0 + C_4 \cdot h^2 \tag{12}$$

where P_0 and C_4 are also determined from the experimental data corresponding to this part of the curve.
The constant P_0 represents the initial deviation, which may arise from the initial contact load definition at the surface and/or due to the indenter tip imperfection. In micro-indentation, the influence of the indenter tip geometry is less pronounced than in nano-indentation since the influence of the rounded tip is sensitive only within a range of approximately 30 to 50 nm, depending on the size of such a defect (Chicot, 2009). For this reason, eq. 12 can be applied in micro-indentation over the entire loading curve by neglecting the effect of the rounded tip indenter. To consider the possible deviation of the zero contact, the constant load P_0 is introduced into the equation related to the Martens hardness definition (Table 2) in order to calculate a "dynamic" Martens hardness by considering the indentation depth reached by the indenter during the indentation:

$$HM = \frac{(P - P_0)}{26.43 \cdot h^2} \tag{13}$$

Then, by introducing eq. (12) into eq. (13), the dynamic Martens hardness becomes:

$$HM = \frac{C_4}{26.43} \tag{14}$$

which allows the relationship of constant C_4 with hardness. As a result, the hardness number is constant.
In order to take into account the indentation size effect, Chicot et al. (2010a) introduced eq. 7, expressing the Martens hardness as a function of the hardness length-scale factor, into the eq. 14 to express C_4 and, thereafter, into the eq. 12 to finally obtain the indentation loading curve function as follows:

$$P = P_0 + 26.43 \cdot \left(HM_0^2 + \frac{H_{LSF}^2}{h} \right)^{1/2} \cdot h^2 \tag{15}$$

As a conclusion, the proposed model representing the applied load (P) as a function of the indentation depth (h) involves three parameters: (*i*) the dynamic Martens macro-hardness (HM_0), (*ii*) the hardness length-scale factor (H_{LSF}) and (*iii*) a corrective load (P_0), considering the rounded tip effect of the indenter and the zero shifts.
The model is applied on the dense β-TCP ceramic. Figure 5 shows that eq. 15 adequately represents the loading curve and allows the determination of ISE parameters very close to those presented in figure 4d. Note that this methodology requires only one loading curve whereas classical approaches to study ISE require numerous indentation experiments to be accurate.

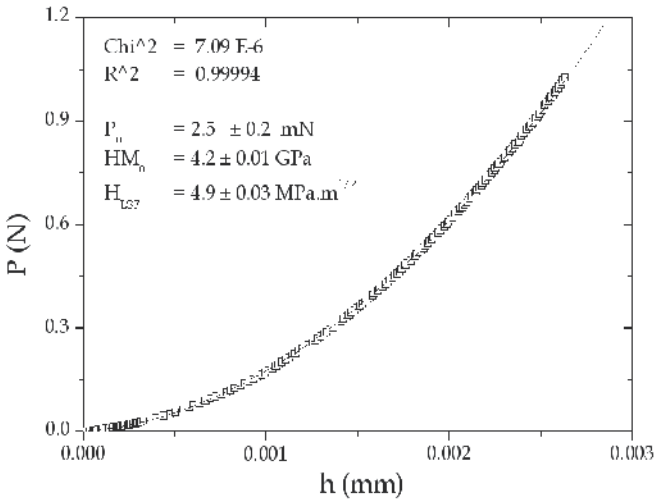

Fig. 5. Modelling of the loading curve (eq. 15) and values of the fitting parameters.

2.4 Hardness of thin films

For thin coated materials, direct measurement of the film hardness using conventional micro-hardness testers is not possible for a large range of indentation loads because the substrate undergoes a part of the plastic deformation during the indentation process. This phenomenon interferes when the indentation depth exceeds one tenth of the film thickness (Sun et al., 1995). In this case, the measured hardness number H_C is the result of the two contributions of the film and of the substrate. Then, to determine the true film hardness it is necessary to separate these two contributions. Numerous models suppose a linear additive law to express the measured hardness, H_C, as a function of the film hardness, H_F, and of the substrate hardness, H_S, as follows:

$$H_C = H_S + a \cdot (H_F - H_S) \tag{16}$$

where the film coefficient, a, is associated with the film contribution.
The difference between the models comes from the expression describing the variation of the coefficient, a, as a function of the indent diagonal, the film thickness and elastic properties of both the film and the substrate. One of the earliest works was that of Bückle (1973), who defined the coefficient as a function of weighting factors associated with the volume of each layer of an influence zone affected by the indentation. Later, a more

successful model was due to Jönsson and Hogmark (1984), which considered the load supporting areas under the indent associated with the substrate and the film. From geometrical considerations, these authors expressed the film coefficient by the following relation:

$$a = C\left(\frac{t}{d}\right) - C^2\left(\frac{t}{d}\right)^2 \tag{17}$$

where t is the film thickness and d the indent diagonal. C is a constant equals to 1 for low H_F/H_S (ductile films) and 0.5 for high H_F/H_S (brittle films).
Considering that this model does not represent the real deformation behaviour during indentation, other authors have searched to link the film coefficient to the volumes of the plastic zones developed under the indent. This was proposed originally by Sargent (1979), followed by Burnett and Rickerby (1987a, 1987b) and Bull and Rickerby (1990) who used an interface parameter χ calculated from the following relations:

$$a = \frac{V_F}{V} \text{ with } V = V_F + \chi \cdot V_S \text{ and } \chi \propto \left(\frac{E_F \cdot H_S}{E_S \cdot H_F}\right)^q \text{ for } H_F > H_S \tag{18}$$

where E_F and E_S are the elastic modulus of the film and substrate, respectively. Nevertheless, the exponent q and, as a consequence, χ, could be considered as adjustment parameters.
In order to avoid the introduction of such fitting parameters, Chicot and Lesage (1995) proposed a model based on the superposition of two hypothetic systems representing the volumes of the plastic deformation in the film and in the substrate under the indent. The mathematical development led to the following expression:

$$a = \frac{3}{2}\left(\frac{t}{d}\right)\left(\pi \cdot tg\xi\right)^{1/3}\left[\left(\frac{H_F}{E_F}\right)^{1/2} + \left(\frac{H_S}{E_S}\right)^{1/2}\right] - 2\left(\frac{t}{d}\right)^3\left(\pi \cdot tg\xi\right)\left[\left(\frac{H_F}{E_F}\right)^{3/2} + \left(\frac{H_S}{E_S}\right)^{3/2}\right] \tag{19}$$

where ξ is the indenter semi-angle (74°). In addition, when the diagonal length is higher than that of the thickness, the second term becomes negligible.
In the two cases, supposing that E_F and E_S are known, the determination of H_F is possible, using a simple routine program applied to each couple of values for t and d. Basing their reasoning on the former model put forward by Burnett and Rickerby (1987a, 1987b), Ichimura et al. (2000) proposed an expression, which is a simplified form of eq. 19:

$$a = 3\left(\frac{t}{d}\right)\left(tg\xi\right)^{1/3}\left(\frac{H_F}{E_F}\right)^{1/2} \tag{20}$$

Another way to consider the problem was proposed by Korsunsky et al. (1998) who developed a model based on the work of indentation associated with the deformation energy of the two materials and their interface under the indent:

$$a = \frac{1}{1 + k_K \cdot \beta^2} \tag{21}$$

where β is the relative indentation depth (d/7t) and k_K a fitting parameter. H_F is determined by fitting the experimental values of H_C in terms of β.
On the basis of geometrical considerations about the dimensions of the indent, Puchi-Cabrera (2002) proposed the computation of the composite hardness where two constants, k_P and n_P, represent material parameters:

$$a = \exp\left(-k_P \cdot \beta^{n_P}\right) \tag{22}$$

The above-mentioned models express the composite hardness H_C as a linear additive law in terms of the film and substrate hardness (eq. 16) comparable to a "series relation". Contrarily, Lesage et al. (2006) propose to consider a parallel relation:

$$\frac{1}{H_C} = \frac{1}{H_S} + a\left(\frac{1}{H_F} - \frac{1}{H_S}\right) \tag{23}$$

where the calculation of the film coefficient, a, is extensively described in Lesage et al. (2006). As an example, Chicot et al. (2008) studied the hardness of a TiN ceramic thin film (t = 1.1 μm) deposited on a stainless steel substrate (AISI 316L) by means of Magnetron Sputtering. Figure 6 shows the cross-section and the top view of the TiN film.

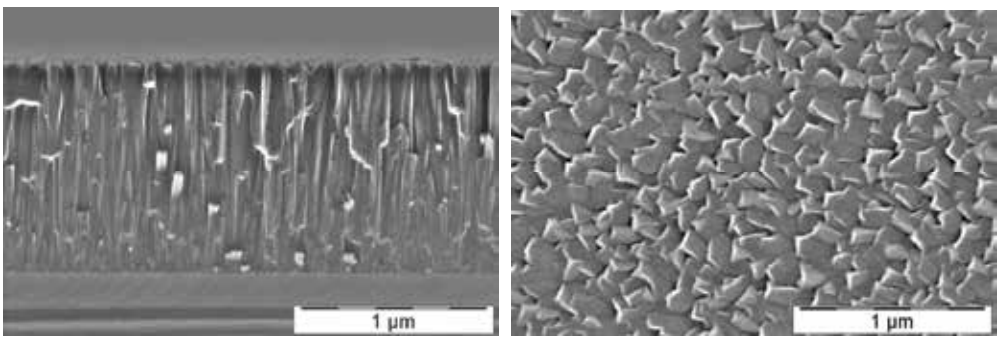

(a) (b)

Fig. 6. Cross-section (a) and in-plane-view (b) of the TiN film (SEM SE 20 kV 100000x) performed at ENEA in Brindisi.

In order to improve the accuracy of the film hardness determination, Chicot et al. (2008) employed three complementary approaches, i.e. Vickers hardness (HV) and Knoop hardness (HK_P) by using usual indentation tests (Table 1) and the contact hardness (HIT) deduced from load-depth curves analysis performed with a Vickers indenter (Table 2). Figure 7a represents the different hardness numbers as a function of the applied load on the same graph clearly showing disparities between the different techniques employed.

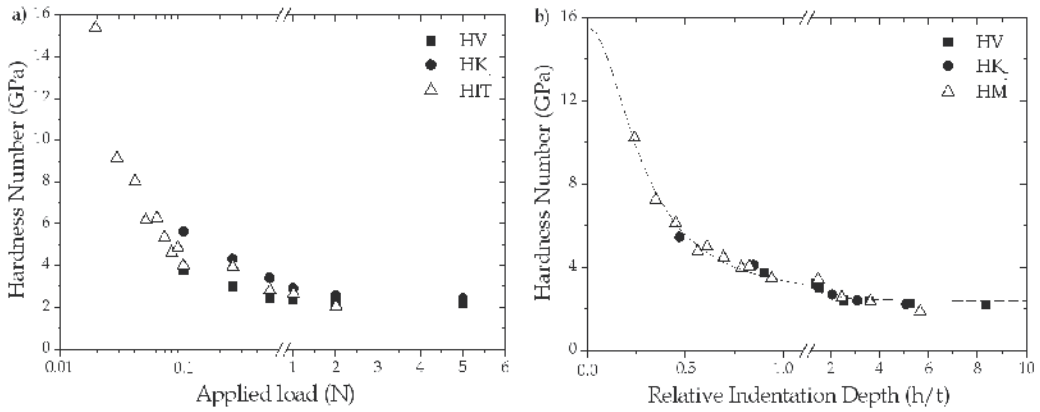

Fig. 7. (a) Hardness numbers from Vickers, Knoop and contact hardness calculations as a function of the applied load and (b) corrected hardness values as a function of the relative indentation depth.

In order to validly compare the indentation results obtained by the three methodologies, we converted Knoop hardness according to the eq. 4 and employed Martens hardness instead of HIT, which can vary to a great extent compared to Vickers or Martens hardness. As a result, Figure 7b shows that the consideration of the Vickers hardness, the Knoop hardness (HK_T) converted in an equivalent Vickers Hardness (eq. 4) and the Martens hardness (HM) allows the representation of all the hardness numbers as a function of the relative indentation depth on a unique curve. Finally, we have applied some thin film hardness models to determine the film hardness by using separately each set of hardness data. The macro-hardness of the film is collected in Table 4. Note that to give relevant prediction values; the model of Korsunsky requires indentation data for which the relative indentation depth is close to 0.1 thus explaining in this case that the predictive values are so low for Vickers and Knoop indentations.

TiN, t = 1.1 µm	Models	Jönsson et al. (1984)	Chicot et al. (1995)	Korsunsky et al. (1998)	Lesage et al. (2006)
Hardness (GPa)	Vickers (HV)	18.7	17.0	5.6	21.0
	Knoop (HK_T)	18.0	16.2	6.9	18.7
	DSI (HM)	18.8	16.8	16.3	17.4

Table 4. TiN ceramic thin film macro-hardness calculated by different film hardness models.

By analysing a loading curve performed on a thin film, it is possible to determine the ISE parameters of the film only by using eq. 15 to fit the part of the loading curve which is not affected by the substrate, i.e. for $h < t/10$. As an example, this fitting equation is applied on the loading curve obtained on the TiN thin film. Figure 8 shows the experimental load-depth curve obtained on the coated system and, as a reference, the substrate hardness also modelled by eq. 15.

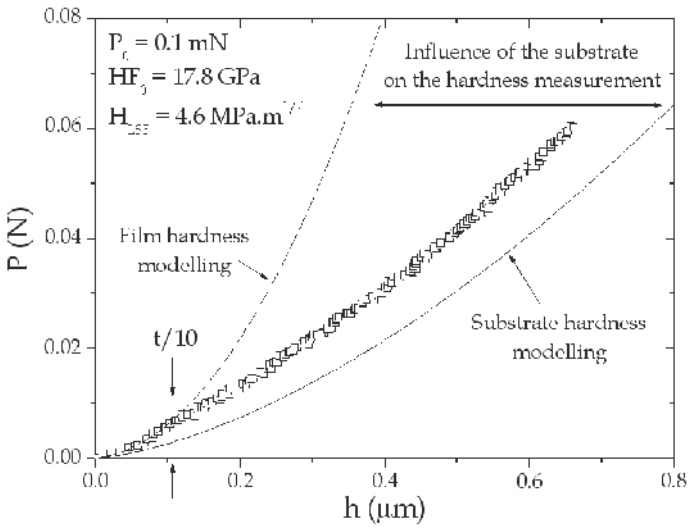

Fig. 8. Loading curve for the TiN thin film of 1.1 μm of thickness modelled by eq. 15.

It is clear that the measured hardness changes from the film hardness for lowest loads to the substrate hardness for highest loads. Then, by fitting the experimental data for which the indentation depth is lower than 10 % of the film thickness, i.e. 0.1 μm for t = 1.1 μm, we obtained the ISE parameters of the film as indicated in figure 8. The film macro-hardness obtained, i.e. 17.8 GPa, agrees very well with the hardness predicted values collected in Table 4. It is also clear that the accuracy of this methodology will depend on the range of hardness data available for applying the loading curve model.

3. Bulk modulus

3.1 Marshall's Method

The theoretical background for determining the bulk modulus of a material using the Knoop indentation test has been given by Marshall et al. (1980). The authors described a method for calculating the hardness/modulus ratio of a material from measurements of the Knoop indent diagonals. The decrease in the length of the indent diagonals is caused by elastic recovery of the material and, consequently, it can be related to the hardness/modulus ratio by the following equation:

$$\frac{w'}{L'} = \frac{w}{L} - \alpha \frac{HK_P}{E} \tag{24}$$

where w′ and L′ are the minor and the major diagonals of the measured Knoop indent. Contrarily, w and L are the minor and major diagonals of the ideal Knoop indent for which L/w equals to 7.11. HK_P is the Knoop hardness calculated by the relation given in Table 1 and E is the bulk modulus. α is a constant equal to 0.45 (Marshall et al., 1980). Note that the major diagonal is not affected by the elastic recovery after the withdrawal of the indenter, then L′ is equal to L. In addition, when considering the Knoop hardness HK_T (Table 1), the coefficient α becomes equal to 0.5. Applied to the dense β-TCP ceramic (Fig. 9) using P = 5 N

and 10 indentation tests, we found 4.57 ± 0.12 GPa for HK_P and 162.0 ± 26.5 GPa for the bulk modulus.

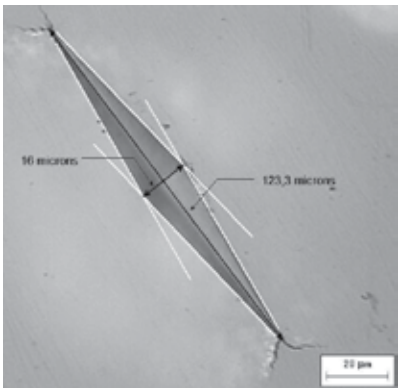

Fig. 9. Optical micrograph of a Knoop indentation performed on the dense β-TCP ceramic.

3.2 Oliver and Pharr method

Oliver and Pharr (1992) proposed that the bulk modulus could be calculated from the total compliance, $C_T = 1/S$ (Fig. 2b), of the specimen and of the instrument, which results from the contribution to the depth-measurement deflections of the load frame, added to the displacement into the material. Indeed, when load is applied, the reaction force is taken up by deflection of the load frame and it is this deflection that is typically added to the depth registration. The deflection is usually linearly proportional to the applied load in the manner of a linear spring (Fischer-Cripps, 2006). The correction takes the form of a product of the instrument compliance, C_f, and the load, P. This product must be subtracted from the depth recorded by the instrument:

$$h = h_{meas} - C_f \cdot P \tag{25}$$

where h and h_{meas} are the sole indentation depth into the material and the measured indentation depth by the instrument, respectively.
Oliver and Pharr (1992), based on the original work of Doerner and Nix (1986), proposed the following relation:

$$\frac{1}{S} = \left(\frac{dh}{dP}\right) = C_t = C_f + \frac{\sqrt{\pi}}{2}\frac{1}{\beta \cdot \gamma \cdot E_R\sqrt{A_C}} \tag{26}$$

where C_t is the total compliance, β is a correction factor which depends on the shape of the indenter and A_C is the projected contact area of the elastic contact measured from the indentation hardness impression. E_R is the reduced modulus defined as:

$$E_R = \left(\frac{1-\nu_m^2}{E_m} + \frac{1-\nu_i^2}{E_i}\right)^{-1} \tag{27}$$

where E_m, ν_m represent the bulk modulus and Poisson's ratio of the material and E_i, ν_i the elastic modulus and Poisson's ratio of the indenter, respectively.
The coefficient β is considered as a pure geometric factor for indenters which are not described as bodies of revolution like the pyramidal square-based Vickers indenter. The correction factor β is linked to the indenter geometry. King (1987) proposed a value of 1.012 for a Vickers indenter, whereas Dao et al. (2001) proposed a value of 1.07. Using a three dimension simulation of the Vickers indentation, Antunes et al. (2006) obtained 1.05 independently on the mechanical properties of the material. For a spherical indenter, the coefficient β is equal to 1. Furthermore, to explain the overestimation of the elastic modulus calculated by application of eq. 26, Hay et al. (1999) pointed out that the assumptions in Sneddon's solution were overlooked, especially in the boundary conditions. Indeed, in Sneddon's solution for indentation of an elastic half-space by a rigid cone or a spherical indenter, radial inward displacements of surface points inside the circle of contact occur. To consider this effect, the authors introduced a complementary correction factor γ in the eq. 26 which depends on the indenter shape.

3.3 Bulk modulus by Vickers and spherical indentations

The contact stiffness is very important in IIT since it is required to calibrate the indentation depth prior to the calculations. However, Chicot et al. (2009a and 2010b) have shown that it was not possible to calibrate the instrument prior to the bulk modulus calculation since the compliance value varies to a great extent as a function of the testing conditions; this phenomenon is also confirmed by Fischer-Cripps (2004). That is why in practice, we unfixed the compliance value and represented the contact stiffness as a function of the contact area according to eq. 26. For Vickers micro-indentation and by assuming a perfect contact area, i.e. by neglecting the top defect of the indenter, the projected contact area is then equal to:

$$A_C = 24.5 \cdot h_c^2 \tag{28}$$

By introducing eq. 28 into eq. 26, we obtained a linear relation between the inverse of the contact stiffness, (dh/dP), and the inverse of the contact indentation depth, h_c:

$$\left(\frac{dh}{dP}\right) = C_f + \sqrt{\frac{\pi}{24.5}} \frac{1}{2 \cdot (\beta\gamma) \cdot E_R} \cdot \frac{1}{h_c} \tag{29}$$

For Vickers indentation, the correction factor γ introduced by Hay et al. (1999) is only Poisson's ratio dependent as follows:

$$\gamma = \pi \frac{\pi/4 + 0.1548 \cot\lambda (1-2\nu)\left[4(1-\nu)\right]^{-1}}{\left(\pi/2 - 0.8312 \cot\lambda (1-2\nu)\left[4(1-\nu)\right]^{-1}\right)^2} \tag{30}$$

where λ (= 70.3°) is the semi-vertical angle of a conical indenter having the same area to depth ratio as the Vickers indenter (Veprek et al., 2006), i.e. $\pi \tan^2\lambda = 4\tan^2\xi$, where ξ (68°) is the semi-angle between the two opposites faces of the pyramid.

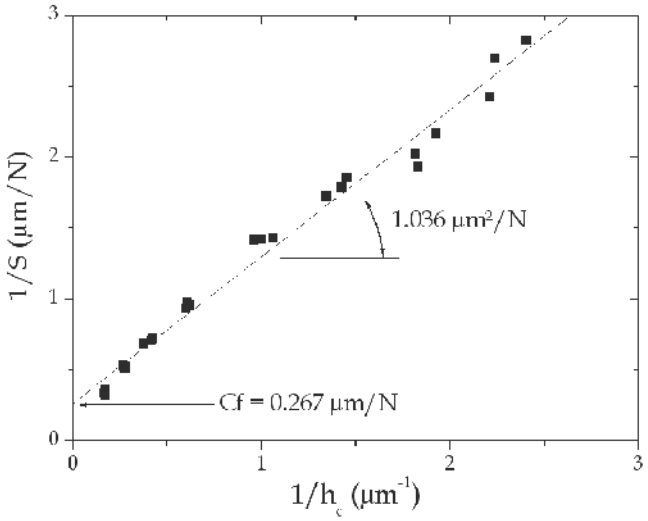

Fig. 10. 1/S as a function of $1/h_c$ for Vickers IIT performed on the dense β-TCP ceramic.

Figure 10 represents the inverse of the contact stiffness as a function of the inverse of the contact indentation depth obtained from Vickers indentation performed on the dense β-TCP ceramic. As a result, the representation is linear and therefore, the slope is directly linked to the bulk modulus of the material according to eq. 29. Then, by considering the elastic properties of diamond, i.e. 1140 GPa for the elastic modulus and 0.07 for the Poisson's ratio (Field and Telling, 1999) and by taking 0.3 for the Poisson's ratio of the material leading to 1.067 for the correction factor γ, the slope is reduced to $0.1598/E_R$. As a consequence, the reduced modulus is equal to 154.2 GPa and therefore, the bulk modulus of the dense β-TCP ceramic is equal to 162.1 ± 5.3 GPa. Note that this value is very close to the bulk modulus obtained by applying the Marshall's method.

For spherical indentation, Hertz's theory for sphere/plane contact provides three useful expressions:

1) The relation between the maximum indentation depth, h_m, and the contact indentation depth, h_c:

$$h_m = 2 \cdot h_c \tag{31}$$

2) The relation between the applied load, P, and the contact radius, a_c, where R is the spherical indenter radius:

$$P = \frac{4E_R a_c^3}{3R} \tag{32}$$

3) The relation between the total displacement and the contact radius:

$$h_m = \frac{a_c^2}{R} \tag{33}$$

By combining eq. 32 and eq. 33, we may write:

$$P = \frac{4}{3} E_R \sqrt{R}\, h_m^{3/2} \tag{34}$$

The derivation of the applied load compared to the maximum indentation depth leads to the following expression:

$$\frac{dP}{dh} = 2 E_R \sqrt{R}\, h_m^{1/2} \tag{35}$$

As a consequence, to take into account the frame compliance and relation 31 between h_m and h_c, we expressed the inverse of the contact stiffness as a function of the square root of the contact indentation depth as follows:

$$\left(\frac{dh}{dP}\right) = C_f + \left(\frac{1}{2 \cdot \gamma \cdot E_R \cdot \sqrt{D}}\right) \frac{1}{\sqrt{h_c}} \tag{36}$$

where the correction factor γ, introduced by Hay et al. (1999) for a spherical indenter depends on the Poisson's ratio, the contact radius and the sphere indenter radius as follows:

$$\gamma = 1 + \frac{2(1-2\nu)}{3\pi(1-\nu)} \cdot \frac{a_c}{R} \tag{37}$$

Note that to be valid, eq. 31 must be verified. For the dense β-TCP ceramic, we plotted in figure 11 the contact indentation depth as a function of the maximum indentation depth.
Figure 11 shows a deviation compared to eq. 31, which occurs for the highest indentation depths associated to loads higher than 1 N. That is why the corresponding indentation data are not considered for the bulk modulus calculation. Figure 12 represents the inverse of the contact stiffness as a function of the contact indentation depth reciprocal in the case of spherical indentations.

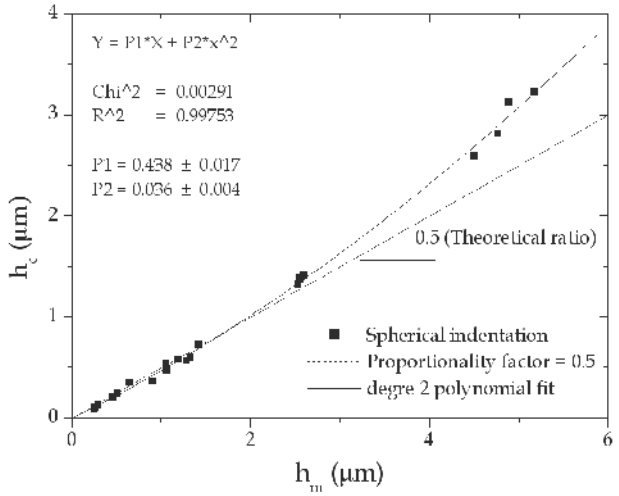

Fig. 11. h_c versus h_m for spherical indentation performed on the dense β-TCP ceramic.

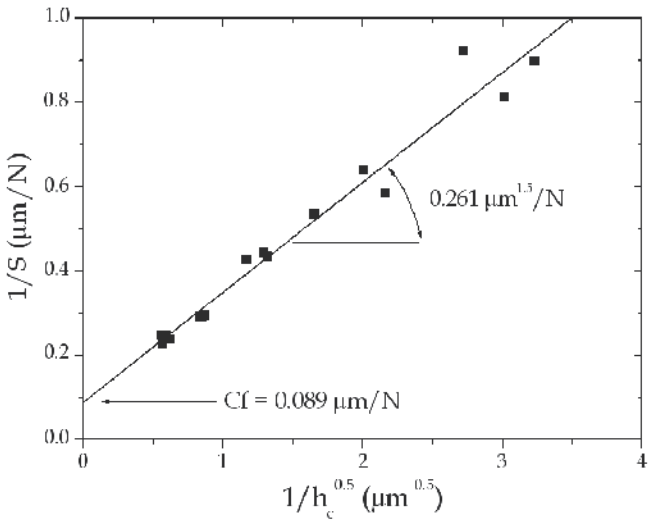

Fig. 12. 1/S as a function of $1/h_c^{0.5}$ for spherical IIT performed on the dense β-TCP ceramic.

Figure 12 confirms a linear variation that allows neglecting the correction factor, eq. 37, introduced by Hay et al. (1999) for spherical indentation which will lead to a non linear representation of the experimental data. The slope is proportional to the reduced modulus by $0.0354/E_R$ since the spherical indenter radius is equal to 100 µm. In this condition, the reduced modulus is equal to 135.6 GPa. By considering the elastic modulus and the Poisson's ratio of 540 GPa and 0.2 for the elastic properties of the tungsten carbide spherical indenter, the bulk modulus of the material is then equal to 162.6 ± 10 GPa, which is the same value found by Vickers indentation and by Marshall's method.

3.4 Bulk modulus of thin films

For a massive material, the inverse of the contact stiffness is a linear function of the inverse of the contact indentation depth obtained from Vickers indentation (Fig. 10), the corresponding slope being linked to the bulk modulus of the material. Then, instrumented indentation tests performed on a thin film would give a straight line when the substrate does not interfere with the measurement. On the contrary, the influence of the substrate is determined by two asymptotic limits corresponding to straight lines associated to the substrate behaviour for highest applied loads and to the film behaviour for the lowest applied loads, respectively. This phenomenon generally occurs for usual loads in micro-indentation and jointly for thin films. Figure 13 represents schematically the indentation results, which would be obtained from indentations performed on a hard film deposited onto a soft substrate.

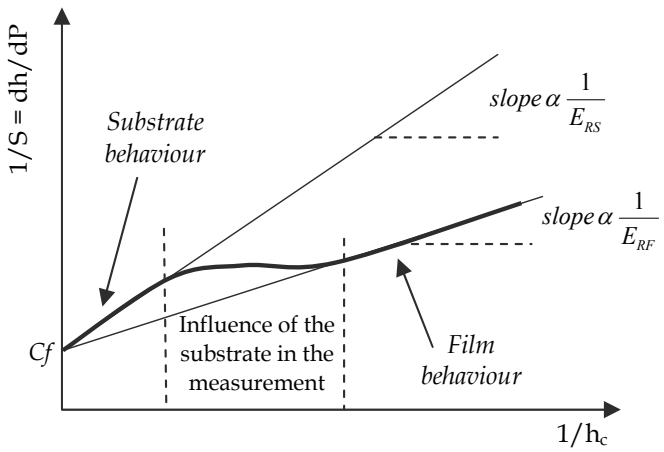

Fig. 13. Shematic representation of the contact stiffness variation of a coated system (hard film on soft substrate).

To represent correctly this behaviour, it is clear that an analytic model should consider the two limits, those of the film and of the substrate behaviours. The model proposed by Tricoteaux et al. (2010) is based on that of Korsunsky et al. (1998) initially developed for hardness measurement (eq. 21). Indeed, this model considers two asymptotic limits for the representation of the measured hardness of a coated material as a function of the relative indentation depth. Then, Tricoteaux et al. (2010) similarly suggested transposing eq. 16 devoted to hardness calculation, to the contact stiffness as follow:

$$\frac{1}{S_C} = \frac{1}{S_S} + a(h_c) \cdot \left(\frac{1}{S_F} - \frac{1}{S_S} \right) \tag{38}$$

where S_C, S_S and S_F are the contact stiffness corresponding to the *composite* material (substrate + film), the substrate and the film respectively. $a(h_c)$ represents the film contribution which depends on the contact depth.
By combining eq. 21, eq. 26 and eq. 38, we obtained the following expression for determining the bulk modulus of the film:

$$\frac{1}{S_C} = C_f + \left(\frac{1}{2\beta} \sqrt{\frac{\pi}{24.5}} \frac{1}{\gamma_S E_{RS}} \right) \frac{1}{h_c} + \frac{1}{h_c} \left(\frac{1}{1 + \frac{k}{t^2} h_c^2} \right) \left(\frac{1}{2\beta} \sqrt{\frac{\pi}{24.5}} \right) \left(\frac{1}{\gamma_F E_{RF}} - \frac{1}{\gamma_S E_{RS}} \right) \tag{39}$$

where E_{RF} and E_{RS} are defined according to the relation (27) for the film and the substrate, respectively.
From a general point of view, eq. 39 can be simply presented as follows, where the coefficients Pi are fitting parameters allowing the determination of the elastic properties:

$$\frac{1}{S_C} = P_1 + \frac{P_2}{h_c} + \frac{P_3}{h_c\left(1 + P_4 h_c^2\right)} \tag{40}$$

By comparing eq. 40 to eq. 39, we observed that the parameter P_2 only depends on the bulk modulus of the substrate, whereas P_3 depends on both substrate modulus and film modulus. As an example, the model is applied on TiCN PECVD thin films with film thickness of 2.2 μm deposited on a stainless steel substrate. Figure 14 shows a very good fit of the experimental data with a correlation coefficient R^2 very close to 1.

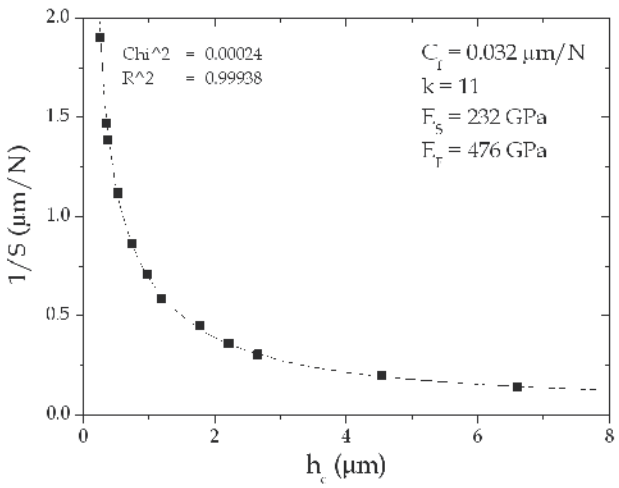

Fig. 14. Model for bulk modulus calculation of thin film applied to a TiCN thin film of 2.2 μm in thickness.

From the fitting parameters, the calculated value of the bulk modulus of the film is equal to 476 GPa in agreement with the values given by Karlsson et al. (2000) for similar coatings. Note that the bulk modulus of the substrate can be considered as unknown parameters. In this case, the model has been applied and the bulk modulus deduced from P_2 has been found to be equal to 232 GPa, which is a reasonable value.

4. Tensile mechanical properties

The true-stress and true-strain determined by uniaxial tensile tests are equivalent to spherical indentation stress and strain through the following expressions (Herbert et al., 2001):

$$\sigma_{\text{indentation}} \approx \frac{p_m}{3} \approx \sigma_{\text{uniaxial tension}} = \sigma \tag{41}$$

$$\varepsilon_{\text{indentation}} \approx 0.2\frac{a_c}{R} \approx \varepsilon_{\text{uniaxial tension}} = \varepsilon \tag{42}$$

where p_m is the mean pressure equivalent to the Meyer hardness calculated for spherical indentation, a_c is the contact radius and R the nominal radius of the indenter. Note that the ratio is sometimes taken equal to 2.8.
The mean pressure is calculated by:

$$p_m = \frac{P}{\pi \cdot a_c^2} \tag{43}$$

It is important to note that eq. 41 and eq. 42 are applicable in the limit of a fully developed plastic contact, i.e. when a_c/R is close to 0.16 independently of the magnitude of the non-dimensional parameter σ_y/E and the Poisson's ratio of the material. Moreover, in order to represent the plastic domain in tensile stress-strain deformation, different relations can be employed (Hollomon, 1945; Swift, 1952; Ludwik, 1909), the Hollomon's law being probably the most used:

$$\sigma = K_H \cdot \varepsilon^{n_H} \tag{44}$$

where K_H and n_H are the strength coefficient and the strain-hardening exponent, respectively.
In order to be valid, the stress expressed in eq. 44 must be calculated considering the plastic strain. In practice when Hollomon's law is not verified, the Ludwik's law is preferred to the Swift's law:

$$\sigma = \sigma_y + K_L \cdot \varepsilon^{n_L} \tag{45}$$

where K_L and n_L are the strength coefficient and the strain-hardening exponent, corresponding to this law, respectively.
From Hollomon's law, Alcala et al. (2000) combined equations (42), (43) and (44) to write:

$$p_m = 2.8 K_H \cdot \left(0.2 \frac{a_c}{R} \right)^{n_H} \tag{46}$$

Matthews (1980) by analyzing work-hardening materials following eq. 43 and eq. 44 provided an alternative expression for the mean contact pressure, p_m:

$$p_m = \frac{6 \cdot K_H}{(2 + n_H)} \cdot \left(\frac{8 \cdot a_c}{9\pi \cdot R} \right)^{n_H} \tag{47}$$

Based on the Ludwik's law, Huang et al. (2007) suggested representing the mean pressure as the function of the flow stress, σ_{flow}, and taking into account the indentation size effect as follows:

$$p_m = 2.8 \cdot \sigma_{flow} = 2.8 \cdot \sigma_{ref} \cdot \sqrt{\left[f(\varepsilon) \right]^2 + \frac{\ell}{R}} \tag{48}$$

where ℓ represents the ISE in spherical indentation. The stress, σ_{ref}, and the function, f, are deduced from Ludwik's law as follows:

$$\sigma = K_L\left(\frac{\sigma_y}{K_L} + \varepsilon^{n_L}\right) = \sigma_{ref}\cdot f(\varepsilon) \tag{49}$$

Then, by combining relations (42), (48) and (49), it is possible to express the applied load as a function of the indentation depth over the entire loading curve:

$$p_m = 2.8\cdot K_L\cdot\left(\sqrt{\left[\left(\frac{\sigma_y}{K_L}\right)+\left(0.2\frac{a_c}{R}\right)^{n_L}\right]^2+\frac{\ell}{R}}\right) \tag{50}$$

On the other hand, Gao (2006) proposed the introduction of strain-hardening and indentation size effect for conical and spherical indentation tests in the expanding cavity models (ECMs). The author expressed the ratio between the mean pressure, p_m, and the yield stress, σ_y, as a function of the contact radius to the indenter tip radius ratio. The proposed relations depend on the mechanical behaviour of the tested material and on the shape of the indenter.
Then, for spherical indentation, the relations are:
- For elastic perfectly plastic when no strain gradient effect is considered,

$$\frac{p_m}{\sigma_y} = \frac{2}{3}\cdot\left[\frac{7}{4}+\ln\left(\frac{1}{4}\frac{E}{\sigma_y}\frac{a_c}{R}\right)\right] \tag{51}$$

- For elastic perfectly plastic with strain gradient effect, factor c,

$$\frac{p_m}{\sigma_y} = \frac{2}{3}\cdot\left[\frac{7}{4}+\ln\left(\frac{1}{4}\frac{E}{\sigma_y}\frac{a_c}{R}\right)\right]-\frac{12c}{5E}\left[\left(\frac{9}{16}\frac{E}{\sigma_y}\frac{a_c}{R}\right)-\left(\frac{1}{4}\frac{E}{\sigma_y}\frac{a_c}{R}\right)^{-2/3}\right]\cdot\frac{1}{a_c^2} \tag{52}$$

- For elastic strain-hardening when no strain gradient effect is considered,

$$\frac{p_m}{\sigma_y} = \frac{2}{3}\cdot\left\{1+\frac{3}{4}\left(\frac{1}{4}\frac{E}{\sigma_y}\frac{a_c}{R}\right)^{n_H}+\frac{1}{n_H}\left[\left(\frac{1}{4}\frac{E}{\sigma_y}\frac{a_c}{R}\right)^{n_H}-1\right]\right\} \tag{53}$$

- For elastic strain-hardening with strain gradient effect, factor c,

$$\frac{p_m}{\sigma_y}=\frac{2}{3}+\frac{1}{2}\left(\frac{1}{4}\frac{E}{\sigma_y}\frac{a_c}{R}\right)^{n_H}+\frac{2}{3n_H}\left[\left(\frac{1}{4}\frac{E}{\sigma_y}\frac{a_c}{R}\right)^{n_H}-1\right]-\frac{12c}{5E}\cdot\left[\left(\frac{9}{16}\frac{E}{\sigma_y}\frac{a_c}{R}\right)-\left(\frac{1}{4}\frac{E}{\sigma_y}\frac{a_c}{R}\right)^{-2/3}\right]\cdot\frac{1}{a_c^2} \quad (54)$$

And for Vickers indentations where λ is defined in eq. 30, the relations are deduced from those for conical indentations:

- For elastic perfectly plastic when no strain gradient effect is considered,

$$\frac{P}{24.5\cdot\sigma_y}=\frac{2}{3}\cdot\left[\frac{7}{4}+\ln\left(\frac{1}{3}\frac{E}{\sigma_y}\cot\lambda\right)\right]\cdot h^2 \quad (55)$$

- For elastic perfectly plastic with strain gradient effect,

$$\frac{P}{24.5\cdot\sigma_y}=\frac{2}{3}\cdot\left[\frac{7}{4}+\ln\left(\frac{1}{3}\frac{E}{\sigma_y}\cot\lambda\right)\right]\cdot h^2-\frac{12c}{5E}\cdot\left(\frac{\pi\tan\lambda}{24.5}\right)^2\cdot\left[\left(\frac{3}{4}\frac{E}{\sigma_y}\cot\lambda\right)-\left(\frac{1}{3}\frac{E}{\sigma_y}\cot\lambda\right)^{-2/3}\right] \quad (56)$$

- For elastic strain-hardening when no strain gradient effect is considered,

$$\frac{P}{24.5\cdot\sigma_y}=\frac{2}{3}\cdot\left\{1+\frac{3}{4}\left(\frac{1}{3}\frac{E}{\sigma_y}\cot\lambda\right)^{n_H}+\frac{1}{n_H}\left[\left(\frac{1}{3}\frac{E}{\sigma_y}\cot\lambda\right)^{n_H}-1\right]\right\}\cdot h^2 \quad (57)$$

- For elastic strain-hardening with strain gradient effect,

$$\frac{P}{24.5\cdot\sigma_y}=\left\{\frac{2}{3}+\frac{1}{2}\left(\frac{1}{3}\frac{E}{\sigma_y}\cot\lambda\right)^{n_H}+\frac{2}{3n_H}\left[\left(\frac{1}{3}\frac{E}{\sigma_y}\cot\lambda\right)^{n_H}-1\right]\right\}\cdot h^2-\frac{12c}{5E}\cdot\left(\frac{\pi\tan\lambda}{24.5}\right)^2\cdot\left[\left(\frac{3}{4}\frac{E}{\sigma_y}\cot\lambda\right)-\left(\frac{1}{3}\frac{E}{\sigma_y}\cot\lambda\right)^{-2/3}\right] \quad (58)$$

Note that relations (55) to (58) correspond to the extended relations (9) and (12). Then, the second terms in eq. 56 and eq. 58 can be also associated with the zero shift P_0 in eq. 12. Independently of that, the determination of the tensile mechanical properties without any prior information on the mechanical behaviour of the material can be obtained by fitting these relations, allowing the determination of the yield stress, σ_y, strength coefficient, K_H or K_L, strain-hardening exponent, n_H or n_L, elastic modulus, E, and the constants, c or ℓ, characterizing the indentation size effect or the zero shift. A discussion about the value of these parameters must be helpful for identifying the mechanical behaviour of the material.

As an example, for studying the mechanical behaviour of the dense β-TCP ceramic, we plotted the indentation stress-strain data (Fig. 15) where the mean pressure under a sphere to plane contact is calculated by applying relation (43) and the ratio (a_c/R) is calculated from eq. 33, where h_m represents the indentation depth reached during the indentation test. In addition by combining eq. 32 and eq. 43, we may express the mean pressure as a function of the ratio (a_c/R) as follows:

$$P_m = \frac{4E_R}{3\pi}\frac{a_c}{R} \text{ with } \frac{a_C}{R} = \sqrt{\frac{h_m}{R}} \quad (59)$$

By taking into account the reduced modulus of the dense β-TCP ceramic equal to 135.5 GPa for spherical indentation (see part 3.3), we plot eq. 59 in figure 15 where the dash straight line corresponds to the theoretical Hertzian elastic response. As it is clearly seen, the Hertzian theory is verified until a limit value, p_y, which corresponds to the yield indentation stress as earlier demonstrated by Zhu et al. (2008).

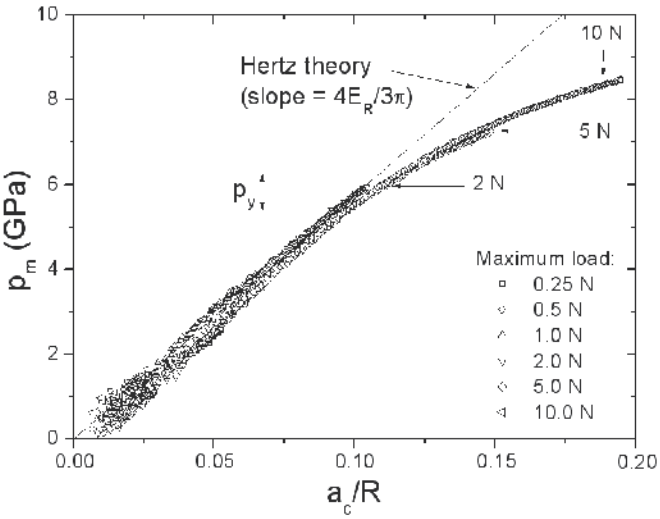

Fig. 15. Indentation stress-strain curve deduced from spherical IIT performed on the dense β-TCP ceramic.

For modelling the plastic domain of the dense β-TCP ceramic, we consider the indentation data drawn from spherical indentations for which the applied loads give a mean pressure higher than 5.5 GPa that seems to be the limit, p_y, between elastic and plastic domains as shown in figure 15. Without any information about the mechanical behaviour of such a ceramic, we applied the models of Alcala et al. (2000), Matthews (1980) and Huang et al. (2007) and the expanding cavity models developed for elastic perfectly plastic materials and for elastic strain-hardening materials by Gao (2006). Table 5 collects the values of the mechanical parameters according to the tested models.

	Spherical indentations							Vickers indentations			
Eq. n°	(46)	(47)	(50)	(51)	(52)	(53)	(54)	(55)	(56)	(57)	(58)
K_H, K_L (GPa)	21.7	21.4	7.4	-	-	-	-	-	-	-	-
n_H, n_L	0.60	0.60	0.18	-	-	- 0.60	- 0.65	-	-	0.14	0.16
σ_y (GPa)	-	-	1.8	6.6	6.0	8.2	8.3	2.1	2.2	1.8	1.8
E (GPa)	-	-	-	165	159	122	118	162	157	155	135
ℓ (μm)	-	-	-0.047	-	-	-	-	-	-	-	-
c (N)	-	-	-	-	- 0.95	-	0.03	-	0.03	-	0.03

Table 5. Tensile mechanical properties deduced from the different models applied to spherical and Vickers IIT performed on the dense β-TCP ceramic.

It is noticeable that the models of Alcala et al. (2000), eq. 46, and Matthews (1980), eq. 47, give the same values for the strain-hardening exponent, n_H, and for the strength coefficient, K_H, which lead to the same representative curve in figure 16a. Contrarily, the model of Huang et al. (2007) allows a better fit of the experimental data (Fig. 16a) but gives very different parameters since it considers the Ludwik's law instead of the Hollomon's law.

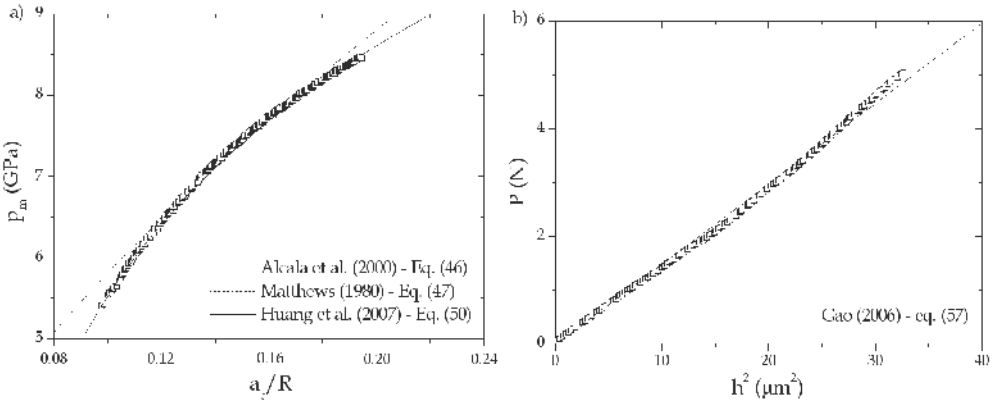

Fig. 16. Models representing a) $p_m = f(a_c/R)$ for spherical IIT and b) $P = f(h^2)$ for ECM and Vickers IIT performed on the dense β-TCP ceramic.

On the other hand, even if the expanding cavity models are able to adequately represent the experimental data, some values indicated in table 5 have no physical meaning such as the negative value for the work-hardening exponent. In the other cases of ECMs, the bulk modulus is in a good agreement with the theoretical value. Additionally, it can be seen that the introduction of the ISE has no significant influence on the values of the tensile parameters. For ECMs, eq. 55 to eq. 58, the bulk modulus is close to 160 GPa as already found by spherical indentations. However, the yield stress is three times less but of the same order of magnitude than the value found by the model of Huang et al. (2007). This difference has been observed by Zhu et al. (2008) who have highlighted the influence of the spherical indenter radius on the yield indentation stress. On the other hand, it is very interesting to note that the coefficients in the Ludwik's law deduced from the application of the model of Huang et al. (2007), eq. 50, are the same than those obtained by the expanding cavity model in the case of an elastic strain-hardening behaviour by considering or not the indentation size effect in the ECM developed for Vickers indentation, as shown in figure 16b. As a result, we can conclude that the tensile mechanical properties of the dense β-TCP ceramic in the non elastic domain can be modelled by Ludwik's law as follows, when the stress is expressed in GPa:

$$\sigma = 1.8 + 7.4 \cdot \varepsilon^{0.18} \tag{60}$$

5. Vickers Indentation Fracture Toughness

The Vickers indentation test is often used for determining the fracture toughness of ceramics. This method consists in indenting the ceramic with a Vickers indenter in order to generate cracks at the extremities of the indent. Afterwards, the toughness is calculated from the

dimensions of the indent diagonals and of the crack lengths. Since the Vickers Indentation Fracture (VIF) test is not standard, the calculated value for the toughness is called Kc instead of KIc. In practice, it is generally admitted that the cracks can be developed following radial-median or Palmqvist modes as represented in figure 17.

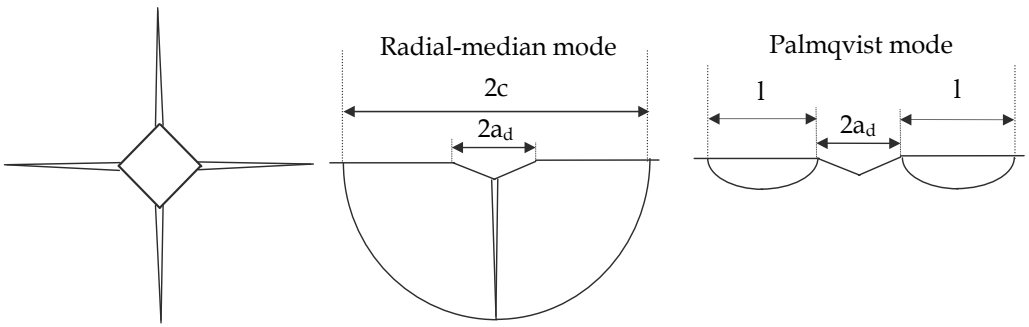

Fig. 17. Schematic representation of Vickers indentation cracks according to radial-median and Palmqvist modes.

The Vickers Indentation Fracture toughness can be calculated from various relationships depending on the load, indent diagonal, cracks length and Young's modulus to hardness ratio. Ponton & Rawlings (1989) have collected close to 20 crack equations depending on the cracking mode. More recently, Chicot et al. (2009b) have compared these relations and proposed to consider the average relations as follows according to the cracking mode:

$$\text{For Radial-median cracks: } Kc_{(R-M)} = 0.0154 \cdot \left(\frac{E}{HV}\right)^{1/2} \cdot \frac{P}{c^{3/2}} \tag{61}$$

$$\text{For Palmqvist cracks: } Kc_{(P)} = 0.0089 \cdot \left(\frac{E}{HV}\right)^{2/5} \cdot \frac{P}{a_d l^{1/2}} \tag{62}$$

Obviously, Kc must be an intrinsic parameter of the material, then the ratios $(P/c^{3/2})$ and $(P/a_d l^{1/2})$ of eq. 61 and eq. 62 should be constant independently of the applied load. In addition, eq. 62 is connected to the indent half diagonal, a_d, which is load dependent due to the indentation size effect. The simplest mathematical relation between the half-diagonal a_d and the load P is given by the Meyer's law (1908) (Table 3). By introducing Meyer's law into eq. 62, we may write the two following proportionality relations:

$$\text{For Radial-median cracks: } c \propto P^{2/3} \tag{63}$$

$$\text{For Palmqvist cracks: } l \propto P^{2\left(1-\frac{1}{n}\right)} \tag{64}$$

Then the cracking mode can be identified by comparing the experimental slope of ln c = f (ln P) to 2/3 or the experimental slope of ln l = f (ln P) to 2(1 – 1/n) for Radial-median and Palmqvist cracking modes, respectively.
However, in some cases, neither of these proportionality relations is verified because the cracking mechanism does not correspond to the usual cracking modes but to an intermediate state. Based on the cracking toughness relations from Miranzo et al. (1984) and on the work of Chicot et al. (2009b), we suggest the following expression to calculate VIF toughness for an intermediate cracking mode:

$$Kc_{(I-M)} = (\alpha - \beta \cdot q) \cdot f\left(\frac{E}{HV}\right) \cdot \frac{P}{a_d^q c^{(1.5-q)}} \tag{65}$$

where α and β are constants depending on the material, q is a constant ranging between 0 and 1 that describes the intermediate cracking mode and f(E/Hv) is a function which depends on the Young's modulus and the Vickers hardness as follows:

$$f\left(\frac{E}{HV}\right) = \frac{\left[\beta_{exp}^2 / \delta\right] - 1.5}{0.75} \text{ with } \delta = \frac{2}{3} \cdot \left(1 + \ln\beta_{exp}\right) \text{ and } \beta_{exp} = 0.768 \cdot \left(\frac{E}{HV}\right)^{0.408} \tag{66}$$

The two constants α and β are calculated by considering the two limit conditions for eq. 65. Indeed, when q = 0, $Kc_{(I-M)}$ corresponds to the Radial-median cracking mode (eq. 61) and when q = 1, $Kc_{(I-M)}$ corresponds to the Palmqvist cracking mode (eq. 62). Afterwards the exponent q is calculated from the following relation:

$$q = \left(\frac{1.5 \cdot s - 1}{s}\right) \cdot n \tag{67}$$

where s corresponds to the experimental slope of ln c = f (ln P) and n to the Meyer's index.
This methodology is applied on annealed bioglass (55 SiO_2 - 13.5 CaO - 31.5 Na_2O). However, as shown on Figure 18 for this type of very brittle materials, a secondary crack network appears in the vicinity of the four indent edges in addition to the main cracks generated at the four indent extremities. According to Roman et al. (2002), a mean crack length corresponding to an equivalent four cracks network is calculated by dividing the total cracks length by four.

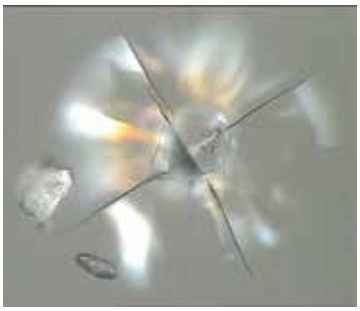

Fig. 18. Optical micrograph of the crack network resulting from Vickers indentation test performed on the (55 SiO_2 - 13.5 CaO - 31.5 Na_2O) bioglass.

For this bioglass, the Young's modulus and the Vickers hardness are equal to 63.6 GPa and 5.15 GPa, respectively and Meyer's index n is equal to 1.88. Figure 19 shows that cracking corresponds to an intermediate mode. Indeed, the slope s of ln c = f (ln P) is equal to 0.815, very different to the theoretical value 2/3 for a radial-median cracking mode. Moreover, the slope of ln l = f (ln P) is experimentally equal to 1.068, which is also different of the theoretical value 2(1-1/n) = 0.936 calculated from the Meyer's index (eq. 64) for a Palmqvist cracking mode. As a result, the exponent q calculated from eq. 67 is equal to 0.78 which is an intermediate value between 0 (Radial-median) and 1 (Palmqvist), the constants α and β in eq. 66 are equal to 0.0169 and 0.0065, respectively, found by equating the toughness calculation to the two limits. The VIF toughness Kc is found equal to 1 MPa.m$^{1/2}$, which is very close to the toughness measured by Rajendran et al. (2002) on SiO_2-CaO-Na_2O-P_2O_5 bioglasses.

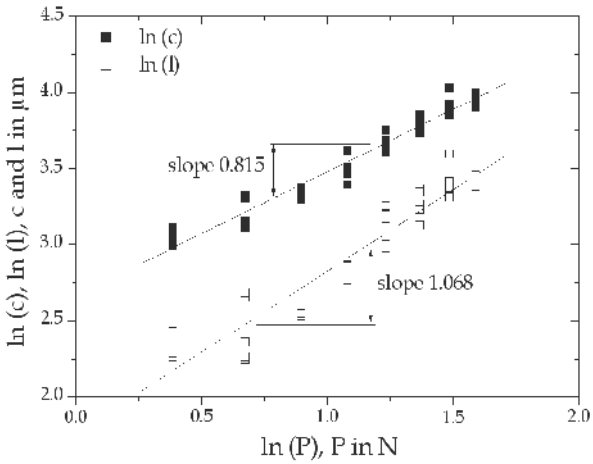

Fig. 19. Crack length criterion applied to results obtained on a SiO_2-CaO-Na_2O bioglass.

6. Adhesive properties of ceramic coatings

6.1 Scratch test

Heavens (1950), was the first to propose that the scratch test could be used for a qualitative evaluation of coating adhesion. Later, Benjamin and Weaver (1960) presented the first analysis by this test and proposed a model to connect the critical applied load, Lc, with the mechanical properties of the substrate and the adhesion of the coating. After, the scratch test has been used extensively for adhesion characterization of hard coatings such as TiN or TiC on steel (Laeng and Steinmann, 1981; Perry et al., 1981; Mittal, 1987). Generally, a Rockwell diamond tip is moved on the film at a constant velocity while a constant normal force (Laeng and Steinmann, 1981) or an increasing normal force is applied with a constant loading rate (Steinmann et al., 1987). During the indentation scratch test, the indenter introduces stresses at the interface between film and substrate causing delamination or chipping of the film. The adhesive property is then represented by the critical load at which the failure of the film is detected. The film failure characterized by the critical load, L_C, can be determined by the change in friction or in acoustic emission, or by observation of the scratch track. Moreover, the intensity of the acoustic emission depends on the type of film failure during the adhesion test e.g. cracking, chipping (cohesive failure) and delamination

(adhesive failure). The scratch test often uses an optical microscope to confirm the critical load. Nevertheless, it is often difficult to identify representative damage of interfacial decohesion and mechanical origins of damages. In addition, Sekler et al. (1988) discussed widely about the different techniques for determining the critical load of coated systems (microscopy, acoustic emission, and normal, tangential and lateral forces). In addition to the L_C calculation, Benayoun et al. (1999) presented different expressions for the film/substrate adhesion energy. Indeed, the expression for the critical shearing, τ_C, given by Benjamin and Weaver (1960), Weaver (1975) and Perry et al. (1981) is:

$$\tau_C = kH \cdot \left(\frac{d_C}{2R}\right) \cdot \left[1 - \left(\frac{d_C}{2R}\right)^2\right]^{-0.5} \tag{68}$$

where H is the hardness of the sample, d_C the scratch track width obtained at the critical load and R the tip radius of the indenter. k a numerical coefficient between 0.2 and 1.
Felder and Laugier (1992) proposed a similar expression:

$$\tau_C = p_m \cdot \left(\frac{d_C}{2R}\right) \text{ with } p_m = \frac{8L_C}{\pi d_C^2} \tag{69}$$

where p_m is the mean indentation pressure for a given critical load L_C.
As an example, figure 20 shows the results of an indentation scratch test obtained for a progressive load scratch (0.1 – 15 mN) on a polymer topcoat. This figure representing penetration depth (Pd), residual depth (Rd) and normal load during post-scan (FnP) signals clearly shows the critical load (L_C1) which corresponds exactly to the fracture point on the optical micrograph (CSM Bulletin, 2008).

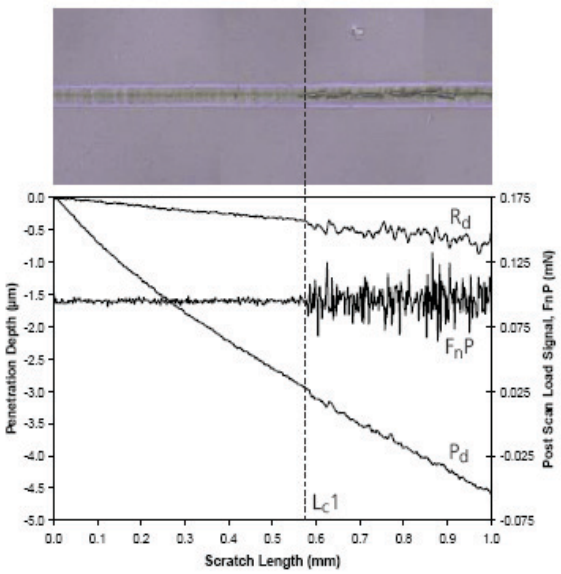

Fig. 20. Scratch test results for a progressive load scratch (0.1 – 15 mN) on a polymer topcoat.

6.2 Interface Indentation Test

Vickers indentation tests performed at the interface between a thick coating and its substrate can create and propagate a crack located in the plane of the interface, as it can be seen in figure 21 (Chicot et al., 1996).

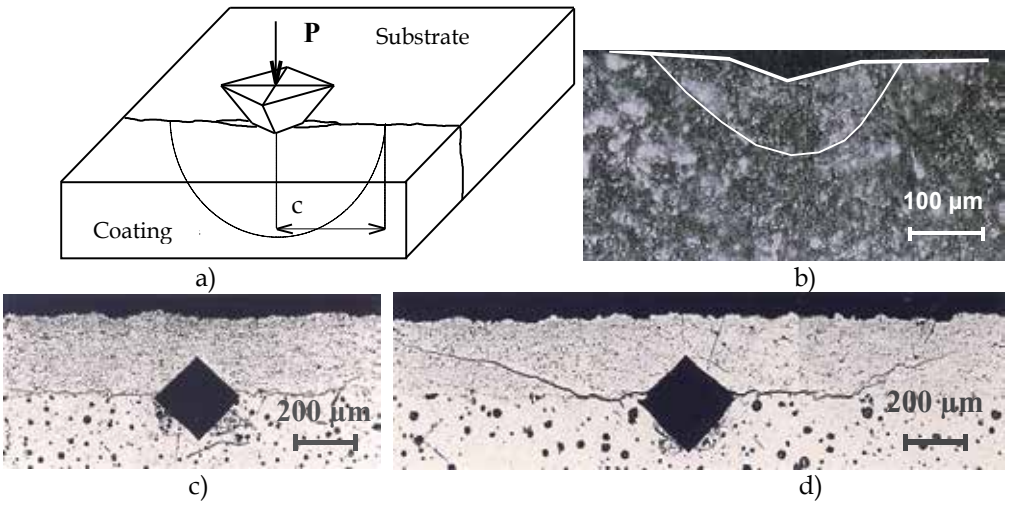

Fig. 21. a) Principle, b) half-penny crack, c) crack located in the plane of the interface and d) deviation of the crack towards the coating. The Vickers indentation test was performed at the interface of a Cr_3C_2/NiCr coating deposited on low carbon steel.

The test consists in measuring the crack lengths as a function of the applied load and to calculate the apparent interface toughness using an expression resulting from the analysis of different models developed for determining toughness of brittle massive materials by indentation. For the interfacial indentation, it was emphasized that the indented material, composed of substrate, coating and interface itself, can be considered as a unique brittle material (Chicot et al., 1996). The methodology is the following:

1) Obtaining a polished cross-section of the coated sample, in order to perform Vickers indentation tests with different applied loads, for which the indent diagonal must be coincident with the coating/substrate interface;
2) For each indentation test, measuring the value of the half indent diagonal (d/2) and the crack length (c), both at the interface;
3) Plotting these data as a function of the applied load in bi-logarithmic scale, as represented schematically in figure 22; where d/2 = f (P) is called "apparent hardness" and c = f (P) the cracking line;
4) Determining the coordinates of the critical point, (P_C, c_c) in figure 22, underneath which no cracking is observed at the interface and which are used to compute the apparent interface toughness of the coating/substrate couple.

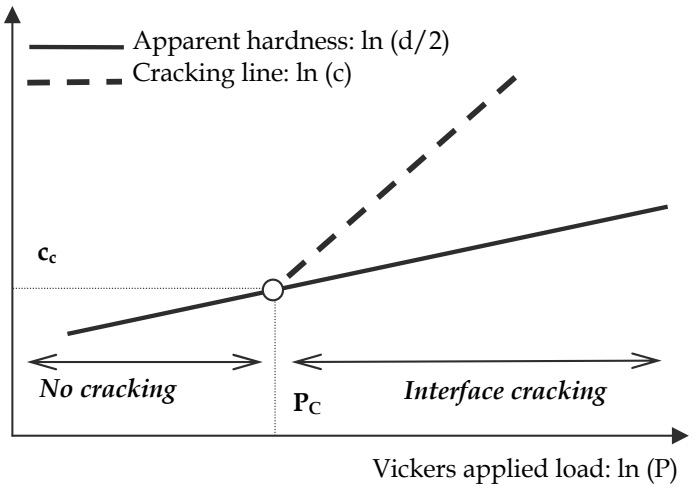

Fig. 22. Schematic representation of the apparent hardness, the cracking line and the critical point used to calculate the apparent interface toughness.

During indentation, a plastic deformation zone is created by sharing the combined local properties of the coating and of the substrate. Eventually, a local crack may be likely to occur in the interface plane if the fracture toughness of this composite interface material is attained. The purpose of the interface indentation test is to give a quantitative measurement of the apparent fracture toughness. Some general formulations found in the literature involve a ratio between elastic modulus and hardness of the material. For the interface material, Chicot et al. (1996) proposed to express this parameter as the square root of the ratio of the elastic modulus (E) divided by the Vickers hardness (HV) at the interface, by considering the mean geometrical features of the substrate and coating couple:

$$\left(\frac{E}{HV}\right)_i^{1/2} = \frac{\left(\frac{E}{HV}\right)_S^{1/2}}{1+\left(\frac{HV_S}{HV_C}\right)^{1/2}} + \frac{\left(\frac{E}{HV}\right)_C^{1/2}}{1+\left(\frac{HV_C}{HV_S}\right)^{1/2}} \tag{70}$$

where the subscripts i, S and C stand for interface, substrate and coating, respectively.
Then, by connecting the critical load used to initiate a crack, P_c, and the corresponding half-indent diagonal, c_c, we propose to calculate the apparent interface toughness representing the adhesion of the coating on its substrate by the following relation, in a similar way than those proposed earlier for bulk materials by Lawn et al. (1980) or Anstis et al. (1981) presented as the eq. 61:

$$Kca = 0.0154 \cdot \frac{P_c}{c_c^{3/2}} \cdot \left(\frac{E}{HV}\right)_i^{1/2} \tag{71}$$

Although this relation is only valid for cracks that are longer than the plastic zone radius, it was emphasized that the crack line can be extrapolated at the critical point. Then, the couple (P_C, c_C) can be used for the calculation of an apparent interface toughness, Kca. The critical point is chosen because when a crack is formed, its propagation is aided by the bending of the coating due to the action of the indenter, which plays the role of a wedge inserted at the interface. Consequently the propagation depends on the coating thickness since a thicker coating will resist to the bending better than a thinner one. Therefore, the slope of the cracking line is affected by the elastic behaviour of the coating. The only point which is not concerned is the crack initiation point, (P_C, c_C).

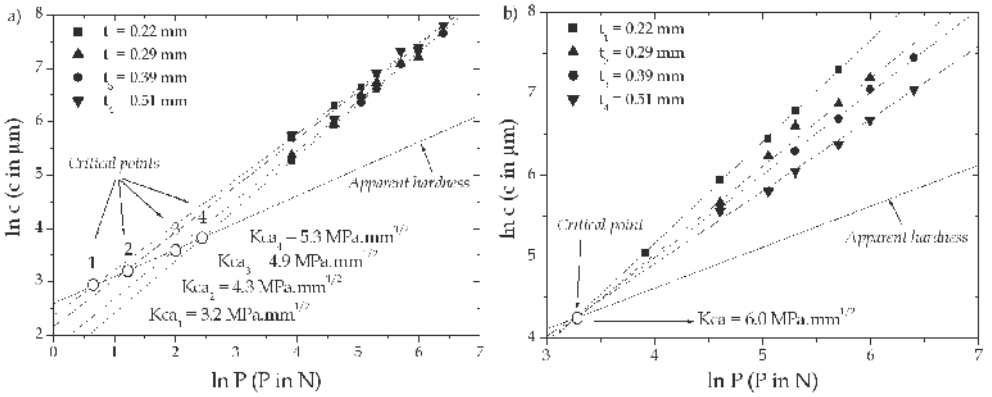

Fig. 23. Interface crack length as a function of the applied load for Cr_3C_2/NiCr thick coatings deposited onto a stainless steel for (a) as-received coated materials and (b) for annealed coated materials.

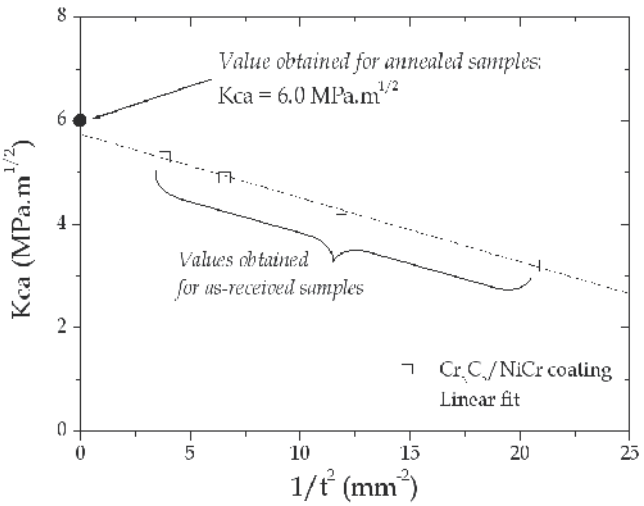

Fig. 24. Interfacial indentation toughness as a function of the coating thickness for as-received and annealed samples.

Figure 23 shows the results of an interfacial indentation test using a Vickers indenter applied to Cr_3C_2/NiCr thick coatings deposited on a stainless steel. Figure 23a shows that

the influence of the residual stress on the interfacial indentation toughness depends on coating thickness. It is remarkable that after an annealing treatment which drastically reduces the residual stress state, we obtain a unique value for the interfacial indentation toughness independently of the coating thickness (Figure 23b).
This result is very important as much as the representation of the interfacial indentation toughness for as-received coatings as a function of the coating thickness leads to the value obtained for annealed samples (Fig. 24).
As a main conclusion, this result allows the expression of the interfacial indentation toughness as a function of the residual stress and the absolute toughness which will be obtained for an infinite coating thickness or, consequently, without any residual stress (Lesage and Chicot, 2002):

$$Kca = Kca_0 + \frac{2}{\sqrt{\pi}} \cdot \sigma_R \cdot c_{c_0}^{1/2} \tag{72}$$

where c_{CO} is the critical crack length corresponding to the absolute toughness Kca_O and the residual stresses σ_R.
From the adhesion characterisation of a thick coating on its substrate, Araujo et al. (2005) reported a detailed discussion of the influence of the residual stress intensity and their repartition throughout the coating on the adhesive properties. In addition, Lesage et al. (2000a, 2000b) discussed the effect of thermal shocks or hydrogen embrittlement on the adhesive properties.

7. Conclusion

The indentation test is very useful for determining some mechanical properties but the results must be discussed with particular attention in order to give sound interpretations. As an example:

- For hardness, it is necessary to provide the indentation testing conditions with which the test has been performed. Moreover, a complete determination of the hardness requires two parameters, i.e. the macro-hardness corresponding to the hardness obtained for an infinite load and a characteristic scale-length depending on the models in order to supply the hardness-load variation.
- For the elastic properties, indentation tests lead to the bulk modulus instead of the Young's modulus. The bulk modulus can be determined by Knoop indentation or by analysing the unloading part of a load-depth curve resulting from instrumented indentation tests when applying spherical or conical indenters if some precautions are taken into account like the introduction of the instrument compliance into the reduced modulus calculation.
- For Vickers indentation fracture toughness, numerous relations are able to give a value according to the cracking mode below the indent. Since the experimental determination of the cracking mode is very difficult, we suggest a relationship able to define the cracking mode through an experimental exponent. In addition, two multiplicative coefficients which are material dependent allow the determination of comparable values with those given in the literature.
- For tensile mechanical properties by indentation, two types of approach can be

employed. One of them is based on Hollomon's law or Ludwik's law and the relations between tensile stress-strain and indentation stress-strain; the other groups of relations are those corresponding to the expanding cavity models, taking into account the indenter type and the indentation size effect. In the example shown here, all the models were tested in order to show that without any prior information on the tensile behaviour of the material, it is very difficult to guaranty the true mechanical behaviour. Nevertheless, some models seem to converge toward a unique Ludwik's law representing the tensile plastic domain.

- For adhesive properties, scratch tests and interfacial indentation tests are helpful to give an adhesive parameter. The choice between the two tests is based on the coating thickness and on the coating hardness. In addition for thick coatings, the interfacial indentation test can give additional information like the influence of the residual stresses or thermal treatments effect on the adhesive properties.

8. References

Abu Al-Rub, R.K. & Voyiadjis, G.Z. (2004). Analytical and experimental determination of the material intrinsic length scale of strain gradient plasticity theory from micro- and nano-indentation experiments. *International Journal of Plasticity*, Vol. 20, No. 6, 1139-1182.

Alcala, J.; Barone, A.C. & Anglada, M. (2000). The influence of plastic hardening on surface deformation modes around Vickers and spherical indents. *Acta Materialia*, Vol. 48, No. 13, 3451-3464.

Anstis, G.R.; Chantikul, P.; Lawn, B.R. & Marshall, D.B. (1981). A critical evaluation of indentation techniques for measuring fracture toughness : I, Direct Crack Measurements. *Journal of the American Ceramic Society*, Vol. 64, No. 9, 533-538.

Antunes, J.M.; Menezes, L.F. & Fernandes, J.V. (2006). Three-dimensional numerical simulation of Vickers indentation tests. *International Journal of Solids and Structures*, Vol. 43, No. 3-4, 784-806.

Araujo, P.; Chicot, D.; Staia, M.H. & Lesage, J. (2005). Residual stresses and adhesion of thermal spray coatings. *Surface Engineering*. Vol. 21, No. 1, 35-40.

Benayoun, L.; Fouilland-Paillé, J. & Hantzpergue, J. (1999). Microscratch test studies of thin silica films on stainless steel substrates. *Thin Solid Films*, Vol. 352, No. 1-2, 156-166 S.

Benjamin, P. & Weaver, C. (1960). Measurement of adhesion of thin films: Proceedings of the Royal Society, London, Vol. 254 A, pp. 163-176.

Bilodeau, G.G. (1992). Regular pyramid punch problem. *Journal of Applied Mechanics*, Vol. 59, No. 3, 519-523.

Bückle, H. (1973). in: J.H. Westbrook, H. Conrad (Eds.), The Science of Hardness Testing and Its Research Applications, ASME, Metal Park, OH, p. 453.

Bull, S.J.; Page, T.F. & Yoffe, E.H. (1989). An explanation of the identification size effect in ceramics. *Philosophical Magazine Letters*. Vol. 59, No. 6, 281-288.

Bull, S.J. & Rickerby, D.S. (1990). New developments in the modelling of the hardness and scratch adhesion of thin films. *Surface and Coating Technology*, Vol. 42, No. 2, 149-164.

Burnett, P.J. & Rickerby, D.S. (1987a). The mechanical properties of wear-resistant coatings. I. Modelling of hardness behaviour. *Thin Solid Films*, Vol. 148, 41-50.

Burnett, P.J. & Rickerby, D.S. (1987b). The mechanical properties of wear-resistant coatings. II. Experimental studies and interpretation of hardness. *Thin Solid Films*, Vol. 148, 51-68.

Briscoe, B.J.; Sebastian, K.S. & Adams, M.J. (1994). The effect of indenter geometry on the elastic response to indentation. *Journal of Physic D: Applied Physic*, Vol. 27, No. 6, 1156-1162.

Cheng, Y.T. & Cheng, C.M. (2004). Scaling, dimensional analysis, and indentation measurements. *Materials Science and Engineering: R: Reports*, Vol. 44, No. 4-5, 91-149.

Chicot, D. & Lesage, J. (1995). Absolute hardness of films and coatings**.** *Thin Solid films*, Vol. 254, No. 1-2, 123-130.

Chicot, D.; Démarécaux, P. & Lesage, J. (1996). Apparent interface toughness of substrate and coating couples from indentation tests, *Thin Solid Films*, Vol. 283, No. 1-2, 151-157.

Chicot, D.; Mercier, D.; Roudet, F.; Silva, K.; Staia, M.H. & Lesage, J. (2007a). Comparison of instrumented Knoop and Vickers hardness measurements on various soft materials and hard ceramics, *Journal of the European Ceramic Society*, Vol. 27, No. 4, 1905-1911.

Chicot, D.; Roudet, F.; Soom, A. & Lesage J. (2007b). Interpretation of instrumented hardness measurements on stainless steel with different surface preparations. *Surface Engineering*, Vol. 23, No. 1, 32-39.

Chicot, D.; Bemporad, E.; Galtieri, G.; Roudet, F.; Alvisi, M. & Lesage, J. (2008). Analysis of data from various indentation techniques for thin films intrinsic hardness modelling. *Thin Solid Films*, Vol. 516, No. 8, 1964-1971.

Chicot, D. (2009). Hardness length-scale factor to model nano- and micro-indentation size effects, *Materials Science and Engineering: A,* Vol. 499, No. 1-2, 454-461.

Chicot, D.; Roudet, F.; Lepingle, V. & Louis, G. (2009a). Strain gradient plasticity to study hardness behaviour of magnetite (Fe3O4) under multicyclic indentation, *Journal of Materials Research*, Vol. 24, No. 3, 749-759.

Chicot, D.; Duarte, G.; Tricoteaux, A.; Jorgowski, B.; Leriche, A. & Lesage J. (2009b), Vickers Indentation Fracture (VIF) modeling to analyze multi-cracking toughness of titania, alumina and zirconia plasma sprayed coatings, *Materials Science and Engineering: A*, Vol. 527, No. 1-2, 65-76.

Chicot, D.; Gil, L.; Silva, K. ; Roudet, F. ; Puchi-Cabrera, E.S. ; Staia M.H. & Teer, D.G. (2010a). Thin film hardness determination using indentation loading curve modelling. *Thin Solid Films*, Vol. 518, No. 19, 5565-5571.

Chicot, D.; Roudet, F.; Zaoui, A. ; Louis, G. & Lepingle, V. (2010b). Influence of visco-elasto-plastic properties of magnetite on the elastic modulus: Multicyclic indentation and theoretical studies. *Materials Chemistry and Physics*, Vol. 119, No. 1-2, 75-81.

Chong, A.C.M. & Lam, D.C.C. (1999). Strain gradient plasticity effect in indentation hardness of polymers. *Journal of Materials Research*, Vol. 14, No. 10, 4103-4110.

CSM Bulletin (2008). Influence of indenter tip radius on the scratch resistance of an automotive clearcoat. CSM Instruments, Advanced Mechanical Surface Testing, No. 25, February 2008.

Dao, M.; Chollacoop, N.; Van Vliet, K.J.; Venkatesh, T.A. & Suresh, S. (2001). Computational modeling of the forward reverse problems in instrumented sharp indentation. *Acta Materialia*, Vol. 49, No. 19, 3899-3918.

Doerner, M.F. & Nix, W.D. (1986). A method of interpreting the data from the depth-sensing indentation instruments. *Journal of Materials Research*, Vol. 1, No. 4, 601-609.

Durst, K.; B. Backes, B. & Goken, M. (2005). Indentation size effect in metallic materials: Correcting for the size of the plastic zone. *Scripta Materialia*, Vol. 52, No. 11, 1093-1097.

Felder, E. & Laugier, M. (1992). Le test de rayure (scratch test) des produits revêtus, Synthèse bibliographique, mars 1992, Rapport de contrat CEMEF-UNIREC.

Field, J.E. & Telling, R.H. (1999). The Young modulus and Poisson ratio of diamond. Research Note, Cavendish Laboratory, Cambridge.

Fischer-Cripps A.C. (2004). A simple phenomenological approach to nano-indentation creep, *Materials Science and Engineering A*, Vol. 385, No. 1-2, 74-82.

Fischer-Cripps, A.C. (2006). Critical review of analysis and interpretation of nano-indentation test data. *Surface and Coating Technology*, Vol. 200, No. 14-15, 4153-4165.

Gao, X.L. (2006). An expanding cavity model incorporating strain-hardening and indentation size effects. *International Journal of Solids and Structures*, Vol. 43, No. 21, 6615-6629.

Giannakopoulos, A.E.; Larsson, P.L. & Vestergaard, R. (1994). Analysis of Vickers indentation. *International Journal of Solids and Structure*, Vol. 31, No. 19, 2679-2708.

Giannakopoulos, A.E. & Larsson, P.L. (1997). Analysis of pyramid indentation of pressure-sensitive hard metals and ceramics. *Mechanics of Materials*, Vol. 25, No. 1, 1-35.

Gong, J.; Wu, J. & Guan, Z. (1999). Analysis of the indentation size effect on the apparent hardness for ceramics. *Materials Letters*, Vol. 38, No. 3, 197-201.

Gong, J.; Wang, J. & Guan, Z. (2002). A comparison between Knoop and Vickers hardness of silicon nitride ceramics, *Materials Letters.*, Vol. 56, No. 6, 941-944.

Hay, J.C.; Bolshakov, A. & Pharr G.M. (1999). Critical examination of the fundamental relations used in the analysis of nano-indentation data, *Journal of Materials Research*, Vol. 14, No. 6, 2296–2305.

Hays, C. & Kendall, E.G. (1973). Analysis of Knoop hardness. *Metallurgy*, Vol. 6, No. 4, 275-282.

Heavens, O.S. (1950). Some factors influencing the adhesion of films produced by vacuum evaporation. Journal de Physique et le Radium, Vol. 11, No. 7, 355-360.

Herbert, E.G., Pharr, G.M., Oliver, W.C., Lucas, B.N. & Hay, J.L. (2001). On the measurement of stress-strain curves by spherical indentation. *Thin Solid Films*, Vol. 398-399, 331-335.

Hollomon, J.H. (1945). Tensile deformation, *Transactions of the American Institute of Mining and Metallurgical Engineers*, Vol. 162, 268-290.

Huang, Y. Feng, X., Pharr, G.M. & Hwang, K.C. (2007). A nano-indentation model for spherical indenters. *Modelling Simulation Material Science and Engineering*, Vol. 15, No. 1, S255-S262.

Ichimura, H.; Rodriguez, F.M. & Rodrigo, A. (2000). The composite and film hardness of TiN coatings prepared by cathodic arc evaporation. *Surface and Coating Technology*, Vol. 127, No. 2, 138-143.

Jönsson, B. & Hogmark, S. (1984). Hardness measurements of thin films = Mesures de dureté sur des couches minces. *Thin Solid Films*, Vol. 114, No. 3, 257-269.

Karlsson, L., Hultman, L, Sundgren, J.-E., (2000). Influence of residual stresses on the mechanical properties of TiC_xN_{1-x} (x = 0, 0.15, 0.45) thin films deposited by arc evaporation. *Thin Solid Films.* Vol. 371, No. 1-2, 167-177.

Kick, F. (1885). Das Gestez der proportionalen Widerstande und seine Anwendung. Delidzig, Felix.

King, R.B. (1987). Elastic analysis of some punch problems for layered medium. *International Journal of Solids and Structures*, Vol. 23, No. 12, 1657-1664.

Korsunsky, A.M.; McGurk, M.R.; Bull, S.J. & Page, T.F. (1998). On the hardness of coated systems. *Surface and Coating Technology*. Vol. 99, No. 1, 171-183.

Laeng, P. & Steinmann, P.A. (1981). Adhesion testing of hard CVD coatings using the scratch test: Proc. 8th. Int. Conf. CVD 1981, Electrochem. Soc., Pennington, NJ, pp. 723-736.

Larsson, P.L.; Giannakopoulos, A.E.; Söderlund, E.; Rowcliffe, D.J. & Vestergaard, R. (1996). Analysis of Berkovich indentation. *International Journal of Solids and Structure*, Vol. 33, No. 2, 221-248.

Lawn, B.R., Evans, A.G. & Marshall, D.B. (1980). Elastic/plastic indentation damage in ceramics: The median/radial crack system. *Journal of the American Ceramic Society*, Vol. 63, No. 9-10, 574-581.

Lesage, J.; Chicot, D.; Araujo, P.; Zampronio, M. & De Miranda P.E.V. (2000a) Role of hydrogen on adhesion of NiCr thermal sprayed coatings. *Thin Solid Films*, Vol. 377, 675-680.

Lesage, J.; Staia, M.H.; Chicot, D.; Godoy, C. & De Miranda P.E.V. (2000b). Effect of thermal treatments on adhesive properties of a NiCr thermal sprayed coatings. *Thin Solid Films*, Vol. 377, 681-686.

Lesage, J. & Chicot, D. (2002). Role of residual stresses on interface toughness of thermally sprayed coatings. *Thin Solid Films*, Vol. 415, No. 1-2, 143-150.

Lesage, J.; Pertuz, A.; Puchi-Cabrera, E.S. & Chicot, D. (2006). A model to determine the surface hardness of thin films from standard micro-indentation tests. *Thin Solid Films*, Vol. 497, No. 1-2, 232-238.

Li, H. & Bradt, R.C. (1993). The micro-hardness indentation load/size effect in rutile and cassiterite single crystals. *Journal of Materials Research*, Vol. 28, 917-926.

Ludwik, P. (1909). Element der Technologischen Mechanik, Springer Berlin, 32-44.

Marshall, D.B.; Noma, T. & Evans A.G. (1980). A simple method for determining elastic-modulus-to-hardness ratios using Knoop indentation measurements, *Journal of American Ceramic Society*, Vol. 65, No. 10, C175-C176.

Matthews, J.R. (1980). Indentation hardness and hot pressing. *Acta Metallurgica*, Vol. 28, 311-318.

Meyer, E. (1908). Untersuchen über Härteprüfung und Härte. *Z. Ver. deutscher Ing.*, Vol. 52, 645-654.

Miranzo, P. & Moya, J.S. (1984). Elastic/plastic indentation in ceramics: a fracture toughness determination method, *Ceramics International*, Vol. 10, No. 4, 147-152.

Mittal, K.L. (1987). Selected bibliography on adhesion measurement of films and coatings. *Journal of Adhesion Science and Technology*, Vol. 1, No. 3, 247-259.

Mukhopadhyay, A. K.; Datta, S. K. & Chakraborty, D. (1990). On the micro-hardness of silicon nitride and sialon ceramics, *Journal of the European Ceramic Society*, Vol. 6, No. 5, 303-311.

Nix, W.D. & Gao, H. (1998). Indentation size effects in crystalline materials: A law for strain gradient plasticity, *Journal of the Mechanics and Physics of Solids*, Vol. 46, No. 3, 411-425.

Oliver, W.C. & Pharr G.M. (1992). An improved technique for determining hardness and elastic modulus using load and displacement sensing indentation experiments, *Journal of Materials Research*, Vol. 7, No. 6, 1564-1583.

Perry, A.J.; Laeng, P. & Steinmann, P.A. (1981). Adhesion measurements on hard thin well-adhering coatings – A Review: Proc. 8th. Int. Conf. CVD 1981, Electrochem. Soc., Pennington, NJ, pp. 475-488.

Ponton, C. B. & Rawlings, D.R. (1989). Vickers indentation fracture toughness test Part 1 Review of literature and formulation of standardized indentation toughness equations. *Materials Science and Technology*, Vol. 5, No. 9, 865-872.

Puchi-Cabrera, E. S. (2002). A new model for the computation of the composite hardness of coated systems. *Surface and Coating Technology*, Vol. 160, No. 2, 177-186.

Qiu, X.; Huang, Y.; Nix, W.D.; Hwang, K.C. & Gao, H. (2001). Effect of intrinsic lattice resistance in strain gradient plasticity. *Acta Materialia*, Vol. 49, No. 19, 3949-3958.

Rajendran, V.; Nishara Begum, A.; Azooz, M. A ; El Batal, F. H. (2002). Microstructural dependence on relevant physical-mechanical properties on SiO_2-Na_2O-CaO-P_2O_5 biological glasses. *Biomaterials*, Vol. 23, No. 21, 4263-4275.

Roman, A. ; Chicot, D. & Lesage, J. (2002). Indentation tests to determine the fracture toughness of nickel phosphorus coatings. *Surface and Coatings Technology*, Vol. 155, No. 2-3, 161-168.

Sangwal, K.; Surowska, B. & P. Blaziak, P. (2002). Analysis of the indentation size effect in the micro-hardness measurement of some cobalt-based alloys. *Material Chemistry and Physic*, Vol. 77, No. 2, 511-520.

Sargent, P.M. (1979). Ph.D. Thesis, University of Cambridge, United Kingdom.

Sekler, J.; Steinmann, P.A. & Hintermann, H.E. (1998). The scratch test: Different critical load determination techniques. *Surface and Coatings Technology*, Vol. 36, No. 1-2, 519-529.

Steinmann, P.A.; Tardy, Y. & Hintermann, H.E. (1987). Adhesion testing by the scratch test method: the influence of intrinsic and extrinsic parameters on the critical load, *Thin Solids Films*, Vol. 154, No. 1-2, 333-349.

Sun, S.; Zheng, S. & Bell, T. (1995). Finite element analysis of the critical ratio of coating thickness to indentation depth for coating property measurements by nano-indentation. *Thin Solid Films*, Vol. 258, No. 1-2, 198-204.

Swift, H.W. (1952), Plastic instability under plane stress. *Journal of Mechanic and Physic of Solids*, Vol. 1, No. 1, 1-18.

Tricoteaux, A.; Duarte, G.; Chicot, D.; Le Bourhis, E.; Bemporad, E. & Lesage J. (2010). Depth-sensing indentation modeling for determination of elastic modulus of thin films, *Mechanics of Materials*, Vol. 42, No. 2, 166-174.

Ullner, C.; Germak, A.; Le Doussal, H.; Morrell, R.; Reich, T. & Vandermeulen, X. (2001). Hardness testing on advanced technical ceramics, *Journal of the European Ceramic Society,* Vol. 21, No. 4, 439-451.

Ullner, C.; Beckmann, J. & Morrell, R. (2002). Instrumented indentation test for advanced technical ceramics, *Journal of the European Ceramic Society*, Vol. 22, No. 8, 1183-1189.

Veprek, R.G.; Parks, D.M.; Argon, A.S. & Veprek, S. (2006). Non-linear finite element constitutive modeling of mechanical properties of hard and superhard materials studied by indentation. *Materials Science Engineering A*. Vol. 422, No. 1-2, 205-217.

Weaver, C. (1975). Adhesion of thin films. *Journal of Vacuum Science and Technology*. Vol. 12, No. 1, 18-25.

Zeng, K. & Chiu, C.-h. (2001). An analysis of load-penetration curves from instrumented indentation. *Acta Materialia*, Vol. 49, No. 17, 3539-3551.

Zhu, T.T., Bushby, A.J. & Dunstan D.J. (2008). Size effect in the initiation of plasticity for ceramics in nano-indentation. *Journal of Mechanics and Physics of Solids*, Vol. 56, No. 4, 1170-1185.

8

Ceramic Materials and Color in Dentistry

Cláudia Ângela Maziero Volpato*, Márcio Celso Fredel**
Analúcia Gebler Philippi* & Carlos Otávio Petter ***
** Department of Dentistry – Federal University of Santa Catarina*
*** Department of Mechanical Engineering – Federal University of Santa Catarina*
**** Department of Mines Engineering – Federal University of Rio Grande do Sul*
Brazil

1. Introduction

The aesthetics of a dental restoration depends on the chosen material, anatomical form, surface texture, translucency and color. This means that, to accurately reproduce the appearance of a natural tooth, considering the patterns of reflection and absorption of the light is not an easy task (Knispel, 1991; Chu et al., 2004).
Ceramics have been widely used in dentistry because of their ability to provide excellent cosmetic results that mimic natural teeth. They are biocompatible, allow adequate reflection and transmission of light, and they exhibit good mechanical strength when subjected to masticatory efforts (Holloway & Miller, 1997). The rapid development of ceramic systems and processing enabled the treatment of teeth in both the anterior and posterior areas, with the primary objectives of properly restoring form, function and aesthetic excellence without the presence of metal.

2. History of dental ceramics

2.1 First porcelains

Ceramics are probably the oldest materials developed by man. Fragments of ceramic utensils, dated 30,000 years BC, helped archaeologists study the behavior of our ancestors. In 1774, the French pharmacist, Alexis Duchateau, dissatisfied with his dentures in ivory, noticed that the ceramic utensils used in handling chemical formulations resisted abrasion caused by the products used, and maintained their color. He suggested that porcelain could be considered as a possible replacement for missing teeth. Later, Duchateau, with the collaboration of a dentist named Nicholas Dubois De Chemant, managed to fabricate the first dental porcelain composition based on "green" traditional porcelain (50% kaolin clay or Chinese - Al_2O_3 SiO_2 $2H_2O$, 25 % feldspar - $K2O$ Al_2O_3 $6SiO_2$ and 25% silica or quartz - SiO_2). However, the prostheses made with these materials were abandoned due to their high opacity. In 1838, Elias Wildman made porcelain that was more translucent, with a brightness closer to that of natural teeth. This porcelain was of the Chinese pariana type,

which is characterized by high translucency. The reduction or complete removal of the kaolin contents allowed an increase in the amount of feldspar, and therefore greater light transmission due to the absence of mullite, resulting in a migration of the porcelain composition from the mullite zone to the leucite zone. (Kelly et al., 1996).

2.2 Association of triaxial porcelain to metal

While providing a high translucency, feldspathic porcelain showed great mechanical fragility, attributed to its crystalline structure, when used in the mouth. Extensive prostheses made from pure porcelain fractures easily due to the propagation of cracks or defects resulting from laboratory processing (McLean, 2001; Sadowsky, 2006; Denry & Kelly, 2008). This clinical observation led to the introduction of metal infrastructures, associated with ceramics, in order to compensate for the low fracture resistance of the porcelain. This association became known as "metalloceramic prosthesis", and represents a milestone in the technological advancement of dental prostheses. From this event, dental porcelains could be used in extensive fixed prostheses, and a series of events took place after the introduction of these prostheses: improved techniques of ceramic processing, formulations of medium and high fusion porcelain and the introduction of vacuum electric furnaces.

The use of metalloceramic prostheses over the last 50 years has minimized the problem with porcelain fragility; however, its aesthetic potential was limited due to the presence of metal. The metal framework acts as a barrier to the transmission of light, giving the prosthetic dental restoration an unaesthetic opaque aspect, with the presence of darkening at the cervical region of the prosthetics. (Raigrodski, 2004).

2.3 Introduction of alumina as the ceramic reinforcing phase

In the search for a material to replace the metal infrastructure of a metalloceramic prosthesis, which presented a similar resistance while also associated the characteristics of aesthetic excellence, McLean and Hughes introduced aluminum oxide (Al_2O_3) as a reinforcing phase in dental porcelain in 1965. The incorporation of strengthening components to the feldspathic glass matrix enabled the construction of ceramic infrastructures without the presence of metal, initiating an era of advances in the development of new ceramic systems and processes routinely used in current dental offices. (Kelly et al., 1996)

The first ceramic infrastructures made of alumina were obtained by a process known as craft ceramic infiltration slipcasting, where an infrastructure of high-density crystal is prepared with a small amount of glass. The ceramic powder reinforced with alumina is mixed with water and applied over a refractory die. The resulting mass is sintered for 10 to 12hs at a temperature of 1140^{o}C. During sintering, the particles fuse and produce a crystalline structure which is opaque and provides low resistance. In a second stage, this structure is infiltrated by a thin layer of molten glass of low viscosity (lanthanum aluminosilicate). With an increase in temperature (1100oC for 4 to 6 hours), the glass melts and penetrates the infrastructure, through capillary action, and creates a ceramic surface with a very low porosity and high flexural strength. Three infiltrating systems (Vita Zahnfabrik, Germany) were developed for this technique of processing: reinforcing with alumina (70% to 85% aluminum oxide) and strengthening with magnesia (70% aluminum oxide and 30% magnesium oxide) or zirconia (67% aluminum oxide and 33% of tetragonal zirconium

oxide). The flexural strength varies according to the reinforcement used: alumina (400MPa), magnesia (300MPa) and zirconia (750MPa). Depending on the strength achieved by the infiltration of the zirconia ceramic system, the construction of fixed prostheses in areas of high masticatory forces might be indicated. However, both the concentration of alumina and zirconia shown in these ceramic systems results in the impoverishment of the optical qualities of the restoration, due to its high opacity (Heffernan et al., 2002a, b). Additionally, the porosity incorporated during the manufacture of the infrastructure can affect the strength of these restorations (Miyazaki et al., 2009).

2.4 Improvement of glass-ceramics

Parallel to the introduction of infiltrated ceramics, glass-ceramics have been improved to be applied in the vacuum injection technique, similar to the traditional technique of metal casting. Two glass-ceramic compositions were introduced: leucite based (IPS-Empress, IvoclarVivadent, Liechtenstein) and lithium disilicate based (IPS-Empress 2, IvoclarVivadent, Liechtenstein). In the first composition, leucite is responsible for strengthening the ceramic, associated with the leucite resulting from the nucleation process (a phenomenon that occurs with increasing temperature), giving a higher flexural strength (120MPa) when compared to feldspathic porcelain, with the increased strength still not enough for extensive restorations. The great advantage of glassy systems is that they exhibit high light transmission, which allows the manufacture of prostheses with high aesthetic demands. In the second composition, the high content of crystalline lithium disilicate enables a volume increase of up to 60%. The crystals generated (elongated crystals of lithium disilicate measuring 0.5 to 5μm and lithium orthophosphate measuring 0.1 to 0.3μm) are smaller than those creased with the leucite reinforced ceramics, and their presence improves the flexural strength of the material (350 MPa), allowing the design of fixed partial prostheses of up to three units. (Heffernan et al. 2002).

The laboratory procedure for producing restorations using these materials consists in the inclusion of waxed patterns in conforming rings with a refractory lining. The wax is burned out in a conventional oven and then the rings are brought to furnace injection, where prefabricated ceramic inserts are melted and injected under heat (about 1150°C) and vacuum hydrostatic pressure (around 0.3 to 0.4 MPa). After the completion of the injection process, the molds are cooled to room temperature, and divestment is performed using jets of glass beads. The prosthesis of these systems can be obtained by two techniques: the restoration is cast in its final shape, and subsequently painted and glazed (the technique of makeup), or the ceramic infrastructure is obtained by injection, typically covered by a ceramic of a lower thermal expansion coefficient (layering technique).

2.5 Consolidation of CAD / CAM technology

The implementation of dental prostheses is a work of art. The dentist, as the potter, is responsible for the aesthetic outcome of the future prosthesis. In entirely handmade restorations, the possibility of errors is directly proportional to the number of variables involved (Miyazaki et al., 2009). The automation and the ability to fabricate ceramic prostheses using a machine-readable technology, design (CAD) and manufacturing (CAM), provide for the elimination of several clinical steps and a reduction of the variables inherent to the production of artistic work. With the CAD/CAM technology, all ceramic prostheses can be fabricated with an infrastructure of pure

aluminum oxide (99.5%), which is crystalline, densely sintered and non-porous. The powder is packaged on a die in a refractory ceramic process known as vacuum uniaxial pressing (1600 1700ºC). The resulting piece has a flexural strength of 600 Mpa and a particle size of 4µ. Clinical procedures consist of obtaining a mold from the prepared area and preparing a die model. The die is positioned on the rotating platform of a scanner unit (CAD) and a probe with a spherical sapphire tip performs digital mapping of the die. The image obtained is sent to the system program, where the operator manipulates the generated image. The completed design of the digital infrastructure is sent via modem to a production station (PROCERA Sandvik®AB, Sweden or PROCERA® Fair Law, USA), where it is possible to industrially manufacture the piece requested (unit CAM). (Sadowsky, 2006; Miyazaki et al., 2009)
Other systems use CAD/CAM technology for machining ceramic blocks with diamond burs and discs. The restoration is carved in blocks of non porous ceramics of varying composition (feldspar, glassy, or aluminized reinforced with zirconia). A CAD unit (micro-camera or scanner) makes a digital reading of the prepared tooth (intra-oral version) or die gypsum (lab version), copying all of the details and transferring this information to a computer where the digital design of the infrastructure is performed. The chosen ceramic block is attached to the CAM unit and undergoes a process of attrition (milling) for about 10 to 30 minutes. The machining can be performed on pre-sintered or fully sintered blocks. The resulting pieces of pre-sintered blocks are shaped into a size 25 to 30% higher than desired (depending on the material batch) to compensate for the shrinkage due to sintering. Units from fully sintered blocks are machined in the ideal size, however, they suffer the stress of the machining process. (Luthard et al., 2004)

2.6 Structural ceramics based on zirconia

Zirconia (ZrO_2) is a ceramic which has been distinguished in the health field by its biocompatibility, bioinercy, high mechanical properties and chemical stability (Chevalier, 2006). Its use in dentistry is relatively new, however, and has proven to be a promising material for making prosthetic infrastructures for single crowns, crowns, bridges, abutments and implant prostheses (Denry & Kelly, 2008). Although there are currently several types of ceramic systems based on zirconia, the 3Y-TPZ has been the most studied and used in dentistry (Vagkopoulou et al., 2009). The polycrystal tetragonal zirconia stabilized with yttria (3Y-TPZ) contains 3mol% yttria oxide (Y_2O_3) as a stabilizer and was first applied in the medical field by orthopedists (Chevalier, 2006). For dental applications, the 3Y-TPZ is synthesized in small grains (0.2 to 0.5 mm in diameter), which minimizes the phenomenon of structural deterioration or destabilization in the presence of saliva, decreasing the subcritical crack growth (CST) (Denry & Kelly, 2008). Pre-sintered blocks are machined with the aid of CAD/CAM, and the specimens are then sintered. This processing reduces the level of tension present and prevents a tetragonal to monoclinic transformation (t → m), which leads to a final surface virtually free of the monoclinic phase. The infrastructure obtained from these blocks is more stable, having a high crystalline structure and a flexural strength around 900 to 1200MPa. Fully sintered blocks are processed by isostatic pressure at a temperature between 1400 to 1500 ° C. This process causes the block to achieve a final density close to 99%, high hardness and low machinability. Thus, robust machining systems must be used, resulting in the formation of a large amount of monoclinic zirconia due to the compression generated by the machining process, which usually results in microcracks on the surface and a susceptibility to degradation at low temperature (subcritical crack growth - SCG) (Kelly & Denry, 2008). Recently, in order to produce ceramic blocks with greater durability and stability under high temperatures and humid environments, the industry

has introduced small amounts of alumina to 3Y-TZP, constituting a variation called TZP-A. However, a disadvantage of the addition of alumina is the reduction of the translucency of the final block (Yang et al., 2009).

2.7 Ceramic nanopowders

Nanotechnology is a collective term for a wide range of applications in structures and processes at the nano-scale. Nanoparticles are smaller than 1 to 100nm, and the atoms on their surfaces are very reactive. With the aid of these particles, it is possible to produce materials that are extremely rigid and resistant (Lamas et al, 1998; Tadakoro & Muccillo 2002). In the case of dental ceramics, this technology has enabled the preparation of nanopowders from zirconia-based ceramic (ZrO_2), alumina (Al_2O_3) and ceria (CeO_2). The resulting nanopowders have been used in the manufacture of industrial ceramic blocks for machining. With the introduction of these powders, the resulting block has a smooth surface, there is a considerable reduction of porosity and internal defects, and increased flexural strength (Yang et al., 2009). The optical properties have also been benefited because, as the nano-sized particles are well below the wavelength of light, they allow light to pass through the material. As handmade ceramics based on alumina and zirconia showed a high opacity; with the introduction of ceramic nanopowders, the current structural ceramics have begun to show an opacity subjected to laboratory control (Manicone et al., 2007).

3. Classification of dental ceramics

Didactically, dental ceramics can be classified by the melting temperature, composition and manufacturing process:

3.1 Melting

This classification was officially established in the 1940s and, more recently, fourth generation has been added, the ultra low-melting ceramics:

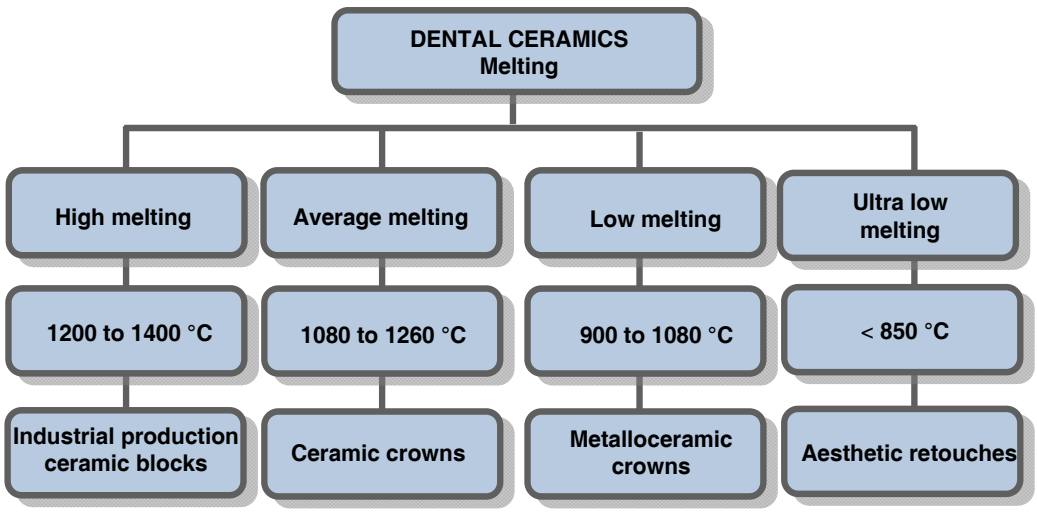

3.2 Composition and manufacturing process

Dental ceramics can be classified, according to their composition, into three distinct groups, which may be obtained by five different processes:

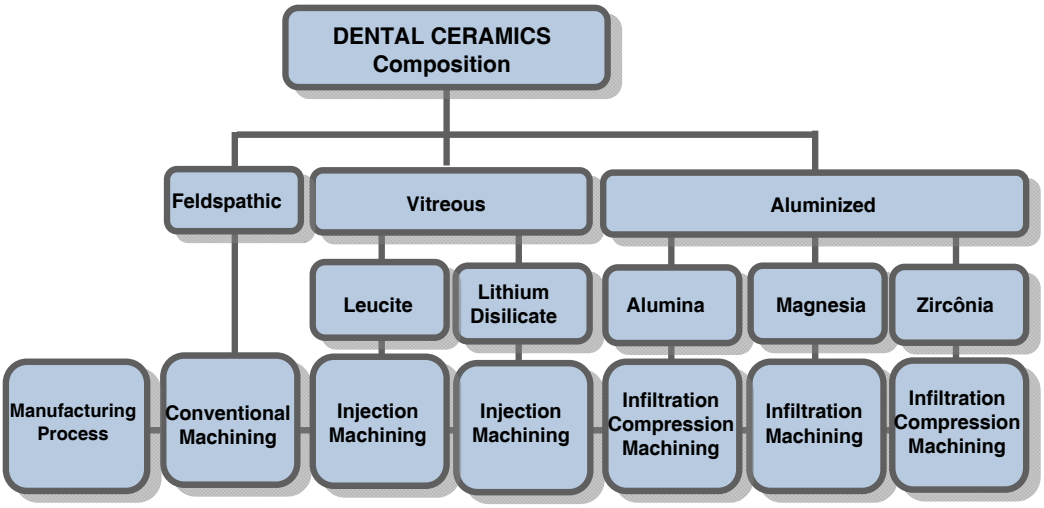

4. Understanding Color

4.1 Phenomenon of color

Color is a complex psychobiophisycal phenomenon resulting from the behavior of light through its wavelengths to the human eye. Color is not a property of the object, but of the light that enters our eyes from it. (O'Brien et al., 1989) Therefore, the real factor responsible for visual perception of color is the light. Without this, we can only see dark, or black. Light is an electromagnetic wave. Electromagnetic waves can be decomposed into multiple wavelengths, giving rise to a broad spectrum from radio waves (with wavelengths in kilometers) to the waves of cosmic rays (wavelengths less than 10 -13m). (Sproull, 2001). The region of light that reaches our eyes is called visible light. It includes the range of 400 to 700nm, and all the colors we know are within this range.

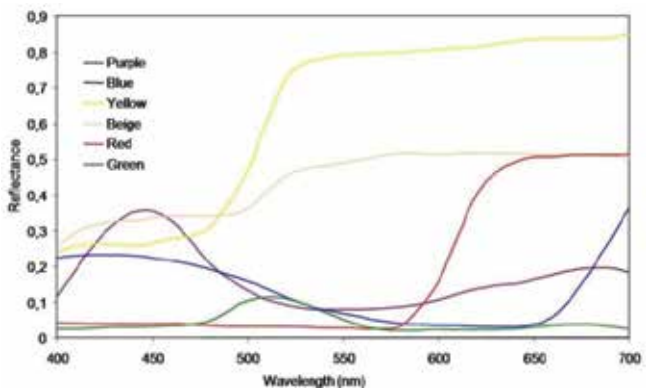

Fig. 1. Spectral curves of colors.
Source: Petter & Gliese, 2000

The color we perceive is a mixture of various wavelengths, and therefore, the color spectrum can be demonstrated from a graphic design known as the spectral curve or spectrum of color (Fig. 1) (Sproull, 2001b).

4.2 Physiology of color

Our eyes have two kinds of light-sensitive cells: rods, which are responsible for defining the shape of objects and night vision, and cones, which are located in the central area and are responsible for daytime vision, identification and differentiation of colors (Gliese & Petter, 2000). When light hits the eyes, it is immediately assimilated by the cells present in the retina. These cells are basically divided into three categories: those with greater sensitivity to red, green or blue; when light activates these cones, critolase, clorolase and cianolase pigments are synthesized, respectively. The amount of pigments produced results in X (red cones), Y (green cones) and Z (blue cones), with each resulting pigment responsible for a colorimetric stimulus. The three pigments generate messages that are simultaneously sent to the brain in the form of tristimulus (X, Y, Z) and, according to the concentration of each pigment, different colors of the object (primary and secondary) are displayed (Sproull, 2001). Described as an abstract science, perception of color involves the participation of three factors that can effectively exist: (Gliese & Petter, 2000; Joiner, 2004)

- **Object to be observed:** The object being viewed may have different physical behaviors in relation to the incident light. If an object is transparent, it acts as an absorbing environment by allowing light to pass through it (light transmission) and allowing us to see through it. If an object is translucent, some light passes through the object and part is reflected, allowing our perceptions regarding the color of that object. If the object is opaque, the reflection of light occurs in a diffuse way, which is responsible for the colorimetric awareness of our eyes (Fig. 1) (Knispel, 1991). Likewise, if the object absorbs all incident light, there is no reflection, and then we will see a dark color or black. If the object completely reflects the incident light, our vision will identify a white object. However, if part of the light energy is reflected and part is absorbed, the display is a colored object. (Joiner, 2004).

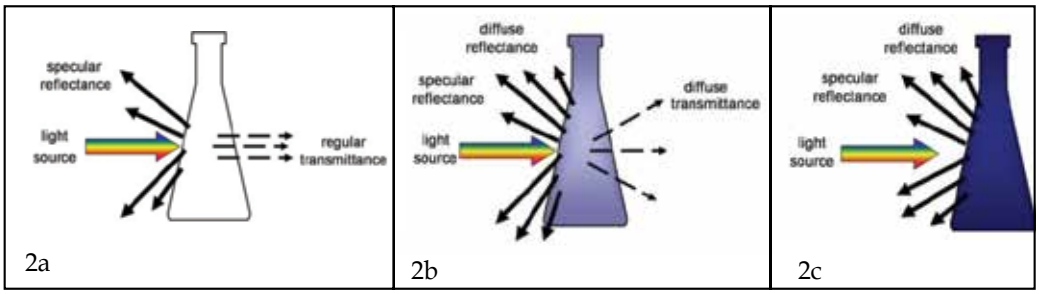

Fig. 2. Light behavior in transparent(2a), translucent (2b) and opaque objects (2c).
Source: Petter & Gliese, 2000

- **Observer:** The observation of an object can be in a visual or an instrumental way. In a visual analysis, the perception of color is a subjective process and the interpretation depends on the observer's visual individuality. If the observer is an individual trained in the analysis of color, they can identify subtle differences in color. Changes in color perception may occur

based on age, duration of exposure of the eye, fatigue or illness related to color, such as color blindness. (Van Der Burght et al., 1990). In instrumental analysis, colorimetric instruments objectively observe and record color. Two types of equipment have been used: colorimeters and spectrophotometers. Colorimeters analyze the values for red, green and blue reflected through filters that simulate sensing photoreceptor cells of the human eye. The tristimulus X, Y and Z coordinates are automatically converted to L*, a*, b* values of the CIE L*a*b* system. (Gliese & Petter, 2000). Spectrophotometers measure and record the amount of light reflected or transmitted from the object through its wavelength. These devices have high precision, sensitivity to measure absolute colors and are equipped with spectral distributions of various illuminants. The most accurate spectrophotometers are those of integrating spheres, called spherical optical, in which the object is exposed to light at different angles and directions for its analysis. (Paravina, 2002).

- **Light source or illuminant**: The illuminant may be a natural or artificial light source, which, according to its origin, can change the perceived color of an object. For example, a white sheet of paper may seem bluer under fluorescent light and more yellowish under a light bulb, returning to its original color in the presence of daylight. This phenomenon is known as metamerism. (Knispel 1991). Aiming to standardize the visual and instrumental analysis of color, the International Commission of I'Eclairage (CIE) has classified illuminants according to their effect on the perception of color. The CIE appointed 3 standard illuminants: A, B and C. Later, the illuminant series D, the hypothetical illuminant E and unofficially the illuminant series F were added (Chu et al., 2004):

Illuminant	CIE definition
A	Tungsten light source with an average temperature of 2,856 K, which produces a reddish-yellow light. Generally used to simulate conditions of incandescent light.
B	Tungsten light source coupled to a liquid filter to simulate direct sunlight with an average temperature of 4,874 K.
C	Tungsten light source coupled to a liquid filter to simulate indirect sunlight with an average temperature of 6,774 K. However, it is not a perfect simulation of sunlight, because it contains a large amount of ultraviolet light needed in the analysis of fluorescence.
D	Series of illuminants representing different conditions of the day. Illuminants D50 and D65 (so called due to temperatures of 5,000 K and 6,500, respectively) are generally used as pattern illuminants and match the reflectance of blue light.
E	It is a theoretical light source, in which an equal amount of energy would be present at all wavelengths. Currently this illumination does not exist, but this value is used as a tool for scholars of hypothetical colorimetry.
F	It involves a series of fluorescent lights. Fluorescent lamps have peaks that are evident in their spectral curves and do not fit the color temperature, therefore, are not considered an officially illuminating pattern. However, as the fluorescent display is widely used, the CIE recommends these illuminations to evaluate colors observed in the fluorescent environment.

Table 1. Series of illuminants

4.3 Colorimetric parameters

In 1936, Munsell (O'Brien et al., 1989) described the three dimensions of color to opaque objects: hue, chroma and value. This language became known worldwide; therefore, it became important to understand the color three-dimensional concept to perform visual and instrumental analysis.

- **Hue or tint:** the first attribute by which a color is identified and distinguished, or the name of the color: blue, yellow, red, green, among others. It corresponds to the wavelength of light reflected by the objects. (Fig. 3) (Sproull, 2001).
- **Chroma or saturation:** indicates the purity of the color, quantifying its saturation. The lighter a color is, the lower its saturation. Moreover, saturation increases as the object is darker. For example, red is a saturated hue, while pink is the same hue, but less saturated. (Fig. 4) (Sproull, 2001).
- **Value or light intensity:** the property which is distinguished by the lightness or darkness of a color. The clearer the color, the greater its value (brightness) and the darker, the lower the value. A good example is the brightness of full white, represented by the maximum value on the intensity scale (100), while black shows the absolute value of 0, or the total absence of light. (Fig. 5) (Sproull, 2001).

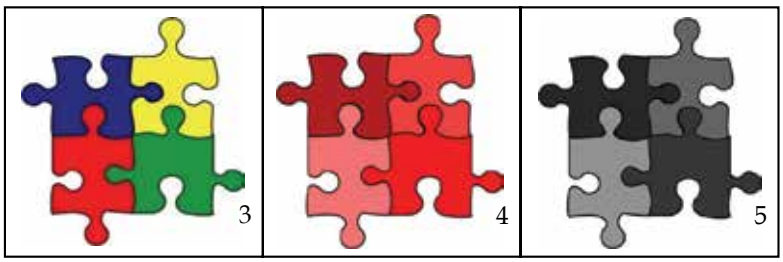

Fig 3. Hues blue, yellow, red and green.
Fig 4. Saturation of the hue red.
Fig 5. Values of light intensities or saturations shown in Figure 3.

4.4 Color space CIEL*a*b*

To improve the precision in color communication of an object, the International Commission of I'Eclairage (CIE) has developed some methods to express the spectral curves in a numerical form. The method used in dentistry is the uniform color space, known as CIEL*a*b*. (Fig. 6) (Rosenstiel & Johnston, 1988). Color space is a numerical area that expresses and references the object's color. Here, L* indicates the lightness coordinate of the object, with values from 0 (absolute black) to 100 (absolute white). The values a* and b* indicates the chromaticity coordinates, showing the three-dimensional position of the object in the color space and its direction. When the coordinate a* is positive (+a*), the object color tends to red. When this coordinate is negative (-a*), the trend is green. This coordination can range from -90 to 70 Δa*. The coordinate b* indicates the direction to yellow (+b*) or blue (-b*), and can vary from -80 to 100 Δb*. (O'Brien et al. 1989; Barath et al., 2003).

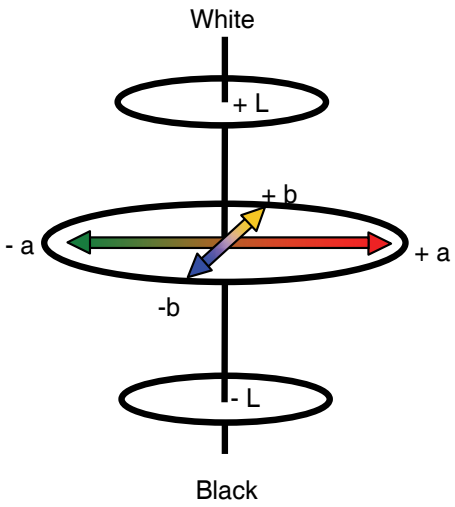

Fig. 6. System CIEL*a*b*
Source: Barath et al., 2003

The achromatic values of color are represented in the axis of lightness (L*), while the spatial projection of data color is presented on the axes of chromaticity (a* and b*) allowing the conceptualization of the components of the chromatic color changes. (Knispel, 1991). The values of the coordinates L* a* b* are obtained from the tristimulus X, Y and Z (generated by light reflected from the object observed) from the following equations, where the values Xn, Yn and Zn correspond to white (Gliese & Petter, 2000):

$$L^* = 116\,(Y/Y_n)^{1/3} - 16 \quad (1)$$

$$a^* = 500[(X/X_n)^{1/3} - (Y/Y_n)^{1/3}] \quad (2)$$

$$b^* = 200[(X/X_n)^{1/3} - (Z/Z_n)^{1/3}] \quad (3)$$

The space between two colorful points is calculated as a color difference (ΔE). The magnitude of this difference can be obtained by the following equation (Gliese & Petter, 2000):

$$\Delta E = ((\Delta L^*)^2 + (\Delta a^*)^2 + (\Delta b^*)^2)^{1/2} \quad (4)$$

Where:

$$\Delta L^* = L^*1 - L^*2 \quad (5)$$

$$\Delta a^* = a^*1 - a^*2 \quad (6)$$

$$\Delta b^* = b^*1 - b^*2 \quad (7)$$

4.5 Clinical significance

As the final judgment of colorimetric evaluation is visual, it has been necessary to establish a relationship between visual and instrumental analysis. In the classic work of Kuehni & Marcus (1979), color differences between samples 1ΔE were perceived and judged acceptable by 50% of observers under ideal conditions of illumination. From this work, Johnston & Kao (1989) assessed this relationship in dentistry. Since there is difficulty in controlling light conditions in the oral cavity, an average difference of up to 3.7 ΔE was considered acceptable by those authors, who suggested an extended visual rating scale (EVRSAM) to understand the clinical significance of the numerical results of instrumental analysis evaluation of color for dental materials.

ΔE	Clinical significance.
0	Excellent esthetics with accurate color choice, not being clinically perceived, or only with great difficulty.
2	Very slight difference in color, with very good aesthetics.
4	Obvious difference, but with an average acceptable to most patients.
6	Poor aesthetics, but within the limits of acceptability.
8	Aesthetics are very poor and unacceptable to most patients.
10	Aesthetics are totally unacceptable.

Table 2. Extended visual rating scale (EVRSAM)
Source: Johnston & Kao, 1988

5. Behavior of color on natural teeth

The color of a tooth is determined by a combination of intrinsic and extrinsic colorimetric effects. The intrinsic properties color are associated with the reflection and absorption of light; with the extrinsic properties related to coloring materials interacting with enamel, such as coffee, tea, tobacco (Chu et al., 2004). When light falls on a natural tooth, four associated phenomena can be described: the transmission of light through the tooth, specular reflection from a tooth's outer surface, diffuse reflection of light from the buccal surface, absorption and scattering of light in the dental tissues. Factors such as enamel thickness, shape, surface texture, dominant color of dentin, double layer effect and light source may further complicate the visual perception of the various nuances of the whole tooth. (Joiner, 2004).

6. Physical characteristics of dental ceramics

6.1 Color stability

The lower the degree of porosity evidenced by a ceramic after laboratory processing, the higher its color stability. This means that industrially manufactured ceramic prostheses show greater color stability when compared to hand crafted prostheses. However, variables, such as the use of extrinsic dyes, number of firings, association with vacuum, type of ceramic material, presence of metal framework and thickness of the ceramic materials, can influence the color stability of ceramics (Brewer et al. 1985; Kourtis et al., 2004).

6.2 Translucency and opacity

Paradoxically, dental ceramics should present both translucency and opacity to mimic dental structures. The opacity is directly related to dentin, because the light passes through enamel and reaches dentin, which, as an opaque body, reflects the light again. On the other hand, enamel behaves like a translucent object, allowing the passage of light, which permits visualization of the dentin while also providing the scattering of light at a wavelength of blue through its hydroxyapatite crystals (Joiner, 2004). There is no ceramic dental product that can simultaneously display characteristics of opacity and translucency in a single material. Therefore, manufacturers have offered ceramics for infrastructure building, opaque ceramic coverage for the construction of the dentin and translucent glazes to be used in layering techniques (Heffernan et al., 2002 a, b).

6.3 Fluorescence

Some substances have capacity to absorb the energy of a non-visible light (ultraviolet, cathode rays or X-rays) and turn it into a visible light, ie light with a greater wavelength than the incident radiation. (Vanini, 1996). When natural teeth are exposed to ultraviolet (UV) light, fluorescence is observed, with an emission spectrum band ranging from white to intense blue light with a wavelength shorter than 400nm. The responsibility for this phenomenon falls with dentin, which has a much more intense fluorescence than enamel (three times more fluorescent), due to the presence of a greater amount of UV photosensitive organic pigment. In order to mimic the behavior of this optical phenomenon, some dental ceramics exhibit fluorescent characteristics similar to teeth in order to create an effect of luminosity. Rare earth metals (europium, terbium, cerium and ytterbium) have been used as luminophor agents in the composition of ceramic powders, because they show an intense blue-white and yellow fluorescence. When a ceramic dental material is not fluorescent, it tends to have an appearance of reduced vitality, presenting a grayish appearance, especially in dark or black lights (Monsenego et al., 1993).

6.4 Opalescence and counter-opalescence

There are properties of transparent or translucent materials which gives those materials a milky appearance, with iridescent reflections that resemble opal stone. This optical phenomenon is attributed to the enamel, as it is a highly mineralized tissue. Enamel acts as a filter and has the ability to selectively forward the long waves, while at the same time, reflect the short waves. Because of this reflection, incisal enamel can be viewed as having a bluish-white color. When long waves that were being transmitted relate to dentin and are reflected back, they give enamel an orange glaze (an effect known counter-opalescence). In ceramics, the effects of counter-opalescence and opalescence are obtained by using different opalescent glazes. Some have a bluish color and others an orange color, depending on the addition of pigments to the ceramic powder. At the time of construction of the prosthesis, the lab tech stratifies enamel into layers, according to the optical nature of the tooth, ensuring the combination of aesthetic effects with regards to fluorescence (Cho et al., 2009).

7. Behavior of color in dental ceramics

7.1 Optical influence of the illuminant

The light source has been identified as one of the factors that most influences the choice of color (Dagg et al. 2004). The type of light source, its intensity and inclination are some of the variables cited in the literature (Barna et al., 1981, Dagg et al. 2004). Due to the three-dimensional nature of color, the behavior of light has been studied; however, its complexity creates a variety of questions of when to use a specific light source. Metamerism is largely responsible for distortions in the selection of color, thus adopting rules to minimize this effect may help in the optical outcome of the ceramics used. As color selection is usually performed under an indirect natural light source, it is prudent to involve fluorescent and incandescent light sources for the selection of color and the evidence of ceramic prosthesis in minimizing landmark metamerism (Volpato et al., 2009).

7.2 Optical influence of the substrate

The type and color of a substrate must be considered when selecting a restorative material, because they influence the final shade of ceramic restorations, mainly with glassy systems. When a substrate has a color similar to the ceramic, the recommended thickness (about 1.5 mm) can be used for vitreous systems. Ceramics, with high translucency and when using layering techniques (such as glass-ceramics based on lithium disilicate), can be fabricated on darkened substrates, such as posts and metal cores, since the dental preparation offers a larger space (about 2.0 mm) (Volpato et al., 2009). However, if this space is not available, systems with a ceramic infrastructure should be used (infiltrated, compact or machined systems), because they are able to provide enough opacity to mask these substrates under a reduced material thickness. (Heffernan et al. 2002b; Koutayas et al., 2003).

7.3 Optical influence of material thickness

The amount of dental reduction while performing the preparation determines the space required for the production of ceramic prostheses. Each ceramic system should ensure that this thickness does not compromise the emergence profile of the restorative work. However, as mentioned above, preparations are not always made on substrates that have a similar color as the tooth. In prostheses with favorable substrates, it is important to communicate the color of the ceramic substrate when fabricating the prosthesis based on this background (Dozic et al., 2003). However, if the substrate is not favorable, it is ideal to utilize more room for the glass-ceramics or to associate infrastructures that provide a degree of opacity that may block the arrival of light to the substrate. Achieving a deeper preparation can improve the ability of a ceramic to hide the substrate, as increasing the thickness of a ceramic material decreases the degree of translucency. (Vichi, Ferrari, Davisdon 2000; Carossa et al., 2001, Nakamura et al. 2002; Dozic et al. 2003, Volpato et al., 2009). However, care must be taken so that wear of the ceramic does not compromise the mechanical properties that are necessary for the dental preparation.

7.4 Optical influence of material composition and manufacturing process

Based on the variety of ceramics available, it is important to understand that the composition and manufacturing process directly influence the optical outcome of the

prosthesis produced, and are important factors for the aesthetic success of the case. For maximum reflection and opacity, the ceramic particles should be slightly larger than the wavelength of light and have a different refractive index of the array where it is incorporated, as a higher refractive index of a material produces greater opacity. (Heffernan et al., 2002a). Ceramic systems using alumina or zirconia have high refractive indices and are therefore used as opacifying elements (Vagkopoulou et al., 2009).

8. Methods of color selecting in Dentistry

8.1 Visual analysis of color

Traditionally, the visual perception of color is the most commonly used selection method in dentistry. This subjective method is based on standardized scales that are composed of representative samples of the average of the colors present in the human dentition. Through this shade guide, you can perform a visual comparison with natural teeth. (Segui et al., 1989). Color selection using scales is extremely complex because the selection process may be influenced by variables ranging from the interpretation of three-dimensional nature of color, to environmental influences. Selections may be inadequate due to factors such as fatigue, age, stress, prior exposure of eyes to light, the observer's visual individuality, inappropriate positioning of the object and an illuminating influence from the environment, and metamerism. Moreover, the human eye can detect small differences in color, but the ability to communicate these differences in terms of magnitude and nature of the difference is very limited. (Knispel, 1991). Despite being widely publicized, prefabricated scales are not representative of the wide range of colors present in natural teeth. These colors are not systematically distributed in the CIEL*a*b* system. Additionally: the material available for use in the dental clinic and laboratory is not the same as the material used in the scales; the thickness of the teeth in the scale does not simulate the clinical condition; most scales have no metallic or ceramic infrastructure; the degree of translucency of the incisal portion; and the characterizations and pigmentation in the cervical third of the scales all make comparison with natural teeth very difficult. These factors may necessitate the observer to get used to a single scale in order to avoid errors during the visual selection of color (Sproull, 2001b).

As color scales have limitations, some factors should be observed to improve their use: the selection of color must be performed at the beginning of the procedure, when the teeth are not dehydrated and the professional is not tired; the color scale should be kept on the same plane of the lower anterior teeth so that light falling on them can be reflected in the same plane to the observer; the scale and teeth should be slightly moistened to facilitate the reflection of light; the operator should look for a maximum of 10 to 15s at each hue and rest by looking at a neutral gray background between observations; the patient should be prepared with a protective clear color so that the color of their clothes does not confuse the operator; the environment must provide the quantity and quality of indirect natural light, usually between 11 and 14 o'clock; and finally, the optical behavior of the color chosen should be reassessed with different artificial illuminations (eg, incandescent light and fluorescent light), in search of a remarkable metamerism that can derail the chosen color. (Chu et al., 2004)

7

8

Fig. 7. Visual selection of color – value
Fig. 8. Visual selection of color - hue and chroma

8.1 Instrumental analysis of color

Colorimeters and spectrophotometers have been used in dentistry for the determination, quantification and comparison of color in the industrial manufacture of materials. Instruments have been designed for clinical use, in order to select the color in the mouth and transmit the data to a laboratory, controlling the result for direct and indirect restorations, tooth whitening, and to minimize subjective visual perception. (Sproull, 2001b). Just as in visual analysis, care must be taken during the selection of an instrumental color: the teeth should be clean and dry for capturing the color, as the presence of plaque and saliva may affect the actual color registered by the equipment; the probe should perpendicularly touch the selected area; and a minimum of three readings should be performed at the cervical, middle and incisal thirds of dental tissues. (Chu et al., 2004)


9

10

Fig. 9. Instrumental selection of color
Fig. 10. Results obtained by oral spectrophotometer

9. Color Communication

The precise communication of color is one of the most important requirements for achieving excellent aesthetic work. This can be achieved by joining two ways: chromatic maps and digital photos.

9.1 Chromatic maps

Since teeth are composed of different shades of color and optical effects, it is necessary to identify: the predominant color (middle third), areas that differ from the predominant color

(cervical and incisal), and the presence of translucent areas, fluorescent effects opalescent effects, and mamelon spots. All of this information must be recorded correctly on a map. These chromatic maps are efficient documents in communicating color variations to the laboratory.

9.2 Digital Photos

Digital photos can be used as a reference for color selection; therefore, they are excellent methods of communication with the laboratory, especially when the laboratory technician is not in the same town as the dentist and patient. The photograph should be taken with the tooth and the scale color that was chosen. If translucent ceramic is to be used in restorations for the rehabilitation of a patient, it is important to photograph the prepared teeth with the color scale in position to inform the lab tech of the substrate color. Translucent areas are best assessed on photographs taken with a black background, because it prevents reflected light from the mouth to strike the enamel again.

Image-editing programs can be used to analyze color dimensions and characteristics of shape and texture. A photo can be digitally converted into grayscale, because value is the quality (not quantity) of the gray color, a colored object photo in grayscale will be the image of its value. Thus, it is possible to compare the value of the scale with the natural tooth, confirming the selection of value. Another process that can be performed is to increase the contrast (+50%) and decrease the brightness (-50%) of the digital photo. The resulting image will enable the display of translucent areas, the precise format of mamelons, the presence of an opalescent halo at the incisal edge, and white spots and cracks, because this is valuable information for the lab tech in the construction of the prosthesis. (Miyashita, 2005)

Fig. 11a, b. Original photo and grayscale to view the value.
Fig. 12a, b. Original photo and increase the contrast and brightness of the digital photo.

10. Conclusion

Since the introduction of metal ceramic crowns, clinicians and researchers have been looking for a restorative system that can associate beauty, strength and durability, but without the presence of a metallic infrastructure. Indeed, dental ceramics are materials that come aesthetically closest to natural teeth. With the improvement of ceramic systems, it has been possible to combine the excellent aesthetic characteristics of this material with a considerable resistance to fracture. It is imperative to understand the phenomenon of color and its variables in the oral cavity, as well as associate different techniques of color selection and communication, in order to get prostheses that look closer to natural dental tissues.

11. References

Barath, V.S.; Faber, F.J. ; Westland, S. & Niedermeier, W. (2003). Spectrophotometric anallysis of all-ceramic materials and their interaction with luting agents and different backgrounds. *Adv Dent Res,* Vol. 17, (Dez, 2003) pp. 55-60, ISSN 1544-0737.

Barna, G. J.; Taylor, J. W. ; King, G. E. & Pelleu, G. B. (1981). The influence of selected light intensities on color perception within the color range of natural teeth. *J Prosthet Dent,* Vol. 46, No. 4, (Oct, 1981) pp. 450-453, ISSN 0022-3913.

Brewer, J. D. ; Akers, C. K. ; Garlapo, D. A. & Sorensen, S. E. (1985). Spectrometric analysis of the influence of metal substrates on the color of metal-ceramic restorations. *J Dent Res,* Vol. 64, No. 1, (Jan, 1985) pp. 74-77, ISSN 0022-0345.

Carossa, S. ; Lombardo, S. ; Pera, P. ; Corsalini, M. ; Rastello, M.L. & Preti, G. (2001). Influence of posts and cores on light trasmission through different all-ceramic crowns: spectrophotometric and clinical evaluation. *Int J Prosthodont,* Vol. 14, No.1, (Jan/Feb, 2001) pp. 9-14, ISSN 0893-2174.

Chevalier, J. (2006). What future for zirconia as a biomaterial? *Biomaterials,* Vol. 27, No. 4, (Jan, 2006) pp. 535-43, ISSN 0142-9612.

Cho, M. S.; Yu, B. & Lee, Y. K. (2009). Opalescence of all-ceramic core and veneer materials. *Dent Mater,* Vol. 25, No. 6 (Jun, 2009) pp. 695-702, ISSN 0109-564.

Chu, S. J. ; Devigus, A. & Mieleszko, A. J. (2004). *Fundamentals of color: shade matching and communication in esthetic dentistry,* Quintessence, ISBN 0-86715-434-9, Chigaco.

Dagg, H. ; O'Conell, N.; Claffey, D.; Byrne, D. & Gorman, C. (2004). The influence of some different factores on the accuracy of shade selection. *J Oral Rehabil,* Vol. 31, No. 9, (Sep, 2004) pp. 900-904, ISSN 0305-182X.

Denry, I. & Kelly, J. R. (2008). State of the art of zirconia for dental applications. *Dent Mater,* Vol. 24, No. 3, (Mar, 2008) pp. 299-307, ISSN 0109-564.

Dozic, A. ; Kleverlaan, C.J.; Meegdes, M.; Zel, J. & Feilzer, A.J. (2003). The influence of porcelain layer thickness on the final shade of ceramic restorations. *J Prosthet Dent,* Vol. 90, No. 6, (Dec, 2003) pp. 563-570, ISSN 0022-3913.

Heffernan, M. J.; Aquilino, S. A.; Diaz-Arnold, A. M.; Haselton, D. R.; Stanford, C. M. & Vargas, M. A. (2002). Relative translucency of six all-ceramic systems. Part I: Core materials. *J Prosthet Dent,* Vol. 88, No. 1, (Jul, 2002) pp. 4-9, ISSN 0022-3913.

Heffernan, M. J.; Aquilino, S. A.; Diaz-Arnold, A. M.; Haselton, D. R.; Stanford, C. M. & Vargas, M. A. (2002). Relative translucency of six all-ceramic systems. Part II: Core and venner materials. *J Prosthet Dent,* Vol. 88, No. 1, (Jul, 2002) pp. 10-15, ISSN 0022-3913.

Holloway, J. & Miller, R.B. (1997). The effect of core translucency on the aesthetics of all-ceramic restorations. *Pract Periodontics Aesthetic Dent,* Vol. 9, No. 5, (June/July, 1997) pp. 567-574, ISSN 1042-2722.

Johnston, W.M. & Kao, E.C. (1989). Assessment of appearance match by visual observation and clinical colorimetry. *J Dent Res,* Vol. 68, No. 5, (May, 1989) pp. 819-822, ISSN 0022-0345.

Joiner, A. (2004). Tooth colour: a review of the literature. *J Dent,* Vol. 32, No. 1, (Suplly, 2004) pp. 3-12, ISSN 0300-5712.

Kelly, J. R. & Denry, I. (2008). Stabilized zirconia as a structural ceramic: An overview. *Dent Mater,* Vol. 24, No. 3, (Mar, 2008) pp. 289-98, ISSN 0109-564.

Kelly, J.R.; Nishimura, I. & Campbell, S. D. (1996). Ceramics in dentistry: historical roots and current perspectives. J Prosthet Dent, Vol 75, No. 1, (Jan 1996) pp. 18-32, ISSN 0022-3913.

Knispel, G. (1991). Factors affecting the process of color matching restorative materials to natural teeth. *Quintessence Int,* Vol. 22, No. 7, (Jul, 1991) pp. 525-531, ISSN 0033-6572.

Kourtis, S. G.; Tripodakis, A. P. & Doukoudakis, A. A. (2004). Spectrophotometric evaluation of the optical influence of different metal alloys and porcelains in the metal-ceramic complex. *J Prosthet Dent,* Vol. 92, No. 5, (Nov, 2004) pp. 477-485, ISSN 0022-3913.

Koutayas, S.; Kakaboura, A.; Hussein, A. & Strub, J. (2003). Colorimetric evaluation of the five different restorative materials on the color of veneered densely sintered alumina. *J Esthetic Rest Dent,* Vol. 15, No. 6, (2003) pp. 353-360, ISSN 1496-4155.

Kuehni, R. G. & Marcus, R. T. (1979). An experiment in visual scaling of small color differences. *Color Res Appl,* Vol. 4, No. 2, (Summer, 1979) pp. 83-91, ISSN 0361-2317.

Lamas, D. G.; Lascalea, G. E.; Walsoe de Reca, N. E. (1998). Synthesis and characterization of nanocrystalline powders for partially stabilized zirconia ceramics. *J Euro Ceramic Soc,* Vol. 18, No. 9, (1998) pp. 1217-21, ISSN 0955-2219.

Luthardt, R. G.; Holzhüter, M.; Rudolph, H.; Herold,V. & Walter, M. (2004). CAD/CAM machining effects on Y-TZP zirconia. *Dent Mater,* Vol. 20, No. 7, (Sep, 2004) pp. 655-62. ISSN 0109-564.

Manicone, P. F.; Iommetti, P. R. & Rafaelli, L. (2007). An overview of zirconia ceramics: basic properties and clinical applications. *J Dent,* Vol. 35, No. 11, (Nov, 2007) pp. 819-26, ISSN 0300-5712.

McLean, J. W. (2001). Evaluation of dental ceramic in the twentieth century. *J Prosthet Dent,* Vol. 85, No. 1, (Jan, 2001) pp. 61-66, ISSN 0022-3913.

Miyashita, E.; Mesquita, A.M.M. & Vasconcellos, D.K. (2006). Seleção de cor, In: *Atualização Clínica em Odontologia.* Luciano Lauria Dib/Mario Sergio Saddy, Artes Médicas Ltda, p. 509-526, 1a ed, ISBN 9788527809, São Paulo.

Miyazaki, T.; Hotta, Y.; Kunii, S.; Kuriyama, S. & Tamaki, Y. (2009). A review of dental CAD/CAM: current status and future perspectives from 20 years of experience. *Dent Mater,* Vol. 28, No. 1 (Jan, 2009) pp. 44-56, ISSN 0109-564.

Monsenego, G.; Burdairon, G. & Clerjaud B. (1993). Fluorescence of dental porcelain. J Prosthetic Dent, Vol. 69, No. 1 (Jan 1993), pp 106-13, ISSN 0022-3913.

Nakamura, T.; Saito, O.; Fuyikawa, J.; Ishigaki, S. (2002). Influence of abutment substrate and ceramic thickness on the colour of heat-presses ceramic crowns. *J Oral Rehabil,* Vol. 29, No. 9, (Sep, 2002) pp. 805-809, ISSN 0305-182X.

O'Brien, W.J.; Groh, C.L.; Boenke, K.M. (1989). A one-dimensional color order system for dental shade guides. *Dent Mater,* Vol. 5, No. 6, (Nov, 1989) pp. 371-374, ISSN 0109-564.

Paravina, R. D. (2002). Evaluation of a newly developed visual sahde-matching apparatus. *Int J Prosthodont,* Vol. 15, No. 6, (Nov-Dec, 2002) pp. 528-234, ISSN 0893-2174.

Petter, C. O. & Gliese, R. (2000). *Fundamentals in Colorimetry*. Ed. UFRGS, Porto Alegre, Brazil.

Raigrodski, J. (2004). Contemporary materials and technologies for all-ceramic fixed partial dentures: a review of the literature. *J Prosthet Dent,* Vol. 92, No. 6 (Dec, 2004) pp. 557-562, ISSN 0022-3913.

Sadowsky, S. J. (2006). An overview of treatment considerations for esthetic restorations: a review of the literature. *J Prosthet Dent,* Vol. 96, No. 6, (Dec, 2006) pp. 433-42, ISSN 0022-3913.

Segui, R. R.; Hewlett, E. R.; Kim, J. (1989). Visual and instrumental colorimetric assessments of small color differences on translucent dental porcelain. *J Dent Res,* Vol. 68, No. 12, (Dec, 1989) pp. 1760-1764, ISSN 0022-0345.

Sproull, R. C. (2001a). Color matching in dentistry. Part I. The three-dimensional nature of colour. *J Prosthet Dent,* Vol. 86, No. 5, (Nov, 2001) pp. 453-457, ISSN 0022-3913.

Sproull, R. C. (2001b). Color matching in dentistry. Part II. Practical applications of the organization of color. *J Prosthet Dent,* Vol. 86, No. 5, (Nov, 2001) pp. 458-464, ISSN 0022-3913.

Tadakoro, S. K. & Muccillo, E. N. S. (2002). Synthesis and characterization of nanosized powders of yttria-doped zirconia. *J Alloys Compd,* Vol. 344, No. 1-2 (Oct, 2002) pp. 186-89, ISSN 0925-8388.

Vagkopoulou, T.; Koutayas, S.O.; Koidis, P. & Strub, J.R. (2009). Zirconia in Dentistry: Part 1. Discovering the nature of an upcoming bioceramic. *Eur J Esthet Dent,* Vol. 4, No. 2, (Summer, 2009) pp. 130-51, ISSN 1862-0612.

Van Der Burgt, T. P.; Ten Bosch, J. J.; Borsboom, P. C. F.; Kortsmit, W. J. P. M. (1990). A comparison of new and convencional methods for quantification of tooth color. *J Prosthet Dent,* Vol.63, No. 2, (Feb, 1990) pp. 155-162, ISSN 0022-3913.

Vanini, L. (1996). Light and color in anterior composite restorations. *Pract Periodontics Aesthetic Dent*, Vol. 8, No. 7 (Sep, 1996) pp. 673-682, ISSN 1042-2722.

Vichi A.; Ferrari, M. & Davidson, C. L. (2000). Influence of ceramic and cement thickness on the masking of various types of opaque posts. *J Prosthet Dent,* Vol. 83, No. 4, (April, 2000) pp. 412-17, ISSN 0022-3913.

Volpato, C. A. M.; Monteiro Jr, S.; Andrada, M. A.; Fredel, M. C.; Petter, C. O. (2009). Optical influence of the type of illuminant, substrates and thickness of ceramic materials. *Dent Mater,* Vol. 25, No. 1, (Jan, 2009) pp. 87-93, ISSN 0109-564.

Yang, S. F. et al. (2009). New nansized Al_2O3 – BN coating 3Y-TPZ ceramics composites for CAD/CAM – produced all-ceramic dental restorations. Part I. Fabrications of powders. *Nanomedicine J,* Vol. 5, No. 2 (Jun, 2009) pp. 232-39, ISSN 1549-9634.

9

Surface quality controls mechanical strength and fatigue lifetime of dental ceramics and resin composites

Ulrich Lohbauer[1], Roland Frankenberger[2] and Norbert Krämer[3]
[1] *University of Erlangen, Erlangen, Germany*
[2] *University of Marburg, Marburg, Germany*
[3] *University of Giessen, Giessen, Germany*

Summary

Objectives: Surface quality strongly influences the mechanical strength of dental restorative materials by a specific surface flaw population. Perfect polishing is thus a highly recommended clinical procedure to ensure maximum mechanical performance. Dental restorations are commonly exposed to masticatory loads much lower than their short time fracture strength. Surface microcracks can grow under subcritical fatigue loads resulting in premature failure of a restoration.
This study was conducted to discuss the relevant parameters on ceramic strength and degradation over time. The aim was to correlate surface roughness, fracture strength, toughness and degradation behavior by slow crack growth with the results of a prospective clinical trial. The fracture strength σ_c and toughness K_{Ic} of a glass ceramic and of a resin composite have been assessed as a function of surface roughness and related to critical flaw sizes a_c, intrinsic microstructure and fractographic findings. The slow crack growth parameters of the clinically used glass ceramic material have been determined using the dynamic fatigue method. Based on a naturally inherent flaw population of the specimens, so called fractureStrength - failureProbability – lifeTime diagrams (SPT) could be derived. This allowed for theoretically predicting the lifetime of a ceramic material. The 12-years follow-up results of a prospective clinical trial have been analyzed according to clinical fractures and correlated with measured lab data on slow crack growth degradation of strength.
Methods: Rectangular specimens were manufactured using two glass ceramic materials (IPS Empress (IEM), IPS E.max Press (EMP), IvoclarVivadent, Liechtenstein) and a resin composite (Tetric EvoCeram (TEC), IvoclarVivadent). Different surface roughness levels were prepared on EMP and TEC using lab grinding/ polishing techniques and quantified under a confocal laser scanning microscope (CLSM).
Fracture strength data were determined in four-point bending. *Weibull* statistics were applied and the parameters m and σ_0 were calculated. The Indentation fracture method was used to calculate fracture toughness for EMP and TEC. Critical flaw sizes were calculated

and related to the microstructural and fractographic features using a scanning electron microscope (SEM).
Dynamic fatigue experiments were performed on IEM in water at four decreasing stress rates from 1.3 to 0.0013 MPas^{-1}. The parameters of subcritical crack growth n and A were calculated. SPT predictions were derived for 1, 4, 8 and 12 years, based on a static crack growth mechanism.
A twelve years clinical recall of a prospective clinical trial was performed using the ceramic restorative material IEM. Bulk, chipping and marginal fractures or detoriations were observed. Failure rates were calculated according to Kaplan-Meier survival analysis and merged into the SPT diagram.
Results: Fracture strength of EMP decreased from 441.4 to 303.3 MPa (R_a = 150 nm to 1.5 µm) and of TEC from 109.8 to 74.0 MPa (R_a =, 300 nm to 50 µm). EMP exhibited a fracture toughness of K_{Ic} = 4.14 MPam$^{0.5}$ and TEC of K_{Ic} = 1.89 MPam$^{0.5}$. Calculated crack lengths for EMP ranged from 28.1 µm (441.4 MPa) to 59.6 µm (303.3 MPa) and for TEC from 94.3 µm (109.8 MPa) to 207.0 µm (74.0 MPa).
The inert fracture strength of IEM was measured to 134 MPa and the Weibull modulus to m=8.1. The subcritical crack growth parameter n was calculated to n=19.2 and the extrapolated crack velocity to A= 0.0014 m/s. Based on a clinical relevant failure probability of P_F = 5 %, material strength was predicted to decrease from initial $\sigma_{0.05}$ = 93 MPa down to $\sigma_{0.05}$ = 33 MPa after 12 years (- 64 %).
The clinical survival rate for the material IEM dropped from 100 % (1 year) to 93 % (4 years), 92 % (8 years) down to 86 % after 12 years. The incidence of inlay defects like chipping and marginal fractures increased from 1 % at baseline, 7 % after 4 years, 26 % after 8 years to 57 % after 12 years.
Significance: The fracture strength of brittle ceramics is determined by surface roughness. A proper polishing procedure is thus essential for maximum strength of glass ceramic materials. Dynamic fatigue experiments showed a dramatic degradation of ceramic strength over time due to a corrosive growth of small surface microcracks. The strength behavior of the investigated resin composite is less influenced by surface roughness.
Clinical data followed the in vitro lifetime predictions in terms of dramatically increased clinical bulk fractures and detoriations from chipping and marginal fractures after twelve years. The clinically observed survival rate seems to match the in vitro lifetime predictions with time. A failure level of P_F = 5% is clinically exceeded after 4 years of clinical service, which corresponds to an theoretical prediction of maximum static loading of 35.5 MPa. Since the slow growth of surface flaws is responsible for fatigue degradation, a perfect polishing procedure right after placement is strongly recommended to keep an optimum strength performance during the whole clinical lifetime. Based on the results on the resin composite, the fatigue lifetime in this case would be expected to be less influenced by surface roughness.

1. Introduction

An increasing amount of all-ceramic materials are being used in restorative and prosthetic dentistry. High demands for aesthetic and biocompatible materials extend the significance of ceramic restorations. Clinically, the main problem having consequently been reported in literature, are fractures such as chipping, marginal and bulk fractures (Molin & Karlsson,

2000; Krämer & Frankenberger, 2005). Major goals of dental ceramic developers are thus the improvement of mechanical properties and reliability through e.g. CAD/CAM processing or hot pressing techniques (Evans, 1990).

Clinical reports of ceramic inlays report bulk fractures to be still a main failure reason of all commercially available ceramic inlay systems, however, only a few controlled prospective clinical studies presented data on clinical long-term performances of different ceramic systems (Molin & Karlsson, 2000; Krämer & Frankenberger, 2005; Pallesen & van Dijken, 2000; Hayashi et al., 2003; Reiss & Walther, 2000). Although adhesively bonded to tooth hard tissues, all-ceramic materials suffer from fractures in up to 20 % of clinically assessed cases (Hayashi et al., 2003). Clinical failures with ceramic inlays and onlays are observed throughout their clinical lifetime. Extended class-I restorations develop marginal fractures in the majority of cases, whereas class-II inlays fail predominantly due to bulk fractures (Molin & Karlsson, 2000). Among the high strength prosthetic restorations, prospective clinical studies using zirconia supported fixed partial dentures (FPDs) reported promising results for an observation time of two to five years (Raigrodski et al., 2006; Tinschert et al., 2008; Sailer et al., 2007; Molin and Karlsson, 2008; Beuer et al., 2009). However, several authors reported up to 15% of minor chipping of the veneering ceramic. Minor clinical failures are thereby due to zirconia framework fractures but to chipping failures within the veneering ceramic.

Ceramic strength in general is limited by the size and distribution of an inherent flaw population. Fracture of brittle ceramics occur without measurable plastic deformation, which is due to the stable atomic bonds of ceramics. In consequence, failure can start from small flaws prior to plastic deformation. This fact is expressed by a low resistance against crack extension, that is characterized by the parameter fracture toughness K_{Ic} (Munz & Fett, 1999). Various approaches have been used to determine the effect of flaws on strength (Davidge & Evans, 1970). Griffith postulated for plane stress conditions an inverse square root relationship between fracture strength σ_c and critical flaw size a_c (Griffith, 1920):

$$\sigma_{c(t=0)} = \frac{K_{Ic}}{(\pi \cdot a_c)^{\frac{1}{2}}} \tag{1}$$

Brittle fracture will occur when the stress intensity K_I at a crack of length a_c exceeds the critical stress intensity factor, i.e. $K_I \geq K_{Ic}$.

One simple method to increase ceramic strength is an accurate surface polishing procedure. Polishing leads to reduction of surface flaw sizes a_c and thus to increased mechanical strength σ_c, as can be seen from eq. 1 (O'Brien, 2002). Intraoral adjustment of a restoration surface after placement induces deep flaws and requires proper polishing especially in load bearing areas and in deep fissures. Also, intensive research is focused on surface polishing of resin composites. A smooth surface is desirable due to optimal biocompatibility (Watanabe et al., 2006). Proper polishing of restorations minimizes possible gingival irritation, surface staining, plaque accumulation, and secondary caries (Venturini et al., 2006). In literature, no indication is provided that proper polishing substantially influences resin composite strength as it is reported for brittle ceramics.

On the long term however, a corrosive degradation and a slow crack growth (SCG) mechanism is reducing the initial fracture strength of a ceramic material (Lohbauer et al., 2002). Numerous studies have shown that catastrophic failure may occur far below the short-time fracture strength due to a slow growth of a subcritical crack up to the critical crack length a_c (Fairhurst et al., 1993; Ritchie & Dauskardt, 1991). Thus, degradation of strength is measured during a period of lifetime (Mecholsky, 1995). Similar characteristics for the fatigue performance of dental ceramics under the special focus of oral environment and loading was observed (Morena et al., 1986). SCG kinetics are strongly influenced by the amount and composition of a glass phase in the ceramic microstructure (Wiederhorn, 1967). The deleterious effect of slow crack propagation may be attributed to the stress-enhanced chemical reaction occurring in the presence of water vapour at a crack tip. This occurs preferentially in silicate base glasses resulting in bond rupture (Charles, 1958). Even moisture levels of 0.017 % relative humidity cause stress corrosion (Wiederhorn, 1967).

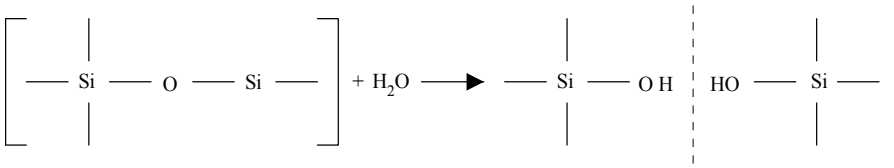

(2)

Fracture resistance of resin composites is discussed controversially in literature. There is the treatment of resin composites as brittle materials, applying linear elastic fracture theory and measuring related material properties such as SCG parameters or fracture toughness (Marshall & Cox, 1985; Fujishima & Ferracane, 1996; Shin & Drummond, 1999). On the other hand, dental composites exhibit plastic and viscoelastic effects or a viscoplastic susceptibility for creep and recovery (El Hejazi & Watts, 1999; Vaidyanathan & Vaidyanathan, 2001; DeGroot et al., 1988). However, in the vicinity of a sharp surface crack tip, blunting occurs by plastic deformation, which reduces the local stress at the crack tip, resulting in cleavage rather than brittle rupture of the atomic bonds (Ashby & Jones, 1996). The brittle response (or respectively the ductility) of a resin composite is depending on variables such as loading rate, temperature and filler loading. Fillers are reported to increase fracture toughness due to microcracking at the crack front or crack bridging mechanisms by second phase particles e.g. filler particles (Evans, 1990). Temperature increase, even far below the glass transition temperature will contribute to a rather ductile material behavior and fast fracture is reported to suppress creep and recovery phenomena (Ashby & Jones, 1996). Fatigue measurements in resin composites postulate a different material response comparing fast fracture with cyclic fatigue (Lohbauer et al., 2003).

This study was performed to discuss influencing parameters on ceramic strength and degradation over time. The aim was to correlate surface roughness, fracture strength, toughness and degradation behavior by slow crack growth with the results of a prospective clinical study. The fracture strength σ_c and toughness K_{Ic} of a glass ceramic and of a resin composite have been assessed as a function of surface roughness and related to critical flaw sizes a_c, intrinsic microstructure and fractographic findings. A long-term prospective clinical study has been performed in our academic environment. Recently, the 12-years follow-up results have been reported (Frankenberger et al., 2008). Based on this glass ceramic material, one aim of this study was to correlate the long-term clinical outcome with measured lab

data on slow crack growth degradation of strength. The SCG parameters of this glass ceramic material have been determined using the dynamic fatigue method (Munz & Fett, 1999). Based on a naturally inherent flaw population of the specimens, so called fractureStrength - failureProbability – lifetime diagrams (SPT) could be derived from the crack growth measurements (Sudreau et al., 1994). This allowed for theoretically predicting the lifetime of a ceramic restoration related to an underlying crack growth mechanisms. SPT diagrams have been derived as a predictive tool for clinical reliability.

Materials and Methods

Materials

Two glass ceramic materials and one resin composite have been assessed in this study.
The clinical study as well as the evaluation of the subcritical crack growth parameters was based on an identical batch of the leucite reinforced glass ceramic system IPS Empress® (IEM, IvoclarVivadent, Schaan, Liechtenstein).
Surface roughness related fracture strength experiments have been performed using the lithiumdisilicate glass ceramic IPS E.max® Press (EMP, IvoclarVivadent) and the direct resin composite Tetric® EvoCeram (TEC, IvoclarVivadent).

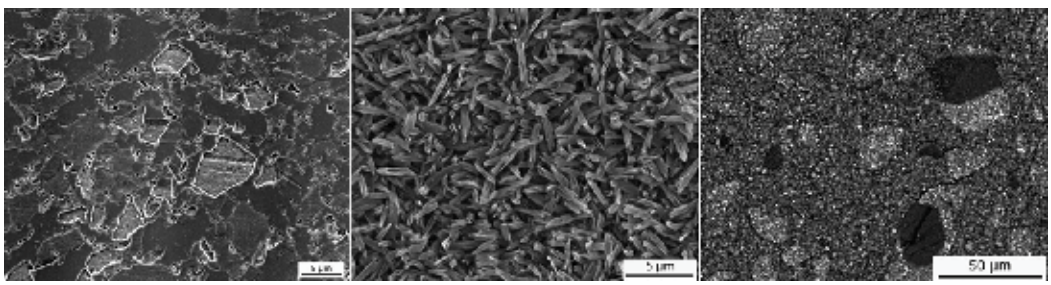

Fig. 1. Microstructure of the investigated materials: a) Leucite reinforced glass ceramic IEM; b) Lithiumdisilicate crystallite habit and size in EMP; c) Filler particle size and distribution of the inhomogenous microfiller TEC exhibiting prepolymeric fillers.

The glass ceramic IEM consisted of a silica based glass fraction of approx. 60 vol % out of the system K_20 - Al_2O_3 - SiO_2. Leucite [K_20 Al_2O_3 4 SiO_2] was the major crystalline phase (40 vol %) exhibiting a mean crystallite size of 1 - 3 µm, as shown in Fig 1a (Höland et al., 2000). EMP mainly consisted of 70 wt % crystalline $Li_2Si_2O_5$ phase of 3 – 6 µm in length (Fig 1b). Beside that a small amount of Li_3PO_4 (lithiumorthophosphate) crystals is embedded in the glassy matrix. EMP is used as a supporting structure and will clinically be veneered with a silicate based feldspathic porcelain. A core material has been selected since the influence of surface defects on the strength performance of veneering porcelains is well understood and since slow crack growth influences are even reduced in high crystalline lithium disilicate structures (Höland et al., 2000). TEC as an inhomogenous microfiller hybridcomposite consists of a dimethacrylic matrix system and 48.5 wt % microfiller hybrids with mean particle sizes of 160 nm to 0.4 and 0.7 µm. Further 34 wt % of prepolymeric fillers are added. Those fillers consist of a pre-polymerized and re-grinded resin composite material and exhibit a mean grain size of approx. 20 - 50 µm. The microstructure is displayed in Fig 1c.

This material has been selected due to the extended filler size distribution which in turn should have an influence on strength versus surface defect performance.

Experimental procedure

For the clinical study the material (IEM) was processed by one dental ceramist according to the manufacturer's instructions for use (IFU) (Krämer & Frankenberger, 2005).

Surface treatment	Mean roughness	EMP			TEC		
	R_a [µm]	σ_0 [MPa]	m	a_c [µm]	σ_0 [MPa]	m	a_c [µm]
untreated	0.429 ± 0.04	-	-		109.8[c]	12.5	94.3
polished	0.214 ± 0.01	441.4[a]	13.3	28.1	-	-	-
4000 grit	0.150 ± 0.02	438.3[a]	4.8	28.5	-	-	-
4000 grit	0.310 ± 0.09	-	-	-	104.4[c]	11.3	104.3
1000 grit	0.646 ± 0.02	370.5[a,b]	7.2	39.9	-	-	-
800 grit	0.835 ± 0.13	-	-	-	109.3[c]	14.6	95.2
500 grit	1.131 ± 0.89	-	-	-	103.8[c]	10.9	105.5
320 grit	1.509 ± 0.15	303.3[b]	10.0	59.6	-	-	-
320 grit	2.075 ± 0.34	-	-	-	96.9[c]	16.5	121.1
120 grit	4.221 ± 1.11	-	-	-	88.7[d]	12.8	144.5
cutting	25.0 ± 4.05	-	-	-	85.6[d]	13.5	155.2
cutting	50.0 ± 6.87	-	-	-	74.0[d]	15.2	207.6

Statistical homogenous subgroups are labelled with superscript letters ($p < 0.05$).
Table 1. Weibull parameters σ_0 and m and the estimated fracture releasing crack length a_c according to the applied surface roughness R_a.

Regarding the lab experiments, IEM and EMP specimens were hot pressed to a final geometry of 25 x 2.5 x 2 mm applying the manufacturer recommended procedure and according to the ISO 6872 standard. TEC specimens with the dimension 25 x 2 x 2 mm were produced using a metal /glass mold and light-curing on five overlapping spots of 8 mm diameter. The upper and lower side of the bar were cured with a commercial halogen light curing unit (Elipar® Trilight (750 mW/ cm²), 3M ESPE, Germany). The illumination time on a single spot was 20 seconds. The procedure followed the manufacturer's IFU and ISO 4049 standard.
All specimen surfaces were grinded under permanent water cooling with silicon carbide paper according to Table 1. The specimen flanges were grinded under an angle of 45° with the specific roughness to prevent fracture releasing stress concentrations. For polishing the samples a 0.25 µm polishing paste was used. The two groups exhibiting an extremely deep roughness of 25 and 50 µm, were treated by a standardized surface cutting technique with a bur. Respective data for surface roughness were determined under a CLSM in reflectance

mode ((TCS SL, Leica, Bensheim, Germany). The confocal z-sections were taken at every 1.6 µm under 1000 fold magnification (HC PL Fluotar 100, NA = 0.9).
All specimens were stored dark and dry for 24 h at 37 °C prior to fracture testing. To evaluate the specific flexural strength and SCG parameters, the four-point-bending test was used. The bars were fixed between four fins (∅ = 2 mm, distance of inner/ outer fins: 10/ 20 mm) and were subsequently loaded until fracture with a crosshead speed of 0.75 mm/ min in an universal testing machine (Z 2.5, Zwick, Germany).

Prospective clinical study design and follow-up

Patients' selection for the clinical study was based on criteria such as a high level of dental hygiene, absence of pain from the tooth to be restored or further restorations planned in the posterior region. 96 inlays (77 %) and onlays (23 %) were placed in 34 patients by six dentists. Whether two surface (n = 45) or three surface (n = 27) restorations exhibited proximal margins below the cementoenamel junction (CEJ). 57 molar and 39 premolar restorations were bonded with a four-step selective-etch adhesive system (Syntac® Classic, IvoclarVivadent), inserted using four different resin composites and light cured for a total of 120 s. The average ceramic dimensions measured prior to insertion have been 1.4 mm below the deepest fissure, 3.5 mm buccal-lingually at the isthmus, and 1.8 mm below reconstructed cusps of onlays. Occlusal contacts were adjusted using finishing burs (Intensiv, Viganello-Lugano, Switzerland) prior to SofLex discs (3MESPE, St. Pauls, MN, USA). Polishing was conducted using felt discs with a polishing gel (Dia-Finish E Filzscheiben & Brinell, Renfert, Hilzingen, Germany).
The restorations were assessed after placement by two calibrated investigators using modified USPHS codes and criteria (major criteria: surface roughness, marginal integrity, tooth integrity, inlay integrity) at the following time periods: baseline, 1, 2, 4, 6, 8, 10 and 12 years. The study was conducted according to EN 540. For specific details and clinical procedure refer to (Krämer & Frankenberger, 2005).
Median survival times have been calculated according to Kaplan-Meier survival analysis. The statistics applied here represent failure rates that correspond to the experimental failure probability P_F since most clinical restorations failed due to fracture. To receive information on fracture releasing clinical loads, those Kaplan-Meier survival times were merged into the experimental SPT lifetime prediction. Experimental lifetime regression lines for 1, 4, 8 and 12 years were calculated to meet the clinical follow-up periods. Clinical incidence of failures as well as of defects were located on the corresponding regression line. This experimental approach might allow for an extrapolation on clinically fracture releasing stress levels.

Fracture strength, slow crack growth and lifetime

According to the assumption of weakest link, the fracture strength of brittle materials is limited by the largest crack in the loaded volume. Hence, a distribution of crack lengths results in a strength distribution which is commonly described by fracture probability $P_{F(\sigma c)}$

$$P_F = 1 - \exp\left[-\left(\frac{\sigma_c}{\sigma_0} \right)^m \right] \tag{3}$$

where σ_0 is the scale parameter (P_F = 63.2%) and m is the Weibull modulus, respectively (Weibull, 1951; Drummond & Mieschke, 1991). The strength data were evaluated according to the two parameter cumulative Weibull distribution by plotting the fracture probability P_F versus fracture strength σ_c.

$$\ln\ln\frac{1}{(1-P_F)} = m\cdot\ln\sigma_c - m\cdot\ln\sigma_0 \tag{4}$$

The parameters m und σ_0 were determined by a maximum likelihood approach. The slope of the regression line within the Weibull plot ln (ln (1/(1 - P_F))) versus ln σ_c indicates the Weibull modulus m and is an indicator for the material homogeneity. The scale parameter σ_0 represents the strength at a failure probability of P_F = 63.2%. However, for reliable use in dentistry the limits for fracture strength are recommended to be set at a failure probability of P_F = 5% (Annusavice & Brennan, 1996). Fracture strength for IEM, EMP, and TEC and dynamic fatigue measurements for IEM were carried out using the 4-point bending technique in a universal testing machine (Z 2.5, Zwick, Germany) according to the European standard EN 843. To ensure inert conditions, the specimens (n=25 per group) were dry stored for 24 h prior to measurements. A constant loading rate dσ/dt of 130 MPas^{-1} was applied. The groups among each other were analyzed using the non-parametric Mann-Whitney U-Test (α = 0.05; SPSS 14.0 for Windows). However, to generate significant differences between the tested groups a Bonferroni correction was applied.
The subcritical crack growth parameters n and A were determined by means of dynamic fatigue, in which the strength of bend specimens is measured as a function of distinct loading rates dσ/dt:

$$\sigma^{n+1} = B\cdot(n+1)\cdot\sigma_c^{n-2}\cdot\frac{d_\sigma}{d_t} \tag{5}$$

where σ is the fracture strength at a given loading rate dσ/dt: [σ_f = f (dσ/dt:)] and σ_c the inert strength at very high loading rates ($\sigma = \sigma_c$). The parameters n and A were determined by linear regression analysis from the plot log σ_f versus log dσ/dt (Peterlik, 1994). The parameter n and A represent the slope and site of the regression line. The extrapolated crack velocity A is calculated as a function of the constant B (Munz & Fett, 1999):

$$B = \frac{2}{A\cdot Y^2\cdot(n-2)\cdot {K_{Ic}}^{n-2}} \tag{6}$$

To calculate A, literature values for fracture toughness (IEM: K_{Ic} = 1.29 MPam$^{0.5}$) and for the function of crack shape ($Y = \pi^{0.5}$) were taken reference (Seghi et al., 1995).
Four dynamic fatigue tests at decreasing loading rates dσ/dt from 1.3 to 0.0013 MPas^{-1} were carried out in distilled water at 37°C.
With the knowledge of the slow crack growth parameters n and A, it is possible to calculate lifetime for certain loading conditions (Munz & Fett, 1999; Sudreau et al., 1994). For a crack

growth mechanism based on static loading (σ = const.) the lifetime t_f is given as (Ritchie & Dauskardt, 1991)

$$t_{f(\sigma=const)} = B \cdot \sigma_c^{n-2} \cdot \sigma^{-n} \tag{7}$$

Merging a material's lifetime with its parameters m and σ_0 of the Weibull distribution it becomes possible to define critical conditions for lifetime or loading strength at a given failure probability P_F. Those distributions may help to select a suitable dental ceramic for a reliable design of specific indications. Chadwick, for example, derived comparable relations for resin composite materials (Chadwick, 1994). On the other hand, by knowledge of clinical failure rates or lifetimes it is possible to establish a threshold value representing a maximum load to failure.

Fracture toughness

In order to calculate the fracture toughness K_{Ic} for the materials EMP and TEC, the measurement of surface hardness, elastic modulus and material density was necessary.
Material density ρ was measured according to Archimedes' principles of buoyancy and surface hardness H by Vickers indentation technique according to

$$H = \frac{P}{b^2} \tag{8}$$

where P is the applied load and b is the average indentation half-diagonal of the Vickers indentation (Anstis et al., 1981). The elastic modulus E was measured by ultrasound velocity method (Halmshaw, 1991). Here, the characteristic time delay of sound velocity μ through a material was measured and related to the elastic modulus

$$E = \frac{(1+\nu)\cdot(1-2\nu)}{(1-\nu)} \cdot \mu^2 \cdot \rho \tag{9}$$

with the material inherent Poisson ratio ν.
The indentation fracture technique (IF) was used to calculate the fracture toughness (Anstis et al., 1981). Flaws of controlled size, shape and location were introduced into the sample surface by Vickers indentations at supercritical indentation loads P_c. Direct measurement of radial crack lengths w led to characterization of the fracture process and thus to calculation of fracture toughness K_{Ic} through (Scherrer et al., 1998; Albakry et al., 2003):

$$K_{Ic} = 0.016 \cdot (E/H)^{0.5} \left(P_c / w^{1.5}\right) \tag{10}$$

Material property data for the resin composite and for the glass ceramic material are summarized in Table 2. Inserting the fracture toughness values in eq. 1, critical flaw sizes a_c can be calculated depending on the test group specific fracture strength σ_c.

	Poisson ratio ν	Density ρ [g/ cm³]	E-Modulus [GPa]	Hardness [GPa]	Fracture toughness K_{Ic} [MPam$^{0.5}$]
IEM					1.29 *
EMP	0.23 **	2.524 ± 0.01	93.8 ± 2.11	5.56 ± 0.26	4.15 ± 0.58
TEC	0.31 ***	2.138 ± 0.01	9.8 ± 0.75	0.62 ± 0.09	1.89 ± 0.43

*: (Anstis et al., 1981) **: (Fujishima & Ferracane, 1996) ***: (Chung et al., 2004)
Table 2. Mechanical properties of the test materials, required for calculation of fracture toughness.

Fractographic examinations were performed under a light microscope (SV11, Zeiss, Germany) on all specimens and under a SEM (Leitz ISI SR 50, Akashi, Japan) on representative samples.

Results

Fracture strength, slow crack growth and lifetime

The characteristic fracture strengths σ_0 for IEM, EMP, and TEC at a failure probability P_F = 63,2 %, their Weibull moduli m and the calculated fracture releasing critical flaw sizes are given in Table 1. The crack lengths a_c were calculated according to eq. 1 inserting the related strength σ_c and fracture toughness K_{Ic} values. Fracture strength for the glass ceramic material EMP decreased from 441.4 to 303.3 MPa and for the resin composite TEC from 109.8 to 74.0 MPa, in both cases with increasing surface roughness. In Table 1, the mean roughness values R_a, determined under the CLSM, are related to the applied surface grinding technique and cover a range between 150 nm and 1.5 µm for the glass ceramic and 300 nm and 50 µm for the resin composite material. The least roughness was generated using the 4000 grit SiC paper. Identical surface grinding technique led to different results for EMP and TEC as Table 1 shows for 4000 and 320 grit.
Statistical significant differences in EMP were found at a surface roughness of R_a = 0.65 µm. However, a linear correlation over the whole roughness range could be proved (R^2 = 0.9265, Fig. 2).
In TEC a wide range of roughness produced statistical homogenous results. Significant differences are observed at a surface roughness of R_a = 4.22 µm. No linear correlation could be proved. Statistical homogenous subgroups are labelled in Table 1. Figures 2 and 3 point out the correlation between fracture strength and the applied surface roughness. Here mean values of EMP and TEC are presented together with their actual standard deviations.

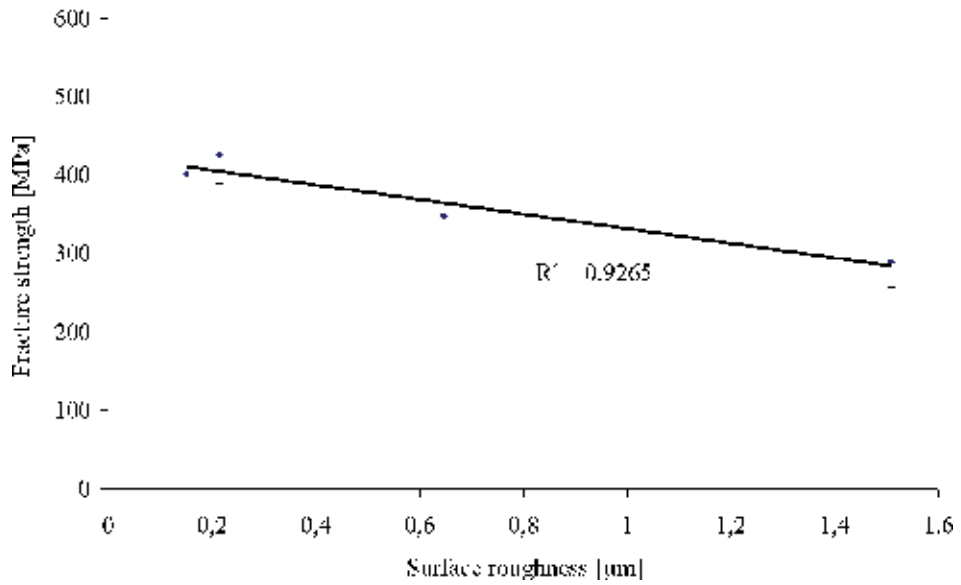

Fig. 2. Correlation between fracture strength σ_c and the applied surface roughness R_a for EMP.

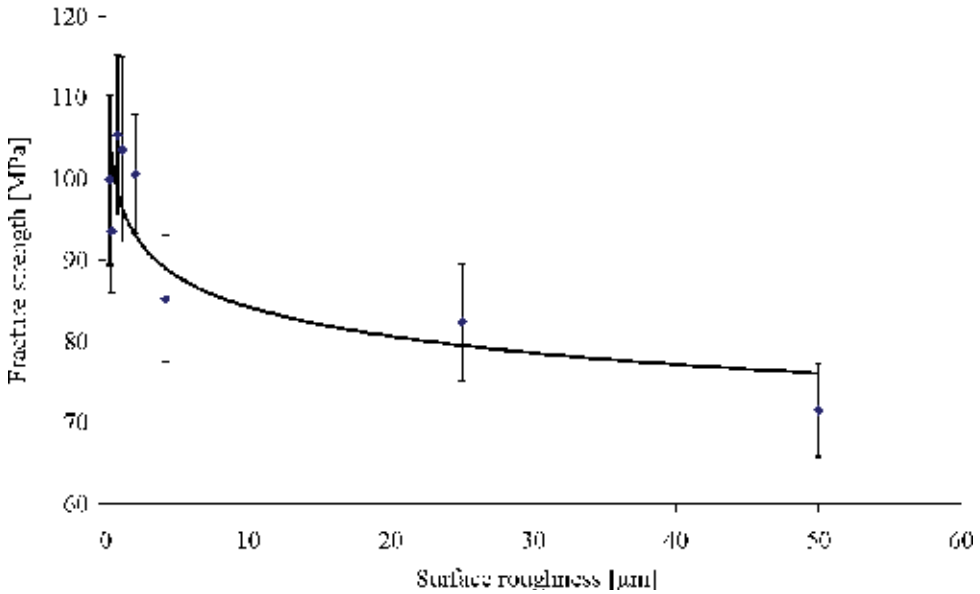

Fig. 3. Correlation between fracture strength σ_c and the applied surface roughness R_a for TEC.

The Weibull distribution of facture strength for IEM is shown in Fig 4. An initial fracture strength of σ_0 = 134.2 MPa and a Weibull modulus of m = 8.1 was calculated for IEM under dry conditions, suppressing the influence of slow crack growth. Setting the failure probability to P_F= 5% the strength is reduced to $\sigma_{0.05}$ = 92.8 MPa. Table 3 summarizes the

measured Weibull data for all loading rates dσ/dt of the dynamic fatigue experiments. The subcritical crack growth performance was determined under wet conditions. Fig. 5 shows the correlation between fracture strength and the applied loading rates (dynamic fatigue). The subcritical crack growth parameters n and A were determined to n = 19.16 and A = 1.41214 mm/s.

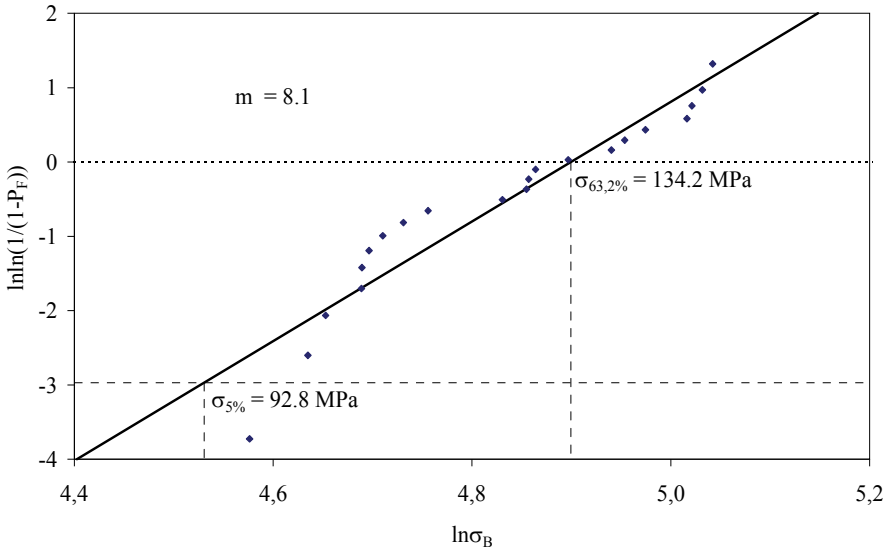

Fig. 4. Distribution of the inert strength data σ_c according to the applied Weibull statistics.

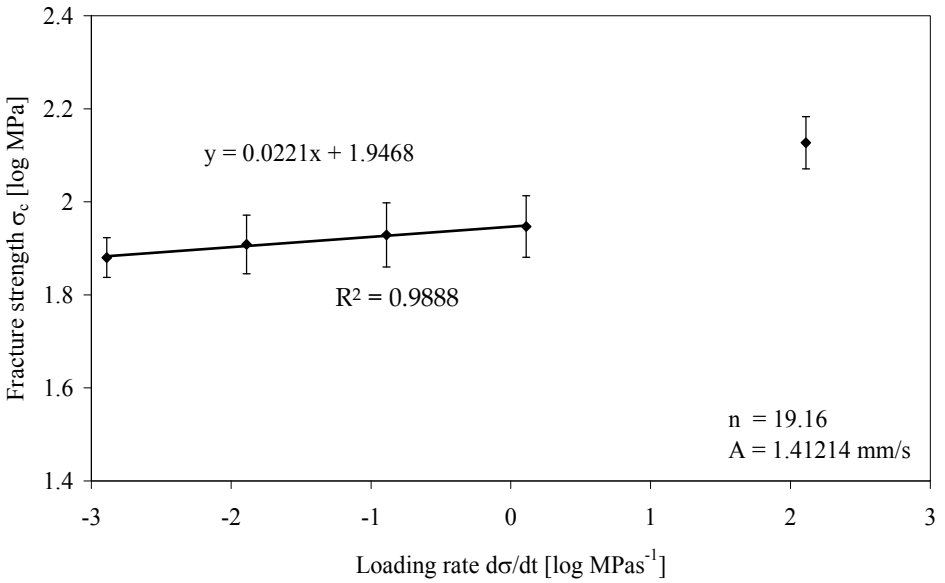

Fig. 5. Dynamic fatigue measurements for IEM in relation to the respective fatigue strength.

Loading rate dσ/dt [MPas^{-1}]	Scale parameter σ_0	Weibull modulus m
130	134.2	8.1
1.3	88.5	6.8
0.13	84.9	6.5
0.013	81.0	7.0
0.0013	75.9	11.1

Table 3. Weibull inert strength and dynamic fatigue data for IEM.

Fig. 6 shows the resulting SPT plots for IEM. The characteristic strength values were estimated for failure probabilities of P_F = 63.2% and P_F = 5%. Predictions were calculated for lifetimes of 1, 4, 8 and 12 years according to the clinical follow-up scedule. In other words, influenced by mechanical and chemical degradation through dynamic loading and humidity, fracture strength of the dental glass ceramic under investigation is theoretically predicted to drop from initial $\sigma_{0.05}$ = 93 MPa down to $\sigma_{0.05}$ = 33 MPa after 12 years (- 64%).

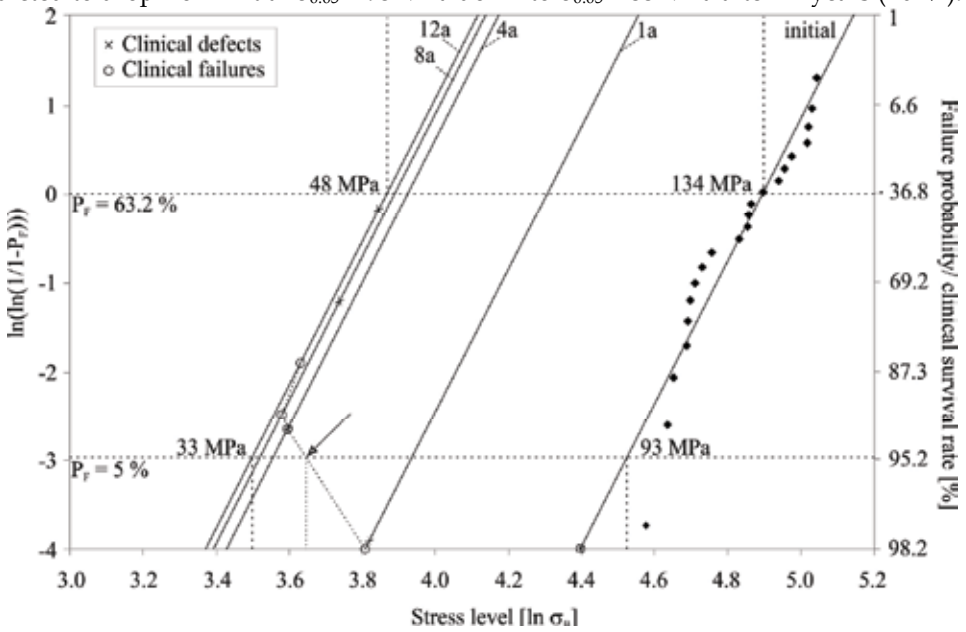

Fig. 6. SPT lifetime predictions for 1, 4, 8 and 12 years under simulated static loading conditions. Clinical survival rates according to Kaplan-Meier algorithm as well as the time dependent incidence of all bulk, chipping, and marginal inlay defects are shown. The arrow indicates the convergence of clinical and experimental lifetimes at 38.5 MPa static loading and for a failure probability of P_F = 5%.

Fracture toughness

Fracture toughness has been calculated according to eq. 10. EMP exhibited a fracture toughness of K_{Ic} = 4.14 ± 0.58 MPam$^{0.5}$ and TEC a reduced performance of K_{Ic} = 1.89 ± 0.43 MPam$^{0.5}$. The values for IEM were taken from literature.

A K_{Ic} = 1.29 MPam$^{0.5}$ is reported for IEM [41]. In Table 2 all values are listed, required for calculation of the fracture toughness values. The elastic moduli were calculated based on the ultrasound velocity through the materials. A far stiffer material response of 93.8 GPa was measured for EMP compared to TEC (9.8 GPa). A comparable material hardness ratio was measured for EMP (5.56 GPa) and TEC (0.62 GPa). Poisson ratio values were taken from literature (Table 2). Since fracture toughness is a material constant, the estimated fracture releasing flaw size increased with decreasing fracture strength. For EMP the crack size ranged from 28.1 µm (441.4 MPa) to 59.6 µm (303.3 MPa) and for TEC from 94.3 µm (109.8 MPa) to 207.0 µm (74.0 MPa). IEM with a fracture toughness K_{Ic} = 1.29 MPam$^{0.5}$ and a characteristic strength of σ_c = 134.2 MPa would match a fracture releasing crack size of a_c = 92.4 µm.

Clinical findings

All patients were satisfied with their restorations. 38 restorations could not be examined after twelve years due to failure or missed recall investigation. Eight patients were not available and one patient lost the inlays due to prosthetic treatment independent from the study.

Cohesive bulk fractures of the ceramic material led to replacement of eleven inlays over 12 years. First catastrophic fractures were observed between 3 and 4.5 years (1 failure in 2nd year, 3 in 3rd year, and 2 in 4th year) late failures after 11 - 12 years (3 failures in 11th year and 2 in 12th year). There was no statistically significant correlation between dimensions of the inlay and fractures observed ($P > 0.05$). The incidence of inlay defects over time increased from 1 % at baseline, 2 % after 1 year, 7 % after 4 years, 26 % after 8 years to 57 % after 12 years. Table 4 summarizes the number and percentage of observed fractures and defects during the whole observation period. Mainly chipping defects in the proximal and marginal regions were observed as shown in Fig. 7. Survival rates from Kaplan-Meier analysis and percentage of fractures are almost identical, since most restorations failed due to fracture.

Median survival rates have been calculated according to Kaplan-Meier survival analysis. The clinical survival rate dropped from 100 % (1 year) to 93 % (4 years), 92 % (8 years) down to 86 % after 12 years. Those results were merged into the SPT lifetime prediction, shown in Fig. 6. Related to their specific location in the SPT diagram, Table 4 exhibits the corresponding critical stress levels, calculated for static loading conditions.

	Baseline	1y	4y	8y	12y
Clinical survival rate	100%	100%	93%	92%	86%
No. of fractures	0 (100%)	0 (100%)	6 (94%)	6 (94%)	11 (88%)
Fracture releasing stress level	81.4 MPa	44.7 MPa	36.6 MPa	35.9 MPa	37.7 MPa
No. of defects	1 (99%)	2 (98%)	5 (93%)	18 (74%)	34 (43%)
Defect inducing stress level	80.4 MPa	45.6 MPa	36.6 MPa	42.1 MPa	46.5 MPa

Table 4. Clinical survival rates according to Kaplan-Meier algorithm, number and percentage (survival rates) of failures and defects and corresponding experimental critical stress levels, calculated for static loading conditions from the SPT diagram for the clinical follow-up periods after baseline, 1, 4, 8, and 12 years.

Discussion

Fracture strength, slow crack growth and lifetime

Both, the EMP glass ceramic and the TEC resin composite suffer from a substantial decrease in strength with increasing surface roughness. A surface roughness of 25 or 50 µm has no clinical relevance but clearly underline the ongoing trend of strength degradation.

A fracture strength of 110 MPa of TEC correlate with the biaxial fracture strength data published within the scientific documentation of the manufacturer (120 MPa). For EMP the literature provides varying fracture strength data. Values from 239 MPa to 303 MPa to 455 MPa are reported, depending on the applied surface roughness and methodology (Albakry et al., 2003b; Sorensen et al., 2000; Annusavice et al., 2001). Fisher et al., for example, found a significant strength decrease from 103 to 65 MPa correlating to either a polished (R_a = 0.2 µm) or a rough (R_a = 5.8 µm) surface of a glass ceramic material (Fischer et al., 2003). However, since a close relation between ceramic strength and surface roughness is proven, little evidence is provided in literature for resin composites (Hayashi et al., 2003; Reiss & Walther, 2000).

Average crystallite size of EMP is 3 – 6 µm. TEC consist of anorganic fillers between 0.4 and 0.7 µm and prepolymeric fillers between 20 – 50 µm. Microstructural dimensions of EMP and TEC are shown in Fig 1b and 1c. The dependency of fracture strength on surface roughness thus leads to the suggestion that neither crystallite size of the glass ceramic material nor filler sizes of the resin composite are strength limiting factors. The statistical treatment of the strength development provides threshold values for both EMP and TEC. No significant increase in fracture strength has been observed below 0.65 µm (1000 grit) in EMP. For TEC a threshold value might be found below 2.1 µm (320 grit).

In vitro measurement of fracture strength and slow crack growth in IEM led to a strength of σ_0 = 134 MPa and a n-value of 19.16. Calculations on the basis of a static crack growth mechanism predict a drop in strength from initial $\sigma_{0.05}$ = 93 MPa down to $\sigma_{0.05}$ = 33 MPa after 12 years (- 64 %). This decrease represents a high sensitivity to slow crack growth of the glass ceramic and was explained by the stress enhanced corrosive effect of water and a high amount of silica glass phase (60 vol %). Compared with literature data, a superior fracture strength was measured (σ_{Lit} = 89 MPa) while the crack growth potential of IEM was calculated being rather conservative estimation (n_{Lit} = 25) (Fischer et al., 2003b). The susceptibility to slow crack growth of the material under investigation is superior to that of feldspathic CAD/CAM materials (n_{Lit} = 16.8), feldspathic veneering porcelain (n_{Lit} = 14.6), or silica-lime glasses (n_{Lit} = 16) (Morena et al., 1986; Wiederhorn, 1967; Lohbauer et al., 2002).

Fracture toughness and critical flaw sizes

Table 2 exhibits the material parameters for density, elastic modulus, hardness and fracture toughness of EMP and TEC. Due to a lack of published data for TEC, the investigated data were compared with the scientific documentation of the manufacturer. The data under investigation clearly correlate with the reported density (2.1 g/cm³), elastic modulus (10 GPa), and hardness (0.58 GPa) published within. Values for EMP also correlate with literature findings for elastic modulus (91 GPa) and hardness (5.5 GPa) (Shin & Drummond, 1999; El Hejazi & Watts, 1999).

Fracture initiating crack length have been calculated from eq. 1 and listed in Table 1. The material fracture strength is thereby related to critical flaw sizes by $\sigma_c \sim 1/ a_c^{0.5}$. Average flaw sizes

between 28 µm (441 MPa) and 60 µm (303 MPa) have been calculated for EMP. TEC exhibits a far wider distribution from 94 µm (110 MPa) until 208 µm (74 MPa), due to a reduced fracture toughness of K_{Ic} = 1.89 $MPam^{0.5}$. It has been shown for linear elastic materials, that prior to catastrophic failure of a brittle material crack extension will occur, thus leading to a differentiation between the initial flaw a_0 and the crack length at fracture a_c. This phenomen has been termed stable crack extension or slow crack growth and is described as a function of loading rate, residual stress state and testing environment (Scherrer et al., 1999). This in turn leads to the suggestion that the fracture initiating flaws under investigation are of smaller size. Chantikul et al. developed a a_c / a_0 ratio of around 2.5 (Chantikul et al., 1981). This means that fracture initiating flaw sizes will be effective between 11 and 24 µm for EMP and between 38 and 83 µm for TEC. However, the results shown here represent a strength degradation related to an applied surface roughness far smaller compared to the above estimation. Quantitative fractography is reported a useful tool to more precisely localize fracture origins and to trace back critical flaw sizes (Mecholsky, 1995b; Kelly et al., 1989).

Fracture toughness data is extremely sensitive on the applied methodology. Amongst a variety of techniques, such as the Chevron-notch-beam test (CNB), the single-etch-notch beam test (SENB) or indentation strength (IS) the indentation fracture technique (IF) has been selected here (Munz & Fett, 1999; Anstis et al., 1981). Guazzato et al. measured a fracture toughness for EMP of K_{Ic} = 3.0 $MPam^{0.5}$ using the IS technique (Guzzato et al., 2004). Fracture toughness for resin composites commonly range between K_{Ic} = 1.2 and 2.0 $MPam^{0.5}$ which in turn matches the fracture toughness under investigation (Manhart et al., 2000; Yap et al., 2004). An increasing fracture toughness of EMP contributes to an improved clinical reliability. The respective underlying toughening mechanisms are shown in Fig. 7.

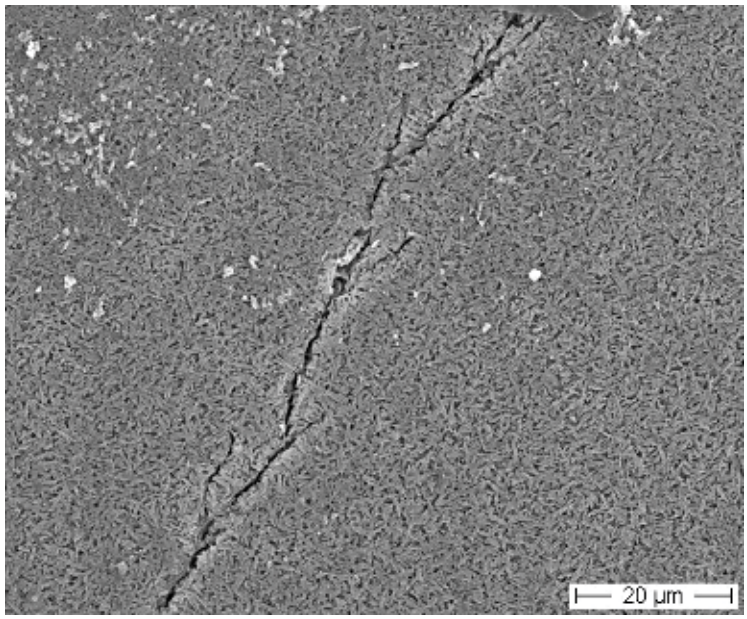

Fig. 7. Crack propagation in EMP showing crack deflection and crack branching. (HF etching for 40 s after fracture).

The needle-shaped lithiumdisilicate crystallites serve as second phase particles, thus inducing crack bowing and crack deflection (twisting and tilting) (Evans, 1990; Davidge & Evans, 1970). Crack branching (Fig. 7) further contribute to increase the material toughness (Evans, 1990). A mixture of intergranular and intragranular fracture in EMP is reported in literature (Guzzato et al., 2004). Composites on the other hand exhibit an inferior fracture toughness. Underlying mechanisms like crack bowing and crack deflection are thereby based on the filler size distribution and content (Evans, 1990; Reiss & Walther, 2000). Crack blunting is a described mechanism which further contributes to toughening in resin composites (Davis & Waters, 1987).

Clinical outcome

The clinical results shown here, emphasize bulk fractures as the main failure reason, clustered between 3 to 4.5 and between 11 to 12 years of clinical service. Of course, clinical success of the present glass ceramic restorations is proved for at least 12 years. Anusavice and Brennan stated a minimum clinical survival time of 5 years (Annusavice & Brennan, 1996).

Analyzing the clinical images resulted in the finding that in each case of catastrophic failure, occlusal adjustments were performed while this trend continued throughout the study. There is considerable indication that most of the fractures were attributed to cyclic, masticatory fatigue (Drummond et al., 2000; Ohyama et al., 1999). Due to the difficult intraoral situation, occlusal corrections may not have been polished sufficiently and those microcracks may have accelerated later catastrophic fractures (see surface roughness R_a in Fig. 8). Therefore, a clinician should pay attention to a careful polish of ceramic surfaces, having been previously subjected to intraoral adjustment in order to prevent this particular problem.

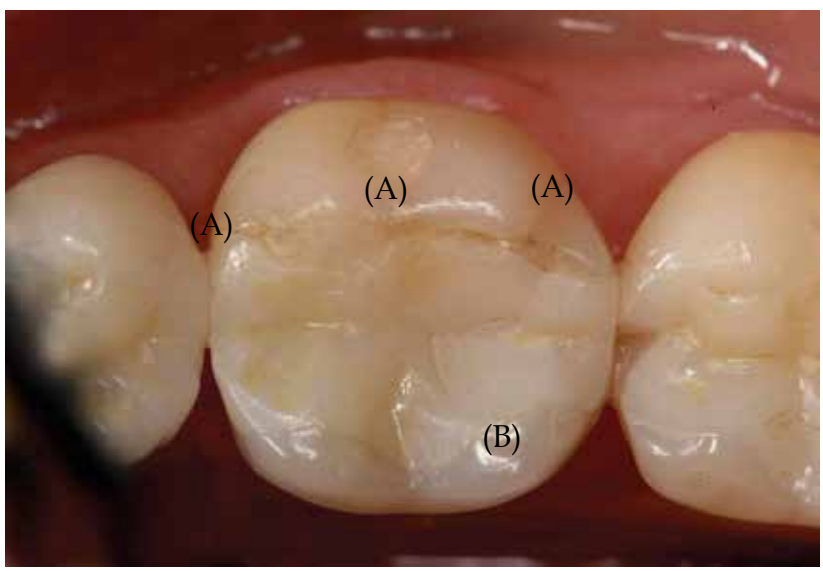

Fig. 8. IEM restoration in the left lower jaw after 8 years. Small marginal and chipping fractures were detected (A). Clinical visibility of increased surface roughness in the occlusal area (B).

Further detoriation of the restorations by marginal and chipping fractures has been observed especially between the 6 and 8 years recall and after 12 years as shown in Table 4. Chippings that have been recorded at the eight years recall seem to be independent from rotary instrumentation during occlusal adjustment directly after luting. During the 8 years recall it was predicted that if deterioration progresses over the next years of clinical service, it might be possible that further failures will occur due to a further decreased marginal quality (Krämer & Frankenberger, 2005). Consequently, late catastrophic fatigue fractures occurred between 11 and 12 years of clinical service. In literature, marginal fractures were frequently observed, especially when luting was performed with materials of low adhesion and wear resistance e.g. glass ionomer cements (Höglund et al., van Dijken & Hörstedt, 1994).
It would be of interest, if size and location of an individual restoration would have influenced the clinical outcome. Neither the number of restoration surfaces nor the size nor the tooth type showed any significant influence on clinical performance over the twelve years period ($p > .05$, Mann-Whitney U-test). No correlation was found between ceramic thickness and fractures. The lowest cusp thickness (0.3 mm) was recorded without having any clinical consequences.

Experimental lifetime calculation and clinical survival rate

In this study exemplary lifetimes have been predicted according to the clinical recall intervals of 1, 4, 8, and 12 years and shown in the SPT diagram (Fig. 6). This, based on static loading conditions and on the associated slow crack growth mechanism. Different static lifetimes t_1 and t_2 were calculated on the basis of eq. 11 (Kelly, 1995):

$$\frac{t_1}{t_2} = \left(\frac{\sigma_2}{\sigma_1} \right)^n \tag{11}$$

Fig. 6 represents clinical survival rates as well as percentage of inlay defects, merged to the experimentally calculated lifetime predictions. Defects here include all bulk, chipping, and marginal fractures. For clinical concerns the question should be addressed to the level of fracture releasing stresses. Since clinical conditions are affected by constant average masticatory loading over time the maximum increase in failure rate is observed after 12 years.
Based on a clinical requirement for a maximum failure rate of $P_F = 5\%$, a fracture releasing static loading of 35.5 MPa was calculated after 4 years or respectively 33 MPa after 12 years (Fig. 6). However, constant static loading does not match clinical relevant average chewing forces but appears to represent far more conservative estimation. Maximum masticatory forces may easily achieve 300 - 400 N, but far reduced average chewing forces of approx. 220 N in the molar region are reported in literature (Pröschel & Morneburg, 2002; Hidaka et al. 1999). Assigning those forces to a contact area of 7 - 8 mm^2 (single molar tooth) result in an average chewing pressure of 27 - 31 MPa. This data range beneath the values from the static experiment after 4 years (35.5 MPa). An underlying failure rate of $P_F = 5\%$ has clinically been exceeded after 4 years and related to an experimentally calculated threshold value of 35.5 MPa, as shown in Fig. 6. In consequence, the clinical failure rate increases to $P_F = 14\%$ after

12 years in-situ. The clustered incidence of failures after 12 years can be explained by exceeding this threshold value and can be related to slow crack growth in the glass ceramic material. A further increased failure rate is expected from future recalls. In order to prevent from further clinical degradation or in order to extend clinical lifetimes, the use of highly corrosion resistant (high n-value) or high strength materials is recommended for use in extended class I and II restorations (Lohbauer et al., 2002).
However, laboratory fatigue testing should meet clinical criteria as there are cyclic loading and intraoral temperature and humidity simulation. Braem predicted 10^6 cycles to represent about one year of real-life contact (Braem, 2001). He approximated 2700 chews per day (three periods of 15 minutes of chewing per day at a chewing rate of 1 Hz). Keeping the chewing frequency, a single in vitro experiment would last for approx. two weeks.
In this context, the dynamic fatigue method should be viewed as an efficient screening tool for evaluating dental materials, rather than as a simulation of actual dental function. In order to predict reliable lifetimes, further influences on damage accumulation should be considered. The effect of contact fatigue or further enhancement of crack growth from cyclic fatigue might play a critical role in predicting clinical lifetimes (Annusavice & Brennan, 1996).

Polishing techniques

A variety of clinical polishing systems are marketed, including particle impregnated rubber cups, disks, and brushes together with different polishing pastes (Watanabe et al., 2006; Venturini et al., 2006). Depending on the treated material and applied technique, a clinical surface roughness between 200 and 30 nm is reported for resin composites as well as for glass ceramics (de Jager et al., 2000; Turssi et al., 2005). After years of clinical service, load bearing restorations are exposed to masticatory degradation. A dramatic increase in surface roughness from 100 - 300 nm to 15 - 40 μm has been measured due to in-vitro abrasive wear simulation on resin composite materials (Turssi et al., 2005). Clinical abrasive wear on glass ceramic inlays and onlays has been reported to increase after 12 years of clinical service (Lohbauer et al., 2008). As a consequence, the authors observed an increasing amount of fatigue failures due to fracture. Those studies point out the significance of surface roughness (fracture releasing crack length) not only on abrasive wear but on the resulting strength of clinically placed restoration. Optimal polishing of a restoration right after placement is thus strongly recommended to guarantee an optimum strength performance and to increase the clinical lifetime.

References

Albakry M, Guzzato M, Swain MV. (2003). Fracture toughness and hardness evaluation of three pressable all-ceramic dental materials. *J Dent* 31:181-188.

Albakry M, Guazzato M, Swain MV. (2003b). Biaxial flexure strength, elastic moduli, and x-ray diffraction characterisation of three pressable all-ceramic materials. *J Prosthet Dent* 89:374-380.

Anstis GR, Chantikul P, Lawn BR, Marshall DB. (1981). A Critical Evaluation of Indentation Techniques for Measuring Fracture Toughness: I, Direct Crack Measurements. *J Am Ceram Soc* 64:533-538.

Anusavice KJ, Brennan AB. (1996). Challenges to the development of esthetic alternatives to dental amalgam in an academic research center. *Trans Acad Dent Mater* 9:25-50.

Anusavice KJ, Della BA, Mecholsky JJ. (2001). Fracture Behavior of Leucite- and Lithia-disilicate-based Hot-pressed Ceramics. *J Dent Res* 80:544.

Ashby MF, Jones DRH. (1996). *Engineering Materials*, 2nd edition. Butterworth Heinemann, Oxford.

Beuer F, Edelhoff D, Gernet W, Sorensen JA. (2009). Three-year clinical prospective evaluation of zirconia-based posterior fixed dental prostheses (FDPs). *Clin Oral Investig* 13, 445-451.

Braem M. (2001). Materials for minimally invasive treatments. In: *Adhesive Technology for Restorative Dentistry*. Roulet JF, Vanherle G. Quintessence Publishing, Berlin.

Chadwick RG. (1994). Strength-probability-time (*SPT*) diagram – an adjunct to the assessment of dental materials? *J Dent* 22:364-369.

Chantikul P, Anstis GR, Lawn BR, Marshall DB. (1981). A Critical Evaluation of Indentation Techniques for Measuring Fracture Toughness: II, Strength Method. *J Am Ceram Soc* 64:539-543.

Charles RJ. (1958). Dynamic fatigue of glass. *J Appl Phys* 29:1657-1662.

Chung SM, Yap AUJ, Koh WK, Tsai KT, Lim CT. (2004). Measurement of Poisson's ratio of dental composite restorative materials. *Biomaterials* 25:2455-2460.

Davidge RW, Evans AG. (1970). The strength of ceramics. *Mater Sci Eng* 6: 281-298.

Davis DM, Waters NE. (1987). An Investigation into the Fracture Behavior of a Particulate-filled bis-GMA Resin. *J Dent Res* 66:1128-1133.

DeGroot R, Van Elst HC, Peters MC. (1988). Fracture mechanics parameters for failure prediction of composite resins. *J Dent Res* 67:919-924.

DeJager N, Feilzer AJ, Davidson CL. (2000). The influence of surface roughness on porcelain strength. *Dent Mater* 16:381-388.

Drummond JL, Mieschke KJ. (1991). Weibull models for the statistical analysis of dental composite data: aged in physiologic media and cyclic-fatigued. *Dent Mater* 7:25-29.

Drummond JL, King TJ, Bapna MS, Koperski RD. (2000). Mechanical property evaluation of pressable restorative ceramics. *Dent Mater* 16:226-233.

El Hejazi AA, Watts DC. (1999). Creep and visco-elastic recovery of cured and secondary-cured composites and resin-modified glass-ionomers. *Dent Mater* 15:138-143.

Evans AG. (1990). Perspective on the Development of High-Toughness Ceramics. *J Am Ceram Soc* 73:187-206.

Fairhurst CW, Lockwood PE, Ringle RD, Twiggs SW. (1993). Dynamic fatigue of feldspathic porcelain. *Dent Mater* 9:269-273.

Fischer H, Schäfer M, Marx R. (2003). Effect of Surface Roughness on Flexural Strength of Veneer Ceramics. *J Dent Res* 82:972-975.

Fischer H, Weber M, Marx R. (2003b). Lifetime Prediction of All-Ceramic Bridges by Computational Methods. *J Dent Res* 82:238-242.

Frankenberger R, Taschner M, Krämer N. (2008). Glassceramic inlays after twelve years: Clinical results. *J Adhes Dent* 10:393-398.

Fujishima A, Ferracane JL. (1996). Comparison of four modes of fracture toughness testing for dental composites. *Dent Mater* 12:38-43.

Griffith AA. (1920) The phenomena of rupture and flow in solids. *Phil Trans Roy Soc London* 221A: 163-198.

Guzzato M, Albakry M, Ringer SP, Swain MV. (2004). Strength, fracture toughness and microstructure of a selection of all-ceramic materials. Part I. Pressable and alumina glass-infiltrated ceramics. *Dent Mater* 20:441-448.

Halmshaw R. (1991). *Non destructive Testing*. 2nd edition, Arnold, London.

Hayashi M, Wilson NH, Yeung CA, Worthington HV. (2003). Systematic review of ceramic inlays. *Clin Oral Investig* 7:8-19.

Hidaka O, Iwasaki M, Saito M, Morimoto T. (1999). Influence of Clenching Intensity on Bite Force Balance, Occlusal Contact Area, and Average Bite Pressure. *J Dent Res* 78: 1336-1344.

Höglund AC, van Dijken JWV, Oloffson AL. (1994). Three-year comparison of fired ceramic inlays cemented with compo- site resin or glass ionomer cement. *Acta Odont Scand* 52:140-147.

Höland W, Schweiger M, Frank M, Rheinberger V. (2000). A comparison of the microstructure and properties of the *IPS Empress 2* and the *IPS Empress* glassceramics. *J Biomed Mater Res* 53:297-303.

Kelly JR, Campbell SD, Bowen HK. (1989). Fracture-surface analysis of dental ceramics. *J Prosthet Dent* 62:536-541.

Kelly JR. (1995). Perspectives on strength. *Dent Mater* 11:103-110.

Krämer N, Frankenberger R. (2005). Clinical performance if bonded leucite-reinforced glass ceramic inlays and onlays after eight years. *Dent Mater* 21:262-271.

Lohbauer U, Petschelt A, Greil P. (2002). Lifetime Prediction of CAD/ CAM Dental Ceramics. *J Biomed Mater Res* 63:280-785.

Lohbauer U, Van der Horst T, Frankenberger R, Krämer N, Petschelt A. (2003). Flexural fatigue behavior of resin composite dental restoratives. *Dent Mater* 19:435-40.

Lohbauer U, Krämer N, Petschelt A, Frankenberger R. (2008). Correlation of in vitro fatigue data and in vivo clinical performance of a glassceramic material. *Dent Mater* 24:39-44.

Manhart J, Kunzelmann KH, Chen HY, Hickel R. (2000). Mechanical properties and wear behavior of light-cured packable composites. *Dent Mater* 16:33-40.

Marshall DB, Cox BN. (1985). The mechanics of matrix cracking in brittle-matrix fiber composites. *Acta Metall* 33:2013-2021.

Mecholsky JJ. (1995). Fracture mechanics principles. *Dent Mater* 11:111-112.

Mecholsky JJ. (1995b). Fractography: determining the sites of fracture initiation. *Dent Mater* 11:113-116.

Molin MK, Karlsson SL. (2000). A randomized 5-year clinical evaluation of 3 ceramic inlay systems. *Int J Prosthodont* 13:194-200.

Molin MK, Karlsson L. (2008). Five-year clinical prospective evaluation of zirconia-based Denzir 3-unit FPDs. *Int J Prosthodont* 21:223-227.

Morena R, Beaudreau GM, Lockwood PE, Evans AL, Fairhurst CW. (1986). Fatigue of dental ceramics in a simulated oral environment. *J Dent Res* 65:993-997.

Munz D, Fett T. (1999). *Ceramics*. Springer, Berlin.

O'Brien WJ. (2002). *Dental materials and their selection*. 3rd edition. Quintessence Publishing, Berlin.

Ohyama TM, Yoshinari M, Oda Y. (1999). Effects of cyclic loading on the strength of all-ceramic materials. *Int J Prosthodont* 12:28-37.

Pallesen U, van Dijken JW. (2000). An 8-year evaluation of sintered ceramic and glassceramic inlays processed by the Cerec CAD/CAM system. *Eur J Oral Sci* 108:239-246.

Peterlik H. (1994). Comparision of evaluation procedures for the subcritical crack growth parameter n. *J Europ Ceram Soc* 13:509-519.

Pröschel PA, Morneburg T. (2002). Task-dependence of Activity/ Bite-force Relations and its Impact on Estimation of Chewing Force from EMG. *J Dent Res* 81:464-468.

Raigrodski AJ, Chiche GJ, Potiket N, Hochstedler JL, Mohamed SE, Billiot S, Mercante DE. (2006). The efficacy of posterior three-unit zirconium-oxide-based ceramic fixed partial dental prostheses: a prospective clinical pilot study. *J Prosthet Dent* 96:237-244.

Reiss B, Walther W. (2000). Clinical Long-Term Results and 10-Year *Kaplan-Meier* Analysis of Cerec Restorations. *Int J Comput Dent* 3: 9-23.

Ritchie RO, Dauskardt RH. (1991). Cyclic Fatigue of Ceramics: A mechanics approach to subcritical crack growth and life prediction. *J Ceram Soc Japan* 99:1047-1062.

Sailer I, Fehér A, Filser F, Gauckler LJ, Lüthy H, Hämmerle CH. (2007). Five-year clinical results of zirconia frameworks for posterior fixed partial dentures. *Int J Prosthodont* 20:383-388.

Scherrer SS; Denry IL, Wiskott HWA. (1998). Comparison of three fracture toughness testing techniques using a dental glass and a dental ceramic. *Dent Mater* 14:246-255.

Scherrer SS, Kelly JR, Quinn GD, Xu K. (1999). Fracture toughness (K_{Ic}) of a dental porcelain determined by fractographic analysis. *Dent Mater* 15:342-348.

Seghi RR, Denry IL, Rosenstiel SF. (1995). Relative fracture toughness and hardness of new dental ceramics. *J Prosthet Dent* 74:145-150.

Shin MA, Drummond JL. (1999). Evaluation of chemical and mechanical properties of dental composites. *J Biomed Mater Res* 48:540-545.

Sorensen JA, Berge HX, Edelhoff D. (2000). Effect of Storage Media and Fatigue Loading on Ceramic Strength. *J Dent Res* 79:217.

Sudreau F, Olagnon C, Fantozzi G. (1994). Lifetime prediction of ceramics: importance of the test method. *Ceram Int* 20: 125-135.

Tinschert J, Schulze KA, Natt G, Latzke P, Heussen N, Spiekermann H. (2008). Clinical behavior of zirconia-based fixed partial dentures made of DC-Zirkon: 3-year results. *Int J Prosthodont* 21:217-222.

Turssi CP, Ferracane JL, Serra MC. (2005). Abrasive wear of resin composites as related to finishing and polishing procedures. *Dent Mater* 21:641-648.

Van Dijken JWV, Hörstedt P. (1994). Marginal breakdown of fired ceramic inlays cemented with glass polyalkenoate (ionomer) cement or resin composite. *J Dent* 22:265-272.

Vaidyanathan J, Vaidyanathan TK. (2001). Flexural creep deformation and recovery in dental composites: *J Dent* 29:545-551.

Venturini D, Cenci MS, Demarco FF, Camacho GB, Powers JM. (2006). Effect of Polishing Techniques and Time on Surface Roughness. Hardness and Microleakage of Resin Composite Restorations. *Oper Dent* 31:11-17.

Watanabe T, Miyazaki M, Moore KB. (2006). Influence of polishing instruments on the surface texture of resin composites. *Quintessence Int* 37:61-67.

Weibull W. (1951). A statistical distribution function of wide applicability. *J Appl Mech* 18:293-298.

Wiederhorn SM. (1967). Influence of water vapor on crack propagation in soda-lime-glass. *J Am Ceram Soc* 50:407-414.

Yap AU, Chung SM, Chow WS, Tsai KT, Lim CT. (2004). Fracture resistance of compomer and composite restoratives. *Oper Dent* 29:29-34.

10

Re-use of ceramic wastes in construction

Andrés Juan*, César Medina*, M. Ignacio Guerra*, Julia Mª Morán*,
Pedro J. Aguado*, Mª Isabel Sánchez de Rojas**,
Moisés Frías** and Olga Rodríguez**
**Escuela Superior y Técnica de Ingeniería Agraria. U of León (León)*
*** Instituto de Ciencias de la Construcción Eduardo Torroja. Consejo Superior de Investigaciones Científicas (CSIC)Madrid*
Spain

1. Introduction

Recent decades have seen a marked upsurge in industrial and economic growth, contributing to an improved quality of life and well-being for citizens. However, we should not lose sight of the fact that every production system creates by-products and waste products which can affect the environment. These effects may occur at any point in the product's life-cycle, whether during the initial phase of obtaining raw materials, during the transformation and production phase, during product distribution or when the end user must dispose of products which are no longer required.

As a result, recent years have witnessed rising social concern about the problem of waste management in general, and industrial waste and waste from the construction industry in particular. This problem is becoming increasingly acute due to the growing quantity of industrial, construction and demolition waste generated despite the measures which have been taken in recent years at European Community, national and regional levels aimed at controlling and regulating waste management, in accordance with sustainable development policies and the Kyoto Protocol. The need to manage these wastes has become one of the most pressing issues of our times, requiring specific actions aimed at preventing waste generation such as promotion of resource recovery systems (reuse, recycling and waste-to-energy systems) as a means of exploiting the resources contained within waste, which would otherwise be lost, thus reducing environmental impact.

In addition to helping protect the environment, use of such waste offers a series of advantages such as a reduction in the use of other raw materials, contributing to an economy of natural resources. Moreover, reuse also offers benefits in terms of energy, primarily when the waste is from kiln industries (the ceramics industry) where highly endothermic decomposition reactions have already taken place, thus recovering the energy previously incorporated during production.

Ceramic waste may come from two sources. The first source is the ceramics industry, and this waste is classified as non-hazardous industrial waste (NHIW). According to the Integrated National Plan on Waste 2008-2015, NHIW is all waste generated by industrial

activity which is not classified as hazardous in Order MAM/304/2002, of the 8th February, in accordance with the European List of Waste (ELW) and identified according to the following codes:
10 Waste from thermal processes.
10 12 Waste from the manufacture of ceramic products, bricks, roof tiles and construction materials.
10 12 08 Ceramic, brick, roof tile and construction materials waste (fired).
The second source of ceramic waste is associated with construction and demolition activity, and constitutes a significant fraction of construction and demolition waste (CDW), as will be addressed in more detail below. This kind of waste is classified by the ELW according to the following codes:
17 Construction and demolition waste
17 01 Concrete, bricks, roof tiles and ceramic materials
17 01 03 Roof tiles and ceramic materials
Globally, the ceramics industry sector is unusual in that it is primarily found in regional concentrations where the majority of agents or industries involved in the system whereby the end ceramic product attains value are located. The development of these ceramic "clusters", with companies in the same or related sectors located in geographical proximity, has enabled the sector globally to attain a state-of-the-art level of progress and technological innovation. The main ceramic "clusters" are located in Brazil, with one in Santa Catarina and two in the state of Sao Paulo; in Portugal, in the Aveiro region; in Castellón, Spain; and in the province of Emilia Romagna, Italy. The ceramics industry in China has also begun to take on greater prominence, representing 35% of global production in recent years.
The ceramics industry is comprised of the following subsectors: wall and floor tiles, sanitary ware, bricks and roof tiles, refractory materials, technical ceramics and ceramic materials for domestic and ornamental use. In both the European Union and Spain, the scale of production within these subsectors with regard to total production follows the same trends, where the production of wall and floor tiles represents the highest percentage with respect to the total, followed by bricks and roof tiles, and finally, the other subsectors, as can be seen in Figures 1 and 2.

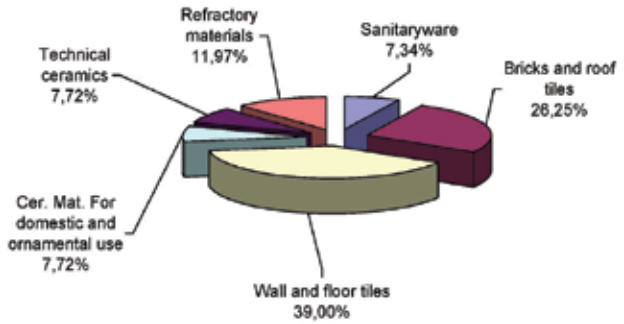

Fig. 1. Scale of production: ceramics industry subsectors in the EU

Ceramic products are produced from natural materials containing a high proportion of clay minerals. Following a process of dehydration and controlled firing at temperatures between 700ºC and 1000ºC, these minerals acquire the characteristic properties of fired clay.

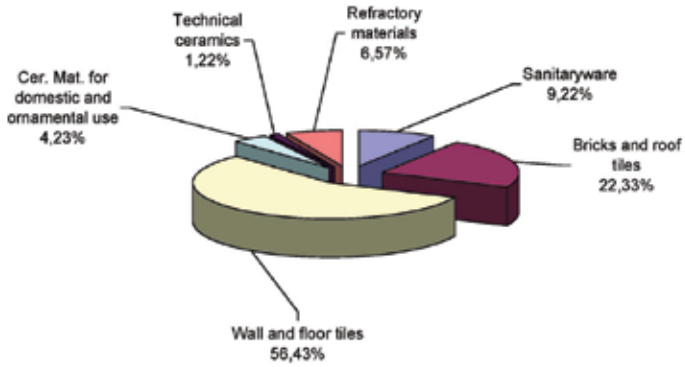

Fig. 2. Scale of production: ceramics industry subsectors in Spain

Ceramic factory waste is not sorted according to the reason for rejection, which may include: breakage or deformation and firing defects.

As regards waste generated by construction activity it is estimated that some 200 million tons of rubble is produced each year in the European Union (EU) as a result of the construction and demolition of buildings. According to data from the Spanish National Plan for Construction and Demolition Waste, 40 million tons are generated annually in Spain, the equivalent of 2 kg per inhabitant per day, which represents a higher figure than that for domestic waste. Within the EU as a whole, 28% of this waste is recycled. Pioneering European countries in this matter include the Netherlands, where 95% of construction waste is recycled, England, with 45% and Belgium with 87%, 17% of which is used in making concrete. In Spain, approximately 10% of total construction and demolition waste is recycled, and reuse mainly consists of using the waste for road subgrade and subbase.

Construction and demolition waste principally consists of two fractions: the stony fraction and the rest (see Table 1). The most important fraction is the stony fraction, comprising ceramic materials (bricks, wall tiles, sanitary ware, etc.), concrete, sand, gravel and other aggregates.

MATERIALS	COMPOSITION (%)
STONY FRACTION	**75**
Bricks, wall tiles and other ceramic materials	54
Concrete	12
Stone	5
Sand, gravel and other aggregates	4
REST	**25**
Wood	4
Glass	0,5
Plastic	1,5
Metals	2,5
Asphalt	5
Plaster	0,2
Rubbish	7
Paper	0,3
Others	4

Table 1. Composition of construction and demolition waste

As can be seen, more than half (54%) corresponds to the ceramic fraction, representing the highest percentage of all materials shown, followed by concrete waste (12%). This illustrates the importance of the treatment and recovery of this kind of waste. In many cases, the possibility of reuse or recycling will depend on the existence of previous studies into the viability of this waste fraction, such as that proposed by this present research.

2. Activated clays from industrial waste with pozzolanic properties

2.1. Introduction

Activators are defined as products which, once incorporated into Portland cement, contribute to the development of the cement's hydraulic and strength qualities. Due to their chemical-mineralogical composition, some products have hydraulic properties in their own right, setting and hardening under water. This is the case for granulated blast – furnace slag or fly ash with high lime content. In contrast, others do not have hydraulic qualities per se, but due to their composition, rich in silica and aluminium oxide compounds, and their extreme fineness, are capable of fixing calcium hydroxide at normal temperatures and in the presence of water in order to create stable compounds with hydraulic properties. These latter are known as pozzolans. The calcium hydroxide necessary for a pozzolanic reaction can come from inert lime or from a hydrating Portland cement.

The use of materials with pozzolanic properties in cement achieves:

- Economic Advantages: Reduced need for clinker production (lower energy consumption).
- Environmental Advantages: Reduced CO_2 emissions (Kyoto Protocol)
- Technical Advantages**:**
  - Long-term mechanical strength
  - Stable resistance to expansion due to the presence of free lime, sulphates and aggregate-alkali reactions.
  - Durable resistance to the action of pure and acid water.
  - Reduced hydration heat
  - Impermeability, reducing porosity and increasing compactness.

Clays are natural materials which do not present pozzolanic activity, although they can be activated thermally. Clay activation is achieved by a dehydration process beginning at around 500ºC and accompanied by the separation of amorphous, very active aluminium oxide, the maximum concentrations of which are achieved at different temperatures, depending on the type of mineral. Clay minerals such as kaolinite or montmorillonite, or a combination of both, acquire pozzolanic properties through controlled calcinations at temperatures between 540ºC and 980ºC. Illite type clays, or schist type clays containing a high proportion of vermiculite, chlorite and mica, need higher temperatures for activation. It is well-known that one of the first materials used as pozzolans were thermally treated clays (Calleja, 1970).

Activated clays may come from natural products, once these have been activated by controlled thermal processes, or from industrial waste.

This present paper presents research on wastes from the paper and ceramics industries, carried out by the Working Group on Materials Recycling at the Eduardo Torroja Institute for Construction Sciences.

2.2. CERAMICS INDUSTRY WASTE

As regards the ceramics industry in Spain, some 30 million tons of ceramic products such as bricks, roof tiles, breeze blocks, etc., were produced in 2006. Although by 2009 the recent industrial crisis had resulted in a 30% drop in production, the industry continues to generate a significant volume of material unsuitable for commercialization.

The percentage of products considered unsuitable for sale and thus rejected depends on the type of installation and the product requirements. Such waste can be considered inert, due to its low capacity for producing contamination. However, dumping constitutes a major disadvantage, producing significant visual impact and environmental degradation. Ceramic factory waste (figure 3), known as masonry rubble, is not sorted according to the reason for rejection, which may include:

- Breakage or deformation, which does not affect the intrinsic characteristics of the ceramic material.
- Firing defects, due to excessive heat (over-firing) or insufficient heat (under-firing), faults particularly associated with the use of old kilns and which may affect the physico-chemical characteristics of the product.

Fig. 3. Ceramic factory waste

Ceramic products are made from natural materials which contain a high proportion of clay minerals. These, through a process of dehydration followed by controlled firing at temperatures of between 700ºC and 1000ºC, acquire the characteristic properties of "fired clay". Thus, the manufacturing process involved in ceramic materials requires high firing temperatures which may activate the clay minerals, endowing them with pozzolanic properties and forming hydrated products similar to those obtained with other active materials.

Research carried out into the influence of firing temperatures on waste product properties has found that the chemical and mineralogical composition of ceramic masonry rubble resulting from incorrect firing temperatures (over- or under-firing) varies significantly from that of products obtained from optimal firing conditions. However, the temperature applied (around 900ºC) is sufficient to activate the clay minerals, with the result that the different rejects acquire similar pozzolanic properties. Furthermore, studies have been carried out into the viability of substituting cement by using ceramic rejects or masonry rubble as raw materials in prefabricated concrete, exploiting their pozzolanic properties

(Frías et al., 2008, Sánchez de Rojas et al., 2001; Sánchez de Rojas et al., 2003; Sánchez de Rojas et al., 2006; Sánchez de Rojas et al., 2007).

Ceramic masonry rubble must be suitably fine in order to be used as a pozzolanic additive in cement, and thus must be crushed and ground until reaching the specific surface, or Blaine value, of around 3500 cm^2/g. This material presents a chemical composition similar to other pozzolanic materials, with a strongly acid nature where silica, aluminium oxide and iron oxide predominate (75.97%), and with a CaO content of 12.41% and an alkali content of 4.22%. Loss through calcination is 3.44% and sulphate content, expressed as SO_3, is 0.79%. Mineralogical composition, determined by X-ray diffraction, mainly comprises the crystalline compounds quartz, muscovite, calcite, microcline and anorthite.

In order to assess pozzolanic activity, an accelerated method is used in which the material's reaction over time with a lime-saturated solution is studied. The percentage of lime fixed by the sample is obtained through calculating the difference between the concentration of the initial lime-saturated solution and the CaO present in the solution in contact with the material at the end of each pre-determined period. This assay is performed by comparing ceramic masonry rubble with two traditional additives described in the standard EN 197-1: 2005 (UNE-EN 197, 2005), fumed silica (FS) and siliceous fly ash (SFA), which are used as a reference.

The results, which are shown in Figure 4, demonstrate that ceramic waste presents pozzolanic activity; at one day, the percentage of fixed lime is 19% of all available lime. This level of activity is lower than that corresponding to the fumed silica considered, but greater than that of the fly ash. After longer periods, fixed lime values tend to equal out, and thus after 90 days very similar results are obtained for all three materials considered. It was also established that the firing temperatures used for producing ceramic material (around 900ºC) are sufficient to activate the clay minerals and thus obtain pozzolanic properties.

Therefore, in the light of these results, it can be stated that rejected ceramic material, or ceramic masonry rubble, presents acceptable pozzolanic properties, since the firing temperatures used in manufacture are ideal for activating the clays from which they are constituted.

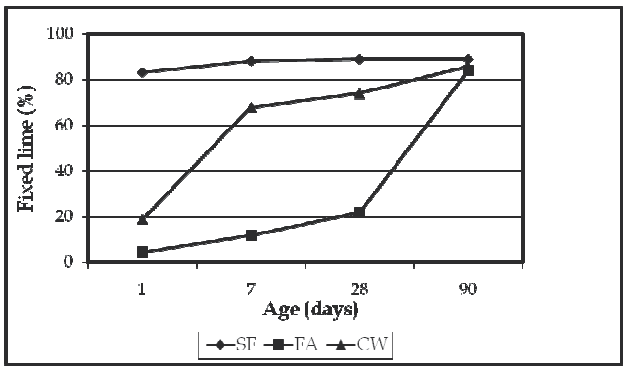

Fig. 4. Pozzolanic Activity

An important factor to be taken into account when studying construction materials is that of durability. The degradation of mortars and concretes caused by aggressive external agents is

usually due to the reaction between these agents and the cement paste. The degrading action of external chemical agents begins on the surface of mortar or concrete, gradually penetrating the interior as porosity, permeability and internal tensions increase and producing loss of mass and a reduction in strength as the degree of degradation advances. There is a long list of aggressive agents and substances; however, the most frequent include soft water, acids and some salts in solution containing soluble sulphates, ammonia and magnesium. In the present case, durability studies were conducted using the methodology reported by Koch & Steinegger (Koch & Steinneger, 1960). For durability assays, agents used included drinking water (the reference), artificial sea water (ASTM D114, 1999), sodium chloride (at a concentration of 0.5 M) and sodium sulphate (at a concentration of 0.5 M). For the cement pastes, ceramic masonry rubble was used as the pozzolanic material, substituting 20% cement. The water/cement ratio was 0.5.

Using the Koch & Steinegger corrosion index, the resistance of pastes to various aggressive agents was established. This index is obtained from the quotient between the flexural-tensile strength values of 56 day old cylinder samples maintained in a determined dilution of an aggressive agent and the values obtained for cylinder samples of the same age maintained in water. For a paste to be considered resistant to a determined aggressive agent, its Koch & Steinegger index value must be greater than 0.7 in this medium.

Results for pastes made with ceramic masonry rubble and CEM I-52.5R cement following standard EN 197-1:2005, where the cement/rubble ratio is 100/0 and 80/20, are shown in figure 5. It can be observed that all the cylinder samples except for the 100/0 samples maintained in sodium chloride, present a Koch & Steinegger index value greater than 0.7, and thus can be considered resistant to different aggressive media. Furthermore, according to the Koch & Steinegger index criteria, all pastes made by partially substituting cement with ceramic material showed better durability than pastes made with 100% cement, with higher index values except in the case of sea water, where values were slightly lower.

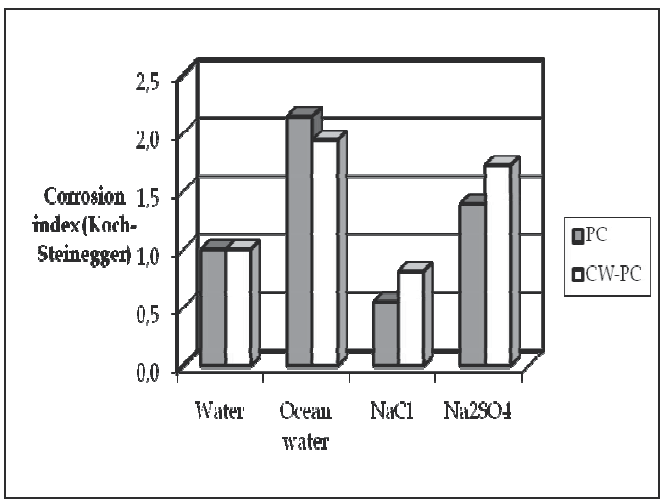

Fig. 5. Koch&Steinegger corrosion index

A study was conducted of the mechanical properties of mortars made according to the standard EN 196-1:2005: I part cement to 3 parts normalized sand, with a water/cement ratio of 0.5. 15% of the cement was substituted with ceramic material.

Results obtained for flexural and compressive strength, given as a percentage with respect to the control mortar (without masonry rubble) at 24 hours and 28 days, are shown in Figures 6 and 7, respectively.

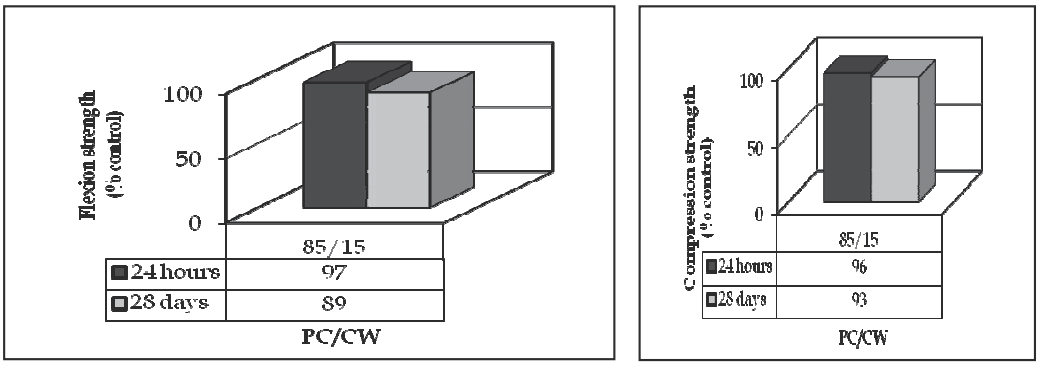

Fig. 6 and 7. Flexural-tensile and compressive strength

As can be seen, both the flexural and the compressive strength values obtained at 24 hours were very similar to those of the control mortar. However, at 28 days, values were slightly lower than those for the control mortar (without ceramic masonry rubble). Nevertheless, in all cases the reduction percentage, calculated with respect to the control, was lower than the degree of cement substitution, indicating that waste materials act as pozzolans, providing mechanical strength.

Therefore, this research confirms that ceramic masonry rubble endows cement with positive characteristics. As regards the economic advantages, these derive from energy savings in cement manufacture. Substituting a material that requires a costly thermal treatment, in this case clinkerization, with a material which is cheaper in energy terms (such as industrial waste which is normally dumped, even though it requires crushing and grinding before use), results in improved energy consumption and makes a positive contribution to environmental conservation.

3.- Ceramic waste as recycled aggregate

3.1. Introduction – Antecedents

Recycled aggregates can be defined as the result of waste treatment and management where, following a process of crushing to reduce size, sieving and laboratory analysis, the waste complies with technical specifications for use in the construction sector and civil engineering.

According to Ignacio (2007) it is not possible to carry out an exhaustive characterization of all kinds of recycled aggregates. Therefore, this topic will be discussed in more general terms by looking at concrete aggregates, asphalt agglomerate aggregates and other recycled aggregates which incorporate aggregates from clean ceramic material waste and aggregates from mixtures.

As mentioned previously, one of the objectives of the new waste reuse and recycling policies in the construction and industrial sectors is to use recycled aggregates as a substitute for conventional natural aggregates, with the aim of reducing both use of natural resources and

environmental impact caused by dumping. According to a Statistical Report by ANEFA (Asociación Nacional de Fabricantes de Áridos-Spanish Association of Aggregates Producers) (2008), consumption of aggregates in Spain in 2007 reached the figure of 479 million tons in the construction sector and 72 million tons in industrial applications (cement, glass and ceramics industries). Meanwhile, sources from the European Aggregates Association (UEPG) indicate that from the total volume of aggregates used by the construction sector in 2007, most (62.7%) was employed for manufacturing concrete, mortar and prefabricated blocks, followed by use in road construction. In the case of industrial use, most (82%) was destined for the manufacture of cement, whilst the remainder was employed for different industrial applications such as the manufacture of lime and plaster, glass and ceramics, among others.

A further important aspect for analysis, as mentioned at the beginning, is the energy factor. The processes involved in cement manufacture, in ceramics production, or in transport, endow construction materials with energy, called *embodied energy*. It has been estimated that of all the embodied energy incorporated in a building, only around 20% corresponds to the construction phase. Therefore, when a defective construction material is discarded, or a building demolished, a huge quantity of embodied energy is wasted. According to data provided by Alaejos (Anon. 2001), one of the best ways to take advantage of this waste is to include it in mortar and concrete manufacturing processes. This reuse not only recovers embodied energy but also reduces the number and size of dumps. A concrete capable of incorporating such waste would constitute an eco-efficient material.

The possibilities for using recycled aggregates in concrete production have been studied in depth, although such research has fundamentally concentrated on reuse of recycled aggregate from concrete. Thus, Sánchez and Alaejos (2003, 2005, 2006) established the possibility of using this kind of waste to substitute up to 20% of conventional coarse aggregate. This maximum substitution percentage is basically due to the high absorption coefficient of this kind of material, although they also established the possibility of reuse in combination with enhanced natural aggregates, and for structural concretes with a compressive strength equal to or less than 50 MPa. It is noteworthy that practically the same limitations are established in appendix 15 (*Recommendations for the use of recycled concrete*) of the recently published Spanish Instructions for Structural Concrete (EHE-2008**).**

Along the same lines, Huete et al. (2005) and Rolón et al. (2007) established maximum reuse limits of 20%, also highlighting the high absorption coefficient of this material and reporting a 6% reduction in strength after 28 days – aspects which could be improved, especially as regards absorption, by the use of superplastifying additives. Other studies have established maximum proportions at 50% (González and Martinez, 2005), although they also emphasized the high absorption coefficient and the need to increase the water/cement ratio by approximately 6% with respect to the reference concrete in order to achieve strength characteristics greater than 30 N/mm^2. Likewise, Domínguez et al. (2004) reported the viability of recycled aggregate reuse in concretes with strengths of 150, 200 and 250 kg/cm^2, establishing the possibility of reuse via a small increase in the quantity of cement employed (2.5%), whilst at the same time stressing the consequent environmental and economic advantages. Along the same lines, Evangelista and de Brito (2007) analysed the feasibility of reusing CDW as fine aggregate in concretes, in proportions of 30% with respect to the reference concrete without noting any relevant reduction in compressive strength. Kim y Kim (2007) demonstrated the possibility of producing recycled concrete (MSC-Modified

sulphur concrete) with better physical properties (compressive strength greater than 78 N/mm² and an absorption coefficient of 0.5%) than those of conventional concrete using a mixture of modified sulphur, recycled aggregates and dust obtained from concrete debris.
Other studies have focused on the reuse of CDW from the stony fraction corresponding to ceramic waste, both in the manufacture of concrete and in pastes and mortars. For example, de Brito et al. (2005) and Correia et al. (2006) reported the use of recycled aggregates of ceramic origin in non-structural concrete, which showed good abrasion resistance and tensile strength and offered the possibility of use as concrete slabs (also due to the greater durability of recycled concrete). As in previous studies, they reported higher absorption rates for recycled aggregates, which could be partially resolved by implementing pre-saturation methods. Other research has demonstrated the possibility of reusing recycled ceramic aggregates as coarse aggregate in structural concrete (Senthamarai and Devadas Manoharan, 2005), although with some reservations until further in-depth research is conducted. Koyuncu et al. (2004) analysed 3 types of ceramic waste (paste, dust and crushed floor tiles) as road subbase filler and as a substitute for natural aggregates in concrete, demonstrating the feasibility of reuse in non-structural concrete (concrete blocks) with a strength of 40-50 kg/cm². Likewise, Binici (2007) used crushed ceramic waste and pumice stone as a partial substitute for fine aggregates in the production of mortar and concrete, finding that the resultant product showed good compressive strength and abrasion resistance, together with less penetration by chlorides which could provide greater protection for the reinforcement used in reinforced concrete. Similarly, Puertas et al. (2006) studied the use of 6 types of ceramic waste as an alternative material in the production of unrefined cement. The research demonstrated the viability of this use, as the waste presented a suitable chemical and mineralogical composition together with a level of pozzolanic activity. Another noteworthy study was that of Portella et al. (2006) in which the possibility of incorporating ceramic waste from electrical porcelain into concrete structures was analysed. This study demonstrated the viability of reuse, although the damaging effect of certain by-products which generated an alkali-aggregate reaction made it necessary to use sulphate resistant cement. Gomes and de Brito (2009) studied the viability of incorporating coarse aggregate from concrete waste and ceramic block waste in the production of new concrete, and concluded that as regards durability, structural concrete can be made using recycled aggregates, but that the 4-32 mm fraction of natural aggregates cannot be totally substituted. Cachim (2009) crushed and used waste from different kinds of ceramic blocks as a partial substitute (15, 20 and 30%) for coarse natural aggregates, observing that with 15% substitution there was no change in concrete strength, whilst when 15-20% was substituted, alterations were noted according to the kind of ceramic block used and when 20-30% was substituted, the recycled concrete showed a reduction in strength regardless of the kind of ceramic block from which the recycled aggregate had been obtained. Silva et al. (2010) analysed the feasibility of using red ceramic waste as a partial and total substitute for natural fine aggregates, finding that at substitution percentages of 20 and 50% results which were at all times superior to those for the reference mortar. However, when natural fine aggregate was totally substituted, behaviour was poorer than that of the reference.
Finally, we should mention the most relevant research carried out to date by members of this research team, López et al. (2007), Juan et al (2007), Guerra et al. (2009), and Juan et al. (2010), in which various mechanical assays have been conducted under laboratory conditions in order to test the use of sanitary ware waste and white ceramic dust. Findings

indicate that reuse is viable, producing strength characteristics greater than for the reference concrete, established as 30 N/mm^2.

3.1. Using sanitary ware waste as recycled aggregate in structural concrete

Spain is the world leader in the ceramic sanitary ware market. The industry produces over 7 million items a year and generates approximately 24 tons of waste a month, which is simply dumped. The percentage of products considered unsuitable for sale, and thus rejected, depends on the kind of installation concerned and the corresponding product requirements.
The reuse of ceramic waste from the sanitary ware industry as a partial substitute for conventional coarse aggregates requires a simple treatment process comprising crushing, using a jaw-crusher, and subsequent washing and sieving.
Two fractions are obtained from crushing; the fine fraction of less than 4 mm in size, and the coarse fraction, over 4 mm in size. It is the coarse fraction (figure 8) which is used as recycled aggregate in the production of recycled concrete.

Fig. 8. Recycled ceramic aggregate

This material has a composition similar to that of other ceramic materials, with a strongly acidic character and a predominance of silica, aluminium and iron oxide (93.81%); CaO content is 0.63% and alkali content, 4.45%. Mineralogical composition, determined by X-ray diffraction, mainly comprises quartz, orthoclase, mullite, hematite and zircon.
In order to assess the suitability of this material in the production of concrete for structural purposes, the physical-mechanical characteristics indicated in table 2 were determined, and the results obtained were compared with those for natural coarse aggregates (gravel), confirming compliance with the specifications given in the Spanish Instruction for Structural Concrete (EHE-08).

Characteristic	Standard
Particle size distribution. Assessment of fine aggregates	EN 933–1
Dry sample density	EN 1097-6
Water absorption coefficient	EN 1097-6
Elongation Index	EN 933-3
"Los Angeles" coefficient	EN 1097-2

Table 2. Characterization of aggregates

The granulometric curves presented in figure 9, were obtained from a granulometric analysis of aggregates (sand, gravel and recycled ceramic aggregates). From an analysis of

these curves it can be seen that all the aggregates present continuous granulometric curves, which would have a positive influence on concrete docility. Furthermore, it should be noted that the curve for recycled ceramic aggregate is very similar to that for natural coarse aggregate.

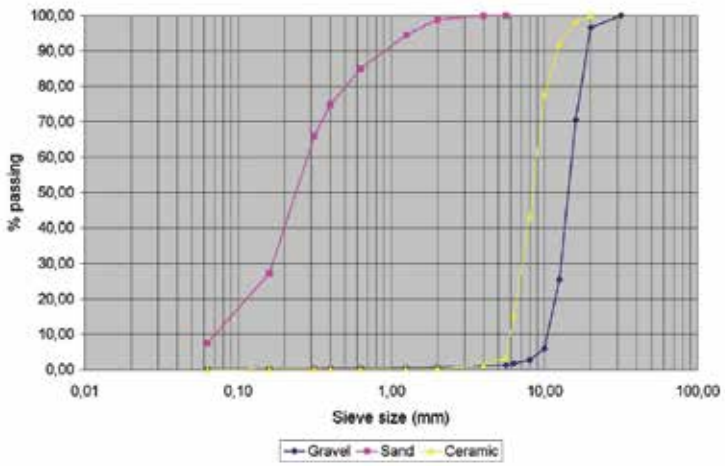

Fig. 9. Aggregate size distribution curves

The results obtained for the other physical-mechanical characteristics determined are presented in table 3.

Characteristic	Gravel	Ceramic	EHE-08
Grading modulus	6,93	6,17	-
Maximum size (mm)	20	12,5	-
Fine content (%)	0,22	0,16	< 1,5
Dry sample real density (kg/dm^3)	2,63	2,39	-
Water absorption coefficient (%)	0,23	0,55	$\leq$ 5
Elongation Index (%)	3	23	< 35
"Los Ángeles" coefficient (%)	33	20	$\leq$ 40

Table 3. Characterization results of aggregates

The results presented in table 3, show that the percentage of fine aggregate in the recycled aggregates is lower than that for gravel. Dry sample density for natural aggregates is higher than that for aggregates of a ceramic origin, enabling us to deduce that concretes made with the latter would be slightly lighter than the reference concrete. As was expected, the absorption coefficient for the recycled aggregate is higher than that of gravel, but this difference is not highly significant and would not, therefore, have much impact on the workability of concrete made with this kind of recycled aggregate. With regards to the elongation index, a substantial difference can be observed between the two aggregates, a result explained by the process used for obtaining the recycled aggregate, which produced an aggregate with irregularly shaped, sharper edges. As for the values obtained for resistance to fragmentation, these indicated that the recycled aggregate presented higher

resistance values than the natural aggregate, leading us to predict that the concretes obtained with the former would have greater compressive strength.
Consequently, in the light of these results, it can be stated that recycled aggregates from crushed ceramic sanitary ware present suitable characteristics for partial substitution of natural coarse aggregates. The natural aggregates used were of a siliceous nature; the gravel comprised pebbles and river sand was used. The cement used was Portland cement without additives (CEM I), which complies with the specifications set down in the Instructions for the Authorization of Cements (Instrucción de Recepción de Cementos (RC-08)); rapid hardening and strength class 52.5 N/mm^2
Mix design was determined following the de la Peña method, a commonly used method for calculating mix proportions for structural concrete, whereby the initial step is to establish the characteristic concrete strength desired. In this case, the aim was to produce recycled concrete for structural purposes with a characteristic strength equal to 30 N/mm^2, and the proportion of gravel to be substituted by recycled ceramic aggregate was set at 15-20 and 25%. As a result of this process, the mixes presented in table 4 were obtained. As can be seen in this Table, all mixes complied with requirements regarding minimum cement content and maximum water/cement ratio given in the EHE-08 to ensure durability.

Type concrete	Materials (kg/dm^3)				
	Sand	Gravel	Ceramic	Cement	Water
Concrete reference (CR)	716,51	1115,82	0,00	398,52	205,00
Concrete containing 15% recycled aggregate (CC-15)	723,48	948,45	162,32	390,36	205,00
Concrete containing 20% recycled aggregate (CC-20)	725,81	892,66	216,43	387,64	205,00
Concrete containing 25% recycled aggregate (CC-25)	728,14	836,87	270,53	384,91	205,00

Table 4. Mix proportions of concretes

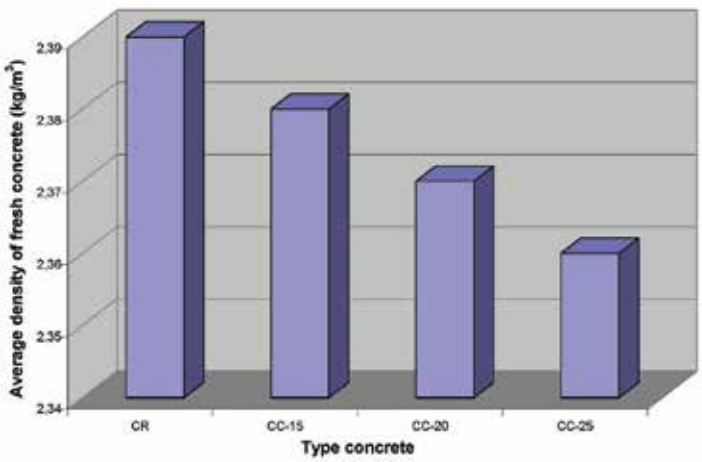

Fig. 10. Average density of fresh concrete

A study of fresh and hardened concrete properties was carried out using 15 x 30 cm cylinder samples made according to the standard EN 12390-1 and cured following standard EN 12390-2. The fresh concrete properties studied were consistency, using the Abram's cone slump test (EN 12350-2), and density (EN 12350-6). Consistency testing showed that all the concrete mixtures presented a soft consistency (6-9 cm), as recommended in EHE-08, section 31.5.

As can be seen in figure 10, results obtained for fresh concrete density studies showed that as the percentage of natural aggregates substituted rose, density of the recycled concrete fell. The results obtained for compressive and tensile splitting strength are shown in figure 11 as a percentage with respect to the reference concrete (with natural aggregates only), for 7, 28 and 90 days in the case of compressive strength, and at 28 days for tensile strength.

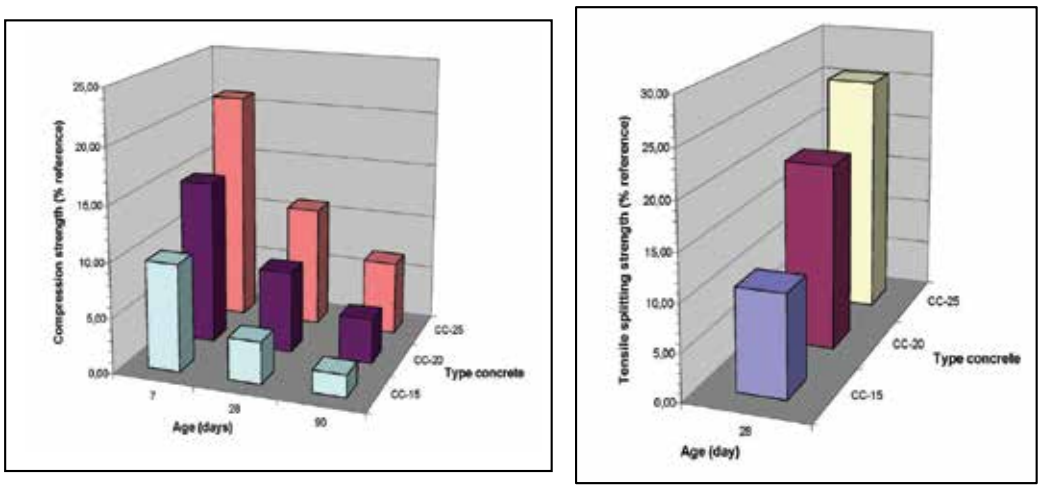

Fig. 11. Compressive and tensile splitting strength

As can be observed, both the compressive and tensile strengths obtained at different ages are higher for recycled concrete than the reference concrete. In addition, as the percentage of conventional coarse aggregate substituted by ceramic coarse aggregate rose, so too did the strength when compared with the reference concrete.

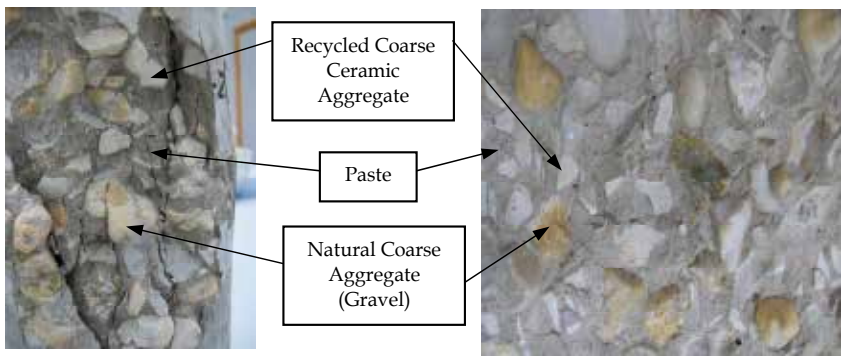

Fig. 12. Specimens showing natural and ceramic recycled coarse aggregates and cement paste

Furthermore, this improved mechanical behaviour on the part of recycled concrete is a consequence of the fact that crushed aggregate presents a greater specific surface area than pebble aggregate and thus their adherence is greater, which in turn results in a more compact aggregate-paste interfacial transition zone (ITZ) in the case of recycled aggregate than in that of natural aggregate (figure 12).
Finally, it should be noted that the different crystalline phases resulting from the hydration process during concrete setting and hardening were identified by X-ray diffraction, the results of which are presented in figure 13.

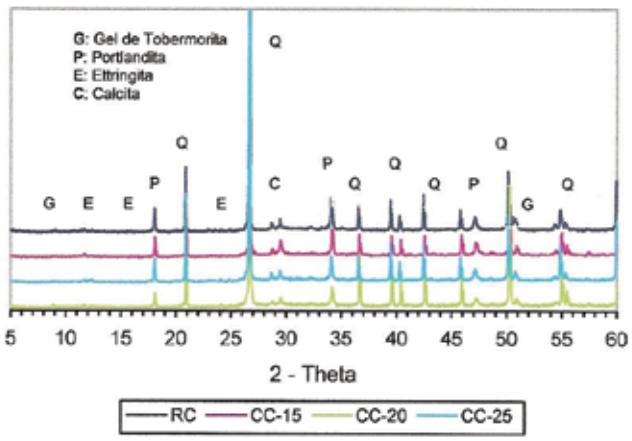

Fig. 13. X–ray diffraction of different concrete pastes

An analysis of the results demonstrates that the introduction of recycled ceramic aggregates has no negative effects on cement hydration, and can thus be considered an inert material.
In the light of the results obtained from the research conducted to date, we can confirm that following prior treatment (crushing, washing and sieving), waste from the ceramic sanitary ware industry can be used to partially substitute natural coarse aggregates, and indeed confers the recycled concrete with positive characteristics as regards mechanical behaviour. The recycled concrete obtained can be used for structural purposes, since its characteristic compressive strength exceeds 25 N/mm², the minimum strength requires for structural concrete.
Reuse of this kind of waste has many advantages, not least of which are the economic advantages, including job creation in companies specializing in the selection and recycling of this kind of material. It goes without saying that reuse is better than recycling; thus, there are considerable environmental benefits to using materials with such a high level of *embodied energy*, such as a reduction in the number of natural spaces employed as refuse dumps and a decrease in the quarrying necessary to extract conventional natural aggregates. Indirectly, all the above contributes to a better quality of life for citizens.
Lastly, it should be noted that the production of **concrete made with recycled aggregates** comprises part of the **correct management of CDW** – Law 10/98, EU ministerial council of the 27th June, 2006 – given that:

- it avoids the use of new raw materials
- it reduces waste generation

- and it makes maximum use of the energy already contained in the waste

Together, these factors constitute one of the basic cornerstones of sustainable development.

4. Acknowledgements

This research has been made possible thanks to funding received from the Spanish research project (AMB96-1095). We also must acknowledge the funding received from the University of León (Spain) under the research project "Recycled eco-efficient concretes produced with ceramic fraction from construction and demolition wastes"

5. References

ANEFA (2008). Primer descenso del consumo de áridos en los últimos 15 años: Informe estadístico anual de ANEFA. *CIC: publicación, mensual sobre arquitectura y construcción*, nº 453, (Julio – Agosto 2008), 48 – 55, 1576-1118.

Anón. (2001) El Plan Nacional se ha fijado unos ambiciosos objetivos. *Cercha,* nº 61, (Octubre 2001), 17-18.

Binici, H. (2007). Effect of crushed ceramic and basaltic pumice as fine aggregates on concrete mortars properties. *Construction and Building Materials*, vol. 21, Issue 6, (June 2007), 1191 – 1197, 0950-0618.

Cachim, P.B. (2009) Mechanical properties of brick aggregate concrete. *Construction and Building Materials*, vol. 23, Issue 3, (March 2009), 1292 – 1297, 0950-0618.

Calleja, J. (1970). Las puzolanas. Ión, No. 340, 341, 343 y 344, (November and December 1969; February and March 1970), 623-638, 700-713, 81-90, 154-160.

Correia, J.R.; de Brito,J.; Pereira, A.S. (2006). Effects on concrete durability of using recycled ceramic aggregates. *Materials and Structures*, vol. 39, No. 2, (March 2006), 169-177, 1359-5997.

de Brito,J.; Pereira, A.S.; Correia, J. R. (2005). Mechanical behaviour of non-structural concrete made with recycled ceramic aggregates. *Cement and Concrete Composites*, vol. 27, Issue 9 – 10, (October – November 2005), 429-433, 0958-9465.

Domínguez, J. A.; Martínez, E.; Villanueva, V. (2004). Hormigones reciclados: una alternativa sustentable y rentable. *Cemento – Hormigón*, nº 867, (Octubre 2004), 34– 45.

EHE, 2008. Instrucción de hormigón estructural. Ministerio de Fomento, Madrid.

Evangelista, L.; de Brito, J. Mechanical behaviour of concrete made with fine recycled concrete aggregates. *Cement and Concrete Composites*, vol. 29, Issue 5, (May 2007), 397 – 401, 0958-9465.

Frías, M., Rodríguez, O., Vegas, I. & Vigil, R. (2008). Properties of Calcined Clay Waste and its Influence on Blended Cement Behavior. *Journal of the American Ceramic Society*, Vol. 91, No. 4, (April 2008), 1226-1230, 0002-7820.

Gomes, M.; de Brito, J. (2009). Structural concrete with incorporation of coarse recycled concrete and ceramic aggregates: durability performance. *Materials and Structures*, vol. 42, No. 5, (June 2009), 663 – 675, 1359-5997.

González, B.; Martínez, F. (2005). Recycled aggregates concrete: aggregate and mix properties. *Materiales de Construcción*, vol. 55, nº 279, (July – September 2005), 53 – 66, 0465-2746.

Guerra, I.; Vivar, I.; Llamas, B.; Juan, A.; Morán, J. M. (2009). Eco-efficient concretes: The effects os using recycled ceramic material from sanitary installations on the mechanical properties of concrete. *Waste Management*, Vol. 29, Issue. 2, (February 2009), 643 – 646, 0956-053X.

Huete, R.; Blandón, B.; Rolón, J. (2005). Posibilidades de aplicación del material granular obtenido a partir de residuos de construcción y demolición de hormigón y cerámica. *Residuos*, nº 85, (Julio – Agosto 2005), 32 – 36, 1131-9526.

Ignacio, J. (2007). Gestión de residuos de construcción y demolición. *Informes de la Construcción*, vol. 59, nº 506, (April – June 2007), 131-132, 0020-0883

Juan, A.; López, V.; Morán, J.M.; Guerra, M. I. (2007). Reutilización de restos de cerámica blanca como áridos para la elaboración de hormigones. *Ingeniería Civil*, nº 147, (July – September 2007), 85 – 90, 0213-8468.

Juan, A.; Medina, C.; Guerra, M. I.; Llamas, B.; Morán, J. M.; Tascón, A. (2010). Re-use of construction and demolition residues and industrial wastes fro the elaboration or recycled eco-efficient concretes. *Spanish Journal of Agricultural Research*, Vol. 8, No. 1, (2010), 25 – 34, 1695-971-X.

Kim Goo – Dae, Kim Tae – Bong (2007) Development of recycling technology from waste aggregate and dust from waste concrete. *Journal of Ceramic Processing Research*, vol. 8, Issue 1, 82 – 86, 1229-9162.

Koch, H.V. & Steinegger, H. (1960), Ein Schnellprüfverfahren für zemente auf ihr Verhalten bei Sulfatangriff, Hauptlaboratorium der Pórtland-Zementwerke Heidelberg A.G.

López, V.; Llamas, B.; Juan, A.; M. Morán, J. M.; Guerra, M. I. (2007). Eco-efficient Concretes: Impact of the Use of White Ceramic Powder on the Mechanical Properties of Concrete. Biosystems Engineering, vol. 96, Issue 4, (April 2007), 559 – 564, 1537-5110.

Koyuncu, H.; Guney, Y.; Yilmaz, G.; Koyuncu, S.; Bakis, R. (2004). Utilization of ceramic wastes in the construction sector. *Key Engineering Materials*, vol. 264 – 268, 2509 – 2512, 1662-9795.

Portella KF, Joukoski A, Franck R, Derksen R (2006) Secondary recycling of electrical insulator porcelain waste in Portland concrete structures: determination of the performance under accelerated aging. *Cerâmica*, (52), 155 – 167

Puertas, F.; Barba, A.; Gazulla, M. F.; Gómez, M. P.; Palacios, M.; Martínez, S. (2006). Ceramic wastes as raw materials in Portland cement clinker fabrication: characterization and alkaline activation. *Materiales de Construcción*, vol. 56, nº 281, (January – March 2006), 73 – 84, 0465-2746.

Rolón, J. C.; Nieve, D; Huete, R.; Blandón, B.; Terán, A.; Pichardo, R. (2007). Characterization of concrete made with recycled aggregate from concrete demolition waste. *Materiales de Construcción*, vol. 57, nº 288, (October – December 2007), 5 – 15, 0465-2746.

Sánchez, M.; Alaejos, P. (2003). Árido reciclado procedente de escombros de hormigón para la fabricación de hormigón estructural. *Cemento – Hormigón*, nº 850, (Junio 2003), 36 – 50.

Sánchez,M.; Alaejos, P. (2005) Recomendaciones para la utilización de árido reciclado en hormigón. *Cercha*, No. 78, (Febrero 2005), 70 – 80.

Sánchez, M; Alaejos, P. (2006). Influencia del árido reciclado en las propiedades del hormigón estructural. *Cemento – Hormigón*, nº 889, (Junio 2006), 54 – 61.

Sánchez de Rojas, M.I., Frías, M.; Rivera, J.; Escorihuela, M.J. & Marín, F.P. (2001). Investigaciones sobre la actividad puzolánica de materiales de desecho procedentes de arcilla cocida. *Materiales de Construcción*, Vol. 51, No. 261, (January-March 2001) 45-52, 0465-2746.

Sánchez de Rojas, M.I., Frías, M., Rivera,J. & Marín, F.P. (2003). Waste products from prefabricated ceramic materials as pozzolanic addition. *Proceedings of 11th International Congress on the Chemistry of Cement*, pp. 935-943, 0-9584085-8-0, May 2003, Alpha, Durban.

Sánchez de Rojas, M.I., Marín, F.P., Rivera, J. & Frías, M. (2006). Morphology and properties in blended cements with ceramic waste materials recycled as pozzolanic addition. *Journal of the American Ceramic Society*, Vol. 89, No. 12, (December 2006), 3701-3705, 0002-7820.

Sánchez de Rojas, M.I., Marín, F., Frías, M. & Rivera, J. (2007): "Properties and performances of concrete tiles containing waste fired clay materials". *Journal of the American Ceramic Society*, Vol. 90, No. 11, (November 2007), 3559-3565, 0002-7820.

Senthamarai, RM.; Devadas Manhoharan, P. Concrete with ceramic waste aggregate. *Cement and Concrete Composites*, vol. 27, Issue 9-10, (October – November 2005), 910-913, 0958-9465.

Silva, J.; de Brito, J.; Veiga, R. (2010). Recycled red – clay ceramic construction and demolition waste for mortars production. *Journal of Materials in Civil Engineering*, vol. 22, No. 3, (March 2010), 236 – 244, 0899-1561.

11

Ceramic Products from Waste

André Zimmer
Instituto Federal de Educação, Ciência e Tecnologia do Rio Grande do Sul
Brazil

1. Introduction

The industrial revolution changed the world; it generated the great humanity progress. But, the industrialization is accompanied by the generation of wastes, which could be negative to the natural environment. Unfortunately, environmental issues were not remembered, as should be.

One general conclusion from Gungor and Gupta (1999) in their literature review is: environmental issues are gaining justifiable popularity among society, governments and industry due to negative environmental developments.

The current state of manufacturing processes consume enormous tons of different forms of natural resources like raw materials, energy, water, etc.

The giant amount of waste generated is still far from being used in its totality as a product or by-product, making technological alternatives needed in order to reduce its possible environmental impact; where, the major potential impacts of its disposal on terrestrial ecosystems include: leaching of potentially toxic substances into soils and groundwater; reductions in plant establishment and growth due primarily to adverse chemical characteristics of the waste; changes in the elemental composition of vegetation growing on the waste; and increased mobility and accumulation of potentially toxic elements throughout the food chain.

There are many reasons to increase the amount of waste being utilized or re-utilized. Firstly, disposal costs are minimized; secondly, less area is reserved for disposal, thus enabling other uses of the land and decreasing disposal permitting requirements; thirdly, there may be financial returns from the sale of the by-product or at least an offset of the processing and disposal costs; and fourthly, the by-products can replace some scarce or expensive natural resources (Ahmaruzzaman, 2010).

Waste such ashes from: coal, municipal solid waste, wood, and so on, have good potential for use in ceramic products. Various ceramics systems have been shown to be suitable for producing products that are thermally and mechanically stable and exhibit good chemical durability. Palomo et al. (1999) activate fly ash for applications in building sites. The studies of Barbieri et al. (1999) and Leroy et al. (2001) are examples of the glass–ceramics obtained using fly ash. The results obtained by Zimmer & Bergmann (2007) indicate that fly ash, when mixed with traditional raw materials, has the necessary requirements to be used as a raw material for production of ceramic tiles.

Ceramic products have the largest range of functions of all known materials. Despite the already existing variety of compounds, the number of processing techniques, and the known diversity of properties and applications of the materials, ceramics are synthesized into glasses, polycrystals, and single crystals, and many forms dictated by their use, including fine powders, fibres, thin films, thick films, coatings, monoliths, and composites. Polycrystalline components are conventionally produced by powder synthesis and forming processes followed by sintering at high temperature compared to polymers processing temperature.

The main advantages of the ceramic processing route include the fact that ceramics can be processed at reasonably low temperatures; a large number of ceramics product is tolerant of variations in waste composition; ceramics exhibits reasonable chemical durability - ceramics are radiation resistant and can suffer changes occurring at different environments as humidity, temperature, sun, salt, wind, and so on.

However, the main concern in the use of a waste as secondary raw material in the formulation of a ceramic product is its immobilization inside the ceramic body after transformations occurred during the ceramic process, at the thermal treatment; which, depending of the ceramic product could fuse, partially fuse or sinter the ceramic formulation.

Ceramics product could be considered interesting in the immobilization of hazardous wastes, because they are able to retain heavy metals in their structure with a significant reduction of volume.

The positive aspects of waste inertization technology in ceramic products are process flexibility since various types of wastes such as sediment and ashes can sometimes be used without preliminary preparation.

There are several ways to start a formulation of one ceramic product, which the easiest form is evaluate the effects of waste addictions in a ceramic formulation.

The properties of ceramic products depend of its composition. Calculating oxide composition of an intended formulation containing waste is a profit compared with simple waste additions. However, relative calculations of compositions are not the only think that influences the manufacture of a ceramic product, it is important too: loss of ignition (outlet material), particle friction (influences the particle mobility), particle size (thinner are more reactive), etc.

There are a number of measurements to determine the nature of the waste besides its compositions. A good characterization is primordial to starts a formulation of a ceramic product using waste. Chemical composition, mineralogical composition, granulometric size distribution and morphologic aspect are important things to be analyzed. But, a good waste characterization is accompanied of thermo-gravimetric analysis (TGA), differential thermal analysis (DTA), and refractoriness and so on to understand the properties that each waste could give to a specifically ceramic product.

The aim of this chapter was to study the use of waste in ceramic formulations with or without traditional raw materials that would result in ceramic products with satisfactory technological properties, allowing its utilization.

It will be discussed the requisites that one waste must have to be added in a ceramic formulation and when ceramics products not support waste.

2. Overview of Researches in Ceramic Waste

The ceramic heat treatment process has been demonstrated as one valid technologies for the inertization and volume reduction of different categories of wastes. The produced ceramic produtct can in fact subsequently be disposed in landfill sites reducing environmental hazard.

As an example of application with the worst waste (radioactive waste) in its reducing environmental hazard was related by Donald et al. (1997) work, where one solution could be the waste form, in other words, the rationale behind the immobilization of radioactive waste materials in glass or ceramic hosts is to provide a solid, stable and durable material that can be more easily stored or disposed of than the current liquid wastes. Immobilization may be accomplished either by dissolution of the waste elements on an atomic scale within the host lattice, or by encapsulation of the waste within an inert matrix. Wasteforms can be temporarily stored at the solidification processing plant (during which time the heat generated by the decay of the fission products decreases), but the longer term strategy is to dispose of them permanently in an underground repository as part of a multibarrier approach. The immobilized waste would therefore form only one part of an engineered system designed to prevent contamination of the biosphere with radioactive elements.

There are many wastes and kind of wastes disposed in landfills that could be used as a ceramic raw material. There are many kinds of ceramic products, it is thus necessary, for the utilization of civil or industrial wastes, to look for ceramic technologies in order to generate components in cementitious, glass or traditional ceramics.

Incineration is a commonly accepted solution throughout the world for managing the increasing production of Municipal Solid Waste (MSW). In the Ferreira et al. (2003) work, three main factors were considered relevant to evaluate fly ash suitability for each application: suitability for processing, technical performance and environmental impact:

- the first factor, suitability for processing, depends on physical–chemical characteristics of the fly ash, such as particle size and chemical properties, that may constitute a limitation for a specific process (although in some cases these characteristics can be adjusted so as to comply to processing requirements);
- technical performance is the second factor considered. Even if fly ash can be easily processed, the final product cannot be used unless it presents good technical properties;
- finally, the third factor considered is environmental impact. Toxicity does not necessarily disappear with fly ash valorisation. The risks imposed on the environment by each possible application must be carefully weighed against creating new pollution sources elsewhere.

Colombo et. al (2003) reviewed waste vitrification technologies and related that analysis of different methods of vitrification, according to physical state and composition of the waste, can offer a guideline for process selection. The vitrification process, initially proposed for high level radioactive waste management, has been demonstrated as one of the most valid technologies for the inertization and volume reduction of different categories of wastes, as testified by a large and growing scientific literature devoted to the topic. The produced glass can in fact subsequently be disposed in landfill sites without posing any environmental hazard.

According to Colombo et. al (2003), the main advantages of the vitrification process are:

- inorganic glasses can incorporate large amounts of heavy metal ions, chemically bonding them inside their inorganic amorphous network;

• the obtained glasses are inert towards most chemical or biological agents, so they can be disposed of in landfills without problems or used for roads, pavements, embankments, etc.;
• the vitrification process can accept wastes of different composition and form, such as liquids, muds, solids or their mixtures. Therefore, a well designed vitrification plant can be flexible enough to treat wastes of various type, without or with a minimal pre-treatment;
• vitrification is a mature technology, and glass-forming systems have been extensively investigated in the academia, so their properties are well known;
• vitrification results in a large reduction in volume of the waste.

In one method for the immobilization of high level radioactive waste (HLW) as reviewed by Donald et al. (1997) a suitable glass host is used to dissolve the HLW to form a glassy (vitreous) homogeneous product that can be cast into suitable forms, including large glass blocks. Under suitable conditions, it is possible to incorporate up to 25-30 wt% HLW into a glass. The choice of glass composition is a compromise between high HLW solubility, manageable glass formation temperature, and low leachability in repository environments. Various glass systems have been shown to be suitable for producing waste glass forms that are thermally and mechanically stable and exhibit good chemical durability. The main advantages of the vitrification route include the fact that glass is a good solvent for HLW; glass can be processed at reasonably low temperatures; glass is very tolerant of variations in waste composition; glass exhibits reasonable chemical durability; and glass is radiation resistant and can accommodate changes occurring during radioactive decay of HLW constituents (Donald et al., 1997).

3. Ceramic Processing

Usually, the ceramic products are manufactured from materials which are solid state, which most often is in powder form. The consolidation of a part can occur with or without fusion of the employed raw material. Even the ceramic products that are manufactured at room temperature or close to it, such as cement and gypsum, its raw materials have undergone a prior heat treatment at high temperatures – more than half melting temperature. During the heat treatment that the material has suffered, a thermal activated atomic diffusion leads to the formation of phases which act as a trapping against the leaching of these elements in their operating life.

However, mostly of time is cost impeditive the use of the class of ceramics called "advanced ceramics", these kind of products are distinguished by their high chemical purity, careful processing and high values of the useful properties.

Advanced ceramics are materials systems more refined, sometimes with special compounds and the processes were developed for high structural performance: biocompatibility, magnetic and electronic applications, among other special application – with specific property from high technological demand.

Ceramic processing is used to produce commercial products that are very diverse in size, shape, detail, complexity, and material composition, structure, and cost. Ceramics are typically produced by the application of heat upon processed natural raw materials (minerals) to form a rigid product.

Ceramic products that use naturally occurring minerals as a starting material most of time undergo special processing in order to control purity, particle size, particle size distribution, and heterogeneity. These attributes have an important character in the final properties of the

finished ceramic. Chemically prepared powders also are used as starting materials for some ceramic products. These synthetic materials can be controlled to produce powders with precise chemical compositions and particle size.
According to Reed (1995), ceramics processing commonly begins with one or more ceramic materials, one or more liquids, and one or more special additives called processing aids. The starting materials or the batched system may be beneficiated chemically and physically using operations such as crushing, milling, washing, chemical dissolving, settling, flotation, magnetic separation, dispersion, mixing, classification, de-airing, filtration, and spray-drying.
Before the development of scientific insights of ceramics processing, the properties of the product were often correlated with changes in a processing operation to identify the more important superficial variables. This empirical approach is still used. However, empirical correlations such as these do not provide a scientific understanding of the fundamental causes of behavior during processing and forming. The probability that adjustments based on empirical correlations alone will produce significant advances is small, because the potential number of unsuccessful combinations of variables is always relatively coarse. Also, empirical correlations may be of little heuristic value when the processing engineer is faced with a lack of reproducibility in manufacturing, an insufficient reliability in the performance of nominally identical products, or when developing new products (Reed, 1995).
Viewed as a science, ceramics processing is the sequence of operations that purposefully and systematically changes the chemical and physical aspects of structure, which we call the characteristics of the system (Reed, 1995).
The objectives of the science of ceramics processing are to identify the important characteristics of the system and understand the effects of processing variables on the evolution of these characteristics. The objectives in process engineering should be to change these characteristics purposefully to improve product quality. Because of the key dependence on controlling characteristics, an understanding of techniques for characterizing the starting materials and the process system at each stage is an integral part of any discussion of ceramics processing (Reed, 1995).

3.1. Characterization of Ceramic Raw Materials

As a starting point for the use of waste as ceramic raw material is the knowledge of the whole environment generator of this waste to be aware of the possible constituents of this waste, including small proportion. It is also necessary to assess whether the process can produce different wastes in different periods. One think should be careful if there is a possibility that the residue present or release corrosive gases when thermally processed (COS, H_2S, HCl, SO_2, NO_x etc.), which can cause problems in the equipment with which it will contact.
The next step is to characterize morphological and dimensional waste constituents with microscopy technique and could supplement with granulometry. In general, smaller dimensions of the components from residue, higher will be the reactivity and the lower will be the fluidity. Likewise, morphology with low aspect ratio is less favourable fluidity and also to its packaging.
The chemical analysis is essential, but it is not easy without knowing beforehand what they may contain the residue and the possible elements of which it consists.

From the knowledge of the chemical composition, it is promising to have an idea of what are the possible applications that a waste may have. Besides the chemical composition, identification and quantitative estimation of the proportions of the various mineral species in a system such as waste polycompost provide important information to get an idea of what the behavior of the residue of an application as ceramic product.
An important factor of mineralogical knowledge is its crystallinity, which could indicate the possible isomorphic replacements, which are more intense in materials of lower crystallinity in comparison to their relative high crystallinity.
However, before proceeding with a possible test of this residue is important to know their loss to fire (LOI), which is more appropriately accomplished by a thermogravimetric analysis (TGA).
Figure 1 shows a TGA analysis of a hypothetical waste, this mass loss is concentrated between 200 and 300 ° C and corresponds to approximately 90% until a temperature of 1000 ° C. If this residue were used, it will results in their almost total escape into the atmosphere.
The loss is linked to the output of volatiles during thermal processing and in some ways is a component that acts against the consolidation of the ceramic material, which can be bad for a dense ceramic or good for a refractory insulating material of low density. In the study of Bragança, Zimmer and Bergmann (2008), for example, is employed wood waste (sawdust) to form the porosity of a refractory insulator. The sawdust can generate output for its porosity and also contributes exothermically to the firing process due to its oxidation reaction - combustion.
It is noteworthy that the volume reduction due to material output is far superior to weight reduction, because the gases that go out have lower density compared with the remains, the latter is usually inorganic.

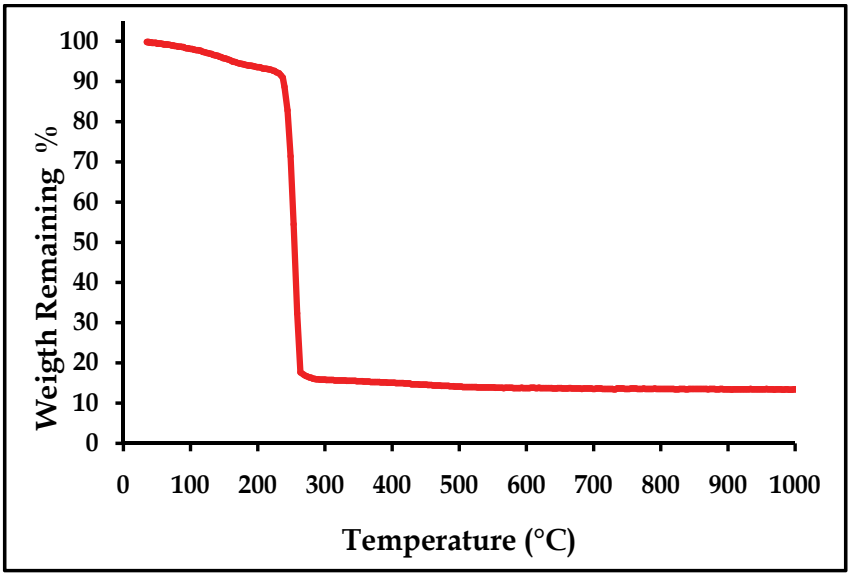

Fig. 1. Thermogravimetric annalysis from a hipotetical waste.

Concerning the size of the particles that form the residue or the grain size, can have sizes either coarse or small (bellow 50 micrometers). There are applications in ceramic products

for a wide range of particle size and if the particle size is very large for an application, it can be milled. The grind is a costly step and demand time, then should be avoided or very well rated for not making its use financially unfeasible.
Another property that can be easily assessed is the pyrometric cone equivalent (PCE). The PCE is a measurement of refractoriness given according to tests made with material in a cone pattern.
The deformation and softening due to the temperature rise are compared to material standards. Cones are designed to deform at certain times during firing, simply to record what happened during the firing (control). The exact moment when the cone is deformed mainly depends on two factors: time and temperature. With this concept in mind, it is necessary take care that PCE and temperature is not the same thing.
Like the PCE, the piroplasticity index (*PI*) could be applied to know firing details of ceramic products The *PI* is a deformation of a specimen of certain size subjected to the action of gravity during firing under specific conditions. The procedure used to determine the rate of piroplasticity during the firing process consists of measuring the deflection of curvature of a specimen on two supports, separated by a distance determined, as shown in Figure 2.

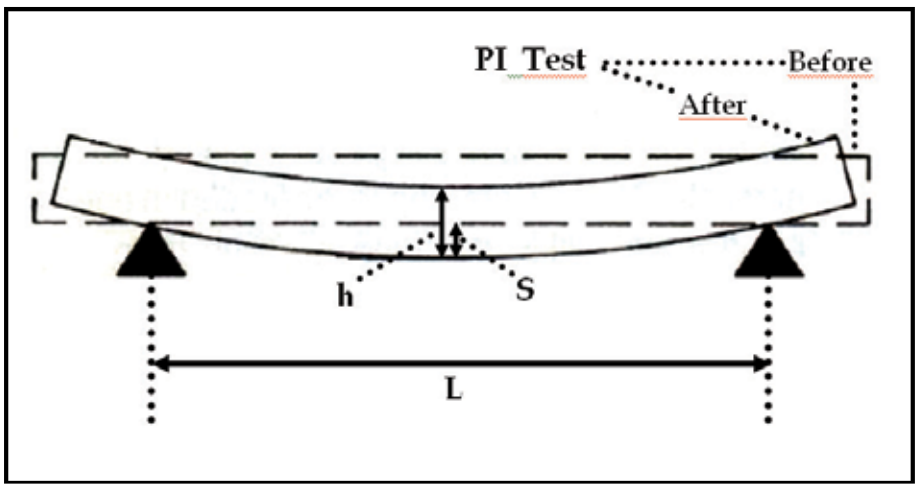

Fig. 2. Scheme of *PI* test.

The equation bellow (1) is applied for determine the *PI*, where h is the thickness of the body, S is the deflection of deformation measured by the deflection of the specimen and L is the distance between the on two supports.

$$PI = \frac{4k^1 S}{3L^4} \tag{1}$$

Finally, an evaluation by a dilatometry curve can provide information about which temperature begins sinter and other information as the phase transformations and coefficients of thermal expansion. However, this analysis should be undertaken only after knowing the temperature where the material begins to soft (PCE temperature), to avoid damage in the dilatometer due to melting of the waste inside the equipment.

Figure 3 shows the dilatometric curve of a hypothetical waste, this at a temperature slightly above 700 °C is the largest expansion of the waste due to increased atomic agitation. However above this temperature, the thermal expansion is suppressed by the beginning of sintering, a phenomenon which is stronger as the temperature increases.

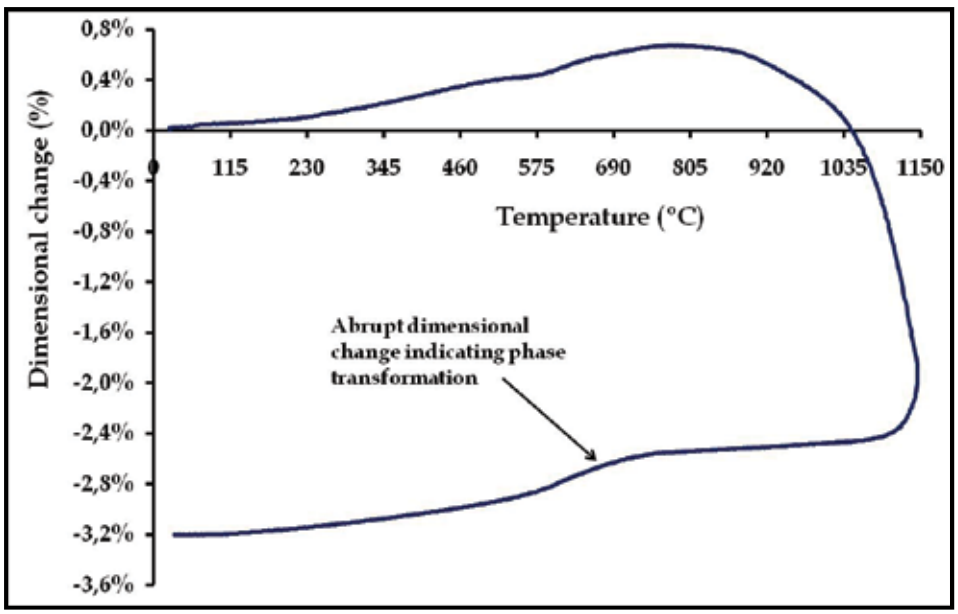

Fig. 3. Expansion/contraction of a hipotetic waste.

3.2. Preparation of Ceramics Formulations

The main types of ceramics products are based on aluminosilicate, potassium silicate (K_2O-Al_2O_3-SiO_2) or magnesium silicates (MgO-Al_2O_3-SiO_2).

The performances of ceramic materials are determined not only by the structure and composition, but also by defects (such as pores), second phases (which can be deliberately added to facilitate processing), and interfaces.

Special groups are zircon and mullite-based ceramics fine as well as low-thermal expansion ceramics in the system Li_2O-Al_2O_3-SiO_2 and borosilicates.

In Figure 4 is shown a schematic ternary diagram with the percentage mole of Al_2O_3, SiO_2 and alkalis. This diagram shows in generic way the molar composition of silica-alumina refractories, glass and traditional ceramics. A diagram like this can be used to verify, for example, as would be the maximum residue, in terms of chemical composition, that could be added to a ceramic formulation, and also serve to show in what area of this graphic take place the formulation with the increasing of the waste amount.

A system graphically expressed in chemical form (generally in oxide form), which could be among others in form of weight too, allows delineate the composition of a formulation and its application as a ceramic product. Ceramic products containing in their chemical composition in the form of oxides Al_2O_3, SiO_2 and alkali oxides and / or alkaline earth metals are widely used and a simplified manner are shown in Figure 4.

As can be seen in Figure 4, each class or type of material has a composition distinct from others and sometimes may have very similar compositions, but most often differ substantially from the heat treatment to which the material is submitted.

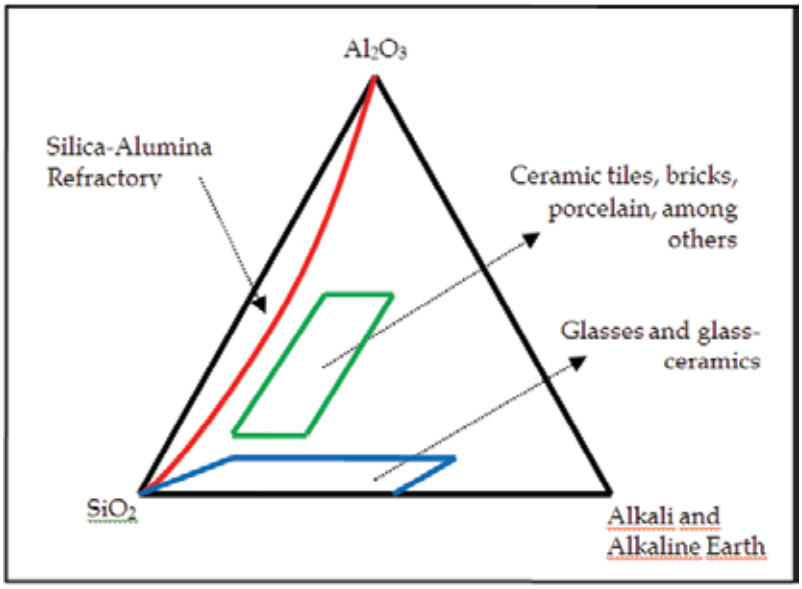

Fig. 4. Typical composition of common ceramic products.

The ceramic materials can be obtained from heat treatments that may be below or above its melting temperature. Among the main ceramic materials that are:

i) Glass - inorganic product of fusion which has been cooled fast enough to pass through its glass transition to the solid state without crystallising;

ii) Glass-ceramics - have an amorphous phase and one or more crystalline phases and could be produced by means of controlled devitrification (or controlled crystallization) of an already amorphous inorganic waste.

iii) Sintered materials – produced from powder, by heating the material below its melting point (solid state sintering) until its particles unite to each other.

Once chosen the method for ceramic manufacture, the next step is to give form into a desired shape for the ceramic raw material. In the ceramic products that will be sintered or chemically bonded with hydratation, this is accomplished by the addition of water and/or additives such as binders, followed by a shape forming process. Some of the most common forming methods for ceramics include pressing, extrusion, slip casting, tape casting and injection molding, among others.

The ceramic raw materials generally in small particles forms are sometimes agglomerated such an atomization to have a good fluidicity and compacticity, principally when will be pressed.

After ceramic shape forming, these material are “green" – they have form close to the final product and their properties are only to manipulate before next steps in the ceramics production. Then, a drying process is necessary to eliminate most of the addictives according to the Bigot curve – Figure 5.

The drying process is important stage where there is appreciable shrinkage that needs to be faster enough to avoid defect because the rapid shrinkage.

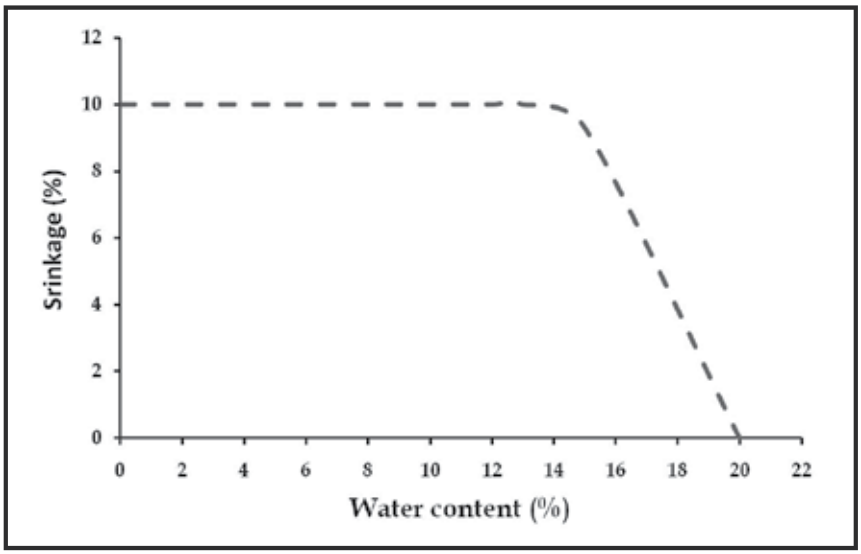

Fig. 5. The Bigot curve.

The heat-treatment called firing is applied to produce a rigid, finished product. Some ceramic products such as electrical insulators, dinnerware and tile may then undergo a glazing process. Some ceramics for advanced applications may undergo a machining and/or polishing step in order meet specific engineering design criteria.

3.3. Sintering temperature

Most of the known rules correspond to raw materials with simple compositions, ie, presenting few constituents. These rules had a margin of error, but provide information that can serve as a reference point.

The Tamman temperature is generally half of the melting temperature and is considered the point at which begins sintering in ceramics materials. The atoms mobility depends of atomic mobility and some factors such as texture, size and morphology. The following semi-empirical relations for Tamman temperatures (2) are more commonly used, where T_T is the Tamman temperature and T_m is the melting temperature.

$$T_T = 0.5T_m \tag{2}$$

Sintering requires the proper compromise of temperature, time and atmosphere to arrive at the desired porosity characteristics. With higher temperatures, longer times, or smaller particles, the bonds grow more rapidly and densification becomes more evident. Sometimes pressure could be additionally applied to increase the sintering effect.

The sintering temperature is selected by considering the material composition and the powder particle size distribution.

Temperature is the most important parameter in the sintering process since the temperature increase the atoms mobility – important factor in the sintering.

3.4. The Eutectic Point

The eutectic temperature shows the lowest possible melting point achievable in the phase diagram elements.

In combination with alumina and silica, eutectics for alkalis occur at significantly lower temperatures than eutectics for alkaline earths. This is one reason alkalis are considered stronger fluxes.

Alkali Eutectic Points:

- Sodia (Na_2-Al_2O_3-SiO_2): 732°C
- Potassia (K_2O-Al_2O_3-SiO_2): 695°C
- Lithia (LiO_2-Al_2O_3-SiO_2): 975°C

Alkaline Earth Eutectic Points:

- Calcia (CaO-Al_2O_3-SiO_2): 1170°C
- Baria (BaO-Al_2O_3-SiO_2): 1250°C
- Magnesia (MgO-Al_2O_3-SiO_2): 1355°C
- Strontia (SrO-Al_2O_3-SiO_2): 1400°C

Phase diagrams can seem like a map to navigate in the melting temperature for different compositions. Each map is developed for a specific group of chemical elements. Usual phase diagram may represent the melting of four materials, which is called a quaternary phase diagram.

No phase diagrams exist for most of the virtually infinite combinations of elements we could come up with. But, if is known that eutectics exist, it is necessary to find a complex composition that will bring our refractory material into the melt.

3.5. Cementitious

The main cementitious materials are the same present in the Portland cement.

There are four principal minerals present in the grain Portland cement: tricalcium silicate (Ca_3SiO_5), dicalcium silicate (Ca_2SiO_4), tricalcium aluminate ($Ca_3Al_2O_5$) and calcium aluminoferrite ($Ca_2(Al,Fe)_2O_5$). The formula of each of These minerals Can Be broken down into the basic calcium, silicon, aluminum and iron oxide (Table 1). Cement chemists use abbreviated nomenclature based on Oxides of Various elements to Indicate chemical formulas of Relevant species, ie C = CaO, S = SiO_2, A = Al_2O_3, Fe_2O_3 = F. Here, traditional cement nomenclature abbreviates the oxide and is shown in Table 1.

Mineral	Chemical Formula	Oxide Composition	Abbreviation
Dicalcium Silicate (belite)	Ca_2SiO_4	$2CaO.SiO_2$	C2S
Tricalcium silicate (alite)	Ca_3SiO_5	$3CaO.SiO_2$	C3S
Tricalcium Aluminate	$Ca_3Al_2O_4$	$3CaO.Al_2O_3$	C3A
Tetracalcium Aluminoferrite	$Ca_4Al_nFe_{2-n}O_7$	$4CaO.Al_nFe_{2-n}O_3$	C4AF

Table 1. Chemical formulae and cement nomenclature for major constituents of Portland cement. Abbreviation notation: C = CaO, S = SiO_2, A = Al_2O_3, F = Fe_2O_3.

The composition of cement is varied depending on the application. A typical example of cement contains 50–70% C3S, 15–30% C2S, 5–10% C3A, 5–15% C4AF, and 3–8% other

additives or minerals (such as oxides of calcium and magnesium). It is the hydration of the calcium silicate, aluminate, and aluminoferrite minerals that causes the hardening, or setting, of cement. The ratio of C3S to C2S helps to determine how fast the cement will set, with faster setting occurring with higher C3S contents. Lower C3A content promotes resistance to sulfates. Higher amounts of ferrite lead to slower hydration. The ferrite phase causes the brownish gray color in cements, so that "white cements" (i.e., those that are low in C4AF) are often used for aesthetic purposes.
The calcium aluminoferrite (C4AF) forms a continuous phase around the other mineral crystallites, as the iron containing species act as a fluxing agent in the rotary kiln during cement production and are the last to solidify around the others.
Although the precise mechanism of C3S hydration is unclear, the kinetics of hydration is well known. The hydration of the calcium silicates proceeds via four distinct phases. The first 15-20 minutes, termed the pre-induction period, is marked by rapid heat evolution. During this period calcium and hydroxyl ions are released into the solution. The next, and perhaps most important, phase is the induction period, which is characterized by very slow reactivity. During this phase, calcium oxide continues to dissolve producing a pH near 12.5. The chemical reactions that cause the induction period are not precisely known; however, it is clear that some form of an activation barrier must be overcome before hydration can continue. It has been suggested that in pure C3S, the induction period may be the length of time it takes for C–S–H to begin nucleation, which may be linked to the amount of time required for calcium ions to become supersaturated in solution. Alternatively, the induction period may be caused by the development of a small amount of an impermeable calcium-silicon-hydrate (C–S–H) gel at the surface of the particles, which slows down the migration of water to the inorganic oxides. The initial Ca/Si ratio at the surface of the particles is near 3. As calcium ions dissolve out of this C–S–H gel, the Ca/Si ratio in the gel becomes 0.8-1.5. This change in Ca/Si ratio corresponds to a change in gel permeability, and may indicate an entirely new mechanism for C–S–H formation. As the initial C–S–H gel is transformed into the more permeable layer, hydration continues and the induction period gives way to the third phase of hydration, the acceleratory period.
After ca. 3 hours of hydration, the rate of C–S–H formation increases with the amount of C–S–H formed. Solidification of the paste, called setting, occurs near the end of the third period. The fourth stage is the deceleratory period in which hydration slowly continues hardening the solid cement until the reaction is complete. The rate of hydration in this phase is determined either by the slow migration of water through C–S–H to the inner, unhydrated regions of the particles, or by the migration of H^+ through the C–S–H to the anhydrous CaO and SiO_2, and the migration of Ca^{2+} and Si^{4+} to the OH^- ions left in solution.

3.6. Oxide Glasses

Oxides glasses can be made from many compositions of silicates, aluminates, borates, phosphates, halides and chalcogenides.
Commercially glasses do not have fixed compositions, but there are many thousands of glasses, every one with a different composition.
It should be emphasised that the ability of a material to form a glass also depends on the cooling rate from the melted glass. This cooling rate is bellowing that the minimum cooling rate sufficiently to crystallization and the final temperature is bellow transition temperature.

There are three classes of components for oxide glasses: network formers, intermediates, and modifiers.
The network formers (for example: SiO_2, B_2O_3, GeO_2) form a continuous three-dimensional random network by themselves. The intermediates (for example: TiO_2, Al_2O_3, ZrO_2, Be_2O_3, MgO, ZnO) are that the cation can enter the network substitucionally, but which cannot by themselves normally form a network. The modifiers (for example: CaO, PbO, LiO, NaO, K_2O) alter the network structure; the cation can enter the network interstitially. Some elements can play multiple roles; e.g. lead can act both as a network former (Pb^{4+} replacing Si^{4+}), or as a modifier.
One possible disadvantage of waste use as a glass raw material is the coloring that could be obtained by the presence of ions in glasses materials that change colour when exposed to light. Frequently wastes present ions that result in a coloured glass, which is sometimes undesirable. Oxides of iron, titanium, chromium, cobalt, cadmium, nickel and cadmium are examples of components that could colour glasses.

4. Future Research

The characterization methods of materials have greatly improved its efficiency due to new technology that simplify its manufacture and also make easier the development of new methods of characterization.
Proper waste characterization is crucial, which will define the applications of each residue. The waste, because its intrinsic characteristics, can hardly be used for advanced applications without prior treatment because the highly costly involved in purification such as: electronic, electrical, and magnetic, among others.
Another aspect to be observed is if the use of waste may be dominantly negative to natural environment than its disposal in a landfill. In some cases, if the residue use requires a different process than a product without waste, which may require much more equipment and energy factors that have more environmental impact.
And not less important, independent of the method employed to conform a ceramic product, it is necessary take in account the pore volume of them, if not different things are being compared. Different ceramic processes and/or equipments employed generally produce different volume of pores in one product that strongly influences its properties. Sometimes some parameters need to be adjusted to the new raw material (waste in this case) develop similar porosities and then similar properties.
As an example, if a waste particles that has appreciable friction between other particles like the fly ash is employed substituting some part of a raw material with low fiction between particles, then it will be necessary a lubricant addictive and/or more strength to consolidate the ceramic product.
The negative environmental advance due to the industrialization must decrease to avoid the surging of untenable world. Therefore, new alternatives and known alternatives must be booth employed to minimize the waste generation and for the total usage of the waste generated.

5. References

Ahmaruzzaman, M. (2010). A review on the utilization of fly ash, Progress in Energy and Combustion Science, Vol. 36, (June 2010) page numbers (327–363), ISSN 0360-1285.

Barbieri, L., Lancellotti, I., Manfredini, T., Queralt, I., Rincon, J.M. & Romero, M. (1999). Design, obtainment and properties of glasses and glass–ceramics from coal fly ash, Fuel, Vol. 78, No. 2, (January 1999) page numbers (271–276), ISSN 0016-2361.

Bragança, S. R.; Zimmer, A.; Bergmann, C. P. Use of mineral coal ashes in insulating refractory brick. Refractories and Industrial Ceramics, p. 320, 2008.

Colombo, P.; Brusatin, G.; Bernardo, E.; Scarinci, G. Inertization and reuse of waste materials by vitrification and fabrication of glass-based products. Current Opinion in Solid State and Materials Science 7 (2003) 225–239.

Donald, I. W.; Metcalfe, B. L.; Taylor, R. N. J. Review - The immobilization of high level radioactive wastes using ceramics and glasses. Journal Of Materials Science 32 (1997) 5851–5887.

Ferreira, C.; Ribeiro, A.; Ottosen, L. (2003). Journal of Hazardous Materials, B96 (2003) 201–216.

Gungor, A.; Gupta, S. M. Issues in environmentally conscious manufacturing and product recovery: a survey. Computers & Industrial Engineering 36 (1999) 811-853.

Leroy, C., Ferro, M.C., Monteiro, R.C.C. & Fernandes, M.H.V. (2001). Production of glass–ceramics from coal ashes, Journal of the European Ceramic Society, Vol. 21, No. 2, (February 2001) page numbers (195–202), ISSN 0955-2219.

Palomo, A., Grutzeck, M.W. & Blanco, M.T. (1999). Alkali-activated fly ashes: A cement for the future, Cement and Concrete Research, Vol. 29, No. 8, (August 1999) page numbers (1323–1329), ISSN 0008-8846.

Reed, J. S. Principles of Ceramics Processing, 2nd Edition. ISBN: 978-0-471-59721-6, 688 pages, January 1995.

Zimmer, A.; Bergmann, C. P. (2007) Fly ash of mineral coal as ceramic tiles raw material. Waste Management (Elmsford), v. 27, p. 59-68.

Edited by Wilfried Wunderlich

This is the first book of a series of forthcoming publications on this field by this publisher. The reader can enjoy both a classical printed version on demand for a small charge, as well as the online version free for download. Your citation decides about the acceptance, distribution, and impact of this piece of knowledge. Please enjoy reading and may this book help promote the progress in ceramic development for better life on earth.

ISBN 978-953-51-5923-0

Photo by parinyabinsuk / iStock

IntechOpen